Bose-Einstein Condensates in Optical Lattices: The Superfluid to Mott Insulator Phase Transition

by

Jongchul Mun

Submitted to the Department of Physics
in partial fulfillment of the requirements for the degree of

Doctor of Philosophy

at the

MASSACHUSETTS INSTITUTE OF TECHNOLOGY

May 2008

Author .....
Department of Physics
May 23, 2008

Certified by .....
Wolfgang Ketterle
John D. MacAurther Professor of Physics
Thesis Supervisor

Certified by .....
David E. Pritchard
Cecil and Ida Green Professor of Physics
Thesis Supervisor

Accepted by .....
Thomas J. Greytak
Professor of Physics, Associate Department Head for Education

Bose-Einstein Condensates in Optical Lattices: The Superfluid to Mott Insulator Phase Transition

by

Jongchul Mun

Submitted to the Department of Physics
on May 23, 2008, in partial fulfillment of the
requirements for the degree of
Doctor of Philosophy

Abstract

^{87}Rb Bose Einstein Condensate in 3D optical lattice was studied in the regime of weak interaction(the superfluid phase) and strong interaction(the Mott insulating phase).

The stability of superfluid currents was studied using a moving optical lattice. The critical momentum for stable superfluid current varies from 0.5 recoil momentum (shallow lattice) to 0 (the Mott insulator) as the system reaches the Mott insulator transition. The phase diagram for the disappearance of superfluidity was studied as a function of momentum and lattice depth. Our phase diagram boundary extrapolates to the critical lattice depth for the superfluid-to-MI transition. When a one-dimensional gas was loaded into a moving optical lattice a sudden broadening of the transition between stable and unstable phases was observed.

A new auxiliary vacuum chamber, which is called the science chamber, was designed and installed to improve optical lattice experimental performance and imaging resolution power. Atoms are transported from the main chamber to the science chamber. By further evaporation cooling, BECs with $N \sim$ 2-3 $\times 10^4$ atoms are produced in a combination trap of two focused IR laser beams. High-resolution imaging was obtained with a 4-lens stack providing a resolution of $\sim 2\mu$m.

The deep Mott insulator(MI) phase was studied using clock shift spectroscopy. Individual MI phases with integer occupation numbers could be addressed through their clock shifts, and their spatial density profile could be imaged ("shell structure"). With increasing trap depth, MI shells expanded from low to high density regions of the cloud.

Thesis Supervisor: Wolfgang Ketterle
Title: John D. MacAurther Professor of Physics

Thesis Supervisor: David E. Pritchard
Title: Cecil and Ida Green Professor of Physics

To my wife, Miso

and my family

Acknowledgments

As I wrote my Ph.D. thesis, I realized that my time at MIT was one of the most precious and exciting moments in my life. Although being a Ph.D. student at MIT has not always been easy and straightforward to me, there has been so much help and support around.

First, I would like to thank Wolfgang Ketterle and Dave Pritchard for providing me the opportunity to work with them. It is a superb experience to have them as supervisors and learn how to face, think, approach and evaluate problems directly from them. Wolfgang's keen insight into physics has always amazed me; He has a wonderful ability to see and find beautiful things from what looks somewhat boring and unimportant. Also, I would like him for his consistent support and encouragement in the middle of many failures and sometimes slow progresses. Dave has always inspired me to see physics in different angles with challenging questions that I had never thought of. Those questions always have guided and helped me gain a solid understanding of my research projects with new insights.

I also owe much gratitude to former people in the Rb lab: Dominik Schneble, Aaron Leanhardt, Erik Streed, Micah Boyd, and Gretchen Campbell. When I joined the Rb BEC lab, I worked with Erik and Dominik. Dominik, who was a then postdoc, helped me be integrated into the group by teaching me about the machine and analysis tools. He also had great sense of humor - even though he did not seem to recognize it - to make it fun to work with him. I thank Erik for his guidance. His kind efforts to introduce me many experimental tools and techniques - especially laser and optics techniques - helped me figure out how to become an experimental scientist.

Micah was one of the people who built the Rb BEC machine, and he had mastery of the machine. Whenever I had problems with running the machine, he was the first person that I could rely on. I thank him for his patience in fixing many technical issues in spite of my many mistakes. I am still missing his many jokes including "Zul∼".

In 2004, I started collaborating with Gretchen. She had great energy and enthu-

siasm in the optical lattice projects. In spite of many initial technical difficulties, we could break through under her consistent and diligent leadership. I still vividly remember the moment when Gretchen and I finally observed the clock shift spectroscopy of the superfluid-Mott insulator transition in the freezing cold lab at 6 AM one day of February. Her enthusiasm and industrious work ethic has inspired me to focus my energy and thoughts on the experiments.

I have also benefited from working with current BEC IVers, Patrick Medley, David Weld, David Hucul, and Hiro Miyake. Patrick was a great lab partner. After simultaneous graduation of Gretchen and Micah, there were only two students left at that moment, Patrick and me. Patrick fitted into the lab very quickly and greatly improved the productivity of the Rb lab with his unique ideas. Patrick's insights into "everything" - regardless to say physics - have always impressed me, and it was delightful to discuss with him on many topics.

Our current postdoc David Weld had brought a boost to the Rb lab. He joined the group when the science chamber was being set up. A number of technical issues could be overcome with a help of his broad and deep understanding of physics. Also, his kind personality and tireless working style helps the Rb BEC lab be more functional and unified. David Hucul and Hiro Miyake are two junior graduate students in the lab. Even though I did not have many opportunities to work with them, I felt their huge enthusiasm whenever I talked with them about physics. I believe that the new crews of the Rb BEC lab will have many successes in the future.

It was fortunate for me to work with many other excellent people in Ketterle group and the center for ultracold atoms(CUA). It is an unique and ideal community for study and research of atomic physics. The weekly CUA seminars helped me learn about a broad range of atomic physics research areas. Most importantly, I could benefit from interactions and discussions with the people in the community. I also thank BEC I, II, III lab people for their kindness to share experimental experiences and generosity to lend me many of their own experimental optics.

My life at Cambridge has never been boring with many people who supported me outside the research group. I like to thank many friends in the first Korean church in

Cambridge and pastor Kim for their fellowship, support, and warm care for me and my wife. I thank KGSA soccer team for giving me the unforgettable memory of the final game in the MIT IM league. Weekly intense basketball games with my KGSA bball team people have provided me energies and refreshments.

I'd like to thank my family for love and support. My parents Seo-Ki Mun, who I believe sees from heaven, and Yeon-Hee Choi have always encouraged me to do my best in whatever I want to do. I thank my parents-in-law Seong-Wan Kim and Won-Hyung Lee for their thoughtful care.

Finally, I thank my wife Miso. I really do not know how to express my gratitude to my lovely one enough for her patient and endless support for my irregular experiment schedule. Every night when I came crazily late from the lab, she always waited for me and never forgot to give me a hug that always touched my heart. Through my days at MIT, her companionship has motivated and inspired me. She is the love of my life.

I give thanks to my shepherd, the LORD. I shall not be in want.

Contents

List of Figures

List of Tables

Chapter 1

Introduction

1.1 Bose-Einstein Condensates

BEC is a quantum mechanical phenomenon occurring at high phase space densities, generally realized at extremely low temperatures. Below a certain critical temperature, a large fraction of bosonic atoms occupy the ground state and form (or condense into) a giant matter wave. In this state, every atom behaves in the same way, and quantum mechanical effects become manifest on a macroscopic scale. A quantum world now becomes macroscopically visible to Alice "through the looking-glass of BEC".

The idea of Bose-Einstein Condensate (BEC) was first suggested by Bose and Einstein in 1924[12, 36, 37]. However, experimental realization of BEC had not been followed for over 70 years. Finally in 1995, the idea of Bose and Einstein was experimentally realized in a dilute atomic gas system of Rb[4] and Na[29] after the development of laser cooling techniques[22, 97, 24]. Nowadays BEC is routinely produced and studied in a number of laboratories over the world.

Since the advent of BEC, the research field of BEC has flourished very rapidly over the last decade, and BEC has been successful in serving as a unique and important test bed in exploring the quantum mechanical world. A number of theories and experiments using BEC have been performed and new possibilities suggested in a wide range of research topics: for example, atom interferometry, atom optics, precision

measurement, quantum computation, low-dimensional physics, quantum simulator of condensed matter system, etc. At the same time, the number of atoms in the BEC family has grown. 10 species of atoms have been reported to be condensed into BEC.

The role of BEC is not limited to studying bosons; its role is extended to the study of fermions. BEC performs as a refrigerator for fermions in achieving low temperature of fermi gases, and the BEC-BCS crossover has been studied very actively both theoretically and experimentally

1.2 Bose-Einstein Condensates in Optical Lattices

An optical lattice is a versatile tool for ultracold atomic physicists. It is employed for sub-recoil cooling [22, 24, 97], atomic clocks [121], atomic lithography [122, 82, 83], etc. When an optical lattice meets BEC, it makes the physics of BEC more interesting and richer.

In recent years, a BEC loaded in optical lattices has been extensively studied as a model system for condensed matter phenomena. Ultracold atomic system in optical lattice is an ideal implementations of the Bose-Hubbard model and it could serve as a "quantum simulator" to investigate condensed matter theories. Many open questions would be challenged and tested with this system. The system of BEC in optical lattice has major advantages over conventional condensed matter systems.

1. The system is defect-free.

2. The interaction is not as complicated as in conventional condensed matter system. The interaction is mainly due to s-wave collisions. (p-wave collisions could be manipulated)

3. The experimental parameters can be controlled easily, precisely and dynamically. This is usually carried out by controlling the optical power of optical lattice laser beams

4. Various optical lattice geometries can be implemented (i.e. simple cubic, triangular, or kagomè lattice geometries[105])

5. Lower dimensional system (1D, 2D) can be achieved

A number of topics in condensed matter theory could be investigated in optical lattice. The quantum phase transition between the superfluid and Mott insulator phase[52, 65, 42], and low-dimensional systems (1D [94, 86, 116, 71], 2D[58]) have been achieved and studied in optical lattices. Various topics have been proposed by theoretical works and wait to be experimentally realized using ultracold atoms and optical lattices: ferro and anti-ferromagnetism[47, 32, 99, 100], disordered systems [45, 79, 109, 23] (Bose glass, Anderson localization), spinor system in optical lattice[31, 56], quantum information[64, 91, 92, 112], frustrated antiferromagnetism[27, 28], dipolar gas system[54, 7], etc.

1.3 The Superfluid to Mott Insulator Transition

A BEC in an optical lattice realizes a nearly ideal system for Bose-Hubbard model. Bose-Hubbard model describes interacting atoms in a periodic potential with only two terms: a kinetic energy term for a hopping process between lattice sites and an interaction energy term for an on-site interaction between atoms in a same lattice site. The transition between the superfluid(SF) phase and the Mott insulator(MI) phase, which is an important paradigm of strongly correlated system where transport is suppressed by particle correlations, is described using this model.

This thesis focuses on the experimental realization and study of the SF-MI phase transition using a ^{87}Rb BEC in 3D simple cubic optical lattice. Transport property and number statistics have been experimentally investigated.

- Transport property: In general, one of the basic characterization experiments for typical condensed matter materials is to measure their conductivities (transport properties) by applying voltage. The transport properties of ultracold atomic system in optical lattice were studied across the SF-MI phase transition by using a moving optical lattice. The critical point for the phase transition is determined from the transport properties.

- Number statistics: Particle-particle correlations, which lead to the suppression of superfluid current in the MI phase, also modifies the number statistics of the system. Utilizing the clock shift in hyperfine transition of ^{87}Rb atoms, the density profile can be measured across the phase transition.

1.4 Outline

The outline of this thesis is as follows. In chapter 2, I discuss basic theory of BEC and the effect of the atom-atom interaction on the excitation spectrum of BEC. The excitation spectrum is modified to have a phonon mode by the presence of the atom-atom interaction leading to the superfluidity. The superfluidity in BEC is also discussed. In chapter 3, I discuss the dynamics of BEC loaded in optical lattice. A introduction to Bose-Hubbard Model and two quantum phases, the superfluid phase and the Mott insulator phase is given. Chapter 4 describes a new experimental setup, the science chamber. The science chamber is designed for optical lattice experiment and high resolution imaging. The experimental procedures such as optical tweezer transport, optical trapping of BEC, and the production of BEC are discussed. A new high resolution imaging lens setup is also described. In chapter 5, optical lattices are discussed as engineering tools of a BEC. Two experiments performed with optical lattices are briefly introduced. In chapter 6, transport property of superfluid in a regime of weak interaction to strong interaction is discussed. The critical point for the quantum phase transition between the superfluid and the Mott insulator phases could be measured from this transport measurement. The transport measurement in 1-D system is also discussed. In Chapter 7, clock shift spectroscopy of the Mott insulator phase is discussed as a density probe. Using two-photon pulse (μwave + rf), each Mott insulator shell could be addressed and imaged. The spatial profile of a Mott insulator could be obtained. Chapter 8 presents experimental demonstration of the quantum Zeno effect using a Rb BEC where the two-photon transition was used to create a coherently driven two-level system.

Chapter 2

Basic Theory

In this chapter, I present a short review of the basic properties of BEC. Since there have been already a number of good review papers, I simply refer to review papers[26, 77, 69, 70, 25], earlier theses[114], and books[96, 55, 107] for a more detailed and general review of BEC. In the following section, interactions in BEC are discussed. Excitation spectrum of BEC and its effect on superfluidity are presented. In the last section, the hierarchy of energy scales relevant to the BEC experiment is discussed.

2.1 Bose–Einstein Condensate

In a system of bosonic particle, as the temperature decreases the number of particles in a ground state increases according to the Bose-Einstein distribution. Below a critical temperature, the occupation number N_0 of the ground state becomes comparable to the total number N of atoms in the system. Such macroscopic occupation in a ground state is called Bose-Einstein condensation. As a quick estimate of critical temperature, dimensional calculation can be done in the following way. A macroscopic matter wave forms when the wave packet of atoms starts to overlap with each other. The thermal de Broglie wavelength of an atom is $\lambda_{dB} = \sqrt{2\pi\hbar^2/mk_BT}$, and the distance between atoms is $n^{-1/3}$ (n : density). The condition for the formation of a macroscopic matter wave is imposed by

$$\lambda_{dB} \sim n^{-1/3} \tag{2.1}$$

providing the critical temperature $k_B T_c \sim \frac{2\pi\hbar^2 n^{2/3}}{m}$. In a system of gas in a harmonic trap, for example, the density n is given by N/R^3 (N : total number of atoms, R : the size of the system). R can be estimated $kT \sim m\omega^2 R^2$ (ω : trapping frequency). The critical temperature is then determined by the condition in Eq. (2.1)

$$k_B T_c \sim \hbar\omega N^{1/3} \tag{2.2}$$

This dimensional estimation is already very close to the calculation of T_c in a system of non-interacting gas in a harmonic trap (see Eq. 2.8).

2.1.1 Non-interacting Atoms

Let us first consider a non-interacting Bose gas in a harmonic trap with trap frequencies ω_x, ω_y, ω_z. The energy spectrum of this system is given by

$$E_{n_x,n_y,n_z} = (n_x + 1/2)\hbar\omega_x + (n_y + 1/2)\hbar\omega_y + (n_z + 1/2)\hbar\omega_z \tag{2.3}$$

The number N and energy E at temperature T are derived from the partition function and Bose-Einstein statistics.

$$N = \sum_{n_x,y,z} \frac{1}{\exp[\beta(E_{n_x,n_y,n_z} - \mu)] - 1} \tag{2.4}$$

$$E = \sum_{n_x,y,z} E_{n_x,n_y,n_z} \frac{1}{\exp[\beta(E_{n_x,n_y,n_z} - \mu)] - 1} \tag{2.5}$$

where μ is chemical potential, and $\beta = (k_B T)^{-1}$. As the temperature T approaches zero, the occupation number of a ground state N_0 becomes $\mathcal{O}(N)$ and chemical potential $\mu \to E_{0,0,0}$. The number of atoms in this system is

$$N = N_0 + \sum_{n_{x,y,z} \neq \{0,0,0\}} \frac{1}{\exp[\beta(E_{n_x,n_y,n_z} - E_{0,0,0})] - 1} \tag{2.6}$$

In the limit of large number $N \to \infty$, the summation can be replaced by the integral ($\sum_{n_{x,y,z}} \to \int_0^\infty dn_x dn_y dn_z$). One gets the atom number in excited states $N_{\rm ex} = N - N_0$,

$$N_{\rm ex} = N - N_0 = 1.202 \left(\frac{k_B T}{\hbar \omega_{\rm ho}} \right)^3 \tag{2.7}$$

with $\omega_{\rm ho} = (\omega_x \omega_y \omega_z)^{1/3}$. The critical temperature for BEC can be determined from this equation by letting $N_0 \to 0$. The critical temperature T_c and the condensate fraction N_0/N are

$$k_B T_c = 0.94 \hbar \omega_{\rm ho} N^{1/3} \tag{2.8}$$

$$N_0/N = 1 - (T/T_c)^3 \tag{2.9}$$

2.1.2 Interacting Atoms

The effective interaction between atoms in BEC is due to s-wave scattering process. The effective two-body interaction may be written as a short range interaction potential $U(\mathbf{r}_1, \mathbf{r}_2) = g\delta(\mathbf{r}_1 - \mathbf{r}_2)$ with interaction strength $g = 4\pi\hbar^2 a_s/m$ (a_s: s-wave scattering length, m: atomic mass). Including this atom-atom interaction term, the many-body Hamiltonian for interacting bose gas in a trap potential $V_{\rm trap}(\mathbf{r})$ is [41]

$$\hat{H} = \int d\mathbf{r} \hat{\Psi}^\dagger(\mathbf{r}) \left(-\frac{\hbar^2}{2m} \nabla^2 + V_{\rm trap}(\mathbf{r}) \right) \hat{\Psi}(\mathbf{r}) + \frac{1}{2} \int d\mathbf{r}_1 d\mathbf{r}_2 \hat{\Psi}^\dagger(\mathbf{r}_1) \hat{\Psi}^\dagger(\mathbf{r}_2) U(\mathbf{r}_1, \mathbf{r}_2) \hat{\Psi}(\mathbf{r}_2) \hat{\Psi}(\mathbf{r}_1) \tag{2.10}$$

with the boson field operators $\hat{\Psi}^\dagger(\mathbf{r})$, $\hat{\Psi}(\mathbf{r})$. When the temperature T is near the critical temperature T_c, the number of atoms in a ground state is macroscopic ($\sim \mathcal{O}(N)$), and the field operator can be separated into two parts: one for the condensate part and the other for the excited state part. The excited state part of the field operator is small compared to the condensate part and can be treated as a perturbation term.

The field operator $\hat{\Psi}(\mathbf{r})$ may be written as

$$\hat{\Psi}(\mathbf{r}) = \Phi(r) + \delta\hat{\Psi}(\mathbf{r}) \tag{2.11}$$

where a complex function $\Phi(\mathbf{r})$ is the expectation value of the operator $\hat{\Psi}(\mathbf{r})$ and the condensate density $n_0(\mathbf{r})$ is given by $n_0 = |\Phi(\mathbf{r})|^2$.(Bogoliubov approximation) The classical field $\Phi(\mathbf{r}) = \langle\Phi(\mathbf{r})\rangle$ is analogous to the classical electric field $E = \langle\hat{E}\rangle$ defined as the expectation value of the operator $\hat{E}$. The complex function Φ may be called order parameter of the condensate (or the condensate wavefunction).

Assuming that the perturbation term $\delta\hat{\Psi}$ is very small and can be ignored, the field operator may be replaced by a c-number $\Phi(\mathbf{r})$. The equation of motion is the Heisenberg equation ($i\hbar\frac{\partial}{\partial t}\hat{\Psi}(\mathbf{r},t) = [\hat{\Psi}(\mathbf{r},t), \hat{H}]$). If one replaces $\hat{\Psi}(\mathbf{r},t)$ by $\Phi(\mathbf{r},t)$, the Heisenberg equation gives the equation for the condensate wavefunction $\Phi(\mathbf{r},t)$

$$i\hbar\frac{\partial}{\partial t}\Phi(\mathbf{r},t) = \left(\frac{\hbar^2}{2m}\nabla^2 + V_{\text{trap}}(\mathbf{r}) + g\,|\Phi(\mathbf{r},t)|^2\right)\Phi(\mathbf{r},t) \tag{2.12}$$

This is Gross-Pitaevskii(G-P) equation. This is a non-linear form of the Schrödinger equation with a normalization condition $\int d\mathbf{r}|\Phi|^2 = N$. The condensate wavefunction $\Phi(\mathbf{r},t)$ can be decomposed into a spatial and temporal part as in $\Phi(\mathbf{r},t) = \phi(\mathbf{r})\exp(-i\mu t/\hbar)$ where μ is chemical potential. Then time independent G-P equation is

$$\mu\phi(\mathbf{r}) = \left(\frac{\hbar^2}{2m}\nabla^2 + V_{\text{trap}}(\mathbf{r}) + g\,|\phi(\mathbf{r})|^2\right)\phi(\mathbf{r}) \tag{2.13}$$

where ϕ can be taken as real. This equation determines the phase of the condensate as well as the density of the condensate. The phase at a given time t is given by $\mu t/\hbar$, and the density by $|\phi(\mathbf{r})|^2$.

When the number of atoms is very large, the kinetic energy term in Eq. (2.13) becomes small compared to the interaction energy term and may be neglected (Thomas-Fermi approximation). Then one gets chemical potential μ and the density profile $n(\mathbf{r})$

$$\mu = V_{\text{trap}}(\mathbf{r}) + g\,|\phi(\mathbf{r})|^2 \tag{2.14}$$

$$n(\mathbf{r}) = |\phi(\mathbf{r})|^2 = \begin{cases} (\mu - V_{\text{trap}}(\mathbf{r}))/g & \text{if } \mu > V_{\text{trap}}(\mathbf{r}) \\ 0 & \text{otherwise} \end{cases} \tag{2.15}$$

The normalization condition of $\phi(\mathbf{r})$ ($\int d\mathbf{r}|\phi(\mathbf{r})|^2 = N$) provides the chemical potential μ

$$\mu = \frac{15^{2/5}}{2}\left(\frac{Na_s}{a_{\text{ho}}}\right)^{2/5}\hbar\omega_{\text{ho}} \tag{2.16}$$

with $a_{\text{ho}} = \sqrt{\hbar/m\omega_{\text{ho}}}$

2.1.3 How strongly do atoms interact?

If there is no interaction in a system, the system is identical to a statistical ensemble of single particle system. Due to lack of interaction, ideal gas atoms do not "see" the presence of other particles and can not "share" the wave function information such as the phase and density. As will be covered later in the chapter 2, a non-interacting system does not show interesting phenomena such as superfluidity, coherence, etc.

In opposite to the non-interacting ideal gas, the presence of interaction makes the real-life gas more complicated as well as interesting and fun to study. Atom-atom interaction in dilute gas system leads to many interesting and remarkable phenomena, one example of which is the superfluidity in BEC.

The next questions then arise; How strongly do atoms interact in a system of BEC and how does it affect the physics? The interaction strength of atoms in BEC is determined by the s-wave scattering length a_s. In order to estimate the interaction strength, this length scale a_s could be compared to another length scale: the interatomic space $n^{-1/3}$. From Bogoliubov theory, the parameter na_s^3 determines the quantum depletion of condensate ($n_{\text{ex}}/n \sim (na_s^3)^{1/2}$), which indicates how much non-zero momentum states are mixed into the ground state of the condensate by the presence of interaction. For ^{87} Rb, the quantum depletion is small $na_s^3 \sim 10^{-6} - 10^{-4}$

$\ll 1$ ($a_s \sim 5$nm, typical density range $n \sim 10^{13}\text{cm}^{-3} - 10^{15}\text{cm}^{-3}$). Under the condition of $na_s^3 \ll 1$, the condensate number N_0 should be close to the total number N. This condition validates the approximation used in the Eq.(2.11) that non-condensate part is neglected.

Another quantity that we can consider is the ratio of two energy scales : kinetic energy and interaction energy. The kinetic energy scale in the condensate is $\sim N\hbar\omega_{\text{ho}} = N\left[\hbar^2/ma_{\text{ho}}^2\right]$. The interaction energy scale is $\sim gn^2V = N\left[g(N/V)\right]$ with a volume $V \sim a_{\text{ho}}^3$. The ratio of kinetic energy to interaction energy is given by

$$\frac{E_{\text{int}}}{E_{\text{kin}}} \sim \frac{N\left[g(N/V)\right]}{N\left[\hbar^2/ma_{\text{ho}}^2\right]} \sim \frac{Na_s}{a_{\text{ho}}} \tag{2.17}$$

Typically the trapping frequency $\omega_{\text{ho}} \sim 2\pi \times 100$Hz ($a_{\text{ho}} \sim 1\mu$m), and $a_s/a_{\text{ho}} \sim 0.005$. For typical number of the condensate $N \sim 10^5 - 10^6$, the ratio of $E_{\text{int}}/E_{\text{kin}}$ is $\sim 500 - 5000$. In large N limit, the interaction energy dominates since the kinetic energy is proportional to N but the interaction energy to N^2. This condition validates the assumption that the kinetic energy term may be neglected in Thomas-Fermi approximation (Eq.2.15)

When BEC is loaded in an optical lattice potential, the kinetic energy is described by hopping matrix element J and the interaction energy is described by on-site interaction element U. The ratio of these two energy scales also plays an important role. When the hopping matrix element dominates ($J \gg U$), tunneling of atoms between adjacent sites keeps the phase of system coherent, and the system shows the superfluidity. On the other hand, when the on-site interaction dominates ($U \gg J$), tunneling process is suppressed("communication" of atoms between adjacent sites stops), and this prevents the system from establishing the phase coherence over long range. This state is called the Mott insulator phase. The ratio of interaction energy to kinetic energy (U/J) determines the quantum phase of the system. The quantum phase transition between the superfluid and the Mott insulator phase will be discussed later in the chapter 3

2.2 Interactions in Bose-Einstein condensates

Atom-atom interactions arise from scattering process between atoms. Scattering process falls in two categories: inelastic process and elastic process. In inelastic scattering, there are several processes: spin exchange process, dipolar process, three-body process. These inelastic collision processes are "bad" collisions for BEC experimentalists since inelastic processes lead to loss of atoms in BEC. In experiments, inelastic scattering rate is generally low enough so that atom loss is not significant on experimental time scales. More details on the ultracold scattering processes and atom loss processes are discussed in Ref. [128, 127, 66, 120]

In elastic process, only s-wave scattering occurs at a very low temperature ("head-on collision"). The temperature is so low that higher partial waves($l \geq 1$) are highly suppressed and do not contribute. The cross section for the elastic scattering is given by $\sigma = 8\pi a_s^2$, which is independent of energy of colliding atoms (a_s: s-wave scattering length). This elastic process provides the effective interaction, two-body interaction potential energy, which is given by a delta function interaction

$$U(\mathbf{r}_1, \mathbf{r}_2) = g\delta(\mathbf{r}_1 - \mathbf{r}_2) \tag{2.18}$$

with $g = \frac{4\pi\hbar^2 a_s}{m}$.

In this chapter, I review the basic theory of excitation in an interacting system with $U(\mathbf{r}_1, \mathbf{r}_2)$. The interaction [Eq. (2.18)] modifies the excitation spectrum from non-interacting free particle type ($\epsilon = p^2/2m$) to the one with linear phonon branch ($\epsilon = sp$). This phonon branch leads to the superfluidity.

2.3 Excitation Spectrum

We shall consider the system of interacting Bose gas with no external trapping $V_{\text{trap}} = 0$. The many-body Hamiltonian is given by Eq. (2.10). With field operators $\hat{\Psi}(\mathbf{x}) = \sum_{\mathbf{k}} (1/\sqrt{V}) e^{-i\mathbf{k}\cdot\mathbf{x}} a_{\mathbf{k}}$, the Hamiltonian is[41]

$$\hat{H} = \sum_{\mathbf{k}} \epsilon^0_{\mathbf{k}} a^\dagger_{\mathbf{k}} a_{\mathbf{k}} + \frac{g}{2V} \sum_{\mathbf{k}_1,\mathbf{k}_2,\mathbf{k}_3,\mathbf{k}_4} a^\dagger_{\mathbf{k}_1} a^\dagger_{\mathbf{k}_2} a_{\mathbf{k}_3} a_{\mathbf{k}_4} \delta_{\mathbf{k}_1+\mathbf{k}_2,\mathbf{k}_3+\mathbf{k}_4} \tag{2.19}$$

with free particle energy $\epsilon^0_{\mathbf{k}} = \frac{\hbar^2 k^2}{2m}$.

As seen in chapter 2.1.3, the parameter na_s^3 is very small in our experimental system, and it may be assumed that the condensate number N_0 is close to the total number $N(N - N_0 \ll N)$. Under this assumption, the contribution of high-order terms containing non-condensate part($a_{\mathbf{k}}$, $\mathbf{k} \neq 0$) becomes small, and the terms containing more than two non-condensate operators $a_{\mathbf{k}\neq 0}$ may be neglected. The interaction part of the Hamiltonian can be truncated up to second order:

$$\hat{H}_{int} \approx \frac{g}{2V} \left\{ a^\dagger_0 a^\dagger_0 a_0 a_0 + \sum_{k\neq 0} \left(4a^\dagger_{\mathbf{k}} a_{\mathbf{k}} a^\dagger_0 a_0 + a^\dagger_{\mathbf{k}} a^\dagger_{-\mathbf{k}} a_0 a_0 + a^\dagger_0 a^\dagger_0 a_{\mathbf{k}} a_{-\mathbf{k}} \right) \right\} \tag{2.20}$$

a_0 (or $a^\dagger_0$) can be replaced by c number $\sqrt{N_0}$, since $N_0 \sim N$. The Hamiltonian in Eq. (2.20) is

$$\hat{H}_{int} = \frac{g}{2V} \left\{ N_0^2 + \sum_{k\neq 0} \left(4N_0 a^\dagger_{\mathbf{k}} a_{\mathbf{k}} + N_0 (a^\dagger_{\mathbf{k}} a^\dagger_{-\mathbf{k}} + a_{\mathbf{k}} a_{-\mathbf{k}}) \right) \right\} \tag{2.21}$$

In a system of fixed atom number $N = \langle \hat{N} \rangle$, N_0 can be replaced using the number operator N. The number operator is given by

$$\hat{N} = N_0 + \sum_{\mathbf{k}\neq 0} a^\dagger_{\mathbf{k}} a_{\mathbf{k}} \tag{2.22}$$

Substitution of Eq. (2.22) into the interaction Hamiltonian (Eq. (2.21)) yields the final Hamiltonian (kinetic energy + interaction energy)

$$\hat{H} = \frac{1}{2} g n^2 V + \frac{1}{2} \sum_{\mathbf{k}\neq 0} \left(2(\epsilon^0_{\mathbf{k}} + ng) a^\dagger_{\mathbf{k}} a_{\mathbf{k}} + ng (a^\dagger_{\mathbf{k}} a^\dagger_{-\mathbf{k}} + a_{\mathbf{k}} a_{-\mathbf{k}}) \right) \tag{2.23}$$

with $n = N/V$. In this Hamiltonian, only N and N^2 terms are kept.

The Hamiltonian (2.23) may be exactly solved using canonical transformation.

The diagonalization of this Hamiltonian can be done by defining new creation and annihilation operators $\alpha_{\mathbf{k}}$, $\alpha^{\dagger}_{\mathbf{k}}$.

$$a_{\mathbf{k}} = u_k \alpha_{\mathbf{k}} - v_k \alpha^{\dagger}_{-\mathbf{k}}, a^{\dagger}_{\mathbf{k}} = u_k \alpha^{\dagger}_{\mathbf{k}} - v_k \alpha_{-\mathbf{k}} \tag{2.24}$$

where the coefficients u_k, v_k are taken to be real and a function of $k = |\mathbf{k}|$. For this transformation to be canonical, a new set of operators should obey the commutation relations($[\alpha_{\mathbf{k}} \alpha^{\dagger}_{\mathbf{k}}] = \delta_{\mathbf{k},\mathbf{k}'}$, $[\alpha_{\mathbf{k}} \alpha_{\mathbf{k}}] = [\alpha^{\dagger}_{\mathbf{k}} \alpha^{\dagger}_{\mathbf{k}}] = 0$). The commutation relations impose the condition on the coefficients u_k, v_k. It can be easily checked that

$$u_k^2 - v_k^2 = 1 \tag{2.25}$$

Substitution of the new operators α's to the Hamiltonian (Eq. 2.23) yields

$$\begin{aligned} \hat{H} = \frac{1}{2} g n^2 V &+ \sum_{\mathbf{k} \neq 0} (...) + \sum_{\mathbf{k} \neq 0} (...) \, \alpha^{\dagger}_{\mathbf{k}} \alpha_{\mathbf{k}} \\ &+ \frac{1}{2} \sum_{\mathbf{k} \neq 0} \left\{ \left(ng(u_k^2 + v_k^2) - 2 u_k v_k (\epsilon_k^0 + ng) \right) (\alpha^{\dagger}_{\mathbf{k}} \alpha^{\dagger}_{-\mathbf{k}} + \alpha_{\mathbf{k}} \alpha_{-\mathbf{k}}) \right\} \end{aligned} \tag{2.26}$$

Two conditions are required to determine the two coefficients u_k, v_k. We have only one condition in Eq. (2.25). The second condition may be chosen to eliminate the last term in the Hamiltonian of Eq. (2.26) by setting

$$ng(u_k^2 + v_k^2) - 2 u_k v_k (\epsilon_k^0 + ng) = 0 \tag{2.27}$$

Using two conditions Eq. (2.25) and Eq. (2.27), the coefficients u and v are given by

$$v_k^2 = u_k^2 - 1 = \frac{1}{2} \left(\frac{\epsilon_k^0 + ng}{\epsilon_k} - 1 \right) \tag{2.28}$$

where

$$\epsilon_k = \sqrt{(\epsilon_k^0 + ng)^2 - (ng)^2} \tag{2.29}$$

The Hamiltonian (2.26) is finally diagonalized with the coefficients u and v given

in Eq. (2.28).

$$\hat{H} = \frac{1}{2}gn^2V - \frac{1}{2}\sum_{\mathbf{k}\neq 0}(\epsilon_k^0 - \epsilon_k + ng) + \sum_{\mathbf{k}\neq 0}\epsilon_k \alpha_{\mathbf{k}}^\dagger \alpha_{\mathbf{k}} \tag{2.30}$$

There are several points to note on this Hamiltonian

1. The ground state of this Hamiltonian $|0\rangle_\alpha$ (the ground state of the condensate) may be defined by

$$\alpha_{\mathbf{k}}|0\rangle_\alpha = 0 \qquad \forall\, \mathbf{k} \neq 0 \tag{2.31}$$

This state is not the same as the ground state of the non-interacting gas since $a_{\mathbf{k}}|0\rangle_\alpha = -v_k\alpha_{\mathbf{k}}^\dagger|0\rangle_\alpha \neq 0$. The atom-atom interaction modifies a non-interacting ground state to a superposition state of unperturbed states.

2. The contribution of unperturbed state of momentum $\mathbf{k}$ to the ground state of the condensate may be calculated from

$$n_k = \langle a_{\mathbf{k}}^\dagger a_{\mathbf{k}}\rangle_\alpha = v_k^2\langle \alpha_{\mathbf{k}}\alpha_{\mathbf{k}}^\dagger\rangle_\alpha = v_k^2 \tag{2.32}$$

The total contribution of non-zero momentum state to the condensate is calculated as following

$$\frac{1}{N}\sum_{\mathbf{k}\neq 0} n_k = \frac{1}{N}\sum_{\mathbf{k}\neq 0} v_k^2 = \frac{8}{3\sqrt{\pi}}(na_s^3)^{1/2} \tag{2.33}$$

This defines the "depletion" of the condensate. In dilute atomic gas system, the depletion of the condensate is very low. However, it could be raised by changing the interaction strength using Feshbach resonances or optical lattices. Experimental study on quantum depletion was done in optical lattices[132].

3. This Hamiltonian may be understood in a quasi-particle picture. An excited state of the condensate is created by applying a quasi-particle creation operator $\alpha_{\mathbf{k}}^\dagger$ to $|0\rangle_\alpha$. A quasi-particle with $\mathbf{k}$ is a superposition of two states (Eq. 2.24); one state where a particle with momentum $\mathbf{k}$ is added by removing one particle in the condensate and the other state where a particle with momentum $-\mathbf{k}$ is removed and it is added to the condensate.

4. The excitation spectrum of the condensate is simply given by $\epsilon_k = \sqrt{\epsilon_k^0(\epsilon_k^0 + 2ng)}$

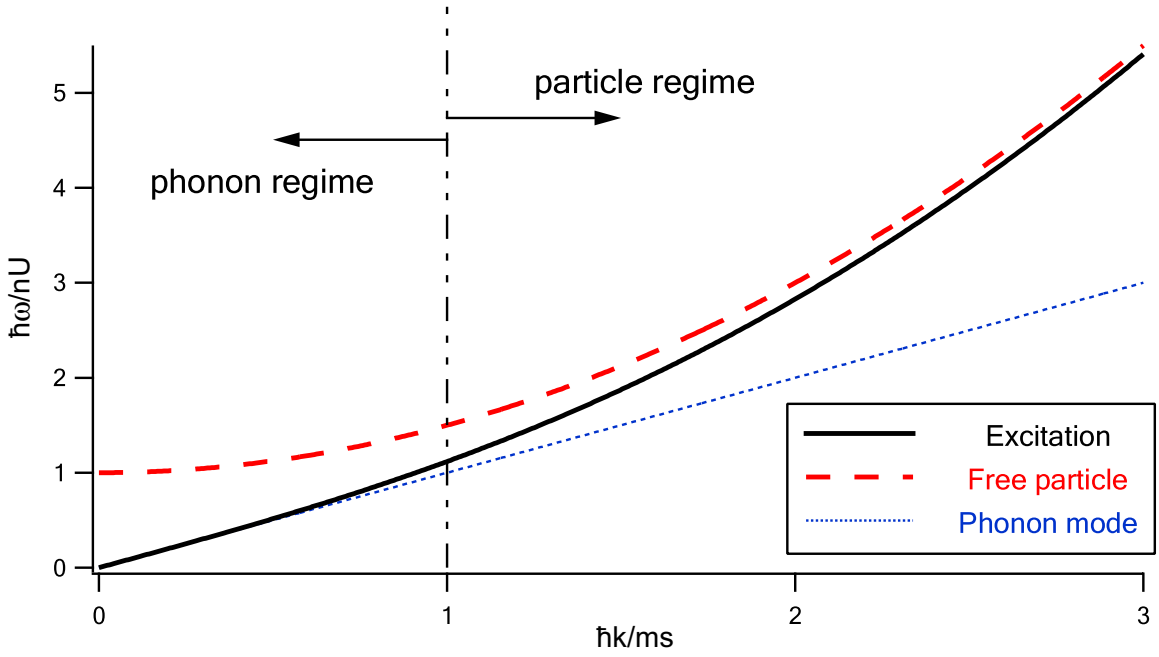

Figure 2-1: Excitation spectrum of BEC. For long wavelength ($\hbar k < mc$, c: speed of sound), the excitation energy is linear to the momentum (phonon mode). The excitation energy becomes free particle spectrum for higher momentum $\hbar k > mc$.

(Eq. (2.29)). There are two regimes, long wavelength (phonon mode) and short wavelength(free particle mode)

$$\epsilon_k = \begin{cases} c(\hbar k) & \text{for } k \to 0 \\ \epsilon_k^0 + ng & \text{for } k \to \infty \end{cases} \tag{2.34}$$

In the regime of long wavelength, the spectrum becomes linear with a sound velocity $c = \partial\omega_k/\partial k = \sqrt{ng/m} = \sqrt{4\pi\hbar^2 a_s n/m^2}$. The quasi-particle operator becomes

$$\alpha_{\mathbf{k}}^\dagger \to a_{\mathbf{k}}^\dagger - a_{-\mathbf{k}} \qquad k \to 0 \tag{2.35}$$

A long wave length quasi-particle has equal contribution from momentum $\mathbf{k}$ and $-\mathbf{k}$, and its wave function has a asymptotic form of $\sin(\mathbf{k}\cdot\mathbf{r})$

In the opposite limit, short wavelength, the spectrum becomes free particle-like

with energy offset ng. The quasi-particle operator becomes

$$\alpha_{\mathbf{k}}^{\dagger} \to a_{\mathbf{k}}^{\dagger} \qquad k \to \infty \tag{2.36}$$

with an asymptotic wavefunction $\sim \exp(-i\mathbf{k}\cdot\mathbf{r})$

The excitation spectrum of the condensate is plotted in Fig. 2-1

2.4 Superfluidity in Bose–Einstein Condensate

The superfluidity is one of the most remarkable phenomena of BEC. For instance, circulating flows are quantized in superfluid matter to form quntized vortices, which were observed in rotating BEC[1, 81]. Superconductivity is also explained in terms of a condensate of fermion-pairs and its superfluidity.

However, BEC does not necessarily imply superfluidity. Superfluidity does not occur in the case of a non-interacting BEC. It is the atom-atom interaction that leads to superfluidity in a dilute gas BEC as shall be discussed in the following section. The condition for superfluidity and the effect of interaction on the superfluidity are discussed.

2.4.1 Landau Critical Velocity

Let us consider the situation where an obstacle object moves with a constant speed in a condensate [Fig. 2-2]. If the object moves very fast, it exerts pressure on the atoms around it and creates flow of atoms (excitations). However, as the speed of the object decreases, the object ceases to create excitations below a certain speed since the energy scale associated with the movement of the object becomes lower than the excitation energy of a condensate.

To be more specific, let us assume that an obstacle object moving with velocity $\mathbf{v}$ has a potential energy $V_{\mathrm{o}}(\mathbf{r})$ on atoms in a condensate and the position of an obstacle is given by $\mathbf{R}_{\mathrm{o}}(t) = \mathbf{v}t + \mathbf{R}_{\mathrm{o}}(0)$ at time t. In the frame of a condensate, the potential energy V_{o} is given by $V_{\mathrm{o}}(\mathbf{r} - \mathbf{R}_{\mathrm{o}}(t))$, which is time-dependent potential

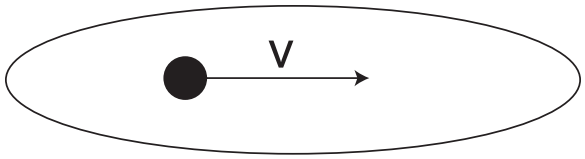

Figure 2-2: An obstacle object moving with the velocity v in the condensate creates excitations if it moves faster than the critical velocity v_c

energy. A time-dependent potential could transfer energy to the system by creating excitations. Fourier transformation of the potential energy shows which mode this potential excites. The fourier transformation gives

$$\tilde{V_{\rm o}}(\mathbf{q},t) = \int d\mathbf{r} e^{-i\mathbf{q}\cdot\mathbf{r}} V_{\rm o}(\mathbf{r}-\mathbf{v}t) = \int d\mathbf{r}' e^{-i\mathbf{q}\cdot\mathbf{r}'} V_{\rm o}(\mathbf{r}') e^{-i\mathbf{q}\cdot\mathbf{v}t} = \tilde{V_{\rm o}}(\mathbf{q}) e^{-i\mathbf{q}\cdot\mathbf{v}t}$$

$$\tilde{V_{\rm o}}(\mathbf{q},\omega) = \tilde{V_{\rm o}}(\mathbf{q})\delta(\omega - \mathbf{q}\cdot\mathbf{v}) \tag{2.37}$$

The Fourier transform of the potential energy of the moving object has the energy $\omega = \mathbf{q}\cdot\mathbf{v}$ at the momentum $\mathbf{q}$. For a given momentum $\mathbf{q}$, this moving obstacle can create excitations with energies ranging from 0 to $\hbar qv$. Excitations would not be generated and the superfluid remains stable as long as the following condition is fulfilled

$$\epsilon_{\mathbf{q}} > \mathrm{Max}\,(\mathbf{q}\cdot\mathbf{v}) = qv \qquad \forall \mathbf{q} \tag{2.38}$$

Therefore the minimal velocity v_c required to create excitations in superfluid is determined by

$$v \geq \mathrm{Min}(\frac{\epsilon_{\mathbf{q}}}{q}) = v_c \tag{2.39}$$

From the excitation spectrum of weakly interacting Bose gas system (Eq. (2.34)), the critical velocity for superfluid is given by

$$v_c = c = \sqrt{\frac{4\pi\hbar^2 a_s n}{m^2}} \tag{2.40}$$

The critical velocity is equal to the sound speed.

2.4.2 Interacting gas vs. non-interacting gas

In a non-interacting gas, the excitation spectrum is simply given by $\epsilon^0_{\mathbf{p}} = \mathbf{p}^2/2m$. The critical velocity vanishes ($v_c = \mathrm{Min}(\epsilon^0_p/p) = 0$), and superfluidity is absent in a non-interacting BEC. The manifestation of superfluidity in a dilute gas BEC is due to atom-atom interactions.

2.4.3 Critical Velocity in Optical Lattices

BEC loaded in optical lattices shows superfluidity. The critical velocity for unstable superfluid flow is the sound speed. However, there exists another type of decay process in the system in optical lattices, called dynamical instability. A dynamical instability occurs due to the modification of the excitation spectrum ϵ_q by optical lattice as will be discussed in the chapter 6.

2.5 Energy Scales in BEC Experiment

In this section, I present the list of energy scales related to typical BEC experiments. Understanding the hierarchy of energy scales is important in studying the physics of ultracold atoms. If the order of energy scales changes, the dynamics becomes completely different. For example, in typical harmonic traps chemical potential μ is higher than the trapping frequency ω_{ho} by 2 to 3 orders of magnitude (Eq.(2.16)). However, when trapping frequency along one axis (for example, z-axis) increases more than chemical potential($\hbar\omega_z \gg \mu$), the atomic motion along the z-axis is frozen and the system behaves as in 2-D instead of 3-D.

In a typical harmonic trap, the order of energy scales is

$$\frac{\hbar^2}{ma_s^2} \gg k_B T_c \sim E_R > \mu \gg \hbar\omega_{\mathrm{ho}} \tag{2.41}$$

In a deep optical lattice(i.e. 35 E_R), the order of energy scales changes to

$$\frac{\hbar^2}{ma_s^2} \gg \hbar\omega_{\mathrm{latt}} \gg k_B T_c \sim E_R > \mu \sim U \gg \hbar\omega_{\mathrm{ho}} \gg J \tag{2.42}$$

Energy		Frequency units
3-body recombination energy	$\hbar^2/ma_s^2$	4.0 MHz
critical temperature for BEC	T_c	$\sim$ 10 kHz
recoil energy ($\lambda = 780$ nm, ^{87}Rb D2 line)	$\hbar^2 k_{Rb}^2/2m$	3.8 kHz
recoil energy E_R ($\lambda = 1064$ nm, Trapping IR laser)	$\hbar^2 k_{IR}^2/2m$	2.0 kHz
meanfield interaction energy	gn	$\sim$ 1 kHz
chemical potential	μ	$\sim$ 1 kHz
hopping matrix @ 35 E_R	J	0.5 Hz
onsite interaction matrix @ 35 E_R	U	1.3 kHz
external trapping	$\hbar\omega_{\rm ho}$	10 $\sim$ 100 Hz
trapping frequency in a optical lattice site @35 E_R	$\hbar\omega_{\rm latt} = \sqrt{4E_R V_{\rm latt}}$	24.0 kHz

Table 2.1: Energy Scales in typical BEC experiments.

Chapter 3

Bose–Einstein Condensates in an Optical Lattice

In this chapter I present how optical trapping works and how the optical lattice is implemented. The Bose-Hubbard model is introduced, and the two quantum phases associated with the Bose-Hubbard model - the superfluid phase and the Mott insulator phase - are discussed. The system considered here is only limited to single species ultracold atoms(^{87}Rb BEC) in simple cubic lattice geometry. More general discussions on ultracold atoms in optical lattice can be found in review articles[87, 78, 11]

3.1 Optical Lattice

3.1.1 Optical Dipole Trap

Atoms in a laser beam are affected by two kinds of forces. One is the dissipative force (or scattering force). It relies on the scattering of light by atoms. Scattering of light impart momentum kicks to atoms and increases the momentum of atoms by amounts of $\hbar\mathbf{k}$ where $\mathbf{k}$ is the wave vector of the laser beam. The rate of scattering γ_p is

$$\gamma_p = \gamma \cdot \rho_{ee} = \gamma \cdot \frac{s_0/2}{1 + s_0 + (2\delta/\gamma)^2} \tag{3.1}$$

where ρ_{ee} is the population in an excited state of two-level system, s_0 is a saturation parameter, δ is a detuning, and γ is a natural line width of atomic transition. A saturation parameter is defined by $s_0 = I/I_{sat}$. I is the intensity of the laser beam, and I_{sat} is a saturation intensity of the transition. The dissipative force $\mathbf{F}_{sc}$ is then given by

$$\mathbf{F}_{sc} = \hbar\mathbf{k}\gamma_p = \hbar\mathbf{k}\left(\frac{\gamma s_0/2}{1 + s_0 + (2\delta/\gamma)^2}\right) \tag{3.2}$$

The other type of force is the dipole force. The dipole force is a conservative force,which can be written as a gradient of a potential energy. This potential energy is the AC stark shift. When the laser is far detuned from resonance (more specifically, $\delta \gg \gamma$), the dipole force $\mathbf{F}_{dip}$ is

$$\begin{aligned} \mathbf{F}_{dip} &= -\nabla V_{dip} \\ V_{dip} &= \frac{\hbar\gamma^2}{8\delta} s_0 = \frac{\hbar\gamma^2}{8\delta}\frac{I}{I_{sat}} \end{aligned} \tag{3.3}$$

Note that the sign of potential energy changes if the sign of the detuning δ changes. When it is blue-detuned ($\delta > 0$), atoms seek lower intensity. For red-detuning ($\delta < 0$), atoms seek higher intensity. Atoms can be trapped (repelled) by focusing a red-detuned (blue-detuned) laser beam.

The intensity profile of a focused gaussian laser beam propagating along z-axis is

$$I(r,z) = \frac{2P}{\pi w^2(z)} e^{-\frac{2r^2}{w^2(z)}} \tag{3.4}$$

where P is the total power of laser beam, and the $1/e^2$ beam waist $w(z)$ is given by $w(z) = w_0\sqrt{1 + (z/z_R)}$. The Rayleigh length z_R of the focus is $z_R = \pi w_0^2/\lambda$ (λ: wavelength of the laser beam). Near the focal point of the laser beam($z \ll z_R$, $r \ll w$), the optical dipole trap can be approximated as a harmonic trap

$$V_{dip}(r,z) \simeq -V_0\left\{1 - 2\left(\frac{r}{w_0}\right)^2 - \left(\frac{z}{z_R}\right)^2\right\} \tag{3.5}$$

with $V_0 = \hbar\gamma^2/8\delta I_{sat}\cdot(2P/\pi w_0^2)$, and the trap frequencies are given by $\omega_r = \sqrt{4V_0/mw_0^2}$, and $\omega_z = \sqrt{2V_0/mz_R^2}$.

3.1.2 Optical Lattice

When two laser beams with the same frequency and polarization propagate in opposite directions, they interfere. This leads to a periodic pattern of the intensity, which acts as a periodic potential for atoms. The interference between two laser beams leads to a total electric field $\mathbf{E}(\mathbf{r},t)$ and intensity $I(\mathbf{r},t)$.

$$\begin{aligned}\mathbf{E}(\mathbf{r},t) &= \mathbf{E}_1(\mathbf{r},t) + \mathbf{E}_2(\mathbf{r},t) \\ &= E_1\mathbf{e}_1\exp[-i(\mathbf{k}_1\cdot\mathbf{r}-\omega_1 t)] + E_2\mathbf{e}_2\exp[-i(\mathbf{k}_2\cdot\mathbf{r}-\omega_2 t)] \qquad (3.6)\end{aligned}$$

$$\begin{aligned}I(\mathbf{r},t) &\propto \mathbf{E}\cdot\mathbf{E}^*(\mathbf{r},t) \\ &= E_1^2 + E_2^2 + 2(\mathbf{e}_1\cdot\mathbf{e}_2)\mathrm{Re}\left[E_1E_2^* e^{-i((\mathbf{k}_1-\mathbf{k}_2)\cdot\mathbf{r}-(\omega_1-\omega_2)t)}\right] \qquad (3.7)\end{aligned}$$

The third term in the above Eq.(3.7) corresponds to the interference of two laser beams, which provides aperiodic potential. There are several things to note on this interference pattern.

1. The polarization product $\mathbf{e}_1\cdot\mathbf{e}_2$ determines the optical lattice contrast. In general, the same polarization (usually linear polarization) is used for both laser beams to maximize the optical lattice depth for a given total power of an optical lattice laser beam.

2. The relative detuning $\Delta\omega \equiv \omega_1 - \omega_2$ gives rise to three different cases :
   $\Delta\omega = 0$: stationary optical lattice
   $0 < \Delta\omega \sim \omega_{rec}$: moving optical lattice
   $\omega_{rec} \ll \Delta\omega$: "time-averaged" optical dipole trap
   (ω_{rec} : recoil frequency, defined by $\hbar\omega_{rec} = \hbar^2k^2/2m$)

- $\Delta\omega = 0$: the interference term becomes a periodic potential $V \sim \sin(\Delta\mathbf{k}\cdot\mathbf{r})$.

When two lattice beam propagate in the opposite direction ($\Delta\mathbf{k} = 2\mathbf{k}$), $V \sim \sin(2kz)$. The period of an optical lattice is given by $2\pi/2k = \lambda/2$, where λ is the wavelength of a laser beam.

The period could be controlled by changing the angle θ between two optical lattice beams. The resulting potential is $V \sim \sin\left(\left[2k\sin(\frac{\theta}{2})\right]z\right)$, and its optical lattice period is $2\pi/(2k\sin(\frac{\theta}{2})) = \lambda/2 \cdot \csc(\theta/2)$.

- $0 < \Delta\omega \sim \omega_{rec}$: The phase of the interference pattern is $(\Delta kz - \Delta\omega t)$, and an optical lattice moves with the speed of $\Delta\omega/\Delta k$. In case of counter-propagating optical lattice beams ($\mathbf{k}_1 = -\mathbf{k}_2$), the speed of the moving lattice is given by

$$v = \Delta\omega/\Delta k = \Delta\omega/2k = \frac{\lambda}{2}\Delta f \tag{3.8}$$

  with $\Delta\omega = 2\pi \times \Delta f$.

- $\omega_{rec} \ll \Delta\omega$: In this case, the interference pattern of two laser beams oscillates fast compared to the characteristic time scale of atomic motion. The motion of atoms is not affected by such rapidly oscillating potentials. In quantum mechanical language, $\Delta\omega$ is far off from energy scale of atomic motion. Consequently, the third term in Eq. 3.7 is averaged-out to zero. Atoms "feel" only the individual optical dipole trapping potentials from each laser beam (i.e. E_1^2, E_2^2 terms in Eq. (3.7)), not the optical lattice potential.).

In our experiment, an optical lattice was created by using two counter-propagating beams with the same frequency and same polarization. The optical lattice potential is then given by (see Eq.(3.5))

$$V_{latt}(r,z) = -V_{latt}\sin(2kz)\left\{1 - 2\left(\frac{r}{\omega_0}\right)^2 - \left(\frac{z}{z_R}\right)^2\right\} \tag{3.9}$$

3.2 Band Structure

The presence of an optical lattice modifies the dynamics of atoms profoundly. The energy spectrum is modified to a band structure, and energy gaps appear between different energy bands. The dynamics of single atoms in a periodic potential can be well described using Bloch's theorem as follows [6].

The Hamiltonian for a single atom in a periodic potential $V(x)$ with a period d (i.e. $V(x+d) = V(x)$) is

$$E\psi(x) = \left(-\frac{\hbar^2}{2m}\frac{\partial^2}{\partial x^2} + V(x)\right)\psi(x) \tag{3.10}$$

A wave function $\psi(x)$ and the periodic potential $V(x)$ may be expanded as

$$\psi(x) = \sum_k c_k \exp(ikx) \tag{3.11}$$

$$V(x) = \sum_K V_K \exp(iKx) \tag{3.12}$$

With the expansions of $\psi(x)$ and $V(x)$, the kinetic energy and potential energy term in the Schrödinger equation are expressed

$$-\frac{\hbar^2\nabla^2}{2m}\psi(x) = \sum_k \frac{\hbar^2 k^2}{2m} c_k \exp(ikx) \tag{3.13}$$

$$\begin{aligned} V(x)\psi(x) &= \sum_{k,K} V_K c_k \exp(i(k+K)x) \\ &= \sum_{k,K} V_K c_{k-K} \exp(ikx) \end{aligned} \tag{3.14}$$

where in the last line, $k \to k - K$.

The Schrödinger equation now reads

$$\sum_k \left\{ \frac{\hbar^2 k^2}{2m} c_k + \sum_K V_K c_{k-K} \right\} \exp(ikx) = E\left(\sum_k c_k \exp(ikx)\right) \tag{3.15}$$

Since plane waves are orthogonal to each other, Eq. (3.15) gives

$$\frac{\hbar^2 k^2}{2m} c_k + \sum_K V_K c_{k-K} = E c_k \tag{3.16}$$

, which is the Schrödinger equation in momentum space. The quasi-momentum k is restricted to the first Brillouin zone($k : -K_x/2 \sim K_x/2$). For a sinusoidal optical lattice potential, the potential energy term V_K is

$$\begin{aligned} V_{latt}(x) &= V_{latt} \sin^2(k_L x) = V_{latt} \left(\frac{e^{ik_L x} - e^{-ik_L x}}{2i} \right)^2 \\ &= \frac{V_{latt}}{4} \left(2 - e^{i2k_L x} - e^{i2k_L x} \right) \\ V_K &= \begin{cases} V_{latt}/2 & K = 0 \\ -V_{latt}/4 & K = \pm K_x \\ 0 & \text{otherwise} \end{cases} \end{aligned} \tag{3.17}$$

where $k_L = 2\pi/\lambda_L$, $K_x = 2k_L$(reciprocal vector) with wavelength λ_L of the optical lattice laser. In Eq.(3.17), the $K = 0$ term gives a uniform energy offset to the Hamiltonian and may be set to zero for simplicity. Second ($K = \pm K_x$) terms give off-diagonal matrix elements to the Hamiltonian and couple the coefficients c_k to only the coefficients $c_{k \pm K_x}$. Consequently, the matrix form of the Hamiltonian in Eq. (3.16) is given by (diagonal matrix) + (symmetric off-diagonal matrix).

$$H = \begin{pmatrix} \ddots & (-1/4)V_{latt} & 0 & 0 & 0 \\ (-1/4)V_{latt} & \frac{\hbar^2 (k+K_x)^2}{2m} & (-1/4)V_{latt} & 0 & 0 \\ 0 & (-1/4)V_{latt} & \frac{\hbar^2 (k)^2}{2m} & (-1/4)V_{latt} & 0 \\ 0 & 0 & (-1/4)V_{latt} & \frac{\hbar^2 (k-K_x)^2}{2m} & (-1/4)V_{latt} \\ 0 & 0 & 0 & (-1/4)V_{latt} & \ddots \end{pmatrix} \tag{3.18}$$

The eigenenergy of this Hamiltonian matrix yields energy band structure $E_n(k)$ (n: band index $= 0, 1, 2, \cdots$) as plotted in Fig. 3-1

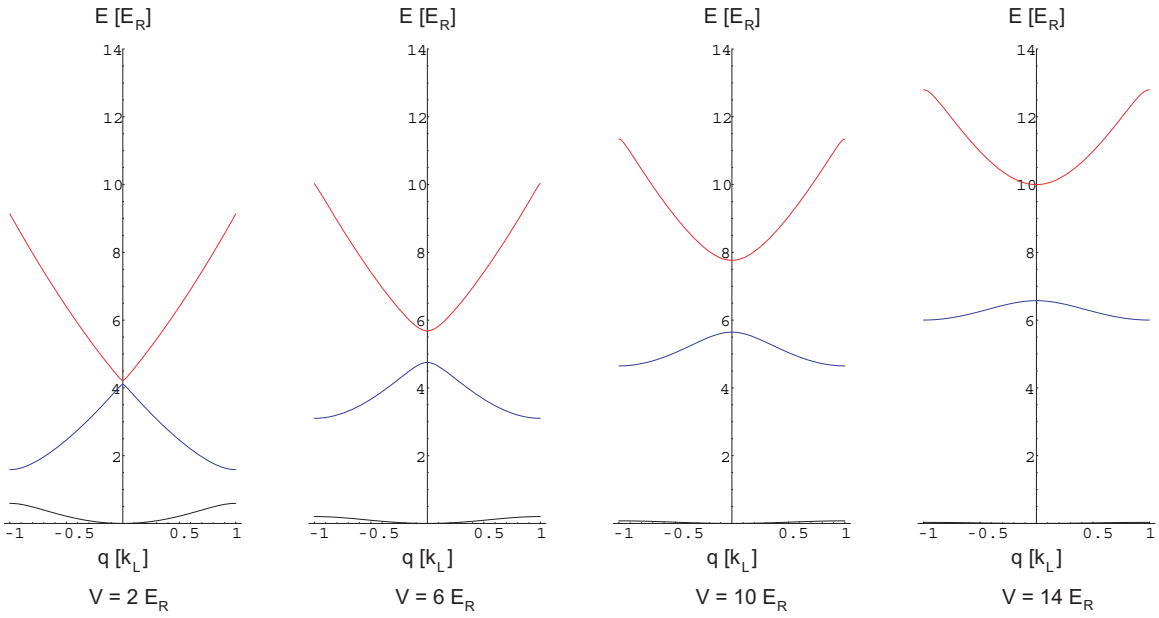

Figure 3-1: Energy band structure in optical lattice. Ground energy band (black curve), second energy band (blue), and third energy band (black) are plotted for various lattice depths $V_{latt} = 2,\ 6,\ 10,\ 14\, E_R$. The energy and momentum is expressed in a unit of recoil energy E_R, and recoil momentum k_L respectively. With increasing lattice depth, the ground band becomes flatter, and energy gap increases.

3.2.1 Wannier Function

A Bloch wave function is not a spatially localized wave function, but distributed over all lattice sites. If the optical lattice depth V_{latt} is relatively deep (tight-binding limit), atoms do not travel far over lattice sites, but stay around a lattice site. Bloch wave functions are not adequate in treating atoms in the tight binding case. A new set of wave functions that are localized near a lattice site is preferred. Such a new set of wave functions can be constructed from the Bloch wave function $\psi_{n,k}$. These new wave functions are called Wannier functions defined by

$$w_n(\mathbf{r} - \mathbf{R}) = \frac{1}{V_0} \int d\mathbf{k} e^{-i\mathbf{k}\cdot\mathbf{R}} \psi_{n,\mathbf{k}}(\mathbf{r}) \tag{3.19}$$

($\mathbf{R}$: position of lattice sites, V_0 : volume of the first Brillouin zone). Fig. 3-2 displays the Wannier function of the lowest energy band at $V_{latt} = 2E_R\,, 6E_R,\ 10E_R$. The Wannier functions w_n are well localized at each lattice sites. They are orthogonal

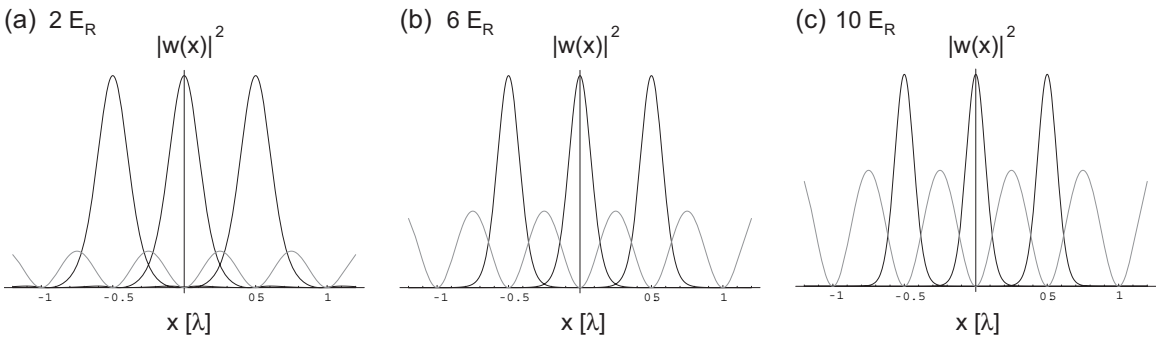

Figure 3-2: Wannier functions $|w(x)|^2$ are plotted for 2, 6, 10 E_R. Gray curves represent the optical lattice potential. A x-axis is scaled with λ and the lattice period $d = 0.5\lambda$. The overlap of Wannier functions between adjacent sites decreases with lattice depth indicating that the hopping matrix element J drops.

at different lattice sites as well as with different band indices.

$$\int d\mathbf{r} w_n^*(\mathbf{r} - \mathbf{R}) w_{n'}(\mathbf{r} - \mathbf{R}') = \delta_{\mathbf{n},\mathbf{n}'} \delta_{\mathbf{R},\mathbf{R}'} \tag{3.20}$$

The Wannier function $w_n(\mathbf{r})$ is also normalized.

$$\int d\mathbf{r} |w_n(\mathbf{r})|^2 = 1 \tag{3.21}$$

3.3 Bose-Hubbard Model

In order to describe the system of interacting ultracold atoms in an optical lattice, one needs to start from the basic many-body Hamiltonian such as Eq. (2.10). The external potential energy term $V_{trap}(\mathbf{r})$ in Eq. (2.10) is now given by sum of the external trapping potential $V_{trap}(\mathbf{r})$ and the optical lattice potential $V_{latt}(\mathbf{r})$. The Hamiltonian is

$$\begin{aligned} \hat{H} = & \int d\mathbf{r} \hat{\Psi}^\dagger(\mathbf{r}) \left(-\frac{\hbar^2}{2m} \nabla^2 + V_{trap}(\mathbf{r}) + V_{latt}(\mathbf{r}) \right) \hat{\Psi}(\mathbf{r}) \\ + & \frac{1}{2} \int d\mathbf{r}_1 d\mathbf{r}_2 \hat{\Psi}^\dagger(\mathbf{r}_1) \hat{\Psi}^\dagger(\mathbf{r}_2) U(\mathbf{r}_1, \mathbf{r}_2) \hat{\Psi}(\mathbf{r}_2) \hat{\Psi}(\mathbf{r}_1) \end{aligned} \tag{3.22}$$

The bosonic field operator $\hat{\Psi}(\mathbf{r})$ can be expanded in Wannier functions $w_n(\mathbf{r})$,

since Wannier functions are a complete basis set. It also may be assumed that the energy scale involved in our system is small compared to the energy of the second band. Wannier functions $w_n(\mathbf{r})$ reduces to only the ground band Wannier functions $w(\mathbf{r}) = w_0(\mathbf{r})$, and the bosonic field operator $\hat{\Psi}(\mathbf{r})$ is given by $\hat{\Psi}(\mathbf{r}) = \sum_i w_0(\mathbf{r}-\mathbf{R}_i)a_i$ with an annihilation operator a_i of atoms as a lattice site i with position $\mathbf{R}_i$ of lattice site.

There are three terms to be considered in the Hamiltonian Eq. (3.22).

- The kinetic energy and lattice potential energy term lead to a hopping matrix element J, which describes hopping (or tunneling) between adjacent sites.

$$-J \sum_{<i,j>} a_i^\dagger a_j \quad \text{with } J = \int d\mathbf{r} w^*(\mathbf{r}-\mathbf{R}_i) \left(-\frac{\hbar^2}{2m}\nabla^2 + V_{latt}(\mathbf{r}) \right) w(\mathbf{r}-\mathbf{R}_j) \quad (3.23)$$

  where $< i, j >$ denote the nearest neighbor lattice sites. Note that the hopping term has negative sign $-J$, since delocalization lowers the kinetic energy (lower the curvature of the wave function).

- The trapping potential energy term gives an energy offset at each lattice site.

$$\sum_i \epsilon_i \hat{n}_i \quad \text{with } \epsilon_i = \int d\mathbf{r} w^*(\mathbf{r}-\mathbf{R}_i) V_{trap}(\mathbf{r}) w(\mathbf{r}-\mathbf{R}_i) \rightarrow V_{trap}(\mathbf{R}_i) \quad (3.24)$$

  where n_i is the number operator $\hat{n}_i = a_i^\dagger a_i$

- The last term is the on-site interaction energy term. We consider s-wave short range interaction and $U(\mathbf{r}_1, \mathbf{r}_2) = g\delta(\mathbf{r}_1 - \mathbf{r}_2)$. The Hamiltonian is given by

$$\frac{1}{2}U \sum_i \hat{n}_i(\hat{n}_i - 1) \quad \text{with } U = g \int d\mathbf{r} |w(\mathbf{r})|^4 = \frac{4\pi\hbar^2 a_s}{m} \int d\mathbf{r} |w(\mathbf{r})|^4 \quad (3.25)$$

With these three terms, the Bose-Hubbard Hamiltonian is obtained from Eq. (3.22) [65, 42]

$$H = -J \sum_{<i,j>} a_i^\dagger a_j + \frac{1}{2}U \sum_i \hat{n}_i(\hat{n}_i - 1) + \sum_i \epsilon_i \hat{n}_i \quad (3.26)$$

3.3.1 U and J Matrix

Two matrix elements U and J can be calculated from Wannier functions $w(x)$[65]. In Fig. 3-3, U and J are plotted as a function of lattice depth V_{latt}. U and J are expressed in units of recoil energy $E_R = \hbar^2 k^2/2m$. J matrix element decreases exponentially with increasing lattice depth, while U matrix element increases more slowly.

3.4 Superfluid Phase

In a homogenous system, the matrix element U and J are the only parameters that define and describe the system. Let us consider two extreme cases: $J \gg U$, $U \gg J$. When the hopping process dominates over the interaction energy ($J \gg U$), particles easily hop between lattice sites (the superfluid phase). On the contrary if $U \gg J$, the energy cost for moving one particle from sites to sites is very high leading to suppression of hopping process. This regime where atomic motion is frozen to each lattice site is called the Mott insulating phase. The transition between the superfluid and Mott insulating phase occurs at a critical point between the two limits. A deep superfluid phase($J \gg U$) is discussed in this section, and a discussion on the deep Mott insulating phase($U \gg J$) followes in the next section

In a case of $U/J \to 0$, the Hamiltonian in Eq. (3.26) becomes $\hat{H} = -J \sum_{<i,j>} a_i^\dagger a_j$, which is a tight-binding model Hamiltonian for atoms in an optical lattice. In a single atom case, the eigenstates of this Hamiltonian are simply given by

$$|\Psi\rangle = \frac{1}{\sqrt{M}} \sum_i e^{-i\mathbf{k}\cdot\mathbf{R}_i} a_i^\dagger |0\rangle \tag{3.27}$$

where the wave vector $\mathbf{k}$ has discrete values in the first Brillouin zone. $\mathbf{k} = (l_x/M_x)\mathbf{K}_x + (l_y/M_y)\mathbf{K}_y + (l_z/M_z)\mathbf{K}_z$ $(l_{x,y,z} = 0, 1, 2, \cdots)$ where $M_{x,y,z}$ are the number of lattice sites along x,y,z axis (total number of lattice sites $M = M_x \cdot M_y \cdot M_z$). The corre-

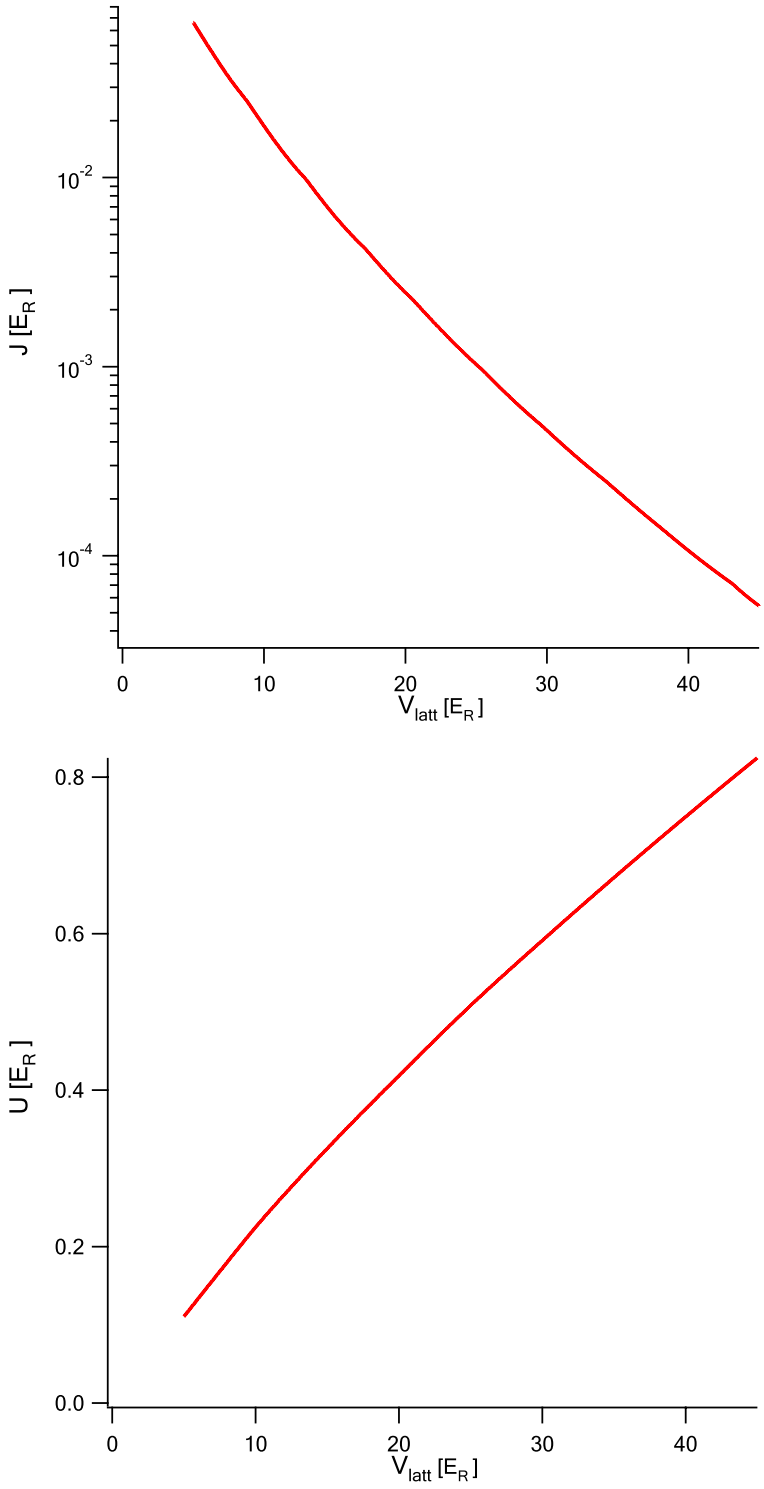

Figure 3-3: U and J matrix elements

sponding eigenenergy could be obtained after a simple algebra.

$$E(l_x, l_y, l_z) = -2J\cos\theta \tag{3.28}$$

with

$$\theta = 2\pi\left(\frac{l_x}{M_x} + \frac{l_y}{M_y} + \frac{l_z}{M_z}\right) \tag{3.29}$$

The band width for the first band is $4J$.

For the N-atom case, the wavefunction of the ground state ($\mathbf{k} = 0$) is

$$|\Psi\rangle \rightarrow \left[\frac{1}{\sqrt{M}}\sum_i a_i^\dagger\right]^N |0\rangle \tag{3.30}$$

The number statistics at a lattice site could be determined from this wavefunction in Eq. (3.30). The probability for S atoms to be at a certain lattice site i in the ground eigenstate $|\Psi\rangle$(Eq. (3.30)) is

$$f(S; N, 1/M) = \binom{N}{S}\left(\frac{1}{M}\right)^S\left(1 - \frac{1}{M}\right)^{N-S} \tag{3.31}$$

This is a binomial distribution for a probability $1/M$ and the number of trial N. The average number per site $\bar{n}$ is given by $\bar{n} = N \times (1/M) = N/M$, and the number fluctuation is $\sqrt{N/M(1-1/M)} \simeq \sqrt{N/M} = \sqrt{\bar{n}}$. In a typical experiment, the total number of atoms N is $\sim 10^4$ to 10^5, the number of lattice sites $M \sim 10^5$, the average number per site $\bar{n} \sim 1$ to 3. When the numbers N, M are very high ($\gg 1$), the binomial distribution becomes the Poisson distribution. Therefore the number statistics of the superfluid phase becomes equal to the Poisson distribution, the number statistics of coherent states. The superfluid ground state can be expressed as a set of coherent states residing at lattice sites i as follows.

$$|\Psi\rangle^{SF}_{U/J\rightarrow 0} \rightarrow \prod_i \left[\exp(\bar{n}a_i^\dagger)\right] |0\rangle \tag{3.32}$$

One important thing to notice about a superfluid coherent state is that it has long

range density correlation. Two states $a_i|\Psi\rangle^{SF}_{U/J\to 0}$ and $a_j|\Psi\rangle^{SF}_{U/J\to 0}$ have a finite overlap for a large separation $|\mathbf{R}_i - \mathbf{R}_j|$.

The superfluid phase ground state, which is a coherent state in the limit of $U/J \to 0$, becomes "squeezed" as the on-site interaction U increases. If U/J is increased to $\gg 1$, the state is completely squeezed into a number state (Fock state).

3.4.1 Energy Spectrum

As discussed in the previous section, in the limit of $J \gg U$ the energy spectrum[80, 72] (Eq. (3.28)) forms a band structure with a width $4J$. The modified energy dispersion relation can be understood in the context of effective mass m^*[73]. The effective mass is defined from the curvature of the energy dispersion relation, $m^* \equiv (\partial^2 E(p)/dp^2)^{-1} \propto 1/J$. The energy dispersion relation is now expressed with effective mass m^* near the momentum $p = 0$ as

$$E(p) = \frac{p^2}{2m^*} \quad \text{with } m^* = (\partial^2 E(p)/dp^2)^{-1}\big|_{p=0} \tag{3.33}$$

The effective mass m^* deviates from the initial mass m in the presence of lattice. With increasing optical lattice depth, the hopping processes are suppressed(lower J) and the effective mass increases. An experimental study of the effective mass of a BEC in an optical lattice has been performed by measuring the frequency of dipole oscillations of a BEC in a variable optical lattice depth [21]. For instance, Fig. 3-1 shows that the lowest band becomes flat due to the increase of effective mass m^* as the lattice depth is raised.

3.4.2 Excitation Spectrum

Excitation spectrum $\epsilon(k)$ in the superfluid phase could be considered in two different range of k.

- Long wavelength excitation ($k \to 0$): For small k, particles in the system behaves as if they have an effective mass m^*. The excitation energy is given by

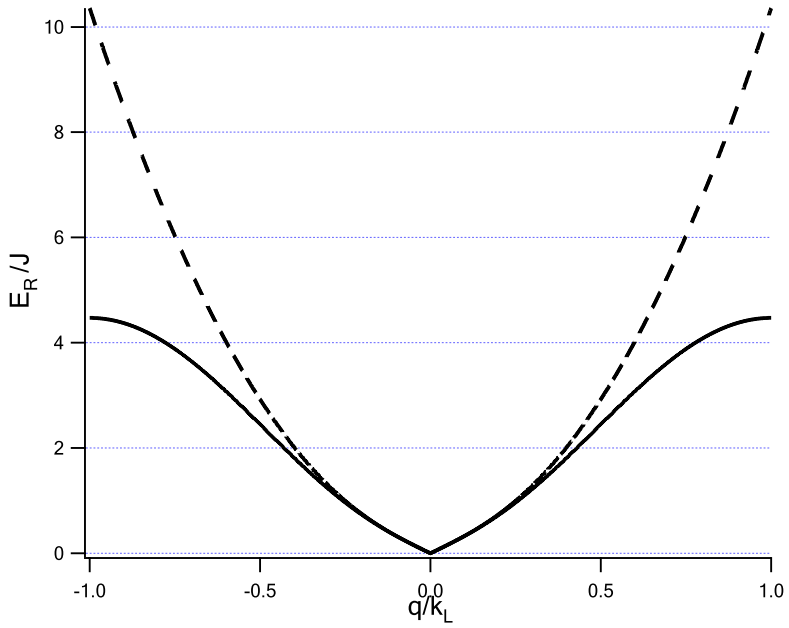

Figure 3-4: Excitation spectrum of the superfluid in optical lattice. The black (dashed) curve shows the excitation spectrum in optical lattice (with no optical lattice, respectively). The spectrum has the linear phonon mode for long wavelength excitation($q \to 0$). In the presence of optical lattice, the spectrum is modified to have an energy band structure (Bogoliubov band).

a linear dispersion relation as in the weakly interacting gas with no lattice (as discussed in chap 2) except for a new effective mass, m^*.

$$\epsilon(k) \sim c^* k \tag{3.34}$$

with a modified sound velocity $c^* \sim \sqrt{U/m^*} \sim \sqrt{U \cdot J}$. The sound velocity c^* in optical lattice decreases with a lattice depth. For more rigorous mathematical methods, see Ref. [124, 72] where the Bogoliubov approach was used for the energy spectrum. Eq. (3.34) shows that the excitation spectrum of the superfluid phase has no energy gap.

- Near the first Brillouin zone ($k \sim k_L$): The periodic condition modifies the excitation spectrum ϵ_k to be periodic and to form a band structure(Bogoliubov band) as in the Bloch band. Near the Brillouin zone boundary, the excitation spectrum bends over instead of bend up as illustrated in Fig. 3-4. In the limit of $J \gg U$, the excitation energy is approximated to $\epsilon(k) \sim -2J\cos(\pi k/k_L)$ for $k \sim k_L$.

3.5 Mott Insulator Phase

3.5.1 Commensurate Filling

For $U/J \gg 1$, the limit opposite to the superfluid phase, the Hamiltonian becomes $(1/2)U\sum_i \hat{n}_i(\hat{n}_i - 1)$. The eigenstates for this Hamiltonian are number states $|n\rangle (n = 0, 1, 2, 3, \cdots)$ (Fock state). The ground state is given

$$|\Psi\rangle_{U/J\to\infty} \to \prod_i (a_i^\dagger)^n |0\rangle \tag{3.35}$$

where the atom number per site $n = N/M$ is integer (commensurate filling)

In Fock state configuration, the first excited state corresponds to a particle-hole excitation ($|n\rangle_i|n\rangle_j \to |n+1\rangle_i|n-1\rangle_j$) as illustrated in Fig. 3-5 (a). The excitation

energy is

$$\begin{aligned} \Delta E &= E_{ptcl} + E_{hole} = (E(n+1) - E(n)) + (E(n-1) - E(n)) \\ &= nU + (-(n-1)U) = U \end{aligned} \tag{3.36}$$

To transport a particle from one site to other in the Mott insulating phase, it requires a minimum energy ΔE (none-zero energy gap in energy spectrum), otherwise the Mott insulating system does not allow particle to "flow"(insulator).

The phase coherence property of the Mott insulator phase is very different from that of the deep superfluid phase. Due to suppressed tunneling process, atoms in lattice sites can not "communicate" and not share their wave function information. Lack of communication leads to absence of density correlation. To be more specific, two states $a_i|\Psi\rangle_{U/J\to\infty}$ and $a_j|\Psi\rangle_{U/J\to\infty}$ have vanishing overlap for any i,j ($\langle\Psi|a_j^\dagger a_i|\Psi\rangle_{U/J\to\infty} = 0$). If J increases from zero, the wave function of atoms can start to tunnel through the lattice spacing more easily so that the atoms become less restricted in "communication". However, even if atoms can "talk" to atoms in other lattice sites, the range of communication is limited to near lattice sites (short-range coherence) as long as the ratio of U/J is above a certain critical value $(U/J)_c$. Below $(U/J)_c$, the long range phase coherence is recovered and the system turns into the superfluid phase.

3.5.2 Incommensurate Filling

What happens to the system if the occupation number is not equal to integer? Let us consider the situation where one particle is added to $n = 1$ Mott insulating phase. Strong interaction limit ($U/J \gg 1$) is still assumed here. In this system, it does not cost energy to transport the added particle to other sites (Fig. 3-5 (b)). The energy spectrum for $\bar{n} = 1 + \epsilon$ becomes gapless and shows superfluidity. This system can be considered as superfluid component resides on top of the frozen background atoms in the Mott insulating phase. The chemical potential for $n = 1 + \epsilon$ is given by U.

Let us consider the opposite case where one particle is taken out of (or one hole

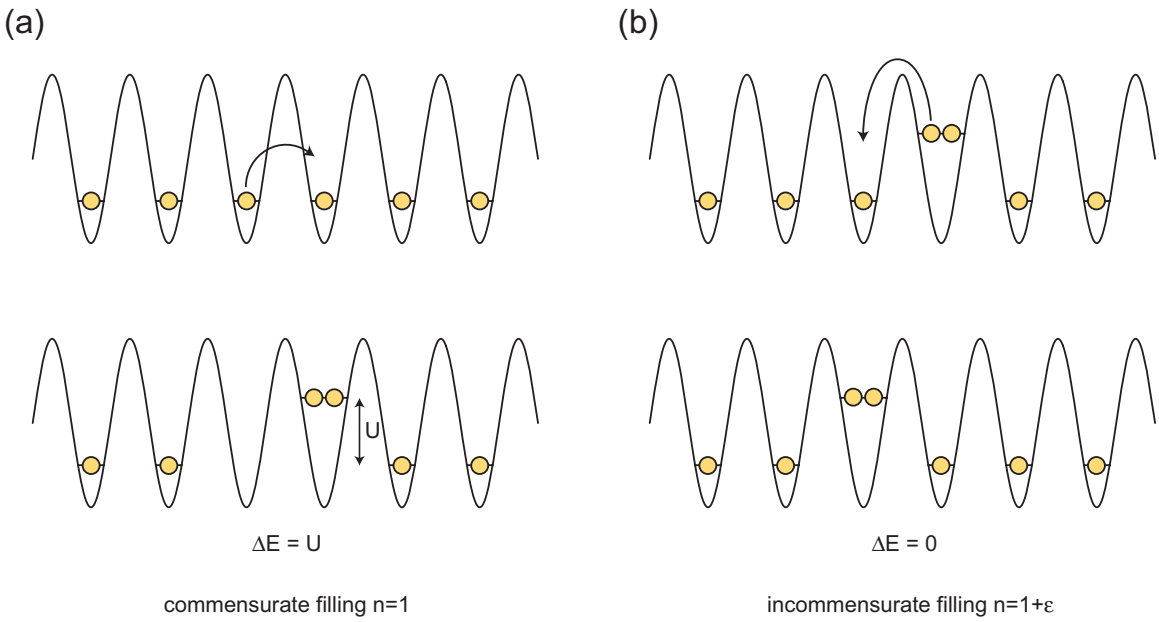

Figure 3-5: Commensurate and incommensurate systems in optical lattice. To move one atom to other site, (a) in commensurate filling the energy cost is equal to the onsite interaction energy U (b) in incommensurate filling additional energy is not required.

is added to) the $n = 1$ Mott insulating system, the energy spectrum also becomes gapless since it does not take energy to move one hole from site to site in the same way as discussed above. On contrary to the $n = 1 + \epsilon$ case, in $\bar{n} = 1 - \epsilon$ system the chemical potential vanishes ($\mu(1 - \epsilon) = 0$). A particle can be "plugged" in one of the empty lattice sites without costing interaction energy with other atoms that are initially occupied in the lattice.

3.6 The Superfluid - Mott Insulator Transition

3.6.1 Qualitative Overview of the Quantum Phase Transition

We have considered two extreme regimes of the parameter $U/J \gg 1, \ll 1$. The state in each limit is very different in terms of energy spectrum and phase coherence. For example, while the deep Mott insulating phase has a finite energy gap $\Delta E = U$, the energy spectrum of the superfluid phase is gapless($\Delta E = 0$). It could be expected that if the system is initially prepared in the deep superfluid phase($J \gg U$) and the

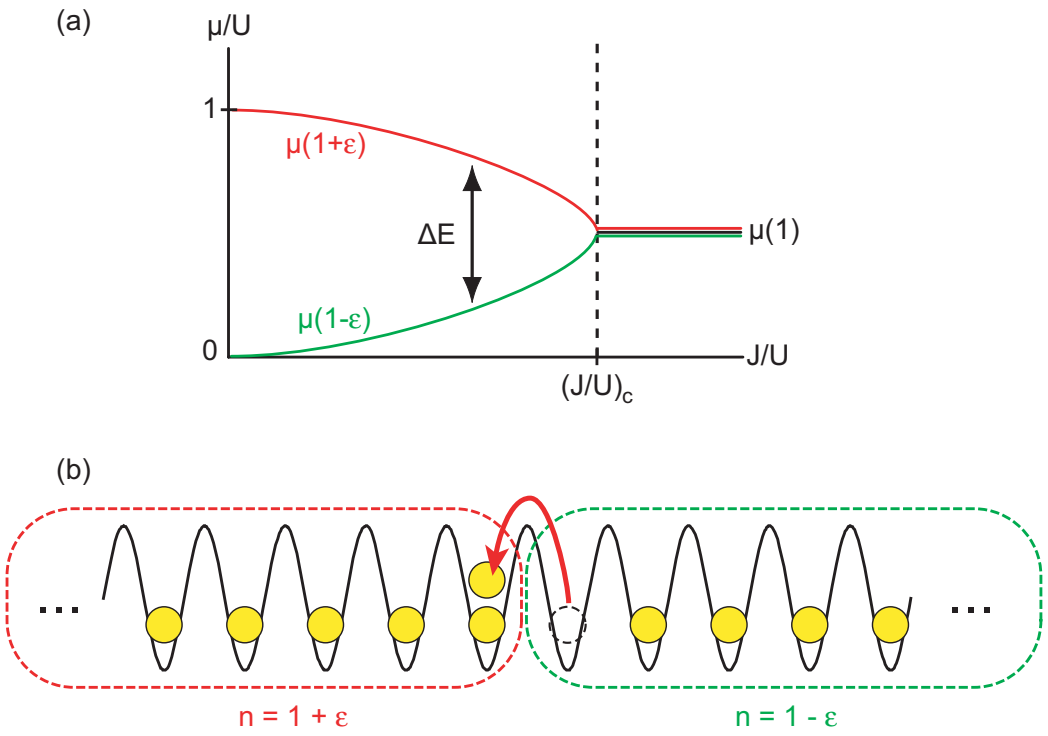

Figure 3-6: Qualitative view of quantum phase transition. (a) The chemical potential for two incommensurate fillings $n = 1 \pm \epsilon$ is displayed as a function of J/U. They differ by U at $J/U = 0$, but become equal at a certain value $(J/U)_c$. At non-zero J/U the energy gap ΔE for the Mott insulator with $n = 1$ is given by the difference of chemical potentials between $n = 1 \pm \epsilon$. (b) Transport of atoms in the $n = 1$ MI phase.

interaction energy U is slowly turned up, the energy gap ΔE becomes non-zero at a certain point $(U/J)_c$ and opens up as U increases.

The quantum phase transition between the two phases may be treated qualitatively in the following way. As discussed in the previous section, in the limit of $J = 0$ the chemical potential μ is very sensitive to the filling factor $\bar{n}$. It is given by $\mu(1+\epsilon) = U$, $\mu(1-\epsilon) = 0$. On the other hand, in the deep superfluid phase($J \gg U$) a chemical potential is a continuous function of a filling factor $\bar{n}$. Consequently, two chemical potentials for $\bar{n} = 1 \pm \epsilon$, that initially differ by U, become infinitesimally close to $\mu(1)$ as the the hopping matrix J is raised up from 0. The chemical potential for the $\bar{n} = 1$ superfluid is given by $\mu(\bar{n} = 1) = 0.5U$. The chemical potential for $\bar{n} = 1, 1 \pm \epsilon$ are drawed qualitatively as a function of J/U in the Fig. 3-6 (a). The two chemical potential meet at a critical point $(J/U)_c$.

Now let us consider the $n = 1$ Mott insulator phase to see how the energy gap ΔE disappear across the phase transition. The energy gap ΔE could be obtained as follows. When a particle hops between sites in the Mott phase, one lattice site, say i, becomes filled with two particles, and the other site j is left empty. The whole system could be considered to be made of two systems with $n = 1 \pm \epsilon$, as depicted in the Fig. 3-6 (b). Then the excitation energy for this infinitesimal transport ($k \to 0$) is the sum of the energy taken for adding one particle to $n = 1 + \epsilon$ system and the energy taken for subtracting one particle from $n = 1 - \epsilon$ system. The energy gap ΔE is given by difference between two chemical potential energies

$$\Delta E = E_{ptcl} + E_{hole} = \mu(1 + \epsilon) - \mu(1 - \epsilon) \tag{3.37}$$

In a $n = 1$ system, the energy gap ΔE (Eq. (3.37)) of the Mott insulating phase decreases as the hopping term J grows as illustrated in the Fig. 3-6 (a). ΔE finally vanishes at a point $(J/U)_c$, and the system turns into the superfluid phase.

3.6.2 Quantum Phase Diagram

So far, the quantum phases have been discussed under the condition that the system is homogenous (no external trapping) and the atom number in a system is fixed. By introducing the chemical potential μ, the condition of fixed atom number may be removed. The Hamiltonian is modified with a chemical potential term

$$H = -J \sum_{<i,j>} a_i^\dagger a_j + \frac{1}{2} U \sum_i \hat{n}_i(\hat{n}_i - 1) - \sum_i \mu \hat{n}_i \tag{3.38}$$

The quantum phase is determined as a function of a chemical potential μ and the parameter J/U.

The quantum phase diagram has been theoretically studied[104] and calculated using various numerical methods such as the Gutzwiller mean-field theory [65, 75], mean-field perturbation methods [124], Quantum Monte Carlo (QMC) method [20, 8, 74, 74], etc. The most recent QMC [20] calculation provides the critical point

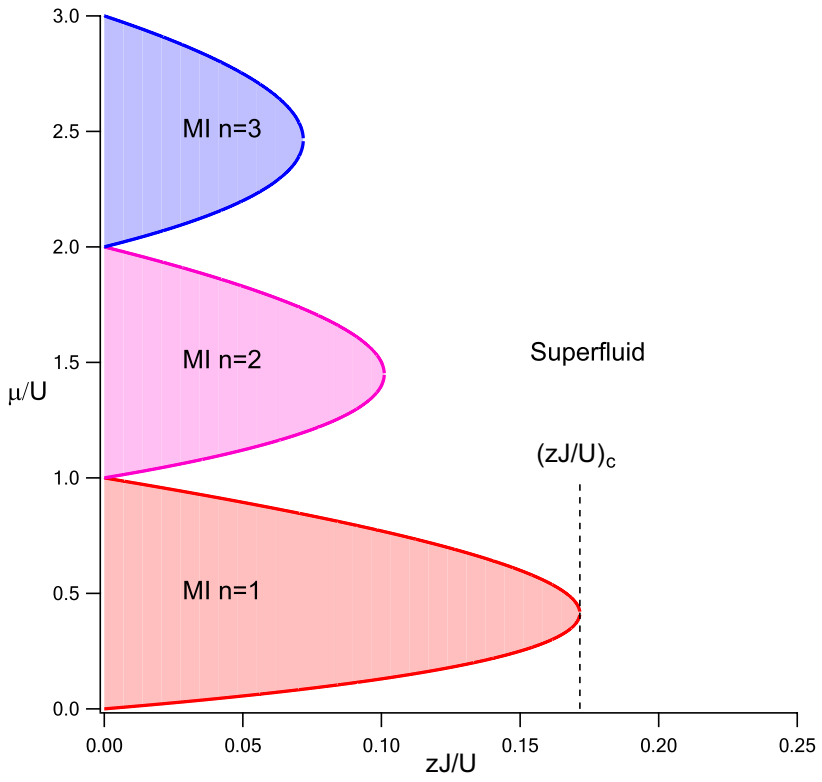

Figure 3-7: Quantum phase diagram calculated using the meanfield approach. The quantum phase is determined as a function of the chemical potential μ and J/U

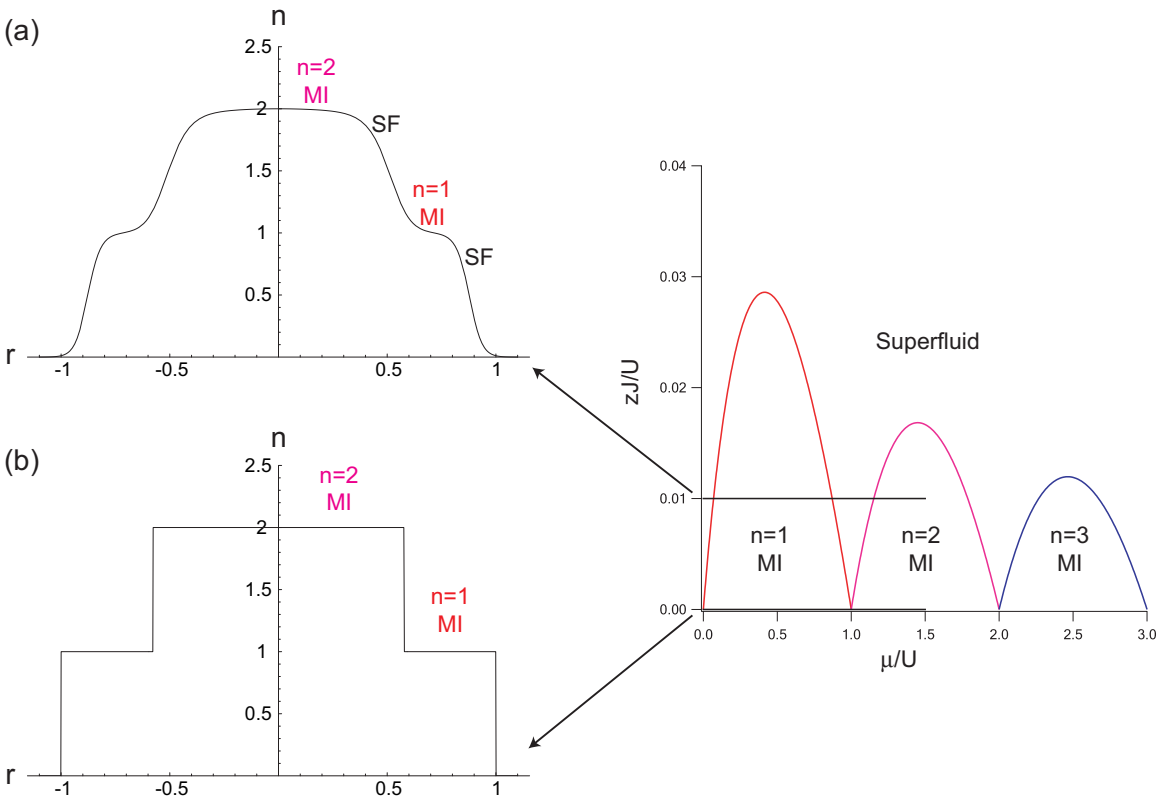

Figure 3-8: Density profile of ultracold atoms in optical lattice for $J/U = 0.01$[(a)] , and $J/U = 0$[(b)] with chemical potential $\mu_0 = 1.5U$. Each quantum phase is surrounded by layers of other quantum phases (formation of "shell structure"). In (a), the density between MI phases varies continuously in the SF shell. In (b) ($J = 0$), the SF components are absent and the density profile becomes step-like with the MI phase.

$(J/U)_c = 1/29.34(2)$ at a filling factor $n = 1$ in a 3D cubic lattice. The mean-field theory predicts the critical point $(J/U)_c = 1/(5.8z)$ for $n = 1$ with $z = 2d$ the number of nearest neighbors. The mean field critical point $(J/U)_c$ in 3D cubic lattice is 1/34.8. The quantum phase diagram derived from the mean field theory is plotted in Fig. 3-7.

3.6.3 Density Profile : "Shell Structure"

In experiments, atoms are normally trapped in an external trap, and the density profile becomes inhomogeneous. If the density change is smooth enough (this condition is generally held in our experiment), a small part of the system localized

near $\mathbf{r}$ may be approximated to be homogenous with the local chemical potential $\mu_{loc} = \mu_0 - V_{ext}(\mathbf{r})$(local density approximation). The Hamiltonian may be written

$$\begin{aligned} H &= -J \sum_{<i,j>} a_i^\dagger a_j + \frac{1}{2} U \sum_i \hat{n}_i(\hat{n}_i - 1) + \sum_i V_{ext}(\mathbf{R}_i)\hat{n}_i - \sum_i \mu \hat{n}_i \\ &= -J \sum_{<i,j>} a_i^\dagger a_j + \frac{1}{2} U \sum_i \hat{n}_i(\hat{n}_i - 1) - \sum_i \mu_{loc}(\mathbf{R}_i)\hat{n}_i \end{aligned} \tag{3.39}$$

The quantum phase is now determined by the *local* chemical potential μ_{loc} as well as U/J.

The local chemical potential μ_{loc} varies from μ_0 (trap center) to 0 (trap edge) in a typical harmonic trap; the quantum phase also changes as a function of position in the trap. It becomes possible in trapped system that several different quantum phases exist simultaneously. For example, for $J/U = 0.1$ and $\mu_0 = 1.5$, the system has 3 different phases; $n = 2$ MI phase near the trap center, two superfluid layers, and $n = 1$ MI phase between the two superfluid layers (Fig. 3-8 (a)). The density profile consists of SF and MI phase layers, which is called "shell structure"[30, 67, 65].

In the limit of $J/U \to 0$, the system is fully frozen, and the quantum phase must be the MI phase at every position in the system. The number fluctuation becomes zero so that the ground state is given by a Fock state. The number of atoms per site is then an integer and determined as

$$\bar{n} = n \quad \text{if} \quad n - 1 < \mu/U < n \tag{3.40}$$

with integer $n = 0, 1, 2, \cdots$. The density profile becomes discontinuous with steplike profile as illustrated in Fig. 3-8 (b).

3.6.4 Time-Of-Flight Images

The phase coherence properties can be estimated from time of flight images. When atoms in the superfluid phase are released from the trap and optical lattice, phase

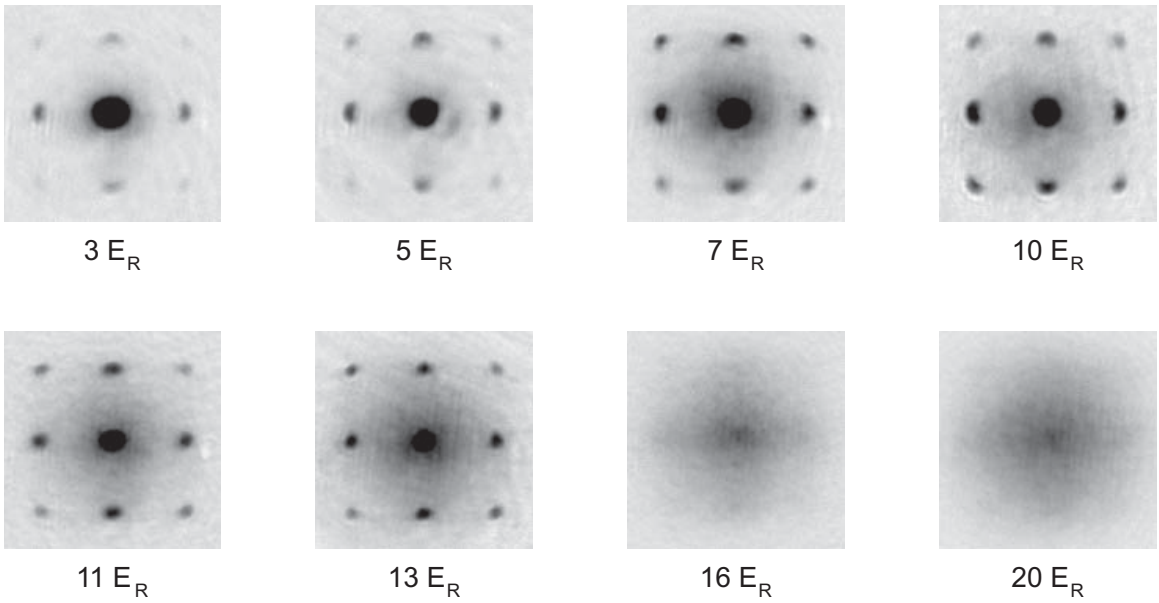

Figure 3-9: Time of flight images of ultracold atoms released from the trap and optical lattice for variable lattice depth. The interference fringe contrast increases with lattice depth. For deep lattice (i.e. 16, 20 E_R), the system is in the Mott insulating phase, and the fringe pattern disappears due to lack of long-range phase coherence. The expansion time was 33 ms.

coherence[53] leads to an interference pattern as depicted in Fig. 3-9. The interference peaks have the momentum of $2k_L$[95]. However, the Mott insulating phase does not have long range phase coherence and does not show the interference pattern in the time-of-flight images. The time of flight images are shown in Fig. 3-9 across the superfluid to the Mott insulating phase transition. The fringe patterns are clearly visible in the superfluid phase with lattice depths of 3 E_R to 13 E_R, while it disappears above 16 E_R where the system is in the Mott insulating phase.

One thing to note on time-of-flight images is that the interference pattern does not provide direct information on the SF-MI phase transition. The interference fringe pattern probes only ground-state properties, and the SF-MI phase transition should be probed by measuring the properties of excitations[101].

Chapter 4

The Science Chamber

In this chapter, I describe our new experimental apparatus, the "Science Chamber". The science chamber is an auxiliary vacuum chamber attached to the main vacuum chamber, of which design is described in Ref. [118]. The main vacuum chamber is equipped with magnetic trap coils and magneto-optical trap(MOT) optics for the production of BEC. Typically BEC is produced and trapped in the main vacuum chamber for experimental study. One drawback of the main vacuum chamber is that there is very limited optical access, since big magnetic coils and laser cooling optics occupy most of space around the main vacuum chamber. Such limited optical access to the main chamber makes it difficult to set up optical lattice laser optics around the main chamber. Typical optical lattice experiments generally require 6 clear laser beam paths to a vacuum chamber.

These problems are fixed by introducing an auxiliary vacuum chamber attached to the main chamber. In this configuration of two vacuum chambers, BEC (or ultracold atoms) is prepared in the main chamber, and transferred to the auxiliary chamber using an optical dipole trap. The role of the main chamber is only to produce a BEC or ultracold atoms, and the experimental part with the BEC is performed in the auxiliary chamber. We call this auxiliary chamber "science chamber", since most of the scientific experiments are carried out in the auxiliary chamber.

The Science chamber concept provides great flexibility in several technical aspects. The design of the science chamber could be customized for each type of experiment,

and the installation of the science chamber could be done easily without breaking the main chamber's vacuum. This makes it easy and quick to switch between different experiments. The scheme of the science chamber has been employed at MIT for the atom chip, hard disk trap, and optical lattice experiment. For more details on the experimental scheme in these experiments, I refer to early theses ([110, 76] for atom chip experiment, [13] for hard disk trap experiment)

In this chapter, only the science chamber and associated optical lattice setup are covered. Detailed description and discussion of other parts of the Rb BEC machine such as the Rb oven, the Zeeman slower, and the main chamber, are given in the Rb BEC machine paper [118], and other theses [117, 13, 15]

4.1 Overview

4.1.1 Vacuum Chamber

The science chamber is designed for optical lattice experiments. The chamber has many viewports for optical lattice laser beams and optical trapping beams, especially accommodating two large viewports for high-resolution imaging. The science chamber is illustrated in the fig. 4-1. In a horizontal plane, there are 6 view ports (the outer diameter $1.25'' \sim 1.5''$), 1 flange for vacuum pumping, and 1 small flange connecting to the main chamber. Two big viewports with the diameter of $4''$ are placed on the top and bottom of the science chamber (along z-axis in Fig. 4-1). All viewport glasses are AR coated for $\lambda = 780$ and 1064 nm.

The science chamber is connected to the main chamber by a flexible bellow on the flange labeled by (a) in Fig. 4-1. The 4-way cross vacuum part, where the ion pump, ion gauge, and Ti-sub pump are installed, is connected to the science chamber on the flange labeled by (b) in Fig. 4-1.

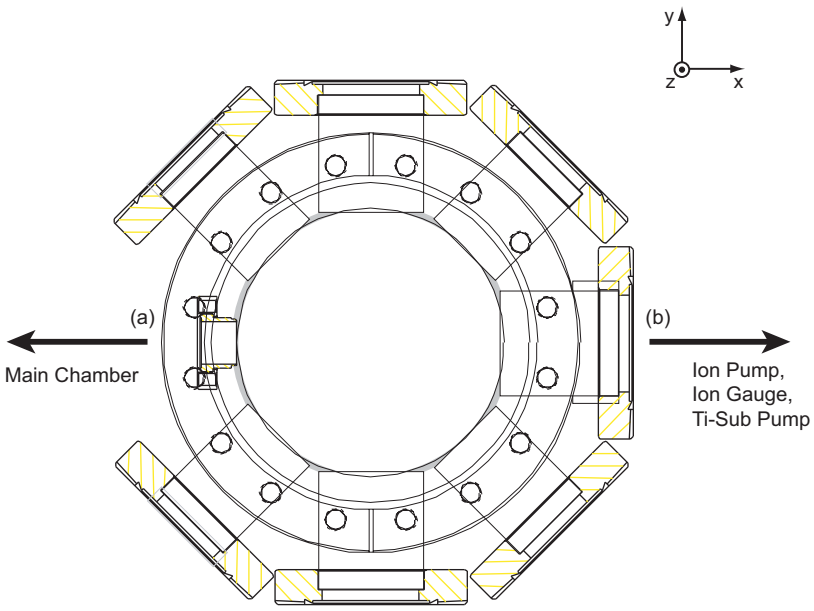

Figure 4-1: Top view of the science vacuum chamber. There are 6 view ports (the outer diameter $1.25'' \sim 1.5''$), 1 flange (b) for vacuum pumping, and 1 small flange (a) connecting to the main chamber. Along the vertical direction there are two $4''$ diameter viewports on the top and bottom of the chamber, which is designed for high resolution imaging.

4.1.2 Bias Coils

For bias B-field, pairs of coils are used in Helmholz configuration. Each of 4 coils with 20 turns (4 turns/layer $\times$ 5 layers = 20 turns) are placed on the four diagonal viewport flanges in Fig.4-1. The dimension of these coils is: outer diameter: $4''$, inner diameter: 2-3/4$''$. Along the vertical direction (z direction), two big coils with 20 turns (5 turns/layer $\times$ 4 layers = 20 turns) are placed on the top and bottom viewports. Its outer and inner diameter are 7-1/16$''$ and $6''$ respectively.

4.1.3 RF, Microwave Antenna

A RF antenna is made of a coil of a thin copper wire wound with five turns ($N = 5$). Its diameter is slightly smaller than the inner diameter of the top viewport flange so that the RF antenna can fit inside the top viewport flange. RF signal is generated by RF synthesizers (model number: Agilent 33250A, or SRS DS345), and the signal is amplified and sent to the RF antenna.

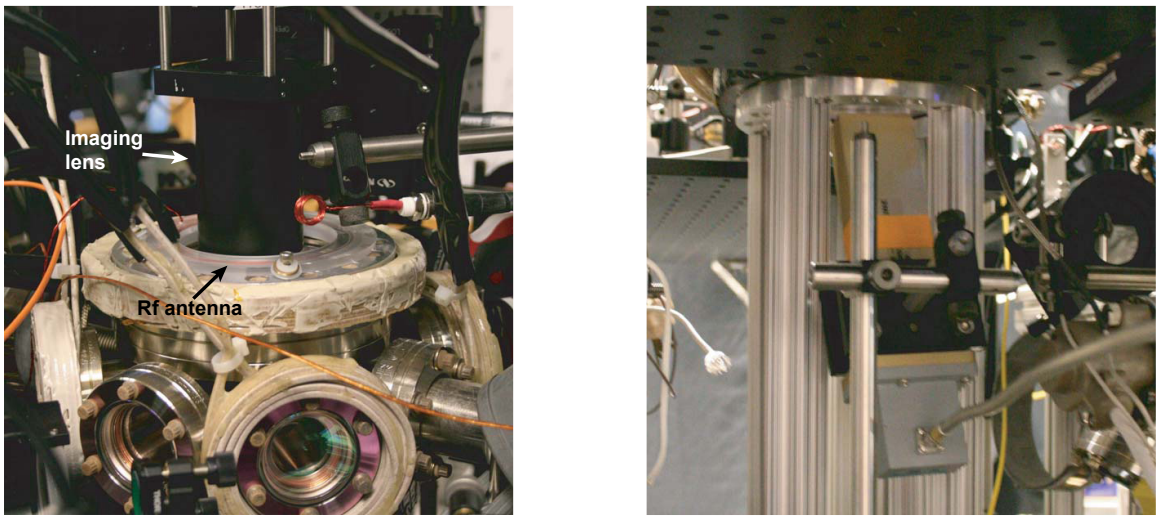

(a) rf antenna (b) microwave antenna

Figure 4-2: Rf and microwave antenna. (a) An rf antenna is installed right above the top viewport with a plastic ring-shape mount. A high-resolution imaging lens stack is also shown above the top viewport flange. The imaging lens is very close to the vacuum chamber for higher numerical aperture(NA). Bias coil pairs are mounted along three perpendicular direction. (b) A microwave antenna is located below the chamber. It is an open-ended rectangular waveguide with a frequency range of 4.90-7.05 GHz.

An open-ended rectangular waveguide is employed as the microwave antenna horn.(Fig. 4-2) Waveguide standard WR-159 (frequency range: $4.90 - 7.05\,\mathrm{GHz}$(F-band)) was used for the 6.8 GHz, ^{87}Rb hyperfine transition. Dimensions of waveguide are $1.590'' \times 0.795''$ (W×H) with a length of $6''$(Manufacturer: Waveline INC. model: 5901-SMAF(Adapter), 5942-2(6 inch-long straight section)). The Agilent microwave synthesizer(model: E8257D-520) and microwave amplifier (Manufacturer: Microwave power INC. L607-37, maximum output power: 37dBm) are used for signal generation and amplification.

For spin flipping ($\Delta m = \pm 1$), the direction of the oscillating magnetic field must be perpendicular to the bias magnetic field direction . The bias magnetic field direction is set along the y-axis in Fig. 4-1. The rf coil's magnetic field direction was set along z-axis. For the microwave antenna, the magnetic field direction is the long axis of the rectangular waveguide and was chosen to lie along the x-axis in Fig. 4-1

In microwave applications, special coaxial cables designed for high frequency signal are required. A typical type of coaxial cables used in the lab, RG-58 works properly only up to few hundreds MHz and has huge attenuation at 6.8 GHz, over 30dB/10m. In our experiment, a rigid cable shielded with aluminium (Pasternack Enterprises, PE34184-60) is used for connecting the amplifier and the microwave antenna, and semi-rigid cable is used between the synthesizer and amplifier.

4.1.4 Ultra High Vacuum in the Science Chamber

The science chamber was pre-baked at 250°C with a turbo and an ion pump before being joined with the main chamber. After its installation, the science chamber was baked out again at 250°C. After the bake out, the Ti-sub pump was fired several times, and the final pressure in the science chamber reached down to between mid-10^{-11} and 10^{-10} Torr, which is acceptable pressure range for ultracold atom experiment.

Compared to the typical pressure in the main chamber, which is below 10^{-11} Torr, the science chamber pressure is relatively high. It is strongly believed that the capacity of the ion pump in the science chamber is not big enough for the vacuum load, and it limits the pressure. The capacity of ion pumps typically used in the main

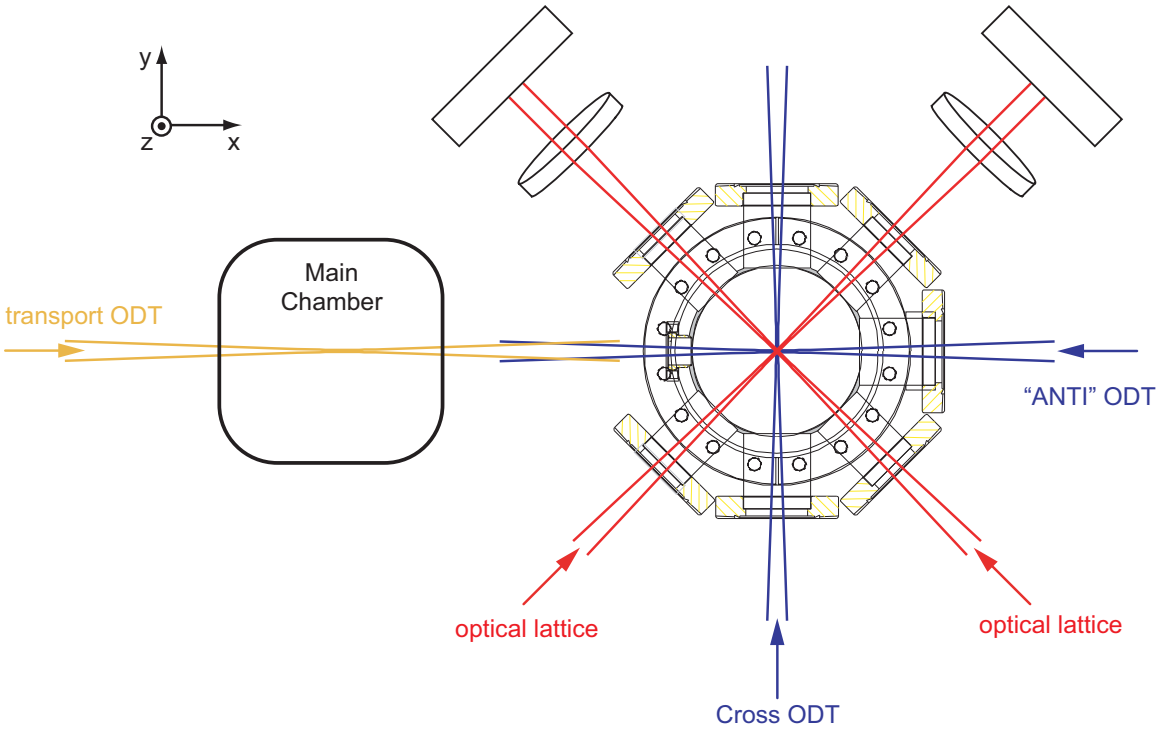

Figure 4-3: IR laser beam set-up in the science chamber.
Three IR laser beams are used for optical dipole trapping: the transport ODT laser beam (yellow beam coming from left), the anti ODT (blue beam coming from right), and the cross ODT (blue beam coming from bottom). The transport ODT transports atoms from the main chamber to the science chamber. The atoms are then transferred to the anti ODT from the transport ODT in the science chamber. A combination ODT (anti ODT + cross ODT) is employed as the main trap.
Three optical lattice laser beams are aligned to the center of ODT. Two horizontal lattice beam directions are chosen along the diagonal directions orthogonal to each other. The vertical lattice (not shown in the figure) is set up along z-direction.

chamber is 55 l/s, while the science chamber ion pump's capacity is considerably small 20 l/s. As a result, when the gate valve between the main chamber and the science chamber opens the science chamber pressure becomes lower due to pumping from the main chamber ion pump. If lower pressure is required in the future, it should be considered to change the ion pump in the science chamber.

4.1.5 IR Laser Beams for Optical Trapping and Lattice

9 optical beam paths are employed for IR laser: 6 beam paths (3 incoming beams and 3 retro-reflected beams to form standing wave) for optical lattices, 3 beam paths

for optical dipole traps(ODT). The configuration of IR laser beams is shown in Fig. 4-3.

The transport ODT laser beam (yellow beam on the left in Fig. 4-3) is aligned to the position of the main chamber magnetic trap. The transport ODT beam captures atoms cooled in the main chamber, then the beam is linearly moved to the center of the science chamber by moving its focus lens using a motorized translation stage. Since the beam path is very long and its focus lens is mounted on the translation stage, the transport ODT beam has mechanical vibration issues not to provide stable trapping potential.

To address these issues, another ODT beam, which we call "anti" ODT (blue beam on the right in Fig. 4-3), is set up in the opposite direction of the transport ODT beam. The anti ODT has the same beam profile and position as the transport ODT except for the laser beam propagation direction. When the transport ODT beam arrives in the science chamber, the transport ODT beam and the anti ODT beam overlap very well so atoms trapped in the transport ODT could be mostly transferred into the anti ODT.

The third ODT beam perpendicular to the anti ODT beam direction (cross ODT in Fig.4-3) is aligned to the focal spot of the anti ODT. The cross ODT provides tight confinement along the long axis of the anti ODT to enhance the evaporative cooling efficiency and to reach below the BEC transition temperature.

Two optical lattices are set up in the horizontal plane as shown in Fig. 4-3. The third optical lattice is aligned along the vertical direction (z-direction).

4.2 Optical Dipole Traps

4.2.1 Optical Trap Transport

In order to deliver ultracold atoms produced in the main chamber, focused IR laser beam is employed as a tweezer and transporter. The optics arrangement for the transport ODT is illustraed in Fig. 4-4. The IR laser beam is magnified and collimated

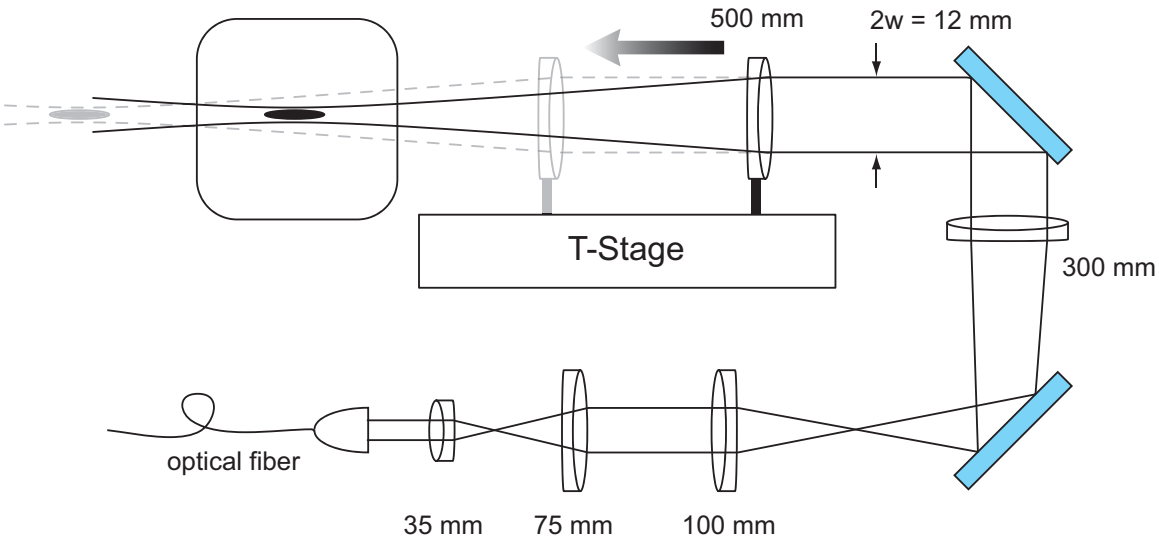

Figure 4-4: Transport ODT optics layout. ODT IR laser beam size is magnified by two telescopes: combinations of 35 mm+75mm, and 100 mm+300 mm lenses. The collimated IR laser beam with $1/e^2$ beam diameter of 12 mm is focused on the atoms by an $f = 500$ mm lens. A translation stage moves the atoms trapped in the ODT by translating the $f = 500$ mm focus lens.

with an $1/e^2$ radius of $\sim 6\,\mathrm{mm}$. The laser beam is then focused on the atoms in the main chamber by a $f = 500\,\mathrm{mm}$ lens, and the $1/e^2$ radius of the focal spot is $w_{\mathrm{ODT}} \sim 30\,\mu\mathrm{m}$. The ODT laser power is linearly ramped up to 600 mW in 2 s to capture the atoms.

Transport of atoms to the science chamber is performed by moving the $f = 500\,\mathrm{mm}$ focus lens(Fig.4-5). An air bearing linear translation stage(Aerotech ABL2075, with a precision of up to $0.1\,\mu\mathrm{m}$) moves the lens. Its motion is precisely controlled by a computer program. A computer program calculates the optimal transport velocity and acceleration, and it drives the translation stage for a given moving distance d and time duration t. Typical transport parameters are $d = 360.80\,\mathrm{mm}$, and $t = 3\,\mathrm{s}$.

After the transport, the transport ODT laser power is linearly ramped down to zero, while the anti ODT laser power is simultaneously ramped up to $600 \sim 700$ mW in 2 s to transfer atoms from the transport ODT to the anti ODT.

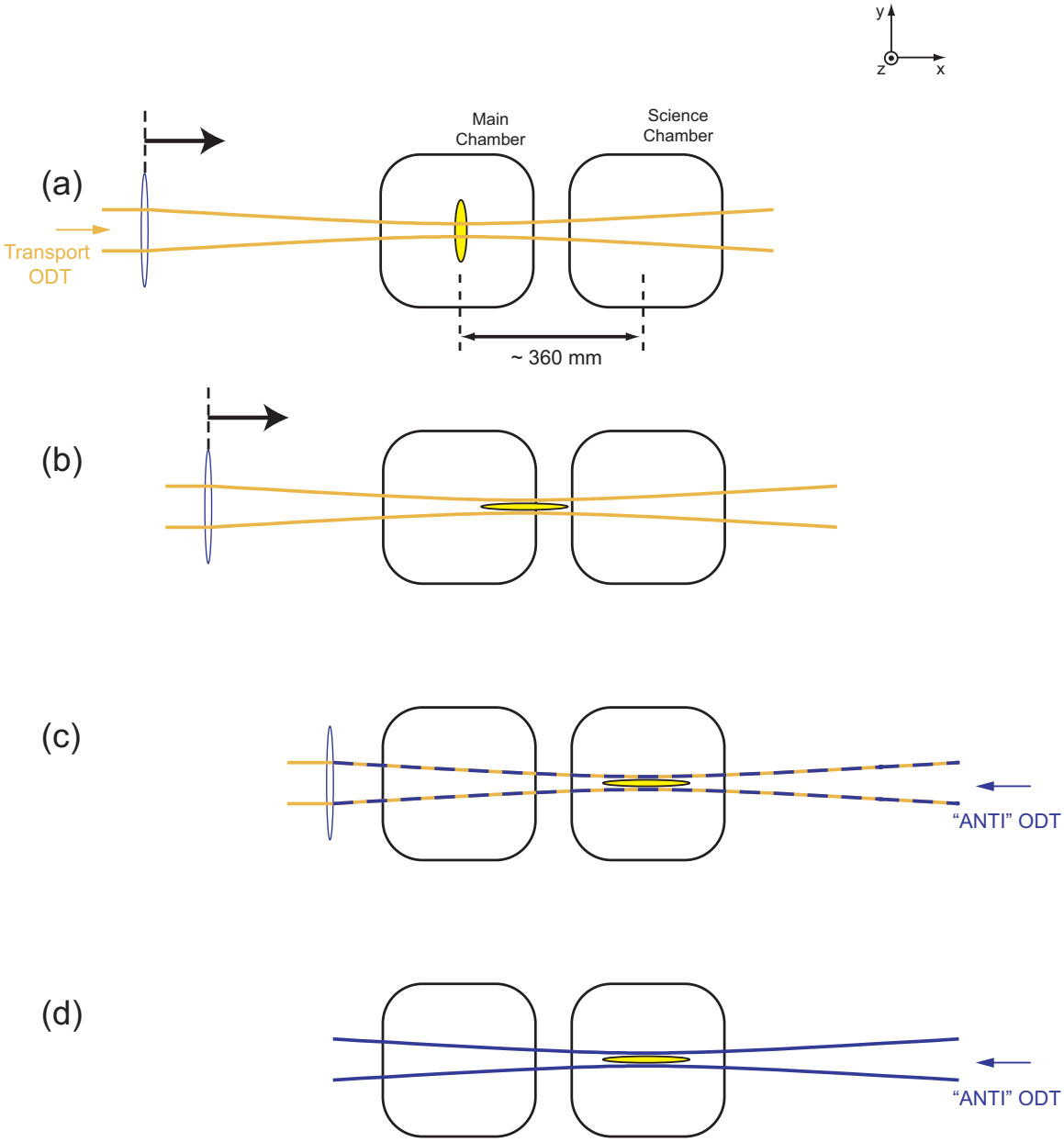

Figure 4-5: Transport of cold atoms. Before transport, atoms are cooled in the main chamber. (a) After cooling is finished, the transport ODT is slowly ramped on to atoms in the main chamber for catching and trapping atoms in the ODT laser beam. (b) The main chamber magnetic trap is turned off suddenly, and atoms are held in the ODT beam for $\sim$ 500 ms until sloshing motion of atoms induced during the sudden turn-off of magnetic trap is suppressed. Transport starts by moving the focus lens. The transport distance is typically $\sim$ 360 mm. (c),(d) Atoms are transferred to the anti ODT beam from the initial ODT beam (see text).

4.2.2 Cross Optical Dipole Trap: Combination trap

The trap geometry of the anti-ODT beam is highly elongated; the trap frequencies are $\omega_\perp \sim 600$ Hz (along the perpendicular direction), $\omega_\parallel \sim 5$ Hz (along the beam propagation axis) at the maximum power $P = 600$ mW. The evaporative cooling process is slow and inefficient with such a low trapping frequency $\omega_\parallel$. In our setup, BEC could not be achieved by evaporative cooling in a single anti-ODT beam.

In order to increase trapping frequency $\omega_\parallel$ along the weak axis of the anti-ODT, an additional ODT laser beam (called the cross-ODT) is utilized. The focus size of the cross ODT is 55μm ($1/e^2$ radius). After the atoms are transported into the anti-ODT, the cross ODT beam is turned on. The power is linearly ramped up to 600 mW in 2 s, providing a high trapping frequency of $\omega_\parallel \sim 200\,\mathrm{Hz}$.

4.3 Production of BEC in the Science Chamber

In typical experiments performed in the main chamber, atoms are cooled and condensed into BEC by the following sequence of cooling techniques: MOT, optical molasses, and rf-induced evaporative cooling in magnetic trap.

A BEC in the science chamber could be produced in two different ways:
there could be two experimental procedures.

1. BEC is made in the main chamber, and transported to the science chamber using the transport ODT.

2. Cold atoms (but not cold enough to condense into BEC) are made in the main chamber, and transported to the science chamber. The BEC is achieved in the science chamber by further evaporation cooling.

Option 1 is normally employed in the Na BEC experiment at MIT.([76, 110]) However, implementation of this scheme is difficult with Rb atoms due to different properties between Rb and Na, such as mass, three body recombination rate, etc.[117] In our experimental setup, it was observed that Rb BEC becomes unstable easily and decay very fast in the transport ODT during the transport.

In contrast to a BEC, the thermal gas can be transported without significant loss, since the thermal gas is relatively immune to heating compared to BEC. The number and temperature of cold atoms transported in the science chamber were found to be stable and sufficient to be condensed into BEC. The scheme # 2 has been exploited as our main cooling scheme offering consistent performance of BEC production.

In scheme # 2 , the cooling sequence in the main chamber is slightly modified; during the last rf-induced evaporation cooling step, the rf ramp is stopped at ~ 500 kHz above the BEC transition. The transport ODT is then ramped in 2 s. The main chamber magnetic trap turns off suddenly, and transport starts as described in section 4.2. After delivery of atoms to the anti-ODT, the cross ODT is turned on to realize a tight combination trap. The evaporation cooling is then performed in the combination trap by ramping down the trap depth in about 2 s. A typical protocol for the production of BEC is shown in Fig.4-6. After ramp-down of the combination trap, atoms are held in a trap for additional 100 ms to allow residual thermal atoms to evaporate. Finally, the BEC is achieved in the combination trap.

Images of a BEC with 13 ms time-of-flight are displayed in Fig. 4-7 In the combination trap, the trapping force is mainly provided by the anti-ODT, since it has a tighter focal spot than the cross-ODT. The trap depth of the combination trap is controlled by varying the anti-ODT laser power. Fig. 4-7 also shows how the BEC fraction (or BEC temperature) is controlled by the final ODT depth.

Typical frequencies of the combination trap are $\omega_\perp = 2\pi \times 150\,\mathrm{Hz}$, $\omega_\parallel = 2\pi \times 25\,\mathrm{Hz}$ (cigar shape), and the atom number N is on the order of 10^4. BEC is prepared in the hyperfine state $|F = 1, m_F = -1\rangle$, same as the initial hyperfine state of cold atoms prepared in the main chamber. We observed that the atoms stay in the same hyperfine state without undergoing spin flip during turn-off of the main chamber magnetic trap coils and transport, even if an additional bias B-field is not applied. It is a combination of the Earth bias field ($\sim 0.5\,\mathrm{G}$) and ambient B-field in the laboratory that prevents atoms from spin flipping. Thanks to the ambient field, the B-field does not cross zero in the path of transport, and the spin of atoms adiabatically follows B-field direction so that atoms are safely delivered to the science chamber without

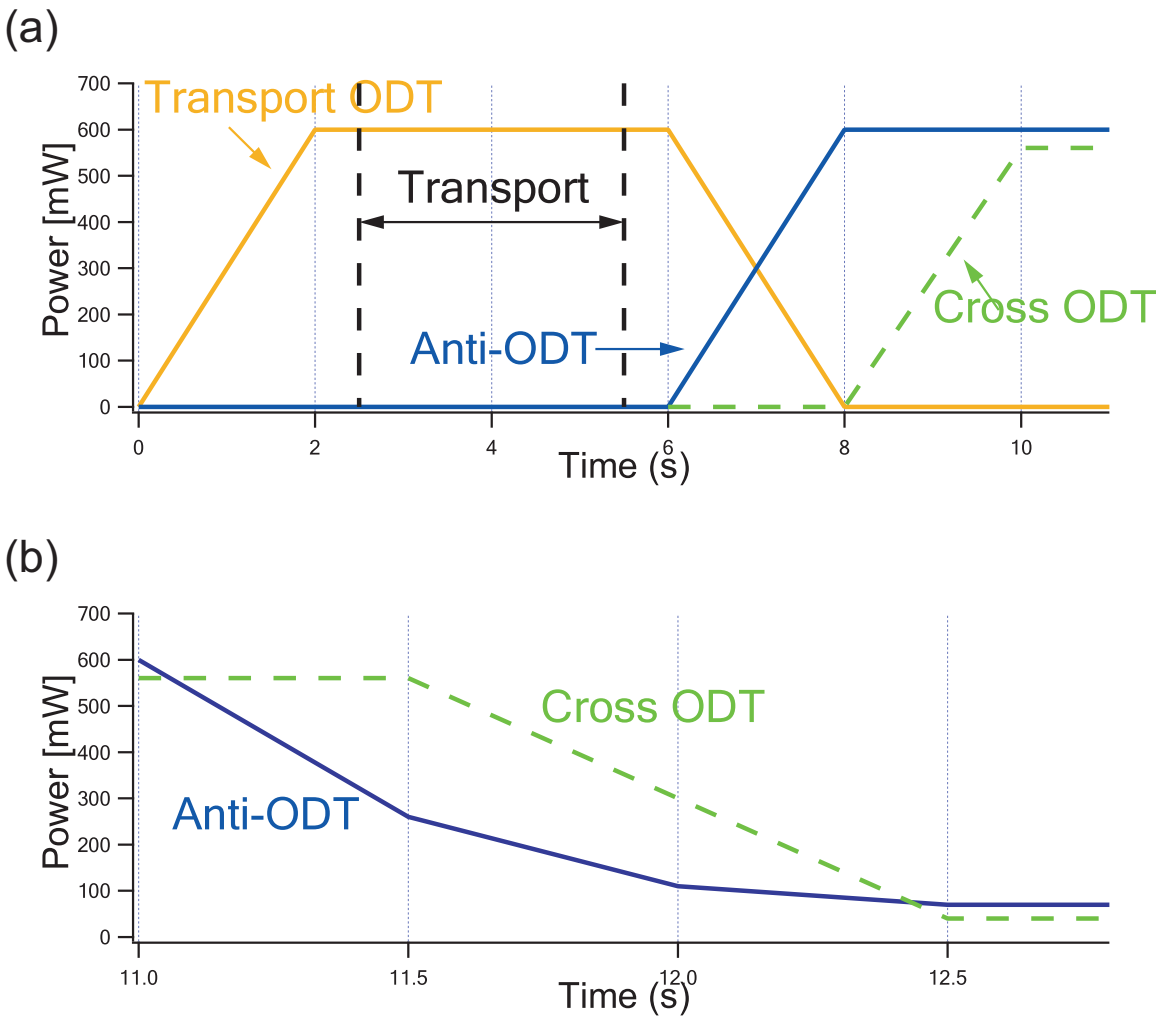

Figure 4-6: Experimental procedure for BEC in the science chamber. (a) Atom transport procedure. The atoms transported to the science chamber are transferred from the transport ODT to the anti ODT between $t = 6$ and $t = 8$ sec. The cross ODT laser beam is then ramped up to form a combination trap (anti ODT + cross ODT). (b) Evaporation cooling procedure in the combination trap. The anti ODT is ramped down first followed by cross ODT. The evaporation cooling is normally performed in a few seconds. After the ramp down of the combination trap depth, atoms are held for another few hundred ms to evaporate residual thermal atoms.

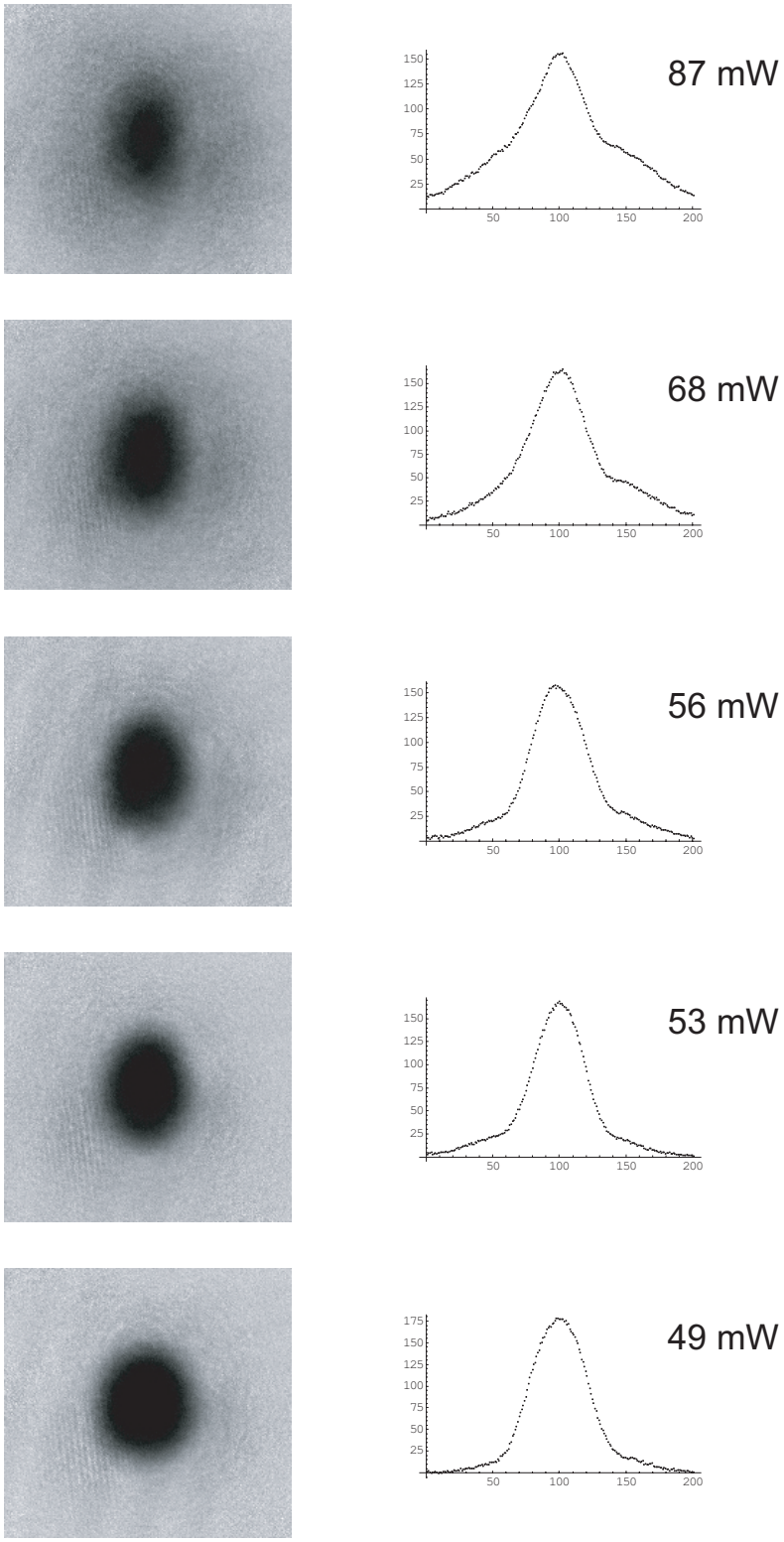

Figure 4-7: Emergence of BEC in the combination trap. BEC emerges from a thermal atomic cloud as the trap depth lowers. The number denoted on the right of plots is the power of the anti ODT, which determines trap depth.

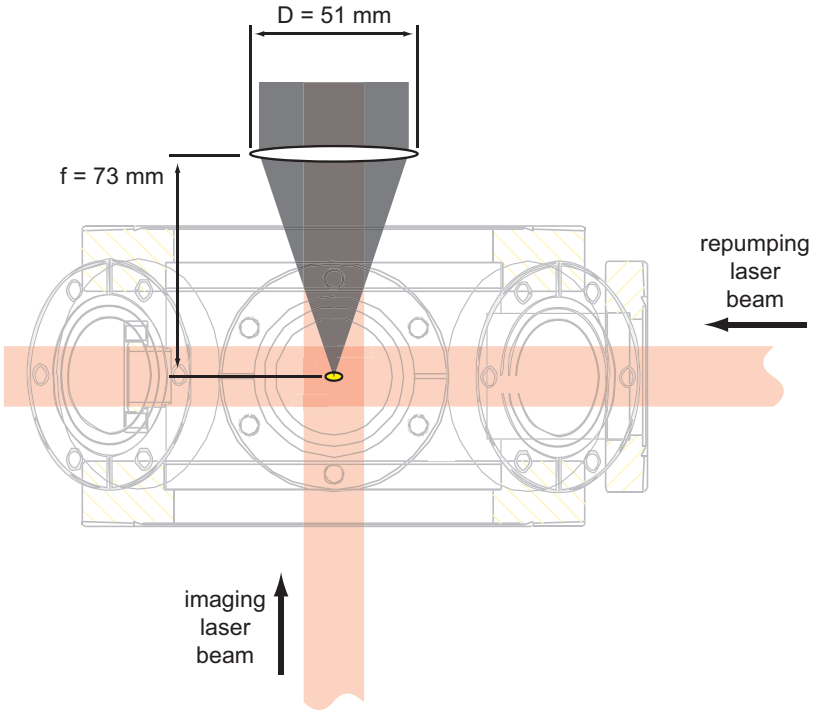

Figure 4-8: Imaging setup for the science chamber.

spin flip.

4.4 Imaging

The science chamber is designed in particular for high-resolution imaging. A big top viewport with a 4″ diameter window is close to the center of the vacuum chamber. Its large solid angle is suitable for high numerical aperture optics. The imaging setup of the science chamber is illustrated in Fig. 4-8.

The imaging process starts with pumping atoms into the $F = 2$ ground hyperfine state using a repumping laser beam tuned to $5^2S_{1/2}F = 1 \rightarrow 5^2P_{3/2}F = 2$ transition. Immediately the imaging beam (cycling transition $5^2S_{1/2}F = 2 \rightarrow 5^2P_{3/2}F = 3$) illuminates the atoms, and the shadow of atoms is collected with a CCD camera (absorption imaging). The duration of the imaging laser pulse is chosen to be short enough to minimize atomic motion during the imaging. Typical exposure time is $50\mu s$.

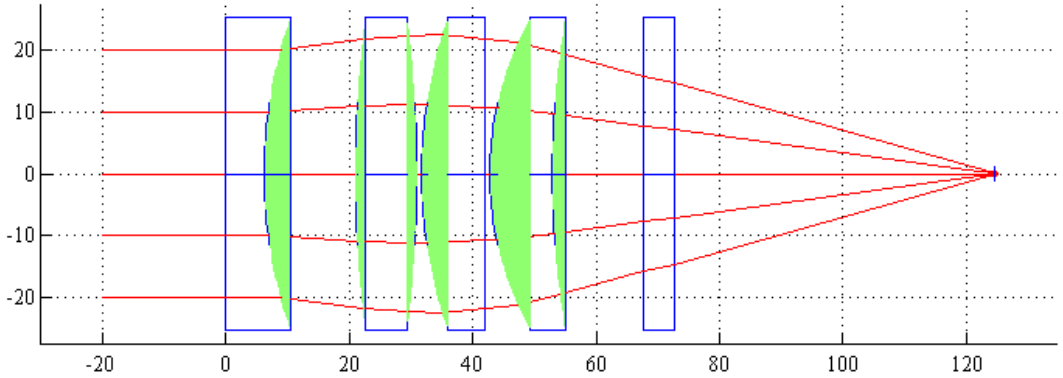

Figure 4-9: The configuration of a high resolution imaging lens. It consists of four 2″-diameter spherical lenses. The rightmost plane glass represents the viewport.

4.4.1 High Resolution Lens

The resolving power of a lens is determined by its numerical aperture (NA). The imaging resolution of a lens is proportional to $\lambda/(\mathrm{NA})$ (λ is wave length of imaging light). To obtain higher NA, a lens should cover a larger solid angle coming from the imaging target.

Four 2, ″ diameter spherical lenses (8 lens surfaces) were assembled for our imaging lens system. 6 out of 8 lens surfaces are spherically curved, and 2 are flat. The configuration of lenses was optimized using a ray-tracer program. Detailed dimensions of the lens stack are given in the appendix A. The focal length of the lens stack is determined to be 73 mm. The numerical aperture for our lens stack is ~ 0.3 providing an optical resolution of $\sim 2\,\mu$m.

After passing the high-resolution lens stack, imaging light ray is sent to 2″ diameter f=750 mm lens to be focused and imaged on a CCD camera. With 73 mm objective lens and 750 mm camera lens, the magnification factor M of the imaging system is ~ 10. In order to avoid optical aberation related with off-center rays such as coma, or astigmatism, both the lens stack and 750 mm lens are mounted on the same optics cage system keeping the center line of lenses aligned.

4.5 Optical Lattice

In our experiment, a 3-D cubic optical lattice potential is employed. Optical lattices are created by retro-reflecting incoming laser beam and forming standing waves. The optical lattice axes were chosen to be along three orthogonal directions.

In general, an optical lattice potential is formed not only by counter propagating laser beams but also by any pair of intersecting laser beams. As a consequence, there would be "unwanted" optical lattice potentials created by interference between two different axis laser beams. The optical lattice potential formed by two laser beams along the different axes (i.e. laser $\#1, \#2$) is given by (see the section 3.1.2)

$$V_{latt}(\mathbf{r}, t) = V_1 + V_2 + 2\sqrt{V_1 V_2}\left\{(\mathbf{e}_1 \cdot \mathbf{e}_2)\mathrm{Re}\left[e^{-i((\mathbf{k}_1 - \mathbf{k}_2)\cdot\mathbf{r} - (\omega_1 - \omega_2)t)}\right]\right\} \tag{4.1}$$

where V_1, V_2 are the potential energy depth induced by each laser beam. The polarizations of two laser beams were chosen to be orthogonal($\mathbf{e}_1 \cdot \mathbf{e}_2 = 0$), and the frequency difference ($\Delta\omega = \omega_1 - \omega_2$) to be very large in order to remove the interference term of Eq.(4.1) between different lattice axes. The frequency detuning $\Delta\omega$ was set to -3, 0, 3, MHz respectively for three lattice laser beams.

Typical optics layout for optical lattices is drawn in Fig.4-10. The IR laser is delivered to the optics setup by an optical fiber. The power of the laser is monitored by a photo diode. This signal is sent to a PID control box, which actively stabilizes and controls the laser power. The polarization of the beam is first set to linear polarization by a polarized beam splitter(PBS) cube. The angle of the linear polarization is then rotated by $\lambda/2$ wave plate to the desired angle. After the IR laser beam size is adjusted by a telescope, it is focused onto the atoms, and is retro-reflected by a dichroic mirror to form the lattice potential. Dichroic mirrors that reflect 1064 nm IR laser but transmit 780 nm light (^{87}Rb D-2 line) are used so that imaging along a lattice axis is possible.

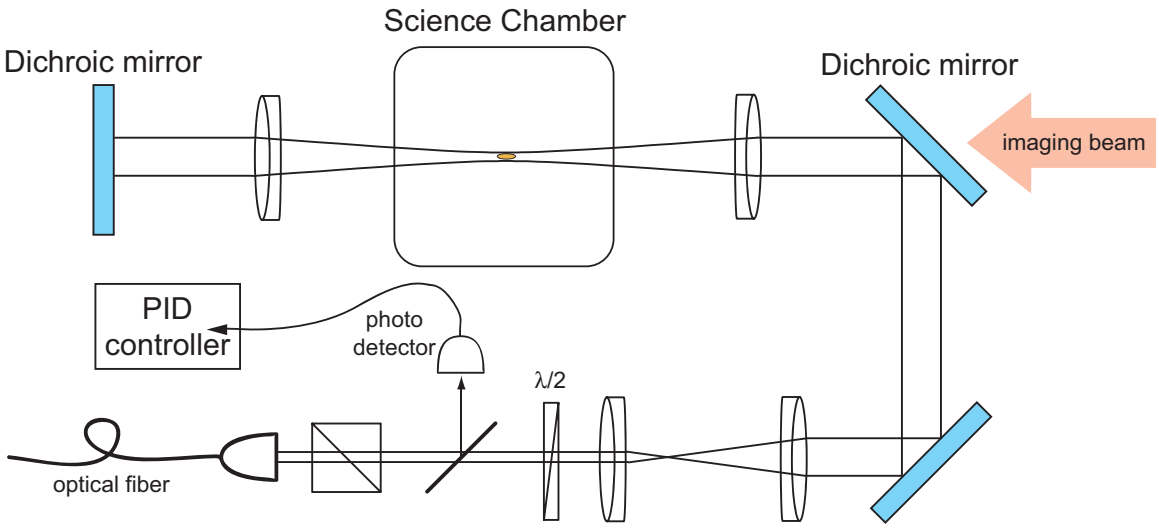

Figure 4-10: Optics layout for the optical lattice setup. An IR laser beam delivered by an optical fiber is focused on atoms. The retro-reflected beam is focused on the atoms again to form a standing wave. Dichroic mirrors (reflects 1064 nm light and transmits 780 nm light) are used for imaging along the lattice axis.

4.5.1 IR Laser System for the Optical Lattice

1064 nm IR laser is employed for our optical lattice. such lasers are commonly used in material processing and medical purpose, and high power is available at affordable cost. Our 1064 nm IR laser system is manufactured by IPG photonics. The laser unit consists of two parts: a seed laser (MODEL:YLD-0.01-1064-SF) and a fiber amplifier (MODEL: YLD-0.01-1064-SF). The seed laser is a 1064 nm ND:YAG single mode laser pumped by a laser diode. Output power is normally $\sim$ 10mW with a linewidth of 100 kHz.[1] The seed laser is coupled into the fiber laser amplifier. Our fiber amplifier laser unit can amplify up to 20 W.

The high power IR laser beam is then distributed to six laser beams: three ODT beams, three optical lattice beams. They are delivered from the laser table to each optics setup on the BEC machine optics table through optical fibers. The IR laser beam setup is illustrated in Fig. 4-11. The IR laser is split into two beams by beam splitter cubes, and the splitting ratio is controlled by $\lambda/2$ waveplate located between

[1] As of 2008, the laser diode of our seed laser unit runs on fixed current mode. Power mode causes frequency instability

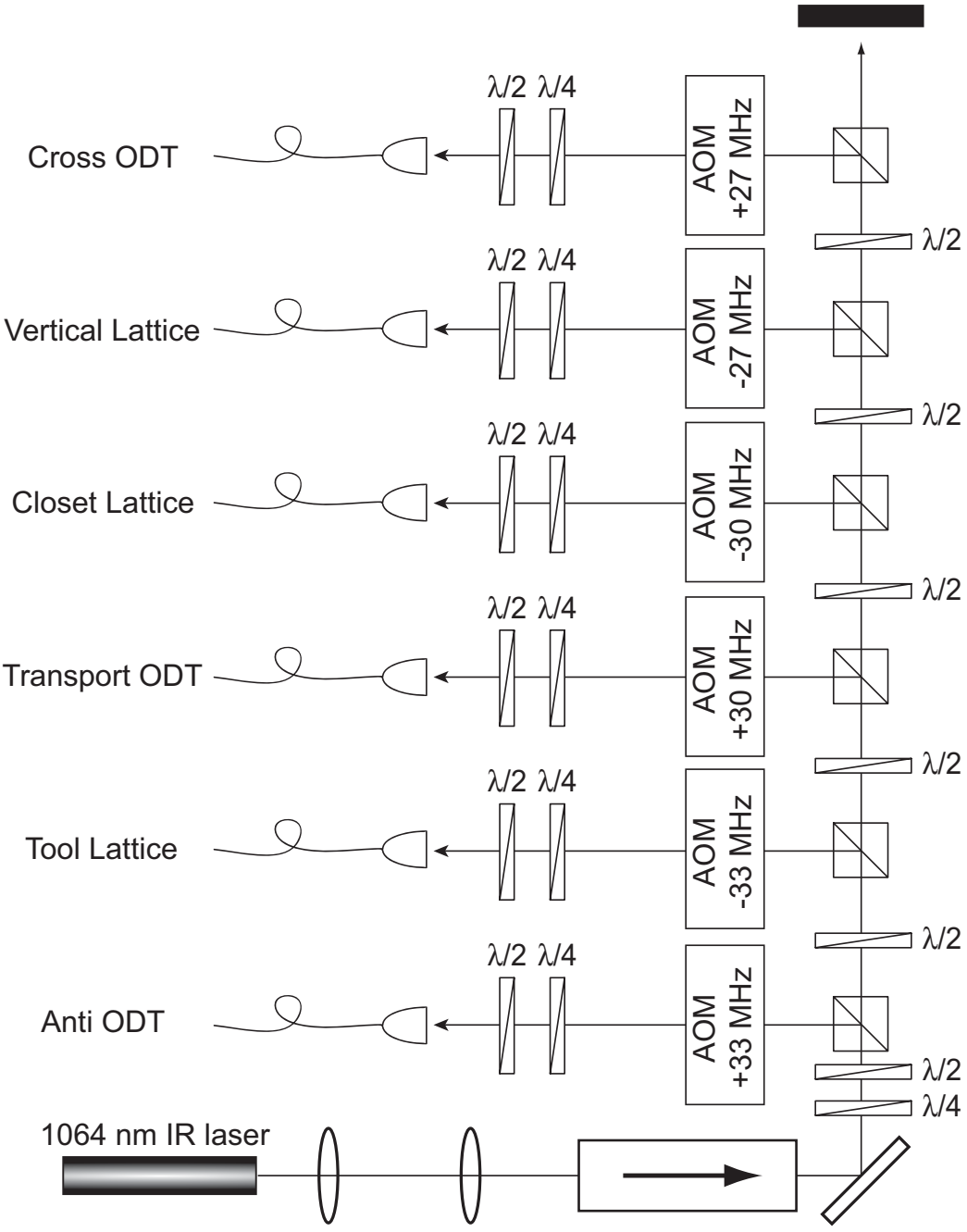

Figure 4-11: IR laser setup. The IR laser beam passes through telescope optics to adjust the beam size to an optical isolator inlet. After the optical isolator, the IR laser beam is split into 6 beams. The power and frequency of each laser beam is adjusted by AOM's. The frequency detunings of laser beams are shown in the figure. Non polarization-maintaining optical fibers are used in our experiments, and the polarization of out-coupled light is adjusted by two waveplates ($\lambda/2$, $\lambda/4$) located before the fiber coupler shown in the figure.

the cubes. The frequency of the laser beams is modulated by AOMs which different frequency offsets relative to the initial $\lambda = 1064\,\text{nm}$ laser beam. This ensures that the interference between different IR laser beams is suppressed.

In general, the laser system for a red-detuned optical lattice must be far detuned from the atomic transition in order to suppress spontaneous light scattering and atom loss. 1064 nm IR laser is sufficiently far detuned from the ^{87}Rb D-2 line(780 nm), for spontaneous scattering rate to be very low. For example the spontaneous light scattering rate γ is $\sim 0.02\,\text{Hz}$ in a deep optical lattice with a depth of $35\,E_R$.

4.5.2 Optical Lattice Alignment

Each axis of the optical lattice beam is aligned as follows

1. **Set up the optics**: Arrange optics for optical lattice as in Fig. 4-10.

2. **Find the position of atoms**: Image a trapped BEC (in-situ) along the lattice axis. Keep the CCD camera at the same position for the next step.

3. **Find and align the lattice laser spot**: Set the CCD camera mode to align mode. Turn on the lattice IR laser beam, and move mirrors or lenses to find the IR laser beam spot on the camera. (**CAUTION**: While finding and locating the laser spot on the CCD camera, attention is required to avoid burning the CCD camera. Focused IR laser beam can damage the CCD chip easily, and the damaged pixel will be permanently dead. **The power of the IR laser system must be turned down to minimum. Additional attenuation of the IR laser beam should be properly done by using high-ND[2] filters.**) Once the laser spot is found, steer and focus it on the same position as of the atoms in the image acquired in step 2.

4. **Retro-reflect the lattice beam**: Set up the retro-reflection mirror. When the retro-reflected laser beam overlaps very well with the initial incoming lattice beam, it is coupled back into the optical fiber delivering the incident beam. This

[2]Normally ND 4-6

back-coupled laser beam follows the exact same beam path of the initial laser beam in the opposite way until it is reflected by the optical isolator shown in Fig. 4-11.

5. **Align the retro-reflection mirror:** The retro-reflection mirror could be aligned by monitoring and maximizing the power of the retro-reflected laser beam rejected from the optical isolator. Typically 5 to 10 % of the initial laser beam is also reflected from the optical isolator and gives huge DC offset in the intensity of the reflected laser beam. The retro-reflected laser beam signal is normally smaller than this DC offset. In order to suppress this DC offset, an optical chopper system is utilized. The retro-reflected laser beam signal now becomes an AC square wave signal oscillating at the chopper frequency. By filtering out the DC component from the signal, only the retro-reflected beam signal is measured.

6. **"Ask" atoms** *how well the optical lattice is aligned*: By applying a short 12.5 μs pulse of the lattice laser beam onto BEC, Kapitza-Dirac(KD) diffraction of atoms is obtained. The final alignment is done by maximizing the intensity of the diffraction pattern.

4.5.3 Lattice Beam Calibration

The depth of optical lattices is calibrated by analyzing the Kapitza-Dirac diffraction pattern of BEC [57]. When a very short pulse of standing wave laser beam is applied to atoms[3], the wavefunction of atoms is modified by the phase imprint from the pulse. The phase imprinted by the AC stark shift of the standing wave pulse is given by

$$\phi(z) = \frac{1}{\hbar}\int_0^\tau dt V_{latt}(z) = \frac{V_0\tau}{\hbar}\cos(2kz) \tag{4.2}$$

[3]The pulse duration τ should be shorter than the photon recoil time scale $1/\omega_R$ so that the atomic motion during the pulse time is considered to be very small. (Kapitza-Dirac regime)

The wavefunction of BEC is modified by the phase factor $e^{i\phi}$

$$|\Phi\rangle \rightarrow e^{-i\phi(z)}|\Phi\rangle_{BEC} = \sum_{n=-\infty}^{\infty} i^n J_n\left(\frac{V_0\tau}{\hbar}\right) e^{i2nkz}|\Phi\rangle_{BEC} \tag{4.3}$$

where the Jacobi-Anger identity is used ($\exp[i\alpha\cos\beta] = \sum_{n=-\infty}^{\infty} i^n J_n(\alpha)\exp[in\beta]$), and J_n's are Bessel functions of the first kind. In Eq.(4.3), the phase factor e^{i2nkz} implies that states with momentum $2n\hbar k$ are populated. The population of the momentum state $2n\hbar k$ is given by

$$P_n = \left[J_n\left(\frac{V_0\tau}{\hbar}\right)\right]^2 \tag{4.4}$$

From images of KD diffraction patterns, populations of each momentum state are measured with various lattice laser powers P. By fitting the measured populations to Eq.(4.4), the lattice depth V_0 is calibrated as a function of the laser power P. Typically $\tau = 12.5\mu$s pulse has been used in the calibration. Note that 12.5 μs is much shorter than a recoil time scale, which is 500 μs for $\lambda = 1064$nm.

For the calibration of optical lattice, different methods, such as Bragg pulse, are also employed in other groups' experiments. (See Ref.[87] for details on calibration methods)

4.5.4 Technical Issues

Several technical issues have been encountered while the science chamber and optical lattice system were built. Two points are addressed in this section.

1. **High power optics**: When IR laser is used for optical lattices or optical trappings, high power is normally required, since the frequency of IR lasers is far-detuned from the atomic resonance. Such a high power laser beam requires high power optics. Optics which are non-compatible with high power leads to residual absorption and beam distortion.

   The distortion is caused by local heating of optics. The temperature increases only near the laser beam path, resulting in a non-uniform temperature distri-

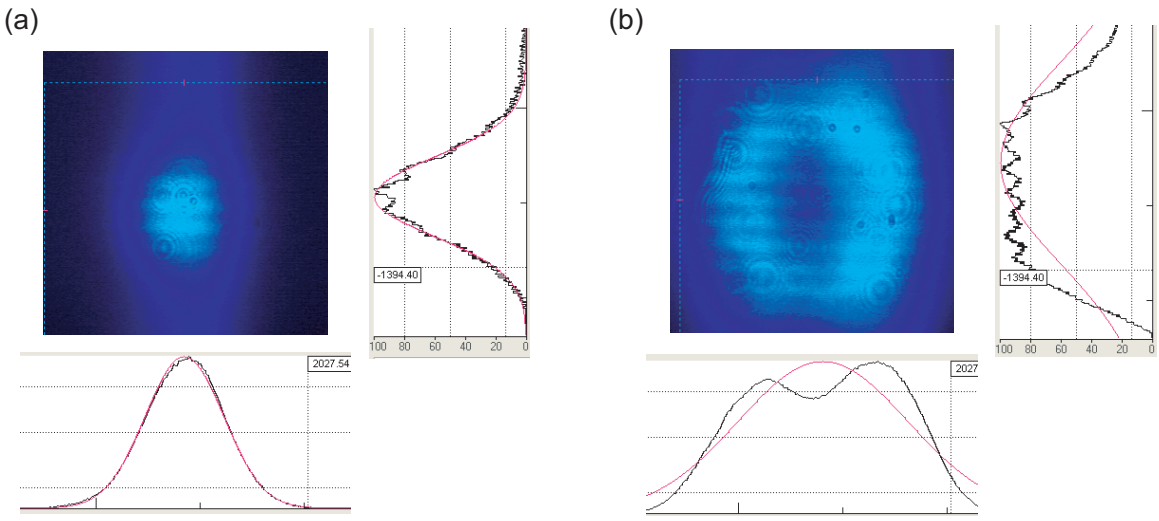

Figure 4-12: Thermal lensing effect in optics. The profile of laser beam was measured after passing a non-high-power PBS cube with (a) low power (1 W), and (b) high power (10 W). With high power, temperature of optics near the center of laser beam increases higher than other part of optics. It results in distortion of laser beam profile such as hollow core shape.

bution. A temperature gradient leads to a non-uniform index of refraction and to distortion of the beam profile. This is the so-called "thermal lensing effect".

When the laser power was higher than $\sim$ 10 W, the thermal lensing effect appeared on polarized beam splitter(PBS) cubes of the IR laser setup described in Fig.4-11. It severely degraded our optical fiber coupling efficiency. Thermal lensing effects on laser beam profile are illustrated in the Fig.4-12. PBS cube is normally made up of two pieces of triangular shaped glass glued together by an adhesive material. It is this adhesive material which leads to the thermal lensing effect. The problem was solved by using high energy PBS cubes in which a pair of triangular shaped glass is *optically contacted* instead of by adhesive material.

Thermal lensing effects also occurred in our optical isolator, which uses normal glued PBS cubes as polarizers. A high power isolator is now employed in our system which uses Brewster window polarizer instead of normal glued PBS cubes.

2. **Mechanical vibration** We have seen the life time and the size of the BEC in either combination trap or optical lattice to be strongly affected by acoustic noise such as talking in the laboratory leading to unstable performance of the machine. There are several suspicious steps where the noise effects are significant: the switch-over from the transport ODT to the anti ODT, the evaporation step in the combination trap, ramping of optical lattice.

   In our experimental setup, nine IR laser beams for ODTs and lattices are focused at the same position, and their beam pathes are quite long. Small mechanical vibrations are able to disturb the laser beam alignment and create sloshing or heating of the atoms. To make things worse, the frequency of mechanical vibrations is similar to the frequency of atomic motion. Even though the noise-sensitive part has not yet been identified , mechanical vibration effects could be reduced by removing all the sound in the laboratory, mainly human talking. Nevertheless, such noise issues must be properly addressed in the near future.

Chapter 5

Manipulation of BEC with an Optical Lattice

This chapter discusses optical lattices as manipulation tools for ultracold atomic experiments. Two experiments performed with Rb BEC using optical lattices as engineering tools[19, 16] are briefly introduced. Please see the reprints included in Appendix G(Ref.[16]) and E(Ref.[19]) for detailed discussions.

5.1 Optical Lattice as a Manipulation Tool

Optical periodic potentials have been employed in a number of a BEC experiments for manipulation and engineering of a BEC. The roles of a optical lattice as a manipulation tool can fall into three categories as follows.

5.1.1 Kaptiza-Dirac Scattering: Two-Way Coherent Splitter

When a very short pulse of an optical standing wave is applied, a BEC is ***coherently*** scattered (Kapitza-Dirac scattering) into momentum states with $p = \pm\, n \times 2\hbar k_L$ along the direction of the standing wave with integers $n = 0, 1, 2, \cdots$ (k_L: recoil momentum of optical lattice laser). Kapitza-Dirac (K-D) scattering has been widely employed as

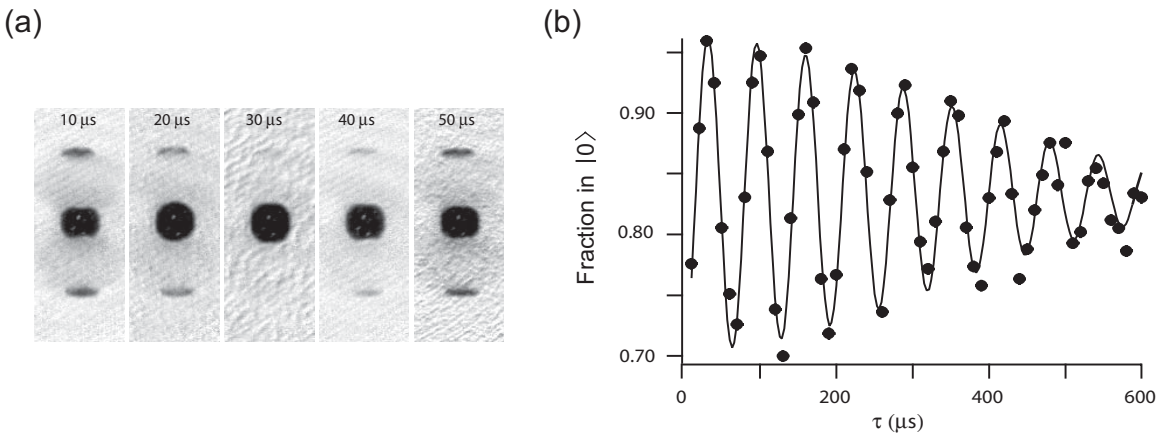

Figure 5-1: Oscillating interference fringes. (a) Time-of-flight images of a BEC with the K-D scattered atom pairs. The fraction of atoms in $|0\rangle$ state oscillates with a time duration τ between two short standing wave pulses. (b) Oscillation of the fraction of atoms in $|0\rangle$.

a coherent splitter of cold atoms[59, 10, 51, 93].

K-D scattering was utilized as a coherent splitter in our experiment of photon recoil momentum measurement[16] for atomic interferometry. In our experiment reported in Ref.[16], a standing wave pulse for K-D scattering was applied to a BEC to prepare two coherent momentum states $|p = \pm 2n\hbar k\rangle$. After time τ the second pulse for K-D scattering was applied, and the two out-coupled momentum states come back to the initial momentum state $|0\rangle$ leading to interference between the initial BEC atoms and the atoms that were out-coupled and then returned to $|0\rangle$. We observed that the interference fringe oscillated with a recoil frequency of a laser light(Fig.5-1). By measuring the frequency of fringe oscillation, the recoil momentum of atoms caused by the absorption of a photon in a dispersive medium was determined to be $n\hbar k$ (n: the index of refraction of gas).

5.1.2 Bragg Scattering: One-Way Coherent Splitter

A "moving" standing wave formed by two laser beams with a slight frequency difference $\Delta\omega$ ***coherently*** populate the states satisfying the Bragg condition: momentum of atom $p = \hbar\Delta k$($\hbar\Delta k$: momentum difference between the two laser beams) and the energy of atom $E(p) = \hbar\Delta w$. This scheme has been used for the study of an excitation

spectrum of a BEC[126, 115], the spectroscopy of a dynamic structure factor[113], matter wave mixing experiments[63, 125], an out-coupler for an atom seed[103], etc. Bragg scattering was utilized as a coherent out-coupler to create a small atom seed for a 4-wave mixing in the experiment presented in the next section.

5.1.3 Optical Lattice: Energy Dispersion Modifier

The modification of an energy dispersion relation from free particle $E^0(p) = p^2/2m$ to the energy band structure$E_n(p)$ in the presence of optical lattices is widely utilized for various purpose. Remarkable phenomena in optical lattices such as Bloch oscillation[9], Landau zener tunneling[89] has been demonstrated in optical lattices. Optical lattices have been utilized to engineer atomic mass in various cases: variable mass[21] for the Josephson junction experiment, very high mass[94] for 1D Tonks gas transition, negative mass[35, 34, 5] for the study of anomalous atomic motions.

As presented in the following section, the 4-wave mixing in 1 dimension was demonstrated by engineering an energy dispersion relation with a optical lattice.

5.2 1D Four Wave Mixing in an Optical Lattice

This section starts with one simple question: in one dimensional situation can two particles with the same velocity collide?

In free space, a collision between two particles in the same momentum state is not possible due to the energy-momentum conservation(or phase matching condition). The energy dispersion in free space is simply given by $E(p) = p^2/2m$, and the energy-momentum conservation law imposes

$$2E(p) \neq E(p+q) + E(p-q) \quad \text{for all} \quad q \tag{5.1}$$

However, in a periodic potential, the energy dispersion relation $E(p)$ becomes the energy band $E_n(p)$ with band indices $n = 1, 2, 3 \cdots$. For the ground band, the energy $E_0(p)$ is bound within bandwidth energy, and the curvature of $E_n(p)$ becomes negative

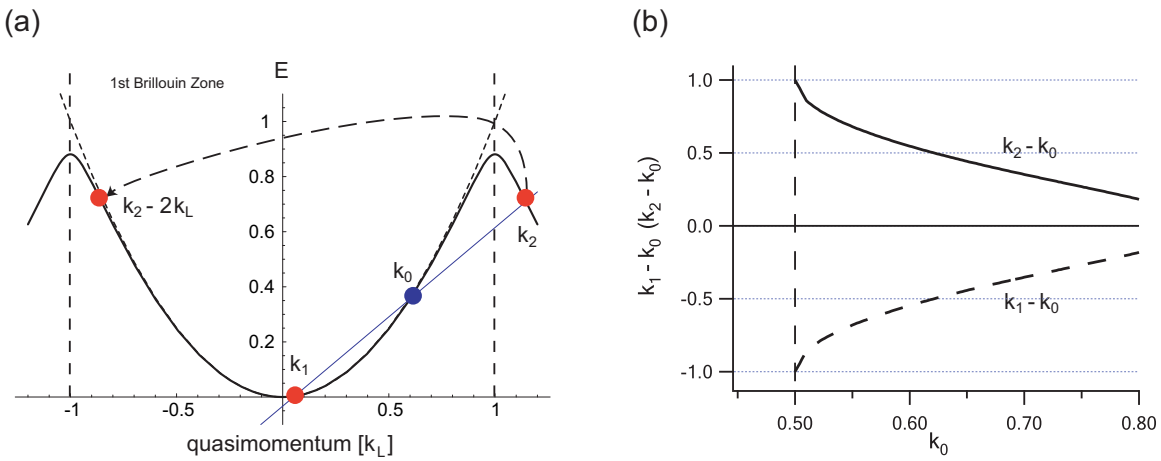

Figure 5-2: The energy dispersion relation and the phase matching condition in an optical lattice with a depth of $0.5E_R$. (a)Black curve(dashed parabolic curve) shows the energy dispersion in an optical lattice (in free space, respectively). The first Brillouin zone is given by $(-k_L,\ k_L)$. In the ground band, two atoms with same quasimomentum k_0 can collide and scatter into two different states with momentum k_1 and k_2 conserving the momentum and energy. The momentum state k_2 outside the first Brillouin zone is the same state with $q = k_2 - 2k_L$ in the first Brillouin zone. (b) A set of quasimomentum states satisfying the energy-momentum conservation in a lattice depth of $0.5E_R$. $\Delta k_i = k_i - k_0\,(i = 1, 2)$ are plotted.

near the first Brillouin zone boundary leading to collisions between two atoms with the same quasimomentum q. This scattering process is illustrated in Fig. 5-2.

For a given momentum k_0, there is one pair of states with k_1 and k_2 satisfying the phase matching condition as shown in Fig. 5-2 (b). For a momentum $k_0 < 0.5k_L$, phase matching condition is not satisfied. At momentum $k_0 = 0.5k_L$ the scattering process becomes possible for $\Delta k_{1,2} = \pm 1k_L$; the two scattered states $k_1 = -0.5k_L$, $k_2 = 1.5k_L$ are indeed the same state with quasimomentum $-k_0 = -0.5k_L$ in the first Brillouin zone.($k_1 \equiv k_2 \pmod{2k_L}$) As k_0 increases from $0.5k_L$, the difference in quasimomenta of the two scattered states, k_1 and $k_2 - 2k_L$, increases ((b) in Fig. 5-2)

For the experimental demonstration, a BEC was loaded into a variable quasimomentum state k_0 by utilizing a moving optical lattice. Experimental description on moving optical lattice is given in the section 6.3.1 and in the appendix E. When BEC was loaded into quasimomentum state $k_0 > 0.5k_L$, a scattering of BEC atoms into two discrete momentum states was observed. Fig. 5-3 shows that the two scattered

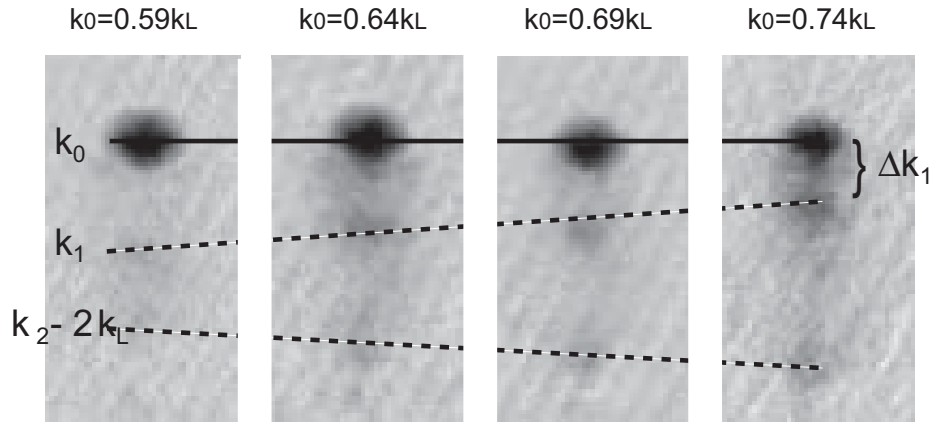

Figure 5-3: Atom pairs scattered from a BEC. A BEC in a quasimomentum state k_0 and two scattered states k_1 and $k_2 - 2k_L$ are imaged after 43 ms of ballistic expansion. As k_0 increases, the momentum of the scattered states changes according to the phase matching condition. Our observation agrees with the phase matching condition predicted in Fig.5-2 (b).

states are confined in the first Brillouin zone with momentum of k_1 and $k_2 - 2k_L$. It was also found that the momentum difference between two scattered states increases with the initial momentum k_0.

When atoms with quasimomentum k_1 were seeded to the condensate of k_0 by using Bragg pulse, the scattering process was observed to be accelerated in generating the two phase matched scattered atoms of k_1, and k_2 (4-wave amplification in 1D: $2k_0 \rightarrow k_1 + k_2$).

Chapter 6

Phase Diagram for a BEC Moving in an Optical Lattice

The stability of superfluid currents in a system of ultracold bosons was studied using a moving optical lattice. The phase diagram for disappearance of superfluidity as a function of momentum was measured in the superfluid phase to the Mott insulating phase. This experimental study was reported in Ref. [88], which is included in Appendix C.

6.1 Introduction

The realization of condensed matter systems using ultracold atoms brings the precision and control of atomic physics to the study of many-body physics. Many studies have focussed on Mott insulator physics, an important paradigm for the suppression of transport by particle correlations. Previous studies of the superfluid(SF)-to-Mott insulator(MI) transition in optical lattices with ultracold bosons [65, 90, 52, 116, 43, 49, 17, 44] adressed the quenching of superfluidity below a critical lattice depth. Here we extend these studies into a second dimension by studying stability of superfluid current as a function of momentum and lattice depth as suggested in Ref. [2]. These transport measurements show the stability of superfluid at finite current, which is a non-equilibrium state.

Transport measurements extend previous work on stationary systems in two regards. First, superfluidity near the MI transition has only been indirectly inferred from coherence measurements, whereas in this work, we characterize the superfluid regime by observing a critical current for superfluid flow through the onset of dissipation. Second, previous studies [65, 90, 52, 116, 43, 49, 17, 44] were not able to precisely locate the phase transition, since the observed excitation spectrum and atomic interference pattern did not abruptly change [52, 43, 49], partially due to the inhomogeneous density. In contrast, the sudden onset of dissipation provides a clear distinction between the two quantum phases. In the SF phase, current flows without dissipation if the momentum does not exceed a critical momentum, while in the MI phase the critical momentum vanishes and transport is dissipative.

6.2 Critical Momentum of Superfluid Current in an Optical Lattice

As discussed in the section 2.4, the stability of superfluid is closely related to the excitation spectrum $\omega(q)$ of system. A relative motion of superfluid opens a decay channel to excitation modes with $\omega_d(q) = q \cdot v$ (v: relative speed of superfluid), and those excitation modes of q' satisfying $\omega_d(q') = \omega(q')$ become populated resulting in fragmentation of the superfluid into such momentum states q'.

The elementary excitation spectrum $\omega(q)$ is modified in the presence of an optical lattice to have a phonon part (long wavelength) and a band structure part (near the 1st Brillouin zone boundary, Bogoliubov band)[72, 123, 84, 124]. In the long wave length limit ($q \to 0$), the excitation spectrum in optical lattice has a phonon branch, and the Landau instability would still occur in optical lattice system when the system moves faster than the sound speed.

Near the first Brillouin zone boundary, the excitation spectrum in an optical lattice deviates from the free space excitation spectrum. In free space, its excitation spectrum is a continuous function from 0 to ∞, while in the optical lattice it is changed

to band structure, a bound and periodic function of quasimomentum q. This gives rise to another type of instability mechanism in optical lattice: dynamical instability.

Two different types of instability are discussed in the following sections

6.2.1 Energetic & Dynamical Instability

A simple but intuitive picture on instabilities in superfluid can be obtained by considering small fluctuations added to the superfluid ground state[130]. A BEC loaded into a one-dimensional optical lattice can be described by the G-P equation (Eq.(2.13)) with a periodic potential $V_{\text{trap}}(x) = V_0 \cos(\frac{2\pi x}{a})$ (lattice spacing $a = \lambda/2$)

$$\mu\phi(x) = \left(\frac{\hbar^2}{2m}\frac{\partial^2}{\partial x^2} + V_0 \cos(\frac{2\pi x}{a}) + g\left|\phi(x)\right|^2 \right) \phi(x) \tag{6.1}$$

The superfluid moving with momentum q in the optical lattice is described by Bloch waves $\phi_q(x) = e^{iqx}\psi_q(x)$. Assume that fluctuations with momentum Q are added to the system. They are expressed also in the form of Bloch waves

$$\delta\phi_{q,Q} = e^{iqx}\left[u_q(x,Q)e^{iQx} + v_q^*(x,Q)e^{-iQx}\right] \tag{6.2}$$

All the wave vectors q, Q and the functions $\phi_q(x)$, $u_q(x,Q)$, $v_q(x,Q)$ have periodic boundary conditions[1]. There are two different wave vectors q and Q: BEC is assumed to flow with momentum $\hbar q$, and we perturb the BEC with wavevector Q to see its stability. The energy change $\delta E_{q,Q}$ associated with fluctuations $\delta\phi_{q,Q}$ can be obtained numerically. Detailed numerical results and mathematical discussions are given in [130, 85]. There are three cases for the value of $\delta E_{q,Q}$

1. $\delta E > 0$: In this situation, the fluctuations increase the energy of the system. If $\delta E_{q,Q}$ is positive for all Q, the system moving with q is stable against fluctuations.

2. $\delta E < 0$: The fluctuating state which has negative $\delta E_{q,Q}$ becomes energetically

[1]The quasimomentum $\hbar q$, $\hbar Q$ is in the first Brillouin zone ($\{-\frac{1}{2}\frac{2\pi}{a} \sim \frac{1}{2}\frac{2\pi}{a}\}$). The functions are periodic with lattice spacing a.

favored. These fluctuation mode can be populated through excitation processes, and the system becomes unstable.

For stationary BEC ($q = 0$), $\delta E_{0,Q}$ is positive for all Q implying that a stationary BEC in an optical lattice is stable. With increasing momentum q, $\delta E_{q,Q}$ approaches zero and finally starts to become negative for Q near 0 (long wavelength excitation) at a critical momentum q_{c1}. Above a critical value q_{c1}, the system can decay through phonon excitations ($Q \rightarrow 0$) resulting in instability.(Energetic (or Landau) instability)

3. δE is imaginary: When q is increased above a certain value $q_{c2} = \frac{1}{4}\frac{2\pi}{a}$ (or quarter of the first Brillouin zone size), $\delta E_{q,Q}$ starts becoming imaginary for Q near the first Brillouin zone boundary ($Q = \pm\frac{1}{2}\frac{2\pi}{a}$). Imaginary energy δE implies that small fluctuations grow exponentially leading to a decay of system.(Dynamical instability)

   The two types of instabilites are distinguished by the quasimomentum Q of the fluctuation modes that induce instability, $Q = \pm\frac{1}{2}\frac{2\pi}{a}$ for the dynamical instability, while $Q = 0$ for the energetic instability. For more discussions on dynamic and energetic instability see Refs. [106, 131, 62]

6.2.2 Decay Process and Elementary Excitation

Decay processes through energetic and dynamical instabilities can be understood in the context of the spectrum of elementary excitation. The excitation spectrum of a BEC moving in an optical lattice is given in Fig. 6-1 for various momentum q of BEC.

The excitation spectrum in Fig.6-1 implies that decay process could occur by exciting two different excitation modes: $Q \sim 0$ and $Q = \pm k_L$.

- $Q \sim 0$ (Energetic Instability): When the BEC moves faster than the sound speed ((b) in Fig. 6-1), the excitation energy near $Q \sim 0$ becomes lower than the unperturbed initial state. The system can lower its energy by exciting phonon modes, and the superfluid becomes unstable.

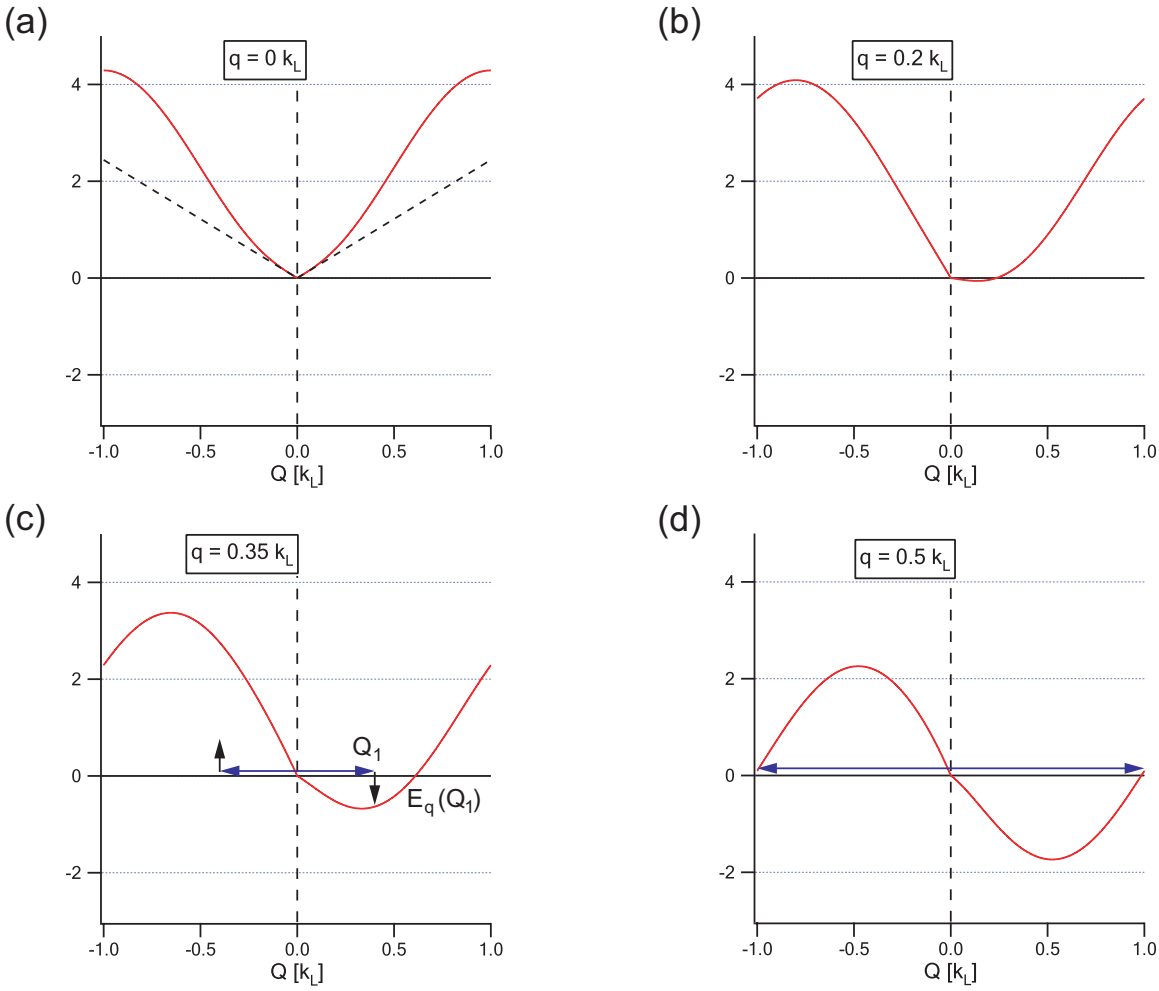

Figure 6-1: Excitation spectrum of a BEC moving in optical lattice with momenta q. In each plot, the energy and momentum are given in the frame of the moving BEC.(not a lab frame) (a) linear phonon mode appears in the spectrum. (b) If the BEC moves faster than the speed of sound, the energy of excitations becomes lower than the energy of the initial unperturbed state. (c) The phase matching condition (momentum-energy conservation) for excitations. (d) Two excitation modes with $Q = \pm k_L$ satisfy the phase matching condition at $q = 0.5k_L$. Those excitation modes are populated leading to fragmentation and instability of the system [Dynamical instability].

Let us consider how BEC emits phonons and decays. In creating (or annihilating) quasi-particles, a phase matching condition (i.e. momentum-energy conservation) must be considered. For example, in (c) of Fig. 6-1 a quasi-particle with momentum Q_1 is emitted to a lower energy $E_q(Q_1)$. The phase matching condition implies that another quasi-particle with momentum should be emitted. As (c) of Fig. 6-1 shows the phase matching condition is not satisfied in the excitation spectrum. Therefore this process is not possible unless additional potential energy or particles are added. For example, in (c) of Fig. 6-1 thermal atoms can take away excess energy $E_q(0) - E_q(Q_1)$ satisfying the phase matching condition. Energetic instabilities induced by thermal atoms have been studied experimentally [106].

- $Q \sim k_L$ (Dynamic Instability): At $q = 0.5k_L$, excitation energy of $Q = \pm k_L$ becomes equal to the energy of the initial state as shown in (d) of Fig. 6-1. In creating a pair of excited particles with $Q = +k_L$, $-k_L$, both momentum and energy are conserved[33, 19].

$$E_q(0) + E_q(0) = E_q(k_L) + E_q(-k_L) \tag{6.3}$$

Above $q_{c2} = 0.5k_L$, the set of excitations that satisfy the phase matching condition expands around $Q = \pm k_L$. The system becomes dynamically unstable for $q > q_{c2} = 0.5k_L$. Fig 6-2 shows that momentum states with $Q = \pm k_L$ are populated at the onset of dynamical instability ($q_{c2} = 0.5k_L$).

6.2.3 Superfluidity in the Regime of Strong Interaction

So far, we have considered superfluid flow in the regime of weak interaction (or in shallow optical lattices). For weak interactions ($U/J \to 0$), the system approaches single-particle physics in a periodic potential well described by Bloch states and band structure. The critical momentum for a stable current-carrying state is 0.5 $\hbar k_L$ [130].

However, these analyses neglect the growing importance of quantum correlations

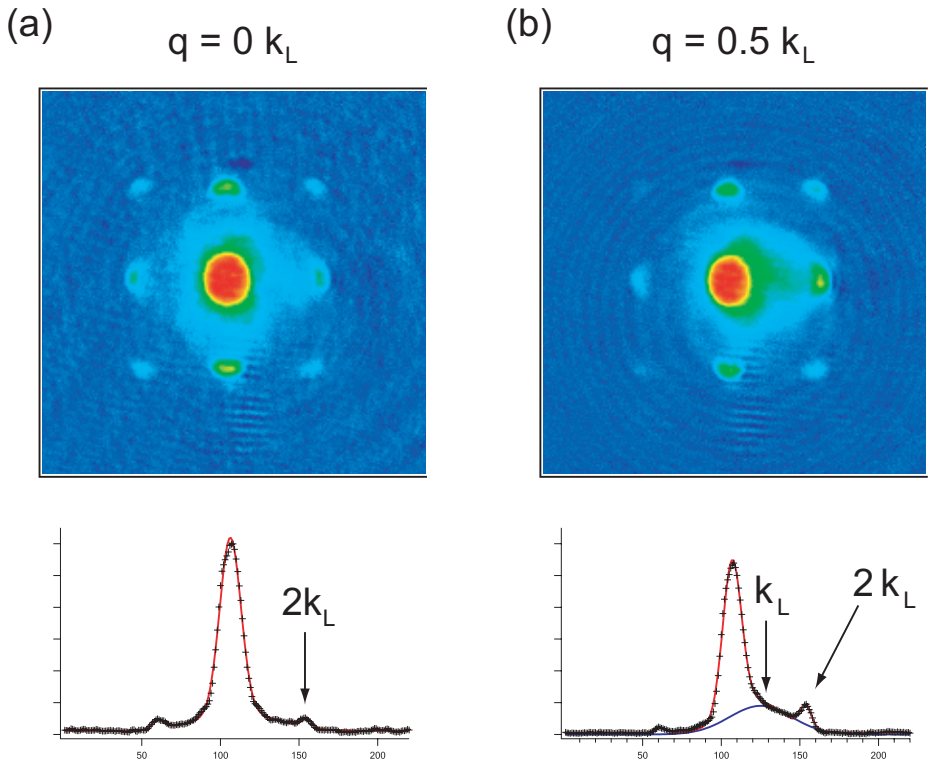

Figure 6-2: The onset of a dynamical instability. Time-of-flight images of interference pattern of BEC released from an optical lattice and the integrated images are shown for a BEC with momentum q = (a) $0\,k_L$ and (b) $0.5\,k_L$. The optical lattice depth was set to $3\,E_R$. (b) shows the population of excited states with $Q = \pm k_L$ at the onset of the dynamical instability. Since the quasi-momentum of two excitation states $Q = \pm k_L$ differ by a reciprocal vector $2k_L$, they are indeed the same state within the first Brillouin zone, and only one momentum component is visible in the image (b).

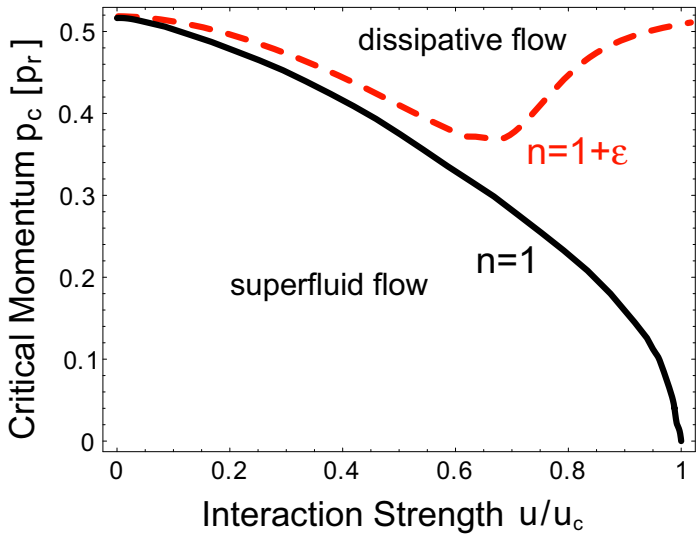

Figure 6-3: Phase diagram for stability of superfluid flow for commensurate and incommensurate filling. Commensurate system turns into the MI phase for $u > u_c$, and the critical momentum vanishes, while incommensurate system is not in the MI phase even for $u > u_c$, and the critical momentum does not vanish. p_r denotes a recoil momentum $\hbar k_L$.

for larger lattice depth which leads to the SF-MI phase transition, where the critical momentum for a superfluid current vanishes ($q_c = 0$). The critical momentum decreases from $0.5k_L$ with increasing interaction parameter U/J, and it vanishes at the MI transition $(U/J)_c$. The critical momentum in between SF and MI phases has been numerically studied using the mean field approach showing that critical momentum decreases smoothly from $0.5\hbar k_L$(weak interaction) to 0 (MI transition) with increasing U/J. The critical momentum is plotted as a function of $u \equiv U/J$ in Fig. 6-3. More detailed discussions of numerical methods are given in ref. [2, 98].

For $u > u_c$, a homogenous system with incommensurate filling $n = 1 + \epsilon$ is not in the MI phase, but stays in the superfluid phase. The $n = 1 + \epsilon$ system may be considered as a dilute superfluid (or holes if ϵ is negative) on top of the MI background atoms, and the critical momentum remains equal to $0.5k_L$ for $u > u_c$. The critical momentum for $n = 1 + \epsilon$ is displayed in Fig. 6-3. The critical momentum decreases from $0.5\hbar k_L$ initially, but increases back to $0.5\hbar k_L$.

6.2.4 Effect of the Inhomogeneous Density Profile

Our measurement of critical momentum of the $n = 1$ system was not limited by the inhomogeneous density profile. For our range of lattice depths, low critical momenta and the onset of dissipation occur only near the formation of MI shells with integer occupation numbers n[2]. The onset of dissipation related to the $n = 1$ domains occurs at smaller momentum than for any other n (Fig.6-3). For instance, with increasing momentum p the $n = 1$ domain becomes unstable first, and this triggers dissipation over the whole atomic cloud[2]. Therefore, the breakdown of superfluid flow in the system was determined by the formation of the $n = 1$ domain and was not smeared out by the inhomogeneous density.

6.3 Experimental Setup

This experiment was performed in the main chamber. For detailed description of the main chamber of the Rb BEC machine, I refer to other theses: Ref. [117, 13] (general machine description), Ref. [15] (optical lattice setup).

A BEC of ^{87} Rb atoms in $|1, -1\rangle$ state was prepared and trapped in a combination of an Ioffe-Pritchard magnetic trap and an optical dipole trap. The number of atoms in the BEC was 2×10^5. The magnetic trap frequencies were $\omega_{x,y} = 2\pi \times 40\,\mathrm{Hz}$ radially and $\omega_z = 2\pi \times 4.6\mathrm{Hz}$ axially. The laser beam for the optical dipole trap was oriented along the x axis. This laser beam was retro-reflected and the polarization of the retro-reflected beam was rotated in order to minimize interference between the two beams[2]. Along the vertical direction (y axis) a lattice was formed by a retro-reflected laser beam. For the z axis, a moving lattice was created by introducing a small frequency detuning δf between the two counter-propagating laser beams using AOMs driven by phase-locked frequency generators. The 3D optical lattice was ramped up exponentially in 160 ms. A x-axis optical lattice is ramped by rotating the polarizations of the retro-reflected beam to increase interference between two counter-propagating beams, while other axes optical lattices were turned on by turning on

[2]The polarization of retro-reflected beam was controlled by liquid crystal variable retarder.

the power. All lattice beams had an $1/e^2$ waist of $100 - 200\mu$m.

6.3.1 Moving Lattice

For transport measurements, we moved an optical lattice [9, 39] which provides more flexibility to change the momentum than exciting a dipole oscillation by displacement of the BEC [21, 40]. A moving optical lattice with velocity $v = \lambda \cdot \delta f/2$ was created along the long axis of the BEC by introducing a small frequency detuning δf between two counterpropagating lattice beams. If the velocity $v(t)$ changes slowly enough not to induce interband excitations, the initial Bloch state $|p = 0\rangle$ of the condensate in the optical lattice adiabatically evolves into the currentcarrying state $|p(t) = -mv(t)\rangle$ where p is the quasimomentum. For increasing lattice depth, the effective mass of atoms $m^* = [\partial^2 E(p)/\partial p^2]$ increases, and the group velocity $v_g = -(m/m^*)v(t)$ decreases. As a consequence, atoms prepared in a moving lattice with quasimomentum $p = -mv$ travel in the frame of the moving lattice with v_g and in the lab frame with velocity $\Delta v = v + v_g = (1 - m/m^*)v$, which approaches v in a deep lattice. Consequently, we observed that in a deep moving lattice atoms were dragged along to the edge of the trapping region limiting the experimental time scale to probe for dissipation. This became an issue for larger values of p and was addressed by first ramping up the lattice with $p = 0$ and then alternating the velocity of the moving lattice, thus performing a low-frequency AC transport measurement instead of DC.

6.3.2 Adiabaticity of Moving Lattice

In order to adiabatically load a BEC in a current carrying state $|p = -mv(t)\rangle$, the optical lattice should be varied slowly enough not to create excitations such as higher band states. The adiabaticity criterion is given

$$\hbar|\langle n, q|\frac{d}{dt}|0, q\rangle| \ll |E_n(q) - E_0(q)| \quad \text{for} \quad n > 0 \tag{6.4}$$

where $|n, q\rangle$ is a state with momentum q in nth band, and $E_n(q)$ is energy of $|n, q\rangle$.

For the momentum change $q(t)$, the adiabatic condition Eq.(6.4) imposes

$$\left|\frac{\lambda}{2}\frac{d}{dt}[\hbar q(t)]\right| \ll \text{band gap} \tag{6.5}$$

The left term in the above condition reads

$$\frac{\lambda}{2}\frac{d}{dt}\left[m\frac{\lambda}{2}\delta f(t)\right] = \frac{(2\pi\hbar)^2}{8E_R}\frac{d}{dt}\delta f(t)$$

Sinusoidal frequency modulation is applied to one of moving lattice beams with $\delta f(t) = f_M \sin(\omega_1 t)$. The adiabatic condition is then given

$$f_M\omega_1 \ll \frac{(\text{band gap})E_R}{(2\pi\hbar)^2} \tag{6.6}$$

The maximum frequency modulation parameters in our experiment ($f_M \sim 5\,\text{kHz}$[3] $\omega_1 = 2\pi \times 10\,\text{Hz}$) satisfies this condition very well (bandgap energy is $\sim$ a few kHz, and recoil energy is 2 kHz).

6.4 Measurement of the Critical Momentum

6.4.1 Experimental procedure

Two sets of experimental procedures were used for measurement of the critical momentum, and our results were consistent for both.(Fig.6-4)

Close to the SF-MI phase transition, the lattice was increased to V_{latt} with a fixed (and small) value of momentum p (dashed arrows in Fig. 6-4). After a variable hold time t_{hold} at V_{latt} the lattice was ramped down to zero, and the magnetic trap switched off. After 33 ms of ballistic expansion, the atoms were imaged and the condensate fraction was determined as a function of momentum by using a bimodal fitting function.

For smaller lattice depths, the lattice was ramped up with $p = 0$ (Fig. 6-

[3] $\delta f = 4\,\text{kHz}$ corresponds to half the recoil velocity $v = (\lambda/2)\cdot\delta f = 0.5\,\hbar k_L/m$.

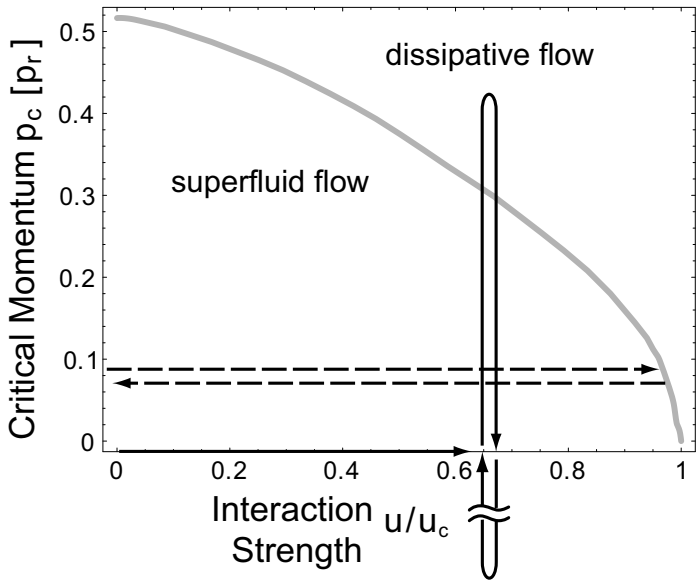

Figure 6-4: Phase diagram showing the stability of superfluid flow in an optical lattice and the experimental procedure. The gray curve shows the predicted boundary between superfluid flow and dissipative flow phases for a three-dimensional gas with a commensurate filling of $n = 1$ atom per site[2]. The solid (dashed) arrows illustrate the experimental trajectory used for small (large) lattice depths (see text for details).

4). Then a sinusoidal momentum modulation of the moving lattice with amplitude $p_M = (m\lambda/2)\, f_M$ was applied by modulating the frequency detuning $\delta f = f_M \sin(\omega_1 t)$ between the counterpropagating lattice beams. The 10 ms period of this momentum modulation ($\omega_1 = 2\pi \times 100\,\mathrm{Hz}$) was slow enough to meet the adiabaticity condition, but fast enough to limit the displacement of the atomic cloud to less than a few μm. Both the trapping potential and the optical lattice were then turned off suddenly. Images were acquired after 33 ms of ballistic expansion. The time-of-filght images in Fig. 6-5 show that superfluid becomes unstable above a certain momentum.

6.4.2 Determination of Critical Momentum

The condensate fraction of the center peak of the superfluid interference pattern was recorded as a function of the momentum modulation amplitude p_M. Several cycles of the momentum modulation were applied to obtain a high contrast between the stable and dissipative regimes. Fig. 6-6 (a) shows how the transition between superfluid and dissipative flows becomes sharper with increasing number of cycles of

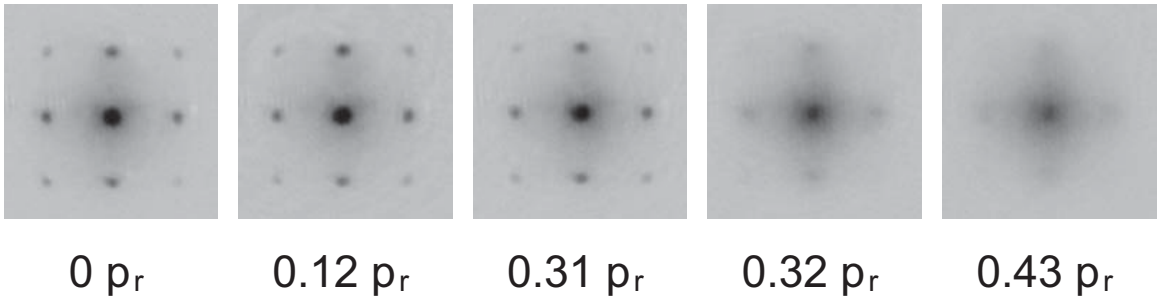

Figure 6-5: Images of interference patterns released from an optical lattice at $u/u_c = 0.61$ moving with variable momentum. Instability occurred between $p = 0.31p_r$ and $0.32p_r$.

the momentum modulation. The critical momentum was determined from a log-log plot of the condensate fraction as a function of momentum p [Fig. 6-6(b)]. The intersection between two linear fit functions was taken as the critical momentum. Our result was found to be consistent for different frequency ω_1 and number of cycles of the momentum modulation.

6.5 The Critical Point for the Quantum Phase Transition

The quantum phase transition from the superfluid to the Mott insulator has the following signatures.

1. Appearance of energy gap ΔE in the excitation spectrum

2. Loss of long-range phase coherence

3. Loss of superfluid current

Most studies of the SF-MI phase transition monitor the coherence in the superfluid phase through an interference pattern observed in the ballistic expansion resulting from a sudden turn-off of the confining potential and lattice. Previous observations of the phase transition found the experimental transition point to lie in the range between 10 and 13 E_R[52]. This uncertainty is related to the inhomogeneous density

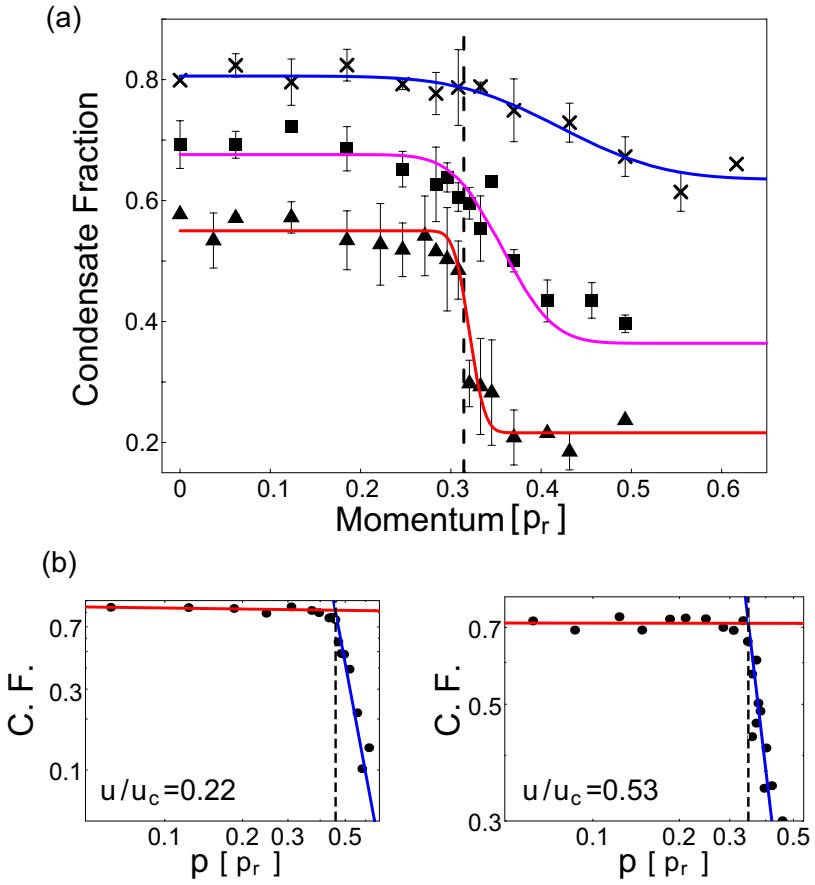

Figure 6-6: Determination of the critical momentum of superfluid flow. Shown is the condensate fraction as a function of a momentum p. (a) Condensate fraction with $u/u_c = 0.61$ for a variable number of cycles of the momentum modulation (one cycle: $\times$ and blue line, two cycles: ■ and purple line, three cycles: ▲ and red line). A dashed vertical line indicates the critical momentum where instability begins to occur. The two and three-cycle data are offset vertically for clarity. These data were fitted with an error function to guide the eye. (b)Condensate fraction on a log-log scale for two different interaction strengths.

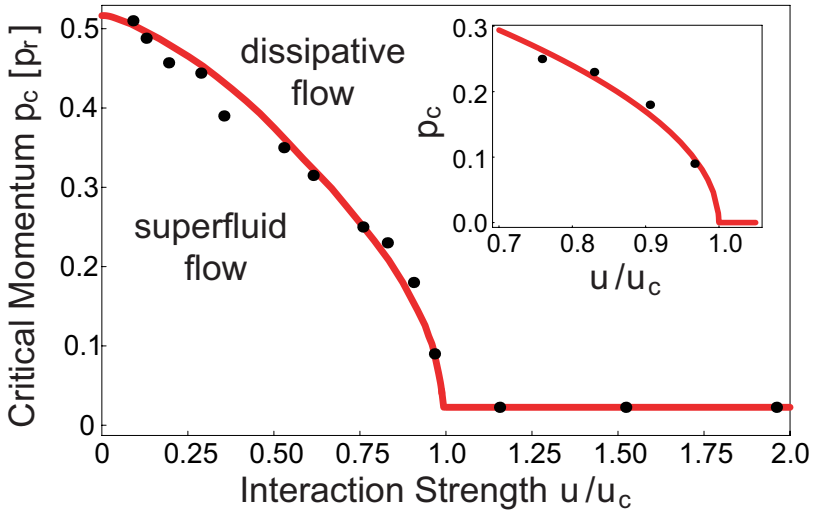

Figure 6-7: Critical momentum for a condensate in a 3D lattice. The solid line shows the theoretical prediction for the superfluid region. The horizontal solid line is a fit to the data points in the MI phase. (Inset) Fit of critical momenta near the SF-MI phase transition.

profile of trapped atoms and to the fact that the visibility of the interference extends beyond the transition point due to short-range coherence in the MI phase[49]. It has been suggested that observed kinks(Fig. 2 of Ref. [49]) in the visibility are linked to the formation of the MI shells with occupation numbers $n = 2$ and 3[49]. Several authors have suggested other features in the momentum distribution beyond coherent interference peaks as a more distinct signature of the phase transition[129, 68]. Here we show that the disappearance of the critical momentum for superfluid flow provides such a signature and allows the determination of the transition point with high precision.

Fig. 6-7 shows the critical momentum measured with various interaction strength u. The critical point u_c for the SF-MI phase transition can be deteremined as the point where the critical momentum vanishes. Near the SF-MI phase transition, the critical momentum approaches zero with the predicted functional form, $p_c \propto \sqrt{1 - u/u_c}$[2]. Fitting the data points close to the SF-MI phase transition with this function, we could determine the critical point for the SF-MI phase transition $u_c = 34.2(\pm 2.0)$ corresponding to $13.5(\pm 0.2)\, E_R$.

Our result agrees with the mean-field theory prediction $u_c = 34.8$ for $n = 1$ SF-MI phase transition[65], and deviates by 2 σ from the predictions of $u_c = 29.34(2)$ of quantum monte carlo calculation[46, 20], which includes corrections beyond mean-field theory. This demonstrates that our method has the precision to identify non-mean-field corrections. However, to turn precision into accuracy, experiments or QMC simulations [129, 46, 20] have to address corrections due to finite size, finite temperature, and finite time to probe the onset of the instability. In our experiment, these corrections seemed to be small, but have not been characterized at the level of 1% in lattice depth.

6.6 Decay of the Superfluid Current in a 1D System

For studing the 1D system, we prepared an array of one-dimensional gas tubes by ramping two pairs of optical lattice beams up to lattice depths of $V_x = V_y = 30E_R$ supressing hopping between the tubes. After a hold time of 10 ms, a moving optical lattice(z-axis) was ramped up to various lattice depths. As in the 3D experiment, a momentum modulation was applied, after which the moving optical lattice was ramped down to zero, followed by the other two optical lattices. The condensate fraction was determined after 33 ms of ballistic esxpansion as a function of the momentum modulation amplitude. The critical momentum, where the onset of dissipation begins, was identified from a log-log plot as in the 3D case. In contrast to sharp transition in 3D experiment, the transition from stable to unstable flow was observed to be broad in the 1D gas. To characterize the width of the transition between stable and dissipative flow regimes, the data was fitted with error function, and the center of the fitted error function was taken as the center of the transition. (Fig. 6-8 (b))

At a very shallow lattice depth of $0.25\,E_R$, a sharp transition was observed, and the measured critical momentum agreed very well with the prediction[2, 98], $p_c = 0.39p_r$. However, slight increase of the lattice depth to $0.5\,E_R$ led to a significant decrease of

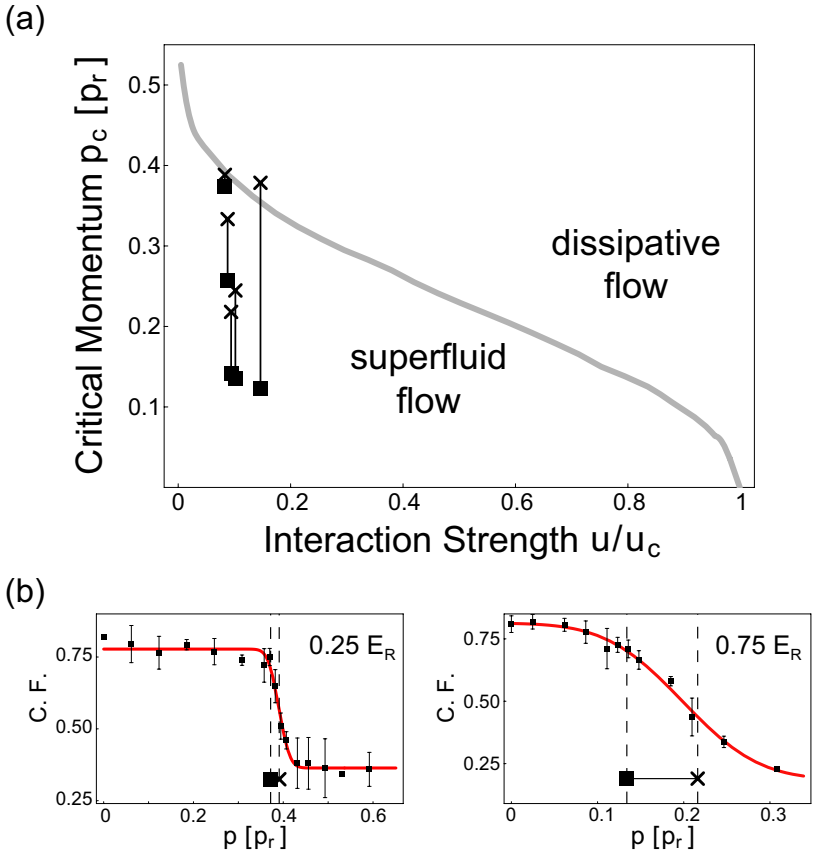

Figure 6-8: Critical momentum for a 1D gas in an optical lattice. (a) The gray line indicates the mean-field theory prediction. The interaction strengths are normalized by the mean-field prediction for $u_c = 5.8 \times 2$[65, 116]. Squares (crosses) represent the measured critical momentum (the center of the transition). Measurements were taken at lattice depths of 0.25, 0.50, 0.75, 1.0, 2.0 E_R. The lines between crosses and squares indicate the width of the transition region. (b) Condensate fraction measured at 0.25 E_R and 0.75 E_R. The data were fitted with an error function. Squares (the critical momentum) and crosses (the center of the transition) are indicated on the plots.

the critical momentum as well as a dramatic broadening of the transition as shown in Fig. 6-8. For lattice depths lager than $2\,E_R$, the transition became very broad and showed complex behavior, and a quantitative anlysis of data could not be obtained.

Our measured critical momentum shows a significant deviation from the mean-field theory calculation[40, 98, 102]. This result is in agreement with the other transport experiment performed with 1D gas at NIST[40]. In the NIST work damped dipole oscillations of a 1D Bose gas was observed, while diople oscillations of a 3D gas showed no damping. They found that the damping coefficient grew rapidly with increasing lattice depth even at very shallow lattice depth. This experimental result is theoretically investigated showing that quantum fluctuation dominates in 1D gas transport leading to significant deviation from the mean-field theory. Our observed broadening of the transition confirms theoretical studies which emphasize the importance of quantum fluctuations in the 1D system. Quantum tunneling out of metastable states which are ignored in the mean-field description can lead to a decay of the superfluid current at very low momentum[98].

6.7 Conclusion

We have used transport studies to connect a well-known dynamical instability for weakly interacting bosons with the equilibrium superfluid to Mott insulator transition. A comparison of 3D and 1D systems confirms the applicability of a mean-field description in three dimensions and the crucial importance of fluctuations in one dimension. The disappearance of superfluid currents at the SF-MI phase transition precisely located the phase transition. Our results illustrate the control and precision of condensed matter physics experiments done with ultracold atoms and their suitability to test many-body theories.

Chapter 7

Spectroscopy and Imaging of the Mott Insulator Shell Structure

This chapter describes experiments on the Mott insulator phase performed in two different apparatuses: the main chamber, and the science chamber. The experiment performed in the main chamber, previously reported in Ref. [18], are briefly introduced. See the reprint included in Appendix D for detailed discussions.

7.1 Introduction

The Mott insulator(MI) is distinguished from a conventional insulator in that carrier particles can not flow in a conventional insulator due to a fully filled energy band, while in the Mott insulator it is the particle-particle interaction that prevents carriers from flowing even in a partially filled conduction band. In the SF-MI transition, this particle-particle interaction drastically modifies atom number statistics from a coherent state (Poisson distribution) to a Fock state.

The number statistics was diagnosed using the clock shift (the mean field shift) with observation that the clock shift spectrum changed from a gaussian shaped peak in a shallow optical lattice to multiple discrete peaks in a deep optical lattice[18](Fig.7-2). This implies that the density distribution in the superfluid phase is continuous, while it turns into discrete occupation numbers in the Mott insulator.

In addition, the clock shift diagnostic tool offers the method to selectively address individual $n = 1, 2, 3, \cdots$ "shells" of the Mott insulator phase by utilizing the frequency of discrete peaks in the clock shift spectrum. With the clock shift scheme, individual Mott insulator shells could be imaged with this scheme.

In this chapter, using clock shift spectroscopy we discuss high-resolution imaging of the Mott insulator shells. In addition, the temperature-dependence of the number statistics of the Mott insulator is presented. This could potentially serve as thermometer for ultracold atomic system.

7.2 Clock Shift Spectroscopy

7.2.1 Clock Shift

When atoms in one hyperfine state are transferred to other hyperfine state, the resonance frequency is shifted by change in interaction energy between atoms in the initial state and final state. Such frequency shift occurs in many applications of a atomic clock, where the hyperfine transition is used as a frequency standard. This frequency shift is called "clock shift", and it normally limits the accuracy of atomic clocks.

In BEC, the interaction energy is given by s-wave interaction, the change in the interaction energy corresponds to $(4\pi\hbar^2 a/m)n$ [60]. For the transition between two hyperfine states ($|1\rangle$, $|2\rangle$), each state experiences a frequency shift

$$\Delta\mu_1/\hbar = \frac{4\pi\hbar}{m}(a_{11}n_1 + a_{12}n_2) \tag{7.1}$$

$$\Delta\mu_2/\hbar = \frac{4\pi\hbar}{m}(a_{22}n_2 + a_{12}n_1) \tag{7.2}$$

where a_{11}, a_{12}, a_{22} are the s-wave scattering length of $|1\rangle - |1\rangle$, $|1\rangle - |2\rangle$, $|2\rangle - |2\rangle$, respectively, and n_1, n_2 are the densities of atoms in states $|1\rangle$ and $|2\rangle$.

The total change in the transition frequency between $|1\rangle$and$|2\rangle$ is

$$\Delta\nu = \Delta(\mu_2 - \mu_1)/\hbar = \frac{4\pi\hbar}{m}\left[(a_{22} - a_{12})\, n_2 - (a_{11} - a_{12})\, n_1\right] \tag{7.3}$$

If we start with all of atoms in state $|1\rangle$, the frequency shift reduces to

$$\Delta\nu = -\frac{4\pi\hbar}{m}(a_{11} - a_{12})n_1 \tag{7.4}$$

The frequency shift $\Delta\nu$ is linearly proportional to the density of atoms n_1 with scattering length difference $a_{11}-a_{12}$. Therefore, the measurement of clock shift $\Delta\nu$ reveals the density profile n_1.

7.2.2 Clock Shift in Optical Lattice

The interaction energy in the Bose-Hubbard model for two bosonic species (two different hyperfine states $|1\rangle$, $|2\rangle$) is [3]

$$\begin{aligned} U(\{n_{1,i}\},\{n_{2,i}\}) &= \frac{1}{2}U_{11}\sum_i n_{1,i}(n_{1,i}-1) + \frac{1}{2}U_{22}\sum_i n_{2,i}(n_{2,i}-1) && (7.5)\\ &\quad + U_{12}\sum_i (n_{1,i}-1/2)(n_{2,i}-1/2) && (7.6)\end{aligned}$$

where $U_{\alpha\beta}(\alpha,\ \beta = 1 \text{ or } 2)$ is the U matrix element between states α and β, $n_{1,i}$, $n_{2,i}$ are the number operators at lattice site i.

Consider the situation where the system is prepared with N atoms in $|1\rangle$, and a weak probe hyperfine transition pulse is applied. the frequency shift is then given as the change in the interaction energy

$$\hbar\Delta\nu = U(N-1,1) - U(N,0) = -(U_{11} - U_{12})(N-1) \tag{7.7}$$

For instance, in the lattice system with a single atom per site ($N = 1$) no interaction energy exists resulting in a zero frequency shift $\Delta\nu = 0$. The difference of matrix

element U in Eq.(7.7)is given by

$$U_{11} - U_{12} = \frac{4\pi\hbar^2(a_{11} - a_{12})}{m} \int d\mathbf{r}|w(\mathbf{r})|^4 \tag{7.8}$$

$$= \frac{a_{11} - a_{12}}{a_{11}} U_{11} \tag{7.9}$$

For ^{87}Rb atom s-wave scattering lengths are given by $a_{11} = 100.44\, a_0$, $a_{12} = 98.09\, a_0$, $a_{22} = 95.47\, a_0$.

7.2.3 Two–Photon Transition

In ^{87}Rb atom there are two hyperfine manifolds in the ground state, $F = 1$ and $F = 2$ separated by $\sim 6.8\,\text{GHz}$. $|F = 1, m_F = -1\rangle$ and $|F = 2, m_F = 1\rangle$ states were chosen as initial ($|1\rangle$) and final ($|2\rangle$) state for our clock shift spectroscopy[18, 119]. The bias magnetic field in the experiment was set to $B_0 \sim 3.23$ G where two hyperfine states experience the same first Zeeman shift and the transition frequency becomes robust against B-field fluctuations[60].

To drive the transition between $|1, -1\rangle$ and $|2, 1\rangle$, two-photon (microwave + rf) transition was used. The frequency of microwave was set to fixed value of $\sim 6,833$ MHz giving a detuning $\Delta = 0.5\,\text{MHz}$ from $|2, 0\rangle$ intermediate state. The frequency of the rf photon ($\sim 1.6 - 1.7\,\text{MHz}$) was varied to probe the frequency shift.

7.2.4 Experimental Procedure

Optical lattice is exponentially ramped up as illustrated in Fig. 7-1. A 100 ms two-photon pulse was then applied to atoms while held in the lattice. Immediately after the two-photon pulse, only the atoms transferred to the state $|2\rangle = |2, 1\rangle$ were selectively imaged using imaging light resonant with the $F = 2 \rightarrow F' = 3$ cycling transition. The atoms that were not transferred and remained in initial state $|1\rangle = |1, -1\rangle$ are transparent to the imaging light. During the imaging, both ODT trap and the optical lattice was kept on for in-situ absorption imaging.

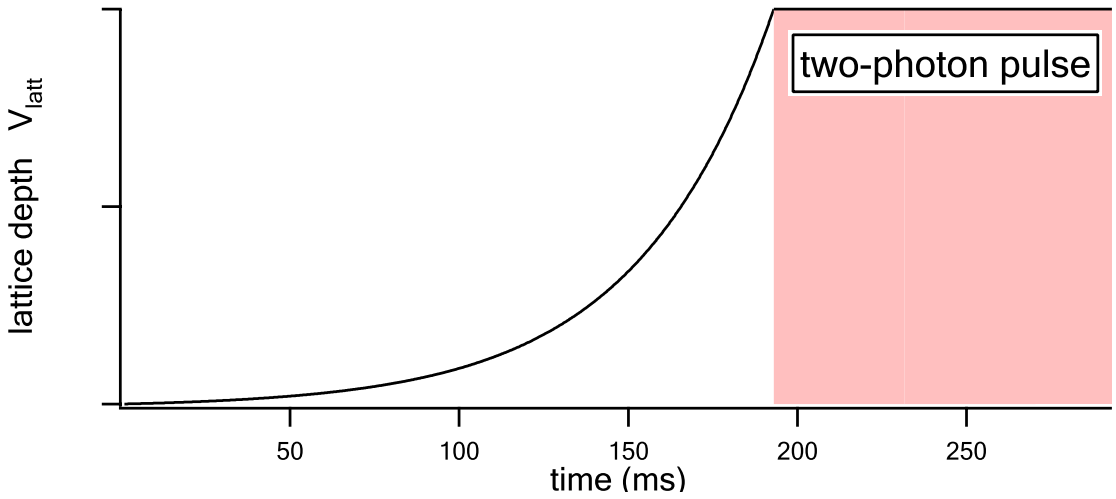

Figure 7-1: Experimental procedure for clock shift spectroscopy. The 3D optical lattice is exponentially ramped up to $V_{latt} = 35\,E_R$ in 193 ms. The exponential ramp curve is $V_{latt}(t) = A\{\exp(t/\tau) - 1\}$ with $A = 15\,E_R/(\exp(4) - 1)$ and $\tau = 40$ ms. A two-photon pulse (microwave + rf) is then applied for 100 ms for clock shift spectroscopy.

7.3 Clock shift spectroscopy of the SF–MI phase transition

For the density profile probe, the clock shift spectroscopy was performed on a BEC across the superfluid-Mott insulator transition with variable lattice depth from $0E_R$ (no lattice, superfluid phase) to $35E_R$ (MI phase). Fig.7-2 shows our observed clock shift spectrum.

For a trapped BEC without optical lattice, a harmonic trapping give the density distribution $f(n) = (15n/n_0)\sqrt{1 - n/n_0}$ (with normalization condition $\int dn f(n) = 1$) varying smoothly from n_0(at trap center) to 0(trap edge). The density distribution $f(n)$ leads to the line shape of clock shift spectrum $I(\Delta\nu)$ with the Eq. (7.4)

$$I(\Delta\nu) = \frac{15\Delta\nu}{\Delta\nu_0}\sqrt{1 - \frac{\Delta\nu}{\Delta\nu_0}} \tag{7.10}$$

with $\Delta\nu_0 = (-4\pi\hbar/m)(a_{11} - a_{12})n_0$. The spectrum of the trapped BEC in Fig.7-2 shows a single continuous peak. As the lattice depth increases, broadening of the line shape was observed (i.e. the spectrum for lattice depth $5E_R$ in Fig.7-2), which is in

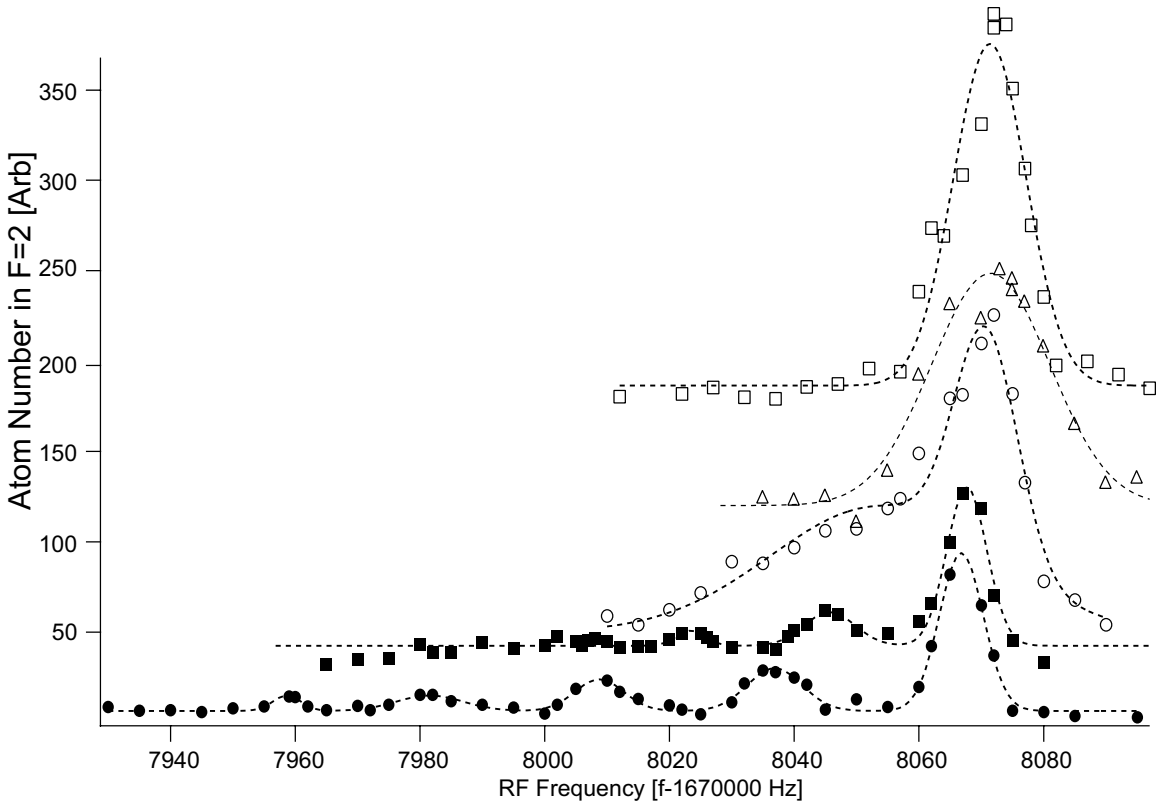

Figure 7-2: Clock shift spectroscopy across the SF-MI transition. Spectrum was measured for lattice depths of 0 E_R (□), 5 E_R (△), 10 E_R (○), 25 E_R (■), 35 E_R (●). The spectra are vertically offset for visual clarity.

agreement with the predicted line width $\sqrt{\langle \Delta\nu \rangle^2} \sim U(\text{interaction})$ of Eq. 7.10.

The clock shift spectrum in Fig. 7-2 changed from a gaussian shaped peak in a shallow optical lattice to multiple discrete peaks in a deep optical lattice(i.e. 25, $35E_R$)(Fig.7-2). This implies that the density distribution in the superfluid phase is continuous, while it turns into discrete occupation numbers in the Mott insulator.

For deep lattices, the separation of the peaks in the spectrum is determined by the difference $\Delta U = U_{11}(a_{11} - a_{12})/a_{11}$ of the onsite interaction energy U. The onsite interaction U_{11} could be obtained from the peak separation (Fig. 7-3). The width of the discrete peaks was measured to be 10 Hz, which is mainly limited by the two-photon pulse time = 100 ms. It was observed in our previous experiment that the width of the discrete peaks could be narrowed down to 1 Hz level by increasing the two-photon interrogation time up to 1 s[13].

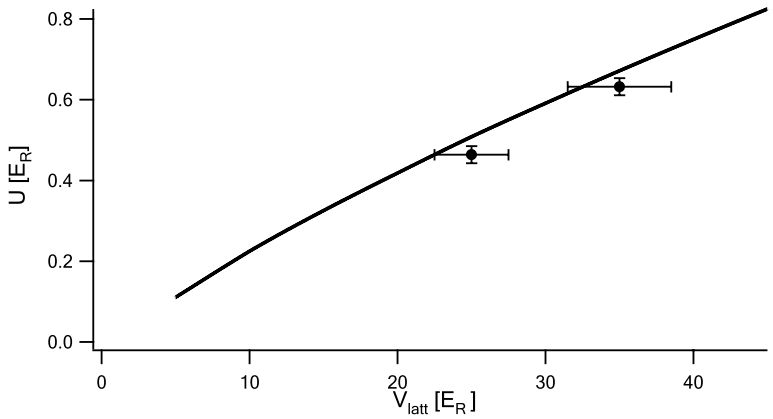

Figure 7-3: Probe of the onsite interaction U. A curve shows the onsite interaction calculated using Wannier functions.(see Fig. 3-3)

7.4 Imaging the Mott Insulator Density Profile

In our first clock shift experiment [18] performed in the main chamber, the details of the density profile in the MI phase could not be obtained due to the low imaging resolution of $\sim 10\mu$m which was mainly limited by lack of optical access. Our newly designed high NA lens improved imaging resolution to $\sim 2\mu$m. In the rest of this chapter, I present the experiments performed in the science chamber utilizing high resolution imaging power.

Each Mott insulator shell could be selectively addressed by using discrete peak frequencies in the clock shift spectrum (Fig.7-2). For instance, atoms in the $n = 1$ MI domain can be transferred to $|2, 1\rangle$ without transferring any other n MI domains using the resonance frequency of the $n = 1$ peak.

Fig. 7-4 shows the image of the $n = 1$ Mott insulator domain. The density profile of a thin slice along a dashed line in Fig. 7-4 (b) shows that the density of the $n = 1$ MI shell drops near the center of cloud where the $n = 2$ MI shell structure resides. The image integrated along x-axis in Fig. 7-4 (c) shows the "flat top" feature indicating that the $n = 1$ MI domain has an empty core[111].

The reconstruction of the 3D density profile of $n = 1$ MI domain was performed using the inverse Abel transform with the assumption of cylindrical symmetry[14]. Over 10 shots were averaged to improve the signal to noise ratio. Fig. 7-4 (d) shows

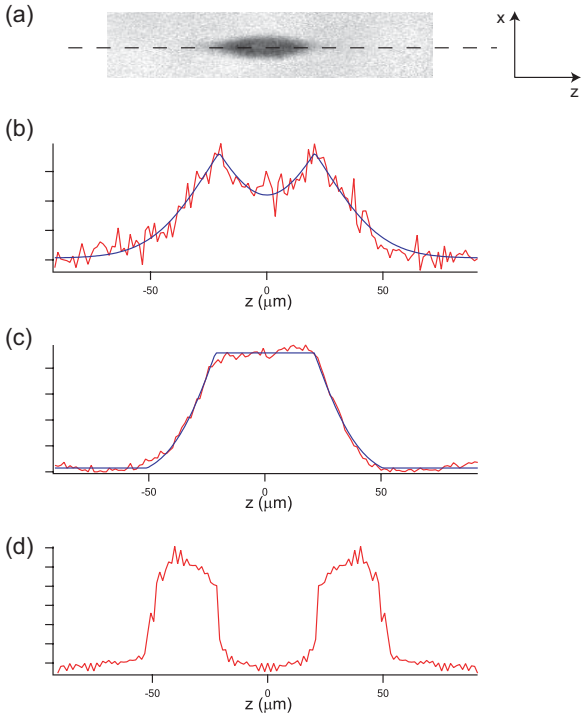

Figure 7-4: Inverse Abel transform of $n = 1$ Mott insulator shell (a) Absorption image of $n = 1$ MI phase. (b) Density profile of single pixel slice along the dashed line drawn in (a). The density is lower near the center of trap. (c) Density profile integrated along the x-axis. It shows a "flat top" feature. (d) Density $\bar{n}_{n=1}(0, 0, z)$ obtained using the inverse Abel transform. It shows the formation of the $n = 1$ MI shell structure.

our reconstructed density profile $\bar{n}_{n=1}(0,0,z)$ along the long axis of the trap. This density profile directly shows the formation of the shell structure in the MI phase.

In the inverse Abel transform, the data is numerically differentiated. The noise in the numerical derivative of a single image was too high and we had to average over 10 shots. Our processed density profile ((d) of Fig.7-4) clearly shows the empty core. The back ground data points outside the atomic cloud have non-negligible noise and were forced to be lower by factor of 5 in the inverse Able transform in these preliminary results. The sharpness of the boundary between $n = 1$ and $n = 2$ MI domains could not be resolved with high accuracy, since we have not yet systematically studied what affects our current resolution.

7.5 Application to Thermometer for Ultracold Atomic Systems

Through the SF-MI phase transition, the initial state of BEC is adiabatically transformed into a set of micro systems at each lattice site. Such adiabatic transitions relate and map the physical quantities between initial and final states. Special emphasis is given to those quantities that are hardly accessible in one state but measurable in the other state, i.e. the entropy and temperature.

The thermodynamics of the micro systems deep in the MI phase can be described in a following simple way by considering only particle–hole excitations [61, 48]. In a single lattice site of a deep MI phase, eigenstates are given by Fock states $|n\rangle$ with energy $E(n) = Un(n-1)/2$. The partition function $Z(\beta, \mu)$ is then expressed as a function of temperature $\beta = 1/k_B T$ and chemical potential μ

$$Z(\beta, \mu) = \sum_n \exp\left[-\beta\left(E(n) - n\mu\right)\right] \tag{7.11}$$

The probability ρ_n that n atoms are occupied in a lattice site can be obtained from

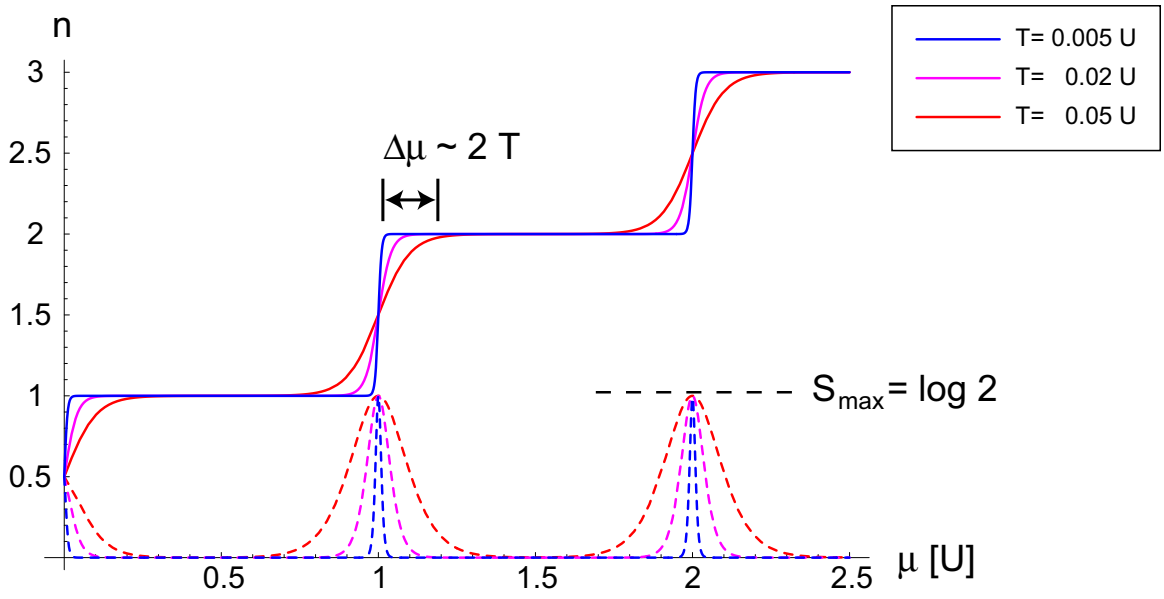

Figure 7-5: Occupation number n and entropy S at variable temperatures $T = 0.005U$, $0.02U$, $0.05U$. At low T, the density profile has plateaus of $n =$ integer with sharp boundaries. As T increases, particle-hole excitations arise near the boundaries and the density varies smoothly. The entropy has a maximum value of $S_{max} = k_B \log 2$ at the center of the boundaries for $T < U$.

the partition function $Z(\beta, \mu)$

$$\rho_n(\beta, \mu) = \frac{\exp\left[-\beta\left(E(n) - n\mu\right)\right]}{Z(\beta, \mu)} \tag{7.12}$$

The occupation number $\bar{n}$ and entropy S are

$$\bar{n}(\beta, \mu) = \sum_n n\rho_n \tag{7.13}$$

$$S(\beta, \mu) = -k_B \sum_n \rho_n \log \rho_n \tag{7.14}$$

They are plotted in Fig. 7-5 for various temperature T.

At $T = 0$, the density profile has density plateaus with sharp boundaries. With increasing temperature the MI domains expands due to particle-hole excitations, and the boundary between different density plateaus becomes broad. At non-zero T ($< U$), the chemical potential range of the MI domains expands by $\Delta\mu \sim 2T$. Inside the boundaries where the density smoothly varies i.e. from 1 to 2, the atom number

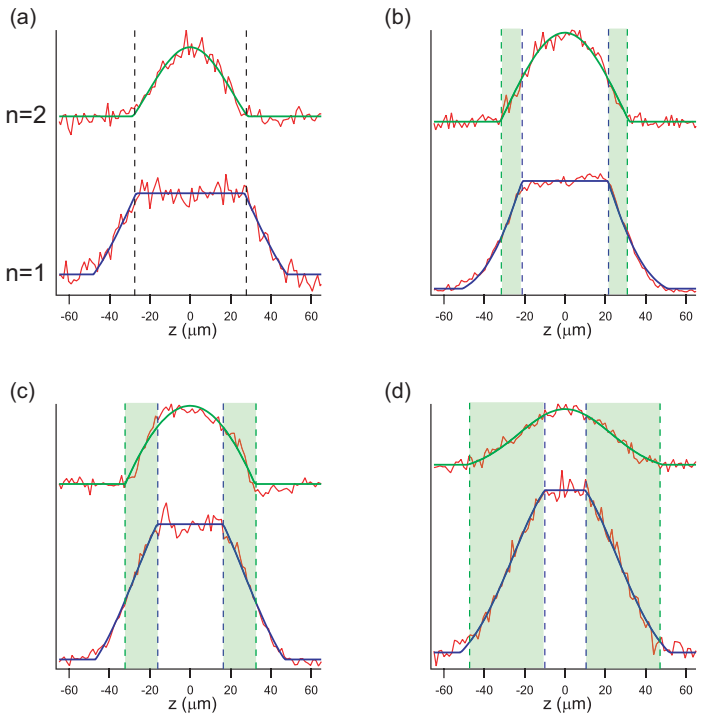

Figure 7-6: Expansion of the MI domains with increasing trap depth and temperature. The integrated density profile $n(z)$ of $n = 1$ (blue) and $n = 2$ (green) MI domains are shown for different trap depths V_{trap}. The trap depths are denoted with respect to the reference trap used in (a): $V_{trap} = 0$ kHz in (a), 7 kHz in (b), 14 kHz in (c), 30 kHz in (d). The boundary between density plateaus (shaded area) becomes broader with increasing trap depth V_{trap}.

fluctuates between 1 and 2 leading to the increase of entropy S. As long as the temperature is lower than the interaction energy ($T < U$), the entropy arises mainly from single particle-hole excitations, and the maximum entropy is given by $S_{max} = k_B \log 2$ at the center of boundaries (dashed line in Fig. 7-5).

To observe the temperature dependence of the MI domain size, the temperature of the system was adjusted by varying the trap depth. For all the trap depths used in our measurement, the condensate fraction was found to be close to 1. In general, it is difficult to precisely determine the condensate fraction near 100 %.[1] Therefore, our measure for temperatrue is the final trap depth V_{trap}, and not the condensate fractions.

The integrated density profiles ($n(z) = \int\int dxdy\, n(x, y, z)$) of $n = 1$ and $n = 2$

[1]This is one of the reasons for employing the MI phase as a thermometer, since precise measurement of thermodynamical quantities of a BEC is a difficult task for small T/T_c

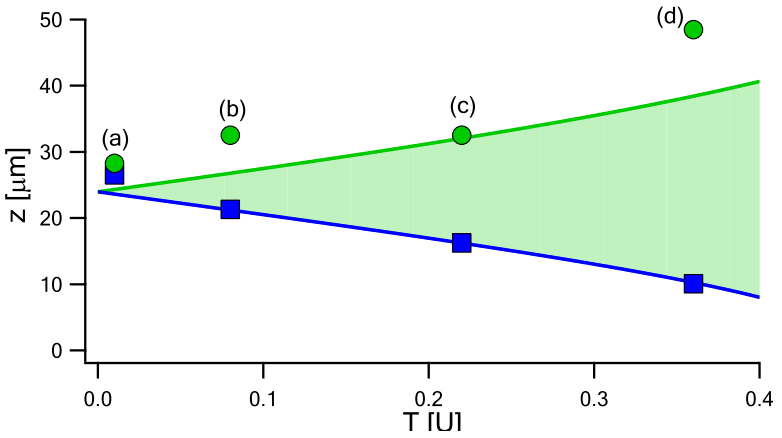

Figure 7-7: The boundary position for the $n = 1$ and $n = 2$ MI domains at variable temperature. A blue (green) curve represents the boundary position of $n = 1$ ($n = 2$, respectively) MI domain calculated for our trap geometry. For comparison, our measurement of boundary position (blue squares: $n = 1$, green circles: $n = 2$) are also displayed with $n = 1$ measurement fitted on the predicted curve: V_{trap} = (a) 0 kHz, (b) 7 kHz, (c) 14 kHz, (d) 30 kHz.

MI domains are shown in Fig. 7-6 for variable trap depths V_{trap}. The "flat top" areas are visible in $n = 1$ density profile. The boundary of the MI domains was determined to be the edges of the "flat top" area for $n = 1$, and the outer edges for $n = 2$ (Fig. 7-6).

We observed that the Mott domains expanded with increasing trap depth V_{trap} (Fig. 7-6). The $n = 1$ MI domain (blue dashed line in Fig.7-6) expanded toward the center of trap, and the $n = 2$ MI domain (green dashed line in Fig.7-6) spreaded outwards from the center. An overlap region of the $n = 1$ and $n = 2$ MI domains was observed to become broader with increasing trap depth V_{trap} (shaded area in Fig. 7-6 (b), (c), (d)).

The curves in Fig. 7-7 shows predicted positions of the MI domain's boundary calculated for our trap geometry. For comparison, our measured boundary positions are also displayed with $n = 1$ measurements fitted on the calculated curve.

Expansion of the overlap area of the $n = 1$ and $n = 2$ domains (shaded area in (b)-(d) of Fig.7-6) implies that the step-like density profile became smoother and continuous. One may expect that the discrete peak structure in the clock shift spectrum becomes continuous due to the change of the density profile to a smooth curve.

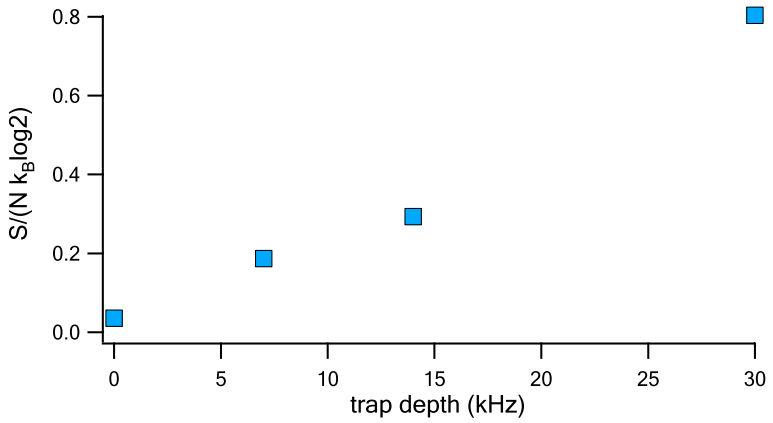

Figure 7-8: Entropy estimated in the MI phase. Entropy per particle is estimated in units of $k_B \log 2$.

However, we observed no significant change in the peak structure of the clock shift spectrum; the position and heights of $n = 1$ and $n = 2$ peaks remained the same. This implies that the state in the overlap area is an *incoherent mixture* (thermal mixture) of Fock states $|1\rangle$, $|2\rangle$: each Fock state $|n\rangle$ contributes to each peak with the probability ρ_n.

Although the smooth density profile of the MI phase at finite temperature is similar to that of the superfluid profile, they are fundamentally different. In the MI case, the state is an incoherent mixture of Fock states $|n\rangle$ with associated probabilities $\rho_n = \exp[-\beta(E(n)-n\mu)]/Z(\beta,\mu)$. The number is determined by an ensemble average, $\bar{n} = \sum_n \rho_n n$ with non-zero entropy. In contrast, the superfluid phase is described by a coherent superposition (pure state) of Fock states $\sum_n c_n|n\rangle$ providing $\langle\hat{n}\rangle = \sum_n |c_n|^2 n$.

The entropy reaches a maximum $S_{max} = k_B \log 2$ near the boundary of the MI domains. The entropy of the system can be estimated by assuming that the entropy is equal to $S_{max} = k_B \log 2$ in the overlap zone and 0 in the pure MI phase domains(non-overlap zone). The estimated entropy is displayed in Fig. 7-8

Entropy has not been experimentally studied in trapped BEC system[2]. Such measurements are challenging particularly for low temperature (small T/T_c). The entropy S of a trapped BEC, for low temperature $T < \mu$, has been predicted in

[2]Specific heat was investigated experimentally[38]

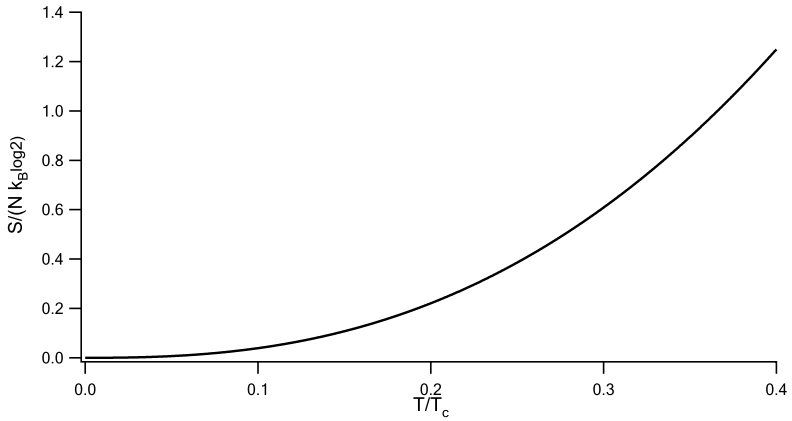

Figure 7-9: Prediction of entropy per particle S/N of a trapped BEC.[50]

theoretical work by Giorgini *et al.* [50]

$$S_i(T,N) = \frac{7A\zeta(3)}{5\sqrt{2}} \left(\frac{15a_sN}{\sigma}\right)^{1/5} \left(\frac{k_BT}{\hbar\omega_0}\right)^{5/2} \tag{7.15}$$

with $\sigma = \sqrt{\hbar/m\omega_0}$, trap frequency ω_0, $A = 10.6$. The entropy S is plotted in Fig. 7-9. From this curve, the initial temperatures T_i of experimental sets (a)-(d) in Fig.7-6 can be estimated by setting $S_i = S_f$: $T_i/T_c =$ (a) ~ 0.05, (b) ~ 0.2, (c) ~ 0.25 (d) ~ 0.35.

7.6 Conclusion

In conclusion, we have imaged individual Mott insulating phases. Detailed density profiles could be obtained with our new high-resolution imaging system. They showed the formation of the MI shell structure. A expansion of the MI domains was observed with increasing trap depth V_{trap}, which determines the initial temperature of the system. The entropy associated with the expansion of the MI domains was estimated. This method should provide an effective way to measure the thermodynamical quantities of ultracold atomic systems.

Chapter 8

Demonstration of Quantum Zeno Effect using a BEC

This chapter briefly introduces the experimental demonstration of Quantum Zeno Effect with a BEC. This experiment was previously reported in Ref. [119]. See the reprint included in Appendix F for detailed discussions.

This is the only experiment described in this thesis in which an optical lattice was not used. Even though the microwave spectroscopy setup was initially designed for optical lattice experiments, microwave transition was first utilized in this experiment to drive Rabi oscillation between two hyperfine states. Two-photon(rf+microwave) transition could be tested and characterized through this experiment before applied to the optical lattice experiments. This experiment is shortly described and I refer to the reprint attached in Appendix F for detailed discussions.

8.1 Quantum Zeno Effect with Pulsed Measurement or Continuous Measurement

The quantum Zeno effect(QZE) is the suppression of transition between quantum states by frequent measurements. Let us consider a two-level system where two levels

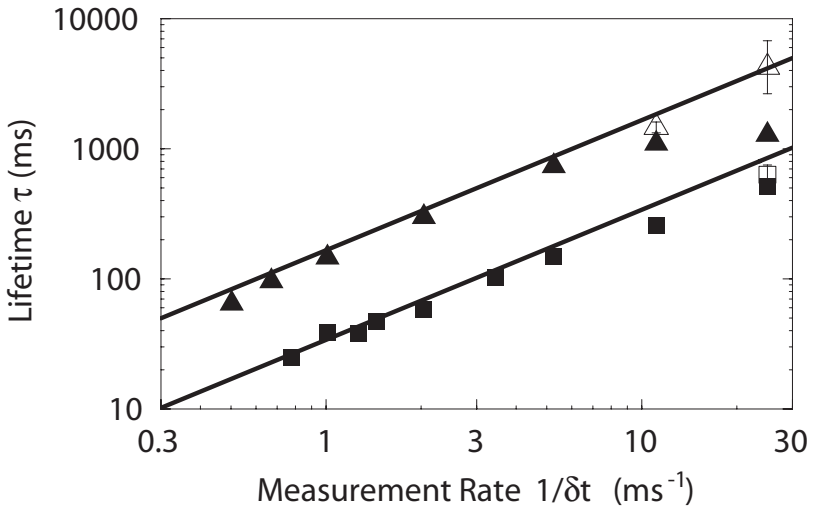

Figure 8-1: Pulsed quantum Zeno effect. Boxes [traingles] are the data points measured with a Rabi frequency $\omega_R/2\pi = 54.6(0.5)$ [24.7(0.1), repectively] Hz. The lifetime τ_{EP} was measured with variable time interval δt. Black lines indicate the predicted QZE lifetime $\tau_{EP} = 4/(\omega_R^2 \delta t)$

$|1\rangle$, $|2\rangle$ are coherently driven at a Rabi frequency ω_R.

8.1.1 Pulsed Measurement

Measurements of the state of the system project the system into one of the two states $|1\rangle$, $|2\rangle$. If the system is initially in $|1\rangle$ and a measurement is made after short time $\delta t (\ll 1/\omega_R)$, the probability for the system to be in $|1\rangle$ is $\approx 1 - (\omega_R \delta t/2)^2$. For N successive measurements the probability for the system to be in $|1\rangle$ is given by

$$P(N) = \left[1 - (\omega_R \delta t/2)^N\right]^2 \approx \exp[-N(\omega_R \delta t/2)^2] = \exp[-(\omega_R^2 \delta t/4)T] \qquad (8.1)$$

with the total free evolution time $T = N\delta t$. The initial state $|1\rangle$ decays with an effective decay rate $1/\tau_{EP}$ instead of normal Rabi oscillation. The effective decay rate $1/\tau_{EP}$ is

$$1/\tau_{EP} = \omega_R^2 \delta t/4 \qquad (8.2)$$

The characteristic time τ_{EP} for the pulsed QZE is much longer than the char-

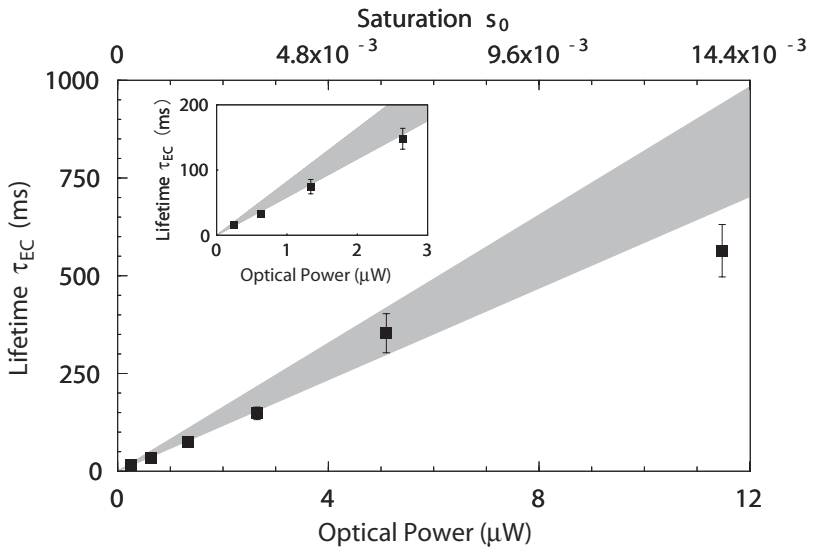

Figure 8-2: Continuous quantum Zeno effect. Rate of continuous measurement γ is linearly proportional to measurement laser beam power. Lifetime τ_{EC} increases with increasing measurement rate γ. Gray bands indicates range of expected lifetimes.

acteristic time $1/\omega_R$ of normal Rabi-type oscillation. This shows the suppression of transition.

To experimentally demonstrate QZE, a BEC prepared with an initial hyperfine state $|1\rangle = |1, -1\rangle$ was driven to state $|2\rangle = |2, 1\rangle$ with the two-photon (rf+microwave) transition. Measurements were performed with a laser beam resonant with the $F = 2 \rightarrow F' = 3$ D_2 transition. The pulsed QZE was observed with a train of repeated pulses of the measurement laser. Fig. 8-1 shows that the lifetime τ_{EP} increases dramatically with a measurement rate $1/\delta t$.

8.1.2 Continuous Measurement

For a continuous measurement, atoms are continuously illuminated with a weak measurement laser beam. If atoms are in state $|2\rangle$, they emit a photon at a rate γ, and those atoms are removed from the system by the photon recoil kick. The population of state $|1\rangle$ decays with a rate $1/\tau_{EC}$ which is given by the optical Bloch equation as [108]

$$1/\tau_{EC} = \omega_R^2/\gamma \tag{8.3}$$

For comparison, let us consider a *pseudo*-continuous measurement scheme where a measurement is performed by a series of randomly distributed pulses. The population in state $|1\rangle$ is after N pulse measurement

$$P(N) = \langle 1 - (\omega_R \delta t/2)^2 \rangle^N \approx \exp\left[-N\omega_R^2 \langle \delta t^2 \rangle/4\right] = \exp\left[-\frac{\omega_R^2 \langle \delta t^2 \rangle}{4\langle \delta t \rangle} T\right]$$

with $T = N\langle \delta t \rangle$. If the probability for measurement pulse during a time interval δt is $\gamma \delta t$, $\langle \delta t \rangle = 1/\gamma$ and $\langle \delta t \rangle^2 = 2/\gamma^2$. The effective decay rate is

$$1/\tau_{EP,random} = \omega_R^2/2\gamma \tag{8.4}$$

Although the continuous measurement beam leads to the same emission rate γ of state $|2\rangle$ as the random pulse measurement case, the decay rates $1/\tau_{EC}$, $1/\tau_{EP,random}$ are different by a factor of 2. While in the random pulse case the wave function evolves without interference of measurement pulses between measurement pulses, in the continuous QZE case the evolution of wave function is continuously intervened by the *presence* of a measurement. Fig.8-2 shows our measurement of continuous QZE.

By matching the observed lifetimes for the pulsed and continuous QZE, we find that each measurement type has the same QZE when $\gamma \delta t = 3.60(0.43)$, which is in agreement with the predicted value of 4. This rules out the pseudo-continuous QZE that gives $\gamma \delta t = 2$ instead of 4.

Chapter 9

Conclusion

Ultracold atoms in optical lattice have proved to be a powerful tool in understanding and simulating conventional condensed matter physics. The superfluid-Mott insulator transition realized in ultracold atomic system illustrates the capability of ultracold atomic system in optical lattice as a quantum simulator for condensed matter physics (especially, Hubbard Model). In particular, quantum magnetism is now actively pursued by many groups using ultracold atoms in optical lattices. In the current stage, some further steps seem to be required for the realization of magnetic ordering in optical lattice. First, the controllability of individual spin states of atoms is needed such as spin-dependent potentials to manipulate the effective spin-spin interaction. Second, the temperature for the magnetic ordering realization must be very low, i.e. compared to Néel temperature. To measure such low temperatures a new thermometer is required. Possibly, additional cooling methods are required to reach anti-ferromagnetic ordering. As a first step toward this goal, in the new science chamber the MI transition was achieved and the spatial density profile of the MI shell structure could be observed with a new high resolution imaging system. The next steps are the implementation of a spin-dependent optical lattice and a new scheme of thermometry. Hopefully, this leads to the exploration of a new forms of magnetic matter with new understandings of and insights into nature. I am confident that the Rb lab will continue to have many exciting moments, and I hope there will be many successes.

In the near future, as further steps spin-dependent optical lattice will be implemented with a new scheme of thermometry. It would bring a new form of magnetic matter with new understandings and insights on nature. I believe the Rb lab will go forward to this goal with many exciting moments, and I hope there would be many successes.

Appendix A

The Configuration of a High Resolution Imaging Lens

This appendix contains the design of our high resolution imaging lens.

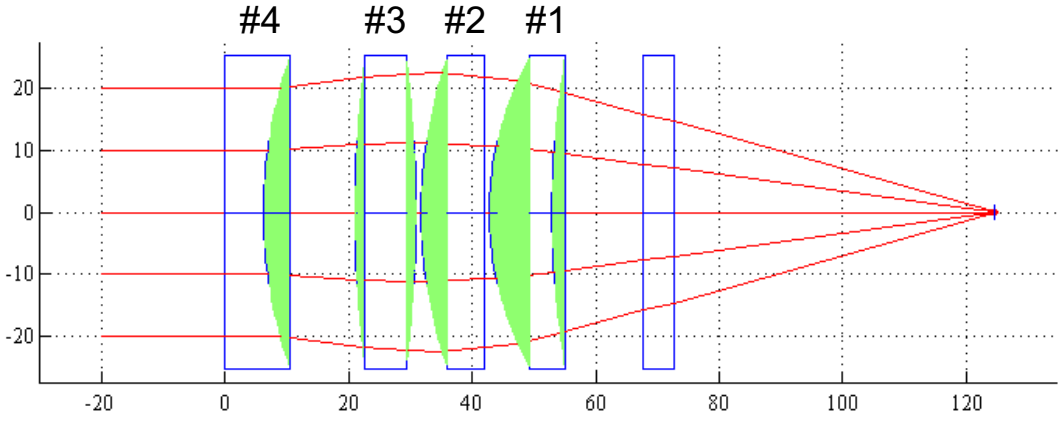

This imaging optics were designed, assembled and tested by postdoc David Weld. The high resolution imaging lens has 4 spherical lenses. The information on the individual lenses and spacers are listed.

- Lens #1: Meniscus shape. (closest to the imaging target)

  R1 = 119.3 mm

  R2 = 47.9 mm

- Spacer #1:

  Length = 0.680″

- Lens #2: Plano-convex shape

  R3= ∞

  R4=77.52 mm

- Spacer #2:

  Length = 0.637″

- Symmetric bi-convex shape

  R5=R6=205.67 mm

- Spacer #3:

  Length=0.767″

- Lens #4: Plano-concave shape

  R7=77.52 mm

  R8=∞

(All spacers are 2″ diameter aluminum tubes with 1/16″ wall) thickness.

The configuration of the high resolution imaging lens was optimized by a ray tracing program. A closeup view of traces of imaging rays in the high resolution lens is shown below.

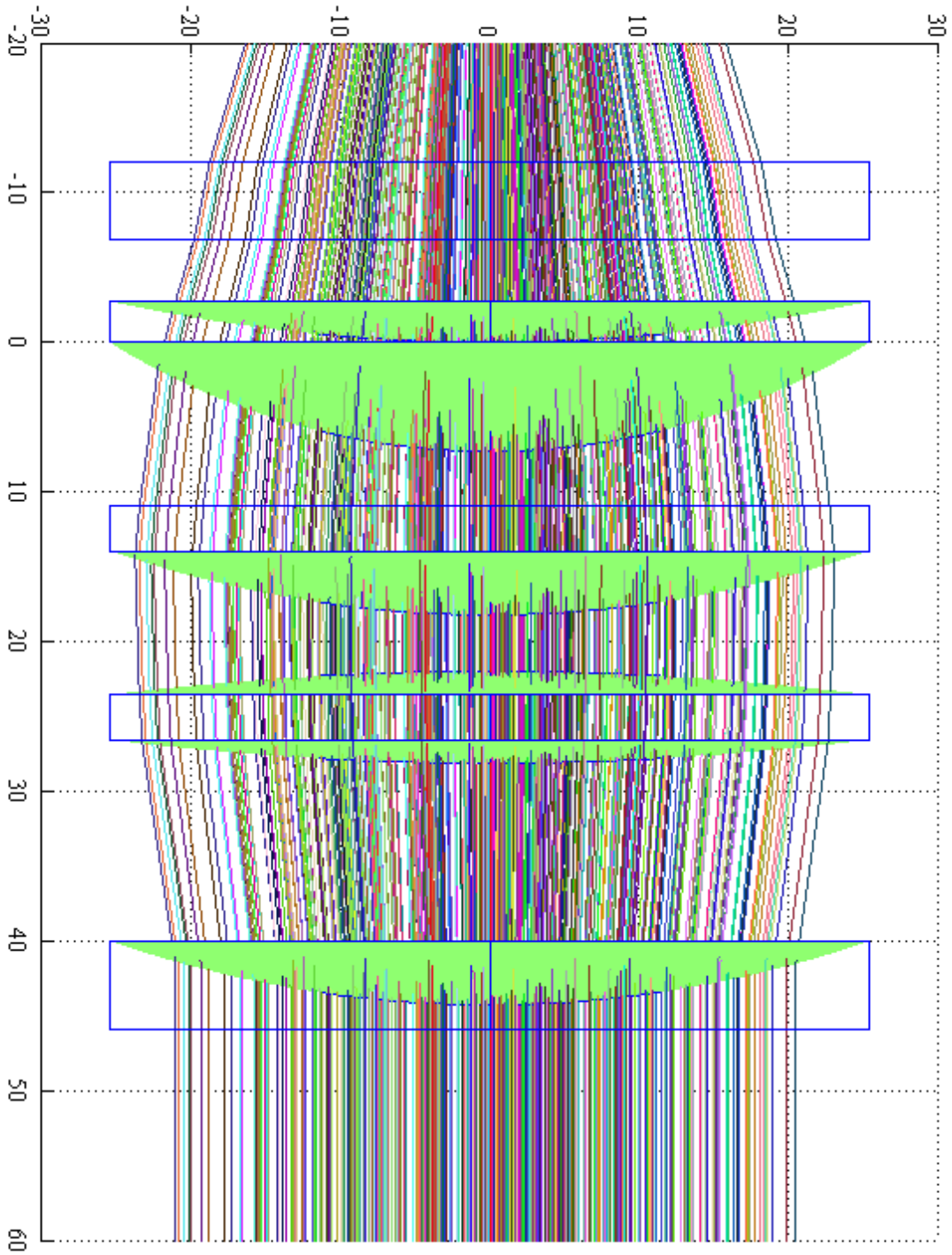
-30
-20
-10
0
10
20
30
-20
-10
0
10
20
30
40
50
60

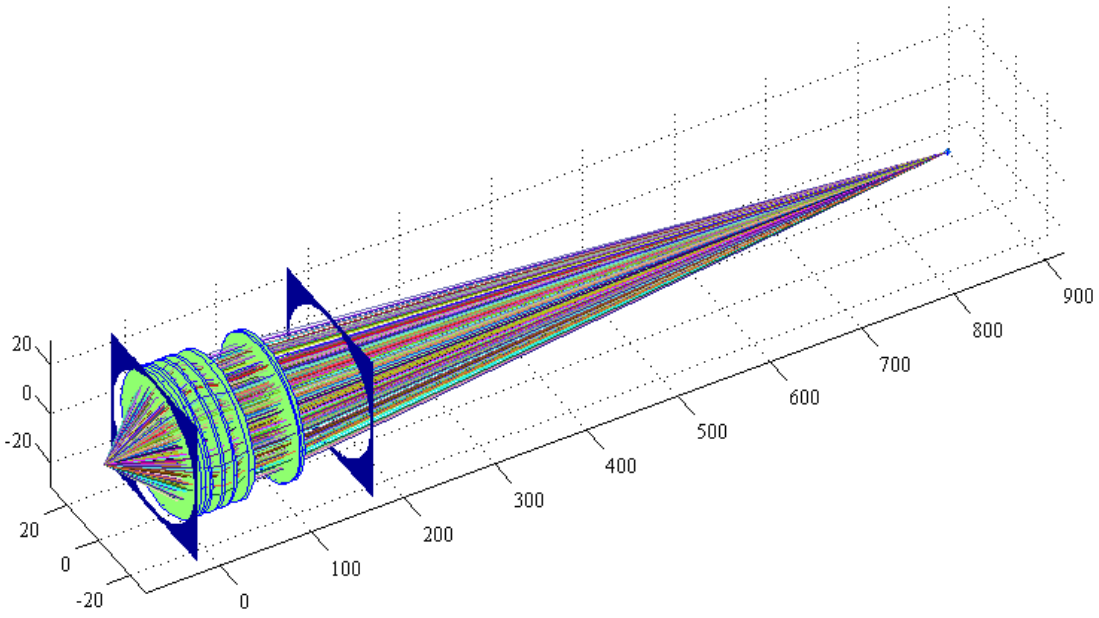
20
0
-20
20
0
-20
0
100
200
300
400
500
600
700
800
900

Appendix B

Designs for Experimental Apparatus

This appendix contains drawings for the science chamber and layout for the 780 nm diode laser optics.

Top view of the science chamber

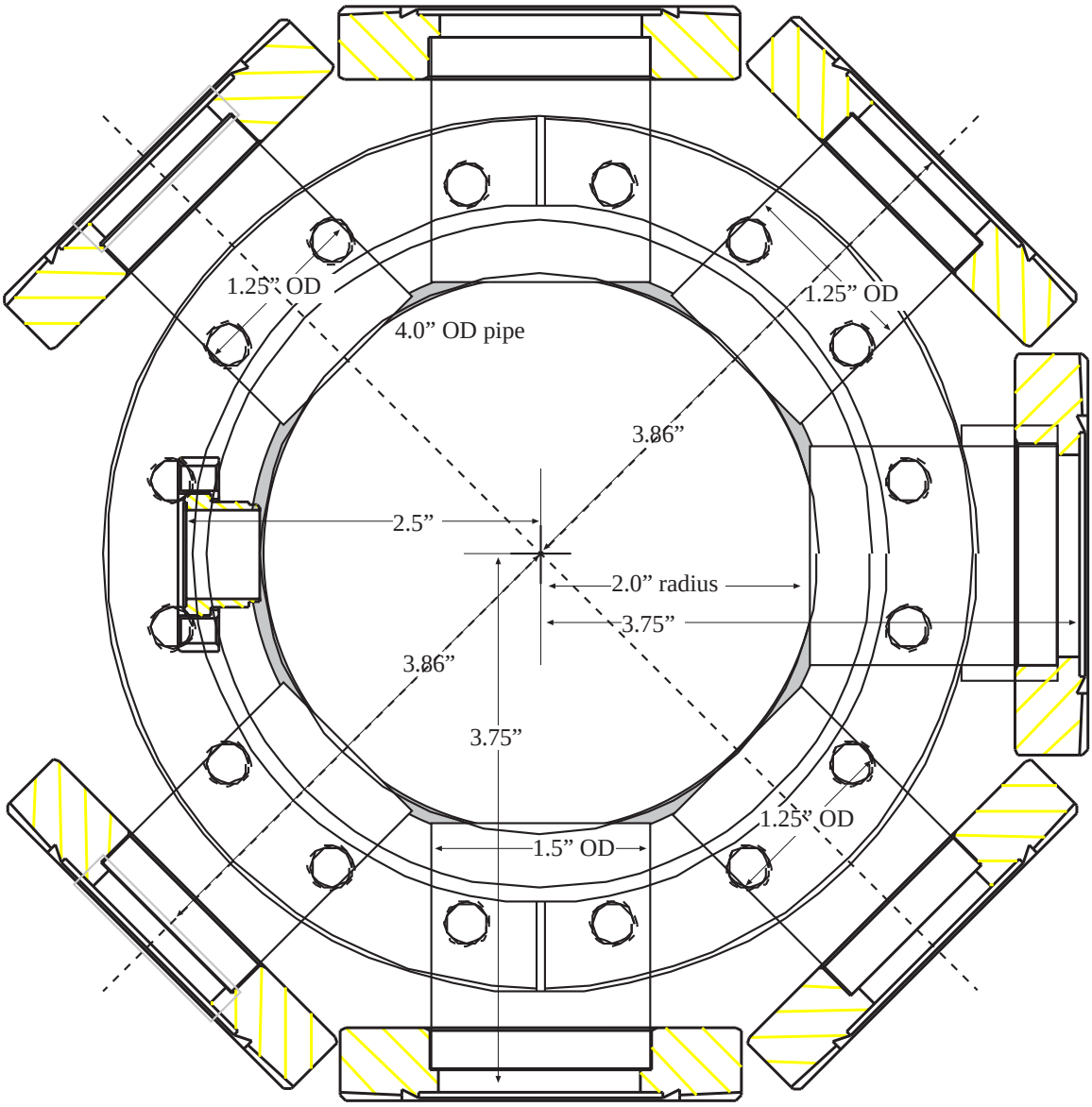

Side view of the science chamber

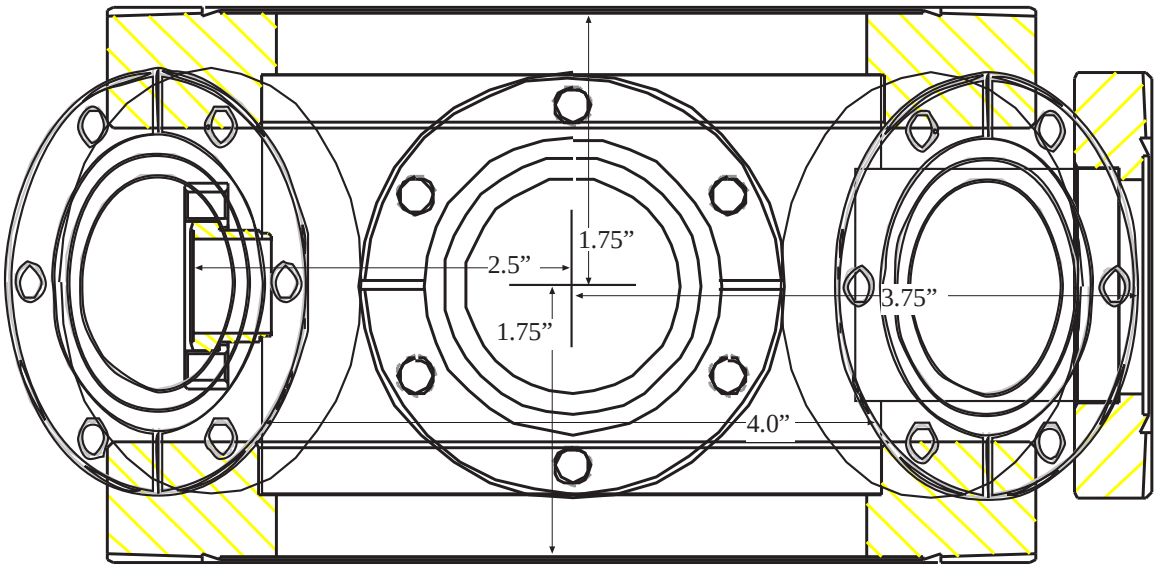

Diode Laser Layout for Rb D2 line

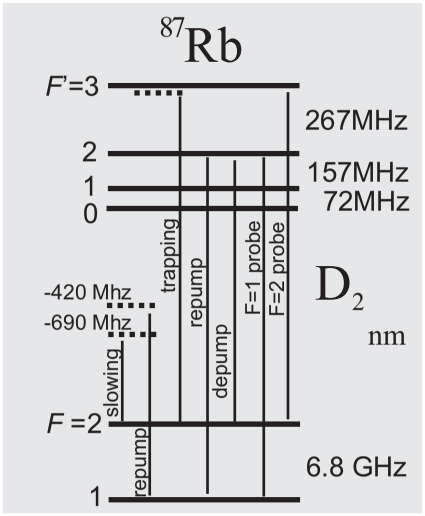

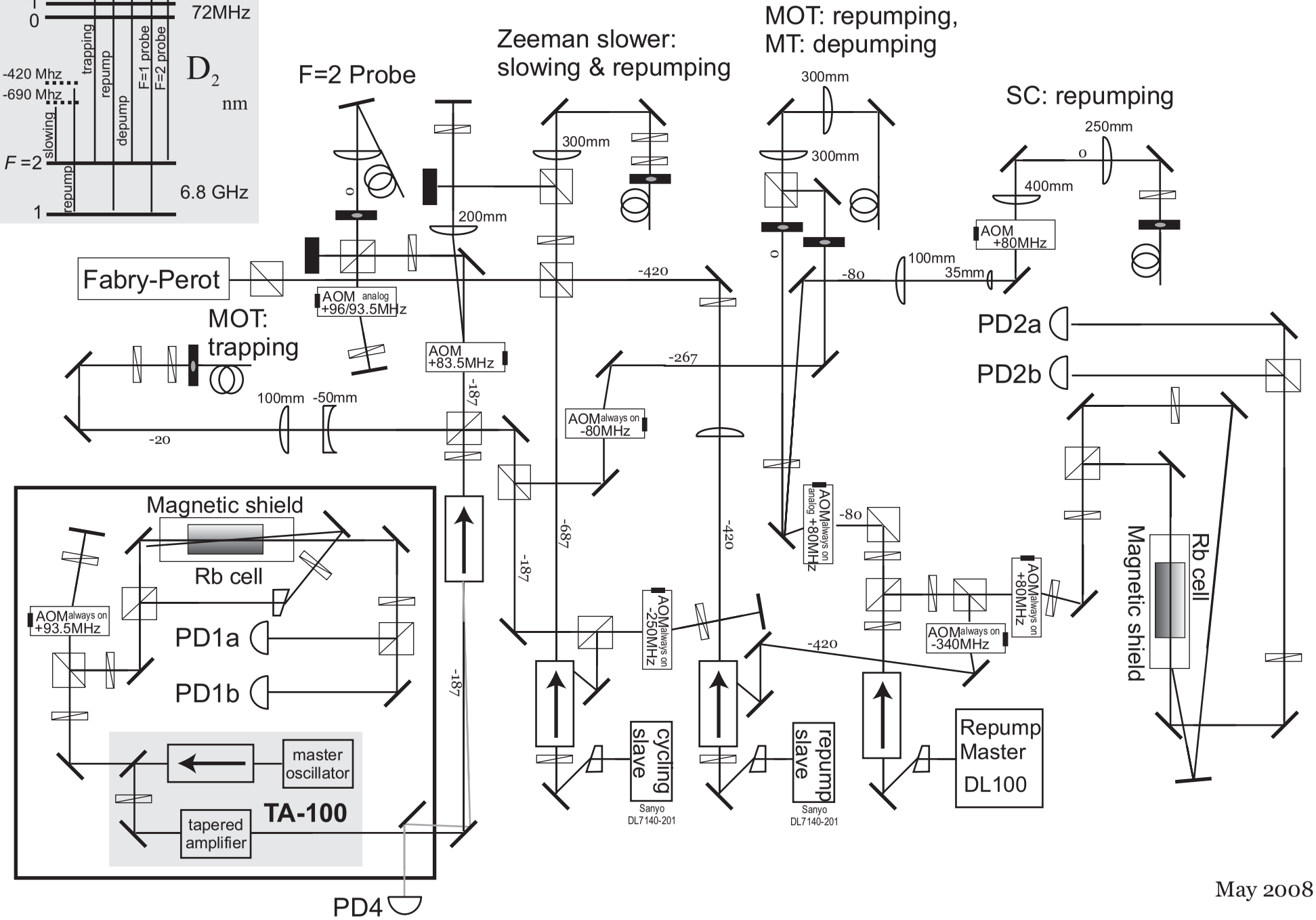

May 2008

Appendix C

Phase Diagram for a Bose-Einstein Condensate moving in an Optical Lattice

This appendix contains a reprint of Ref. [88]: Jongchul Mun, Patrick Medley, Gretchen K. Campbell, Luis G. Marcassa, David E. Pritchard, and Wolfgang Ketterle, *Phase Diagram for a Bose-Einstein Condensate moving in an Optical Lattice*, Physical Review Letters **99**, 150604 (2007).

Phase Diagram for a Bose-Einstein Condensate Moving in an Optical Lattice

Jongchul Mun, Patrick Medley, Gretchen K. Campbell,* Luis G. Marcassa,† David E. Pritchard, and Wolfgang Ketterle

MIT-Harvard Center for Ultracold Atoms, Research Laboratory of Electronics, and Department of Physics, MIT, Cambridge, Massachusetts 02139, USA

(Received 26 June 2007; published 12 October 2007)

The stability of superfluid currents in a system of ultracold bosons was studied using a moving optical lattice. Superfluid currents in a very weak lattice become unstable when their momentum exceeds 0.5 recoil momentum. Superfluidity vanishes already for zero momentum as the lattice deep reaches the Mott insulator (MI) phase transition. We study the phase diagram for the disappearance of superfluidity as a function of momentum and lattice depth between these two limits. Our phase boundary extrapolates to the critical lattice depth for the superfluid-to-MI transition with 2% precision. When a one-dimensional gas was loaded into a moving optical lattice a sudden broadening of the transition between stable and unstable phases was observed.

DOI: 10.1103/PhysRevLett.99.150604 PACS numbers: 05.60.Gg, 03.75.Kk, 03.75.Lm, 05.30.Jp

The realization of condensed matter systems using ultracold atoms brings the precision and control of atomic physics to the study of many-body physics. Many studies have focused on Mott insulator physics, an important paradigm for the suppression of transport by particle correlations. Previous studies of the superfluid (SF)-to-Mott insulator (MI) transition in optical lattices with ultracold bosons [1–8] addressed the quenching of superfluidity below a critical lattice depth. Here we extend these studies into a second dimension by studying stability of superfluid current as a function of momentum and lattice depth as suggested in Ref. [9]. These transport measurements show the stability of superfluid at finite current, which is in nonequilibrium.

Transport measurements extend previous work on stationary systems in two regards. First, superfluidity near the MI transition has only been indirectly inferred from coherence measurements, whereas in this work, we characterize the superfluid regime by observing a critical current for superfluid flow through the onset of dissipation. Second, previous studies [1–8] were not able to precisely locate the phase transition, since the observed excitation spectrum and atomic interference pattern did not abruptly change [3,5,6], partially due to the inhomogeneous density. In contrast, the sudden onset of dissipation provides a clear distinction between the two quantum phases. In the SF phase, current flows without dissipation if the momentum does not exceed a critical momentum, while in the MI phase the critical momentum vanishes and transport is dissipative.

Bosonic atoms in an optical lattice are often described by the Bose-Hubbard Model where the tunneling between nearest neighbor lattice sites is characterized by the hopping matrix element J and the repulsive interactions by the on-site matrix element U [1,10–12]. The dimensionless interaction energy $u \equiv U/J$ determines the quantum phase of the system. For $u > u_c$, the system is in the MI phase, for $u < u_c$, the SF phase. u_c increases with the number of atoms N per site.

For weak interactions ($u \to 0$), the system approaches single-particle physics in a periodic potential well described by Bloch states and band structure. The critical momentum for a stable current-carrying state is 0.5 p_r ($p_r = h/\lambda$ is the recoil momentum of an atom, where λ is the wavelength of the optical lattice light) [13]. At the critical momentum, it becomes possible for two atoms in the same initial Bloch state to scatter into two other states and conserve energy and quasimomentum [14,15]. Instabilities in a 1D optical lattice were studied theoretically using a linear stability analysis of the Gross-Pitaevskii equation [13,16], and experimentally [14,17,18]. The theoretical studies predicted that for increasing lattice depth or increasing atomic interactions the stability of superfluid flow should increase [13,16]: the dynamic instability would stay near 0.5 p_r, whereas the Landau critical velocity and therefore the energetic instability would shift to larger momenta (For more discussions on dynamic and energetic instability, see Refs. [19,20]). However, these analyses neglect the growing importance of quantum correlations for larger lattice depth which leads to the SF-MI phase transition, where the critical momentum for a superfluid current vanishes. In this Letter, we study the decrease of the critical momentum from its value for the weakly interacting regime towards zero at the MI transition (Fig. 1).

Most studies of the SF-MI phase transition monitor the coherence in the superfluid phase through an interference pattern observed in the ballistic expansion resulting from a sudden turn-off of the confining potential and lattice. Previous observations of the phase transition found the experimental transition point to lie in the range between 10 and 13 E_R (with the recoil energy defined as $E_R = p_r^2/2m$, where m is the atomic mass) [3]. This uncertainty is related to the inhomogeneous density profile of trapped atoms and to the fact that the visibility of the interference extends beyond the transition point due to short-range coherence in the MI phase [6]. It has been suggested that observed kinks in the visibility are linked to the formation

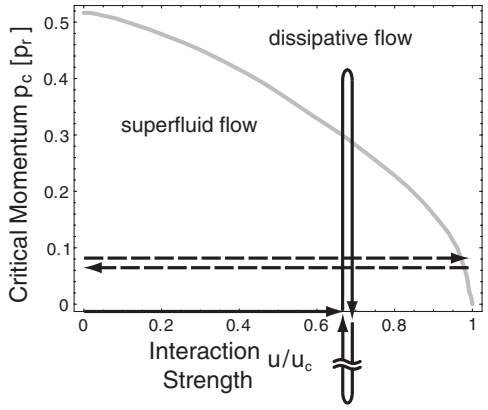

FIG. 1. Phase diagram showing the stability of superfluid flow in an optical lattice and the experimental procedure. The gray curve shows the predicted boundary between superfluid flow and dissipative flow phases for a three-dimensional gas with a commensurate filling of $N = 1$ atom per site [9]. The solid (dashed) arrows illustrate the experimental trajectory used for small (large) lattice depths (see text for details).

of the MI shells with occupation numbers $N = 2$ and 3 [6]. Several authors have suggested other features in the momentum distribution beyond coherent interference peaks as a more distinct signature of the phase transition [21,22]. Here we show that the disappearance of the critical momentum for superfluid flow provides such a signature and allows the determination of the transition point with high precision.

Our measurement was not limited by the inhomogeneous density profile. For our range of lattice depths, low critical momenta and the onset of dissipation occur only near the formation of MI shells with integer occupation numbers N [9]. The onset of dissipation related to the $N = 1$ domains occurs at smaller momentum than for other N domains. For instance, with increasing momentum p the $N = 1$ domain becomes unstable first, and this triggers dissipation over the whole atomic cloud [9]. Therefore, the breakdown of superfluid flow in the system was determined by the formation of the $N = 1$ domain and was not smeared out by the inhomogeneous density. Our criterion, the sudden onset of dissipation, depended on the formation of an insulating shell surrounded by a superfluid region, which occurs only in the inhomogeneous case.

In our experimental setup, a Bose-Einstein condensate (BEC) of ^{87}Rb atoms in the $5S_{1/2}$ $|1, -1\rangle$ state was prepared and trapped in a combination of an Ioffe-Pritchard magnetic trap and an optical dipole trap. The number of atoms in the BEC was typically 2×10^5. The magnetic trap frequencies were $\omega_{x,y} = 40$ Hz radially and $\omega_z = 4.6$ Hz axially. The laser beam for the optical dipole trap was oriented along the x axis. This laser beam was retroreflected and the polarization of the retroreflected beam was rotated in order to minimize interference between the two beams. Along the vertical direction (y axis) a lattice was formed by a retroreflected laser beam. For the z axis, a moving lattice was created by introducing a small frequency detuning δf between the two counterpropagating laser beams using acousto-optical modulators driven by phase-locked frequency generators. The 3D optical lattice was ramped up exponentially in 160 ms. All lattice beams were derived from the same laser operating at $\lambda = 1064$ nm and had an $1/e^2$ waist of 100–200 μm. The lattice depth was calibrated with 1% accuracy by applying a 12.5 μs lattice laser pulse to a BEC and comparing the observed Kapitza-Dirac diffraction pattern of a BEC to theory.

For transport measurements, we moved an optical lattice [17,23] which provides more flexibility to change the momentum than exciting a dipole oscillation by displacement of the BEC [24,25]. A moving optical lattice with velocity $v = \lambda \delta f/2$ was created along the long axis of the BEC by introducing a small frequency detuning δf between two counterpropagating lattice beams. If the velocity $v(t)$ changes slowly enough not to induce interband excitations, the initial Bloch state $|p = 0\rangle$ of the condensate in the optical lattice adiabatically evolves into the current-carrying state $|p(t) = -mv(t)\rangle$ where p is the quasimomentum. For increasing lattice depth, the effective mass of atoms $m^* = [\partial^2 E(p)/\partial p^2]^{-1}$ increases, and the group velocity $v_g = -(m/m^*)v(t)$ decreases. As a consequence, atoms prepared in a moving lattice with quasimomentum $p = -mv$ travel in the frame of the moving lattice with v_g and in the lab frame with velocity $\Delta v = v + v_g = (1 - m/m^*)v$, which approaches v in a deep lattice. Consequently, we observed that in a deep moving lattice atoms were dragged along to the edge of the trapping region limiting the experimental time scale to probe for dissipation. This became an issue for larger values of p and was addressed by first ramping up the lattice with $p = 0$ and then alternating the velocity of the moving lattice, thus performing a low-frequency ac transport measurement instead of dc.

We have used two sets of experimental procedures (Fig. 1), and our results were consistent for both. Close to the SF-MI phase transition, the lattice was increased to V_{latt} with a fixed (and small) value of momentum p (dashed arrows in Fig. 1). After a variable hold time t_{hold} at V_{latt} the lattice was ramped down to zero, and the magnetic trap switched off. After 33 ms of ballistic expansion, the atoms were imaged and the condensate fraction was determined as a function of momentum by using a bimodal fitting function. For smaller lattice depths, the lattice was ramped up with $p = 0$ (Fig. 1). Then a sinusoidal momentum modulation of the moving lattice with amplitude p_M was applied by modulating the frequency detuning δf between the counterpropagating lattice beams. The 10 ms period of this momentum modulation was slow enough to meet the adiabaticity condition, but fast enough to limit the displacement of the atomic cloud to less than a few μm. Both the trapping potential and the optical lattice were then turned off suddenly. After 33 ms of ballistic expansion, the condensate fraction of the center peak of the

superfluid interference pattern was recorded as a function of the momentum modulation amplitude p_M. Several cycles (typically, three to five) of the momentum modulation were applied to obtain a high contrast between the stable and dissipative regimes [Fig. 2(a)].

Figure 2(a) shows how the transition between superfluid and dissipative currents became sharper with increasing number of cycles of the momentum modulation. The critical momentum was determined from a log-log plot of the condensate fraction as a function of momentum p [Fig. 2(c)]. The intersection between two linear fit functions was taken as the critical momentum. Our result was found to be independent of the time period and number of cycles of the momentum modulation at a few percent level.

In the MI phase, stable superfluid flow is not possible and the critical momentum should vanish. However, using the procedure described above, we measured a small critical momentum of 0.02 p_r for lattice depths $V_{\mathrm{latt}} = 14$, 15, 16 E_R. Up to this momentum, the SF-MI phase transition remained reversible. We interpret the nonzero critical momentum as a finite-size effect. For our cloud size of 60 μm, the corresponding Heisenberg momentum uncertainty of 0.018 p_r agrees with our measured critical momentum. In cold atom experiments, some sloshing motion of the cloud in the trapping potential is unavoidable. The momentum uncertainty determined above indicates how much sloshing motion can be tolerated without affecting the observed phase transition.

The critical lattice depth for the SF-MI phase transition can be determined as the point where the critical momentum vanishes. Using the predicted functional form [9] of the approach towards zero, $p_c \propto \sqrt{1 - u/u_c}$, as a fit function for the data points close to the SF-MI phase transition (the data points shown in the inset of Fig. 3) we determined the critical value $u_c = 34.2$ (± 2.0) corresponding to a lattice depth of 13.5(± 0.2) E_R. Our result agrees with the mean-field theory prediction $u_c = 5.8 \times 6 = 34.8$ for $N = 1$ SF-MI phase transition [1] and deviates by 2 σ from the predictions of $u_c = 29.34(2)$ of quantum Monte Carlo (QMC) simulation [26,27], which includes corrections beyond the mean-field theory. This demonstrates that our method has the precision to identify non-mean-field corrections. However, to turn precision into accuracy, experiments or QMC simulations [21,26,27] have to address corrections due to finite size, finite temperature, and finite time to probe the onset of the instability [27]. In our experiment, these corrections seemed to be small, but have not been characterized at the level of 1% in lattice depth.

The mean-field prediction for stable superfluid flow in 1D is similar to that for the 3D system [9]. However, it is well known that fluctuations play a much more important role in 1D. For studying a 1D system, we prepared an array of one-dimensional gas tubes by ramping two pairs of optical lattice beams up to lattice depths of $V_x = V_y = 30\ E_R$ suppressing hopping between the tubes. After a hold time of 10 ms, a moving optical lattice was ramped up along the z axis. As in our 3D experiment, a momentum modulation was applied, after which the moving optical lattice was ramped down to zero, followed by the other two optical lattices. The condensate fraction was determined after 33 ms of ballistic expansion as a function of the

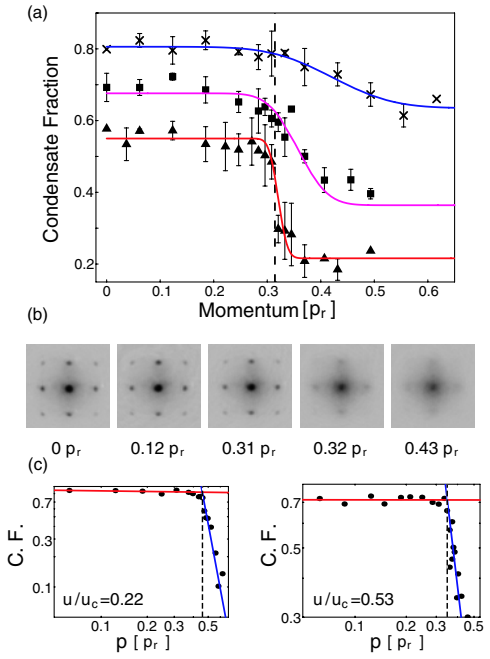

FIG. 2 (color online). Determination of the critical momentum of superfluid flow. Shown is the condensate fraction as a function of a momentum p. (a) Condensate fraction with $u/u_c = 0.61$ for a variable number of cycles of the momentum modulation (one cycle: × and blue line, two cycles: ■ and purple line, three cycles: ▲ and red line). A dashed vertical line indicates the critical momentum where instability begins to occur. The two and three-cycle data are offset vertically for clarity. These data were fitted with an error function to guide the eye. (b) Images of interference patterns released from an optical lattice at $u/u_c = 0.61$ moving with variable momentum. Instability occurred between $p = 0.31 p_r$ and $0.32 p_r$. Some of the triangular data points in (a) were obtained from these images. (c) Condensate fraction on a log-log scale for two different interaction strengths.

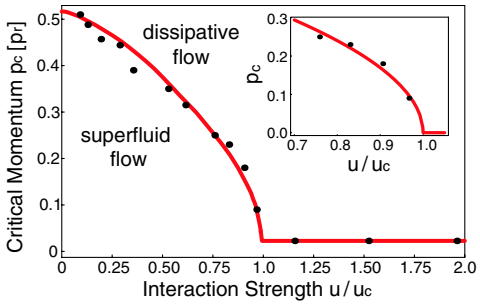

FIG. 3 (color online). Critical momentum for a condensate in a 3D lattice. The solid line shows the theoretical prediction for the superfluid region. The horizontal solid line is a fit to the data points in the MI phase. (Inset) Fit of critical momenta near the SF-MI phase transition.

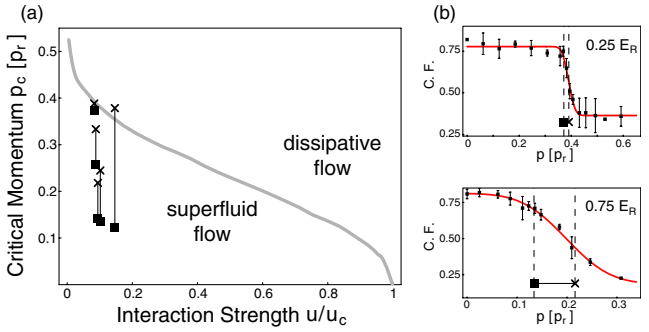

FIG. 4 (color online). Critical momentum for a 1D gas in an optical lattice. (a) The gray line indicates the mean-field theory prediction. The interaction strengths are normalized by the mean-field prediction for $u_c = 5.8 \times 2$ [1,4]. Squares (crosses) represent the measured critical momentum (the center of the transition). Measurements were taken at lattice depths of 0.25, 0.50, 0.75, 1.0, 2.0 E_R. The lines between crosses and squares indicate the width of the transition region. (b) Condensate fraction measured at 0.25 E_R and 0.75 E_R. The data were fitted with an error function. Squares (the critical momentum) and crosses (the center of the transition) are indicated on the plots.

momentum modulation amplitude. The critical momentum, where the onset of dissipation begins, was identified from a log-log plot as in the 3D case. Since the transitions became very broad, we characterized them by an error function fit, with the center of the fitted error function taken as the center of the transition (Fig. 4).

In the 1D system, at a very shallow lattice depth of 0.25 E_R (corresponding to $u/u_c = 0.08$) a sharp transition was observed, and the measured critical momentum agreed very well with the prediction [9,28] of a critical momentum of 0.39 p_r. However, a slight increase of the interaction strength (to $u/u_c = 0.09$ at a lattice depth of 0.5 E_R) led to a significant decrease of the critical momentum as well as a dramatic broadening of the transition as shown in Fig. 4. For lattice depths larger than 2 E_R, the transition became very broad and showed complex behavior, and we could not obtain quantitative fits. Our results show a significant deviation from the mean-field theory predictions and are in agreement with previous works [25,29,30].

The observed broadening of the transition confirms theoretical studies which emphasize the importance of quantum fluctuations in the 1D system. Quantum tunneling out of metastable states which are ignored in the mean-field description can lead to a decay of the superfluid current at very low momenta [28]. In addition to quantum fluctuations, thermal fluctuations provide a mechanism for current decay [28]. In our experiment, we used a "pure" BEC without a discernible thermal component. The close agreement with $T = 0$ predictions indicates that thermal fluctuations were not dominant.

In conclusion, we have used transport studies to connect a well-known dynamical instability for weakly interacting bosons with the equilibrium superfluid to Mott insulator transition. A comparison of 3D and 1D systems confirms the applicability of a mean-field description in three dimensions and the crucial importance of fluctuations in one dimension. The disappearance of superfluid currents at the SF-MI phase transition precisely located the phase transition. Our results illustrate the control and precision of condensed matter physics experiments done with ultracold atoms and their suitability to test many-body theories.

This work was funded by NSF through the grant for CUA. L. G. M. acknowledges support from Coordenacao de Aperfeicoamento de Pessoal de Nivel Superior. We thank E. Demler and A. Polkovnikov for insightful discussions, and David Weld for a critical reading of the manuscript.

*Present address: JILA, Boulder, Colorado 80309, USA.
†Permanent address: Instituto de Fisica de São Carlos, University of São Paulo, São Carlos, 13560-970, SP, Brazil.

[1] D. Jaksch *et al.*, Phys. Rev. Lett. **81**, 3108 (1998).
[2] C. Orzel *et al.*, Science **291**, 2386 (2001).
[3] M. Greiner *et al.*, Nature (London) **415**, 39 (2002).
[4] T. Stöferle *et al.*, Phys. Rev. Lett. **92**, 130403 (2004).
[5] S. Fölling *et al.*, Nature (London) **434**, 481 (2005).
[6] F. Gerbier *et al.*, Phys. Rev. Lett. **95**, 050404 (2005).
[7] G. K. Campbell *et al.*, Science **313**, 649 (2006).
[8] S. Fölling *et al.*, Phys. Rev. Lett. **97**, 060403 (2006).
[9] E. Altman *et al.*, Phys. Rev. Lett. **95**, 020402 (2005).
[10] M. P. A. Fisher *et al.*, Phys. Rev. B **40**, 546 (1989).
[11] W. Krauth, M. Caffarel, and J.-P. Bouchaud, Phys. Rev. B **45**, 3137 (1992).
[12] J. K. Freericks and H. Monien, Europhys. Lett. **26**, 545 (1994).
[13] B. Wu and Q. Niu, Phys. Rev. A **64**, 061603(R) (2001).
[14] G. K. Campbell *et al.*, Phys. Rev. Lett. **96**, 020406 (2006).
[15] K. M. Hilligsøe and K. Mølmer, Phys. Rev. A **71**, 041602(R) (2005).
[16] M. Modugno, C. Tozzo, and F. Dalfovo, Phys. Rev. A **70**, 043625 (2004).
[17] L. Fallani *et al.*, Phys. Rev. Lett. **93**, 140406 (2004).
[18] M. Cristiani *et al.*, Opt. Express **12**, 4 (2004).
[19] L. De Sarlo *et al.*, Phys. Rev. A **72**, 013603 (2005).
[20] B. Wu and J. Shi, arXiv:cond-mat/0607098.
[21] S. Wessel *et al.*, Phys. Rev. A **70**, 053615 (2004).
[22] V. A. Kashurnikov, N. V. Prokof'ev, and B. V. Svistunov, Phys. Rev. A **66**, 031601(R) (2002).
[23] M. Ben Dahan *et al.*, Phys. Rev. Lett. **76**, 4508 (1996).
[24] F. S. Cataliotti *et al.*, Science **293**, 843 (2001).
[25] C. D. Fertig *et al.*, Phys. Rev. Lett. **94**, 120403 (2005).
[26] J. K. Freericks and H. Monien, Phys. Rev. B **53**, 2691 (1996).
[27] B. Capogrosso-Sansone, N. V. Prokof'ev, and B. V. Svistunov, Phys. Rev. B **75**, 134302 (2007).
[28] A. Polkovnikov *et al.*, Phys. Rev. A **71**, 063613 (2005).
[29] A. Polkovnikov and D.-W. Wang, Phys. Rev. Lett. **93**, 070401 (2004).
[30] J. Ruostekoski and L. Isella, Phys. Rev. Lett. **95**, 110403 (2005).

Appendix D

Imaging the Mott Insulator Shells by Using Atomic Clock Shifts

This appendix contains a reprint of Ref. [18]: Gretchen K. Campbell, Jongchul Mun, Micah Boyd, Patrick Medley, Aaron E. Leanhardt, Luis G. Marcassa, David E. Pritchard, and Wolfgang Ketterle *Imaging the Mott Insulator Shells by Using Atomic Clock Shifts*, Sience **313**, 649 (2006).

29. L. Fu, H. Pelicano, J. Liu, P. Huang, C.-C. Lee, *Cell* **111**, 41 (2002).
30. K. Unsal-Kacmaz, T. E. Mullen, W. K. Kaufmann, A. Sancar, *Mol. Cell. Biol.* **25**, 3109 (2005).
31. T. Matsuo *et al.*, *Science* **302**, 255 (2003).
32. N. A. Krucher, L. Meije, M. H. Roberts, *Cell. Mol. Neurobiol.* **17**, 495 (1997).
33. L. E. Anderson, J. E. Morris, L. B. Sasser, R. G. Stevens, *Cancer Lett.* **148**, 121 (2000).
34. J. Hansen, *Epidemiology* **12**, 74 (2001).
35. W. J. Hrushesky, *J. Control. Release* **74**, 27 (2001).
36. G. A. Bjarnason, R. Jordan, *Prog. Cell Cycle Res.* **4**, 193 (2000).
37. www.fgsc.net/fgn47/lgi.htm.
38. S. Gery, N. Komatsu, L. Baldjyan, A. Yu, D. Koo, H. P. Koeffler, *Mol. Cell* **22**, 375 (2006).
39. Supported by grants from the NIH (MH44651 to J.C.D. and J.J.L. and R37GM34985 to J.C.D.), NSF (MCB-0084509 to J.J.L.), and the Norris Cotton Cancer Center core grant to Dartmouth Medical School. We thank R. Rothstein for yeast strain W2105-7b, S. Elledge for plasmid pMH267, and both for helpful discussions.

Supporting Online Material
www.sciencemag.org/cgi/content/full/1121716/DC1
Materials and Methods
Figs. S1 and S2
References

24 October 2005; accepted 11 May 2006
Published online 29 June 2006;
10.1126/science.1121716
Include this information when citing this paper.

Imaging the Mott Insulator Shells by Using Atomic Clock Shifts

Gretchen K. Campbell,[1]* Jongchul Mun,[1] Micah Boyd,[1] Patrick Medley,[1] Aaron E. Leanhardt,[2] Luis G. Marcassa,[1]† David E. Pritchard,[1] Wolfgang Ketterle[1]

Microwave spectroscopy was used to probe the superfluid–Mott insulator transition of a Bose-Einstein condensate in a three-dimensional optical lattice. By using density-dependent transition frequency shifts, we were able to spectroscopically distinguish sites with different occupation numbers and to directly image sites with occupation numbers from one to five, revealing the shell structure of the Mott insulator phase. We used this spectroscopy to determine the onsite interaction and lifetime for individual shells.

The Mott insulator (MI) transition is a paradigm of condensed matter physics, describing how electron correlations can lead to insulating behavior even for partially filled conduction bands. However, this behavior requires a commensurable ratio between electrons and sites. If this condition for the density is not exactly fulfilled, the system will be conductive. For neutral bosonic particles, the equivalent phenomenon is the transition from a superfluid to an insulator for commensurable densities. In inhomogeneous systems, as in atom traps, the condition of commensurability no longer applies: For sufficiently strong interparticle interactions, it is predicted that the system should separate into MI shells with different occupation number, separated by thin superfluid layers (*1*–*3*).

The recent observation of the superfluid-to-MI transition with ultracold atoms (*4*) has stimulated a large number of theoretical and experimental studies [(*5*) and references therein]. Atomic systems allow for a full range of control of the experimental parameters, including tunability of the interactions and defect-free preparation, making them attractive systems for studying condensed matter phenomena. The MI phase in ultracold atoms has been characterized by studies of coherence, excitation spectrum, noise correlations (*4*, *6*, *7*), and molecule formation (*8*). Recently, by using spin-changing collisions, Gerbier *et al*. selectively addressed lattice sites with two atoms and observed the suppression of number fluctuations (*9*).

In this study, we combined atoms in the MI phase with the high-resolution spectroscopy used for atomic clocks and used density-dependent transition frequency shifts to spectroscopically resolve the layered structure of the Mott shells with occupancies from $n = 1$ to $n = 5$ and to directly image their spatial distributions.

Bosons with repulsive interactions in an optical lattice can qualitatively be described by the Hamiltonian (*10*, *1*),

$$\hat{H} = -J\sum_{\langle i,j\rangle} \hat{a}_i^\dagger a_j + {}^1\!/_2 U\sum_i \hat{n}_i(\hat{n}_i - 1) + \sum_i (\varepsilon_i - \mu)\hat{n}_i \quad (1)$$

where the first two terms are the usual Hamiltonian for the Bose-Hubbard model, the last term adds in the external trapping potential, and J is the tunneling term between nearest neighbors, $\hat{a}_i^\dagger$ and $\hat{a}_i$ are the boson creation and destruction operators at a given lattice site. $U = (4\pi\hbar^2 a/m)\int|w(x)|^4 d^3x$ is the repulsive onsite interaction, where $\hbar$ is Planck's constant divided by 2π, m is the atomic mass, a is the s-wave scattering length, $w(x)$ is the single particle Wannier function localized to the ith lattice site, and $\hat{n}_i = \hat{a}_i^\dagger \hat{a}_i$ is the number operator for bosons at site i. The last term in the Hamiltonian is due to the external trapping confinement of the atoms, where $\varepsilon_i = V_{ext}(r_i)$ is the energy offset at the ith site due to the external confinement and μ is the chemical potential.

The behavior of this system is determined by the ratio J/U. For low lattice depths, the ratio is large and the system is superfluid. For larger lattice depths, the repulsive onsite energy begins to dominate, and the system undergoes a quantum phase transition to a MI phase. For deep lattices, the atoms are localized to individual lattice sites with integer filling factor n. This filling factor varies locally depending on the local chemical potential $\mu_i = \mu - \varepsilon_i$ as

$$n = Mod(\mu_i/U) \quad (2)$$

where *Mod* is the modulo and decreases from the center to the edge of the trap.

To prepare the atoms in the Mott insulating phase, we first created a ^{87}Rb Bose-Einstein condensate in the the $|F = 1, m_F = -1\rangle$ state (where F and m_F are the quantum numbers for the total spin and its t component, respectively) by using a combination of an Ioffe-Pritchard magnetic trap and an optical dipole trap. The optical trap was oriented perpendicular to the long axis of the magnetic trap, creating a more isotropic trapping potential that was better matched to the optical lattice. The laser beam for the optical trap had a $1/e^2$ waist ≈ 70 μm and was retroreflected. However, the polarization of the retroreflected beam was rotated such that the interference between the two beams had minimal contrast. The resulting trap had radial and axial trap frequencies of $\omega = 2\pi \times 70$ Hz and $\omega = 2\pi \times 20$ Hz, respectively, where the axial direction is now parallel to the optical trap. A three-dimensional (3D) optical lattice was created by adding two additional retroreflected laser beams derived from the same laser at $\lambda = 1064$ nm. The lattice was adiabatically ramped up by rotating the polarization of the retroreflected optical trapping beam to increase the interference contrast along that axis and by increasing the laser power in the other two axes. The lattice depth was increased by using an exponential ramp with a 40-ms time constant. After ramping on the lattice, all three beams were linearly polarized orthogonal to each other and

[1]MIT-Harvard Center for Ultracold Atoms, Research Laboratory of Electronics, Department of Physics, Massachusetts Institute of Technology, Cambridge, MA 02139, USA. [2]JILA, Boulder, CO 80309, USA.

*To whom correspondence should be addressed. E-mail: gcampbel@mit.edu
†Permanent address: Instituto de Fisica de São Carlos, University of São Paulo, São Paulo 13560-970, Brazil.

had different frequency detunings generated by using acousto-optic modulators. The lattice depth was up to $40E_{rec}$, where $E_{rec} = \hbar^2k^2/2m$ is the recoil energy and $k = 2\pi/\lambda$ is the wave vector of the lattice light. At $40E_{rec}$, the lattice trap frequency at each site was $\omega_{lat} = 2\pi \times 25$ kHz, and the external trap frequencies increased to $\omega = 2\pi \times 110$ Hz and $\omega = 2\pi \times 30$ Hz in the radial and axial directions, respectively.

Zeeman shifts and broadening of the clock transition from the $F = 1$ to the $F = 2$ state were avoided by using a two photon transition between the $|1, -1\rangle$ state and the $|2, 1\rangle$ state, where at a magnetic bias field of ~ 3.23 G both states have the same first-order Zeeman shift (*11*). The two-photon pulse was composed of one microwave photon at a fixed frequency of 6.83 GHz and one radio frequency (rf) photon at a frequency of around 1.67 MHz. The pulse had a duration of 100 ms, and when on resonance the fraction of atoms transferred to the $|2, 1\rangle$ state was less than 20%. After the pulse, atoms in the $|2, 1\rangle$ state were selectively detected with absorption imaging by using light resonant with the $5^2S_{1/2}|2, 1\rangle \rightarrow 5^2P_{3/2}|3, 1\rangle$ transition. For observing the spatial distribution of the Mott shells, we imaged the atoms in the trap. For recording spectra, we released the atoms from the trap and imaged them after 3 ms of ballistic expansion in order to reduce the column density.

When the two-photon spectroscopy is performed on a trapped condensate without a lattice, the atoms transferred to the $|2, 1\rangle$ state have a slightly different mean field energy because of the difference between a_{21} and a_{11} scattering lengths, where a_{21} is the scattering length between two atoms in states $|2, 1\rangle$ and $|1, -1\rangle$ and a_{11} is the scattering length between two atoms in the $|1, -1\rangle$ state. This difference in scattering lengths leads to a density-dependent shift to the resonance frequency, $\Delta\nu \propto \rho(a_{21} - a_{11})$, where ρ is the condensate density (*11*). This collisional shift is commonly referred to as the clock shift (*12*) because of its importance in atomic clocks, where cold collisions currently limit the accuracy (*13*, *14*). When performed on a condensate with peak density ρ_0 in a harmonic trap in the limit of weak excitation, the line shape for the two-photon resonance is given by (*15*):

$$I(\nu) = \frac{15h(\nu - \nu_0)}{4\rho_0\Delta E}\sqrt{1 - \frac{h(\nu - \nu_0)}{\rho_0\Delta E}} \quad (3)$$

where ν_0 is the hyperfine transition frequency and the mean field energy difference is

$$\Delta E = \frac{h^2}{\pi m}(a_{21} - a_{11}) \quad (4)$$

In the case of ^{87}Rb, $a_{21} = 5.19$ nm and $a_{11} = 5.32$ nm (*16*). Both the frequency shift and the linewidth increase with the condensate density. As the lattice is ramped on, the peak density of the condensate in a given lattice site increases as

$$\rho_0(r) = \left(\mu - {}^1\!/_2\, m\omega_{trap}^2 r^2\right)1/U \quad (5)$$

where ω_{trap} is the external trap frequency for the combined magnetic and optical trap, and, by using the Thomas-Fermi approximation μ, the chemical potential, is given by

$$\mu = \left[{}^{15}\!/_{16}\,\frac{(\lambda/2)^3 m^{3/2} NU\omega_{trap}^3}{\sqrt{2}\pi}\right]^{2/5} \quad (6)$$

where N is the total atom number. For low lattice depths, the system is still a superfluid, delocalized over the entire lattice. However, the two-photon resonance line is shifted and broadened because of the increased density, with the center of the resonance at $\nu = \nu_0 + 2\rho_0\Delta E/3h$. For deep lattices in the MI regime, the repulsive onsite interaction dominates, number fluctuations are suppressed, and each lattice site has a sharp resonance frequency determined by the occupation number in the site. The separation between

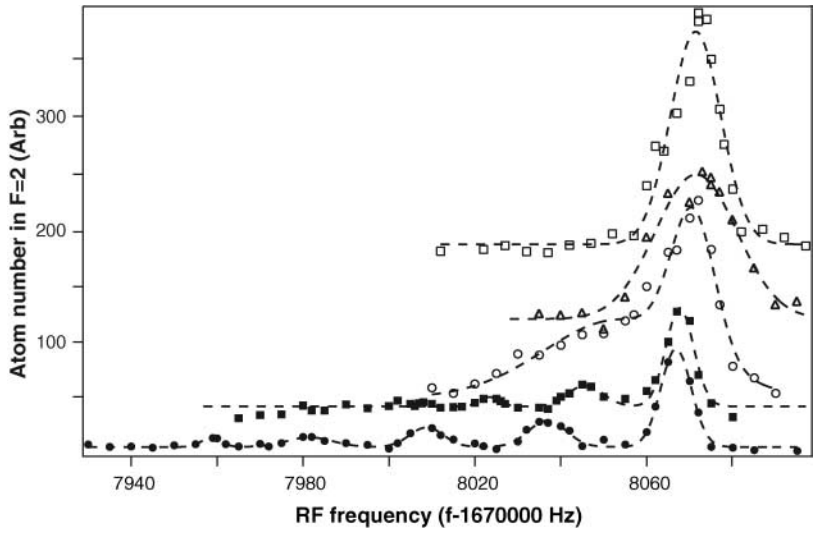

Fig. 1. Two-photon spectroscopy across the superfluid-to-MI transition. Spectra for 3D lattice depths of $0E_{rec}$ (open squares), $5E_{rec}$ (open triangles), $10E_{rec}$ (open circles), $25E_{rec}$ (solid squares), and $35E_{rec}$ (solid circles) are shown. The spectra are offset for clarity. The shift in the center of the $n = 1$ peak as the lattice depth is increased is due to the differential AC Stark shift from the lattice. The dotted lines show Gaussian fits of the peaks.

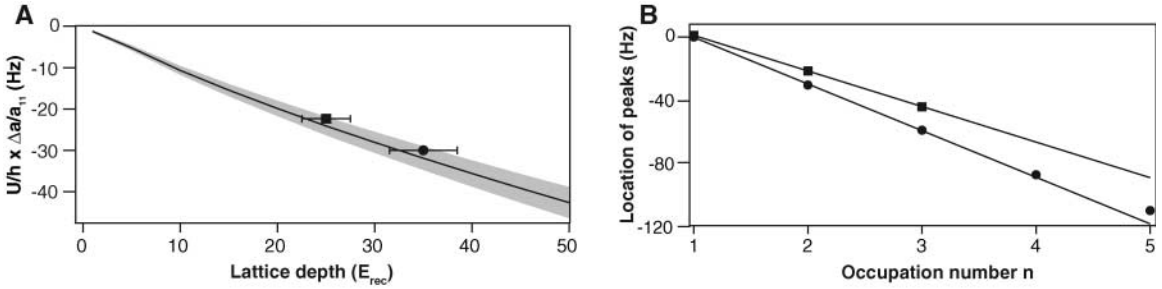

Fig. 2. Probing the onsite interaction energy. (**A**) The separation between the $n = 1$ and $n = 2$ peaks is shown for lattice depths of $V = 25E_{rec}$ (square) and $V = 35E_{rec}$ (circle). As the lattice depth was increased, the separation increased from 22(1) Hz to 30(1) Hz. The shaded area gives the expected value determined from a band structure calculation, including the uncertainty in the scattering lengths. The uncertainty in the measured separation is indicated by the size of the points. (**B**) Location of resonances for all MI phases relative to the $n = 1$ phase for $V = 25E_{rec}$ and $V = 35E_{rec}$. For low site occupation (n values from 1 to 3), the separation between the resonances is roughly constant, implying constant U. For $V = 35E_{rec}$, the separation between the $n = 4$ and $n = 5$ peaks was 22(2) Hz, a 27% decrease from the 30(1) Hz separation between the $n = 1$ and $n = 2$ peaks. The slope of the lines is fit to the separation between the $n = 1$ and $n = 2$ peaks.

the resonance frequencies for the n and $n - 1$ MI phases is given by

$$\delta\nu = \frac{U}{h}(a_{21} - a_{11})/a_{11} \qquad (7)$$

The linewidth of the resonances is no longer broadened by the inhomogeneous density and should be limited only by the bandwidth of the two-photon pulse.

The resonance transitioned from a broadened line to several sharp lines as the lattice depth was increased (Fig. 1). At a lattice depth of $V = 5E_{rec}$, the line was broadened and the line center was shifted slightly because of the increased density. At $V = 10E_{rec}$, the line was shifted and broadened further, and in addition the line shape became asymmetric as the atom number in lattice sites with small occupation was squeezed. For deeper lattice depths, the system underwent a phase transition to a MI phase, and discrete peaks appeared, corresponding to MI phases with different filling factors; for $V = 35E_{rec}$, MI phases with occupancies of up to five were observed.

When the lattice depth was increased inside the MI regime (from $V = 25E_{rec}$ to $V = 35E_{rec}$), the separation between the resonance peaks increased, presumably because of the larger onsite interaction energy as the lattice trap was increased. As given in Eq. 7, the separation between the peaks provides a direct measurement of the onsite interaction energy, U. Our results are in good agreement with calculated values of U (Fig. 2A). Although the separation between the $n = 1$, $n = 2$, and $n = 3$ peaks is roughly constant, for higher filling factors the separation between the peaks decreases; the effective onsite interaction energy becomes smaller for higher filling factors (Fig. 2B). This result shows that for low occupation numbers the atoms occupy the ground state wave function of the lattice site, whereas for larger occupation numbers, the repulsive onsite interaction causes the wave function to spread out, lowering the interaction energy. From a variational calculation of the wave function similar to (*17*), we find that the onsite energy for the $n = 5$ shell should be ~20% smaller than that for the $n = 1$ shell, in agreement with the measured value (Fig. 2B).

The peaks for the different occupation numbers were spectrally well separated. Therefore, on resonance, only atoms from a single shell were transferred to the $|2, 1\rangle$ state. An image of these atoms (without any time of flight) shows the spatial distribution of this shell. Figure 3B shows absorption images for $n = 1$ to $n = 5$ shells. As predicted (*1*), the $n = 1$ MI phase appears near the outer edge of the cloud. For larger n, the radius of the shell decreases, and the $n = 5$ sites form a core in the center of the cloud. The expected radius for each shell was obtained from Eq. 2 by using the measured values for the onsite interaction. The observed radii were in good agreement except for the $n = 1$ shell, which may have been affected by anharmonicities in the external trap. Absorption images taken with rf values between the peaks show a small signal, which may reflect the predicted thin superfluid layers between the insulating shells; however, this needs be studied further with improved signal-to-noise ratio. The expected absorption image of a shell should show a column density with a flat distribution in the center and raised edges. However, because of limitations (resolution and residual fringes) in our imaging system, these edges were not resolved.

Because we were able to address the different MI phases separately, we could determine the lifetime for each shell. For this, the atoms were first held in the lattice for a variable time τ before applying the 100-ms two-photon pulse. For the $n = 1$ MI phase and ignoring technical noise, the lifetime should only be limited by spontaneous scattering from the lattice beams. Even for the deepest lattices, the spontaneous scattering rate is less than 10^{-2} Hz. For the $n = 2$ MI phase, the lifetime is limited by dipolar relaxation, which for ^{87}Rb is slow, with a rate $< 10^{-2}$ Hz. For sites with $n \geq 3$, the lifetime is limited by three-body recombination with a rate equal to $\gamma n(n - 1)(n - 2)$ (*18*), with $\gamma = 0.026$ Hz for our parameters. This gives three-body lifetimes of τ_{3B} of 6.2 s, 1.6 s, and 0.6 s for the $n = 3$, $n = 4$, and $n = 5$ MI phases, respectively. This calculation of γ assumes for the density distribution the ground state of the harmonic oscillator potential, so for higher filling factors the actual lifetime could be higher. We

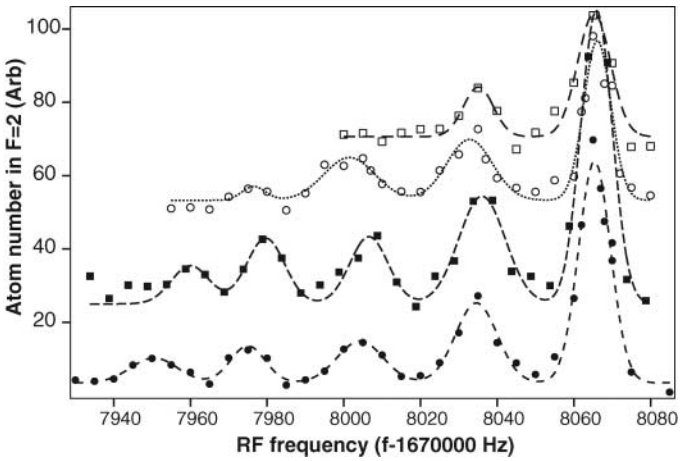

Fig. 4. Lifetime of individual MI shells. The lifetime for each MI phase can be measured independently by adding a hold time before applying the two-photon pulse. Spectra are shown for hold times of 0 ms (solid circles), 100 ms (solid squares), 400 ms (open circles), and 2000 ms (open squares). The lattice depth was $V = 35E_{rec}$ except for the 100-ms hold time, for which it was $V = 34E_{rec}$. The lines show Gaussian fits to the peaks, and the spectra were offset for clarity.

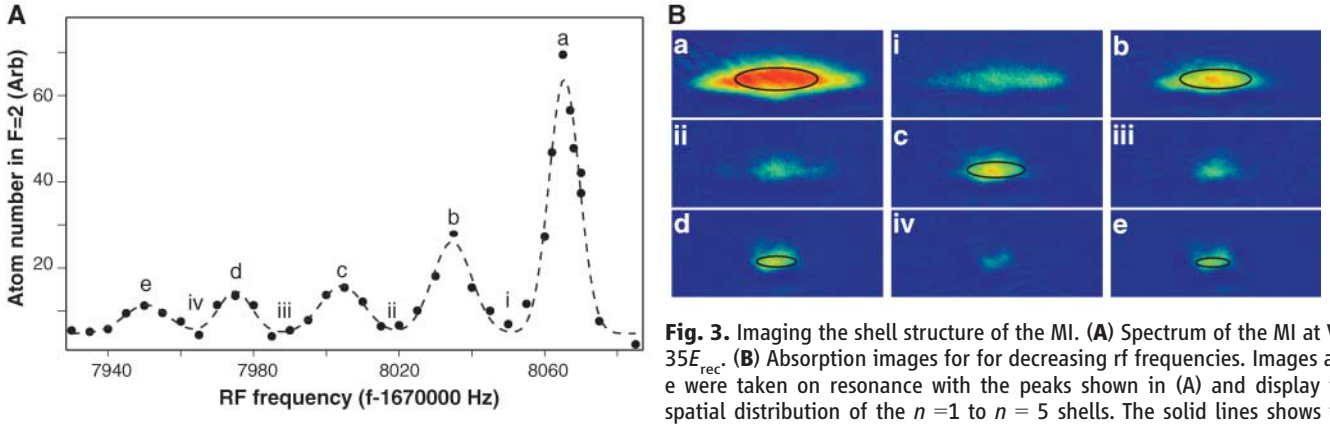

Fig. 3. Imaging the shell structure of the MI. (**A**) Spectrum of the MI at $V = 35E_{rec}$. (**B**) Absorption images for for decreasing rf frequencies. Images a to e were taken on resonance with the peaks shown in (A) and display the spatial distribution of the $n = 1$ to $n = 5$ shells. The solid lines shows the predicted contours of the shells. Absorption images taken for rf frequencies between the peaks (images i to iv) show a much smaller signal. The field of view was 185 μm by 80 μm.

show relative populations as a function of the hold time and derive lifetimes as τ almost equal to 1 s, 0.5 s, and 0.2 s for the $n = 3$, $n = 4$, and $n = 5$ MI phases, respectively (Fig. 4); this is shorter than predicted, which is possibly due to secondary collisions. For $n = 1$ and $n = 2$, lifetimes of over 5 s were observed.

We expect that this method can be used to measure the number statistics as the system undergoes the phase transition. One would expect that the spectral peaks for higher occupation number become pronounced only at higher lattice depth; an indication of this can be seen already in Fig. 1. For low lattice depths, the tunneling rate is still high, but one can suddenly increase the lattice depth and freeze in populations (*19*), which can then be probed with high-resolution spectroscopy. Fluctuations in the atom number could identify the superfluid layers between the Mott shells. In addition, by applying a magnetic gradient across the lattice, tomographic slices could be selected, combining full 3D resolution with spectral resolution of the site occupancy. These techniques may address questions about local properties that have been raised in recent theoretical simulations (*20*). The addressability of individual shells could be used to create systems with only selected occupation numbers (e.g., by removing atoms in other shells). Such a preparation could be important for the implementation of quantum gates, for which homogenous filling is desirable. For atoms other than rubidium, atomic clock shifts are much larger, e.g., for sodium, larger by a factor of 30. Therefore, it should be easier to resolve the MI shells, unless the collisional lifetime of the upper state of the clock transition sets a severe limit to the pulse duration.

Note added in proof: After submission of this work, the vertical profile of an $n = 2$ MI shell was obtained by using spin-changing collisions and a magnetic resonance imaging technique (*21*).

References and Notes

1. D. Jaksch, C. Bruder, J. I. Cirac, C. W. Gardiner, P. Zoller, *Phys. Rev. Lett.* **81**, 3108 (1998).
2. G. G. Batrouni *et al.*, *Phys. Rev. Lett.* **89**, 117203 (2002).
3. B. Marco, C. Lannert, S. Vishveshwara, T. C. Wei, *Phys. Rev. A.* **71**, 063601 (2005).
4. M. Greiner, O. Mandel, T. Esslinger, T. W. Hänsch, I. Bloch, *Nature* **415**, 39 (2002).
5. I. Bloch, *Nature Phys.* **1**, 23 (2005).
6. T. Stöferle, H. Moritz, C. Schori, M. Köhl, T. Esslinger, *Phys. Rev. Lett.* **92**, 130403 (2004).
7. S. Fölling *et al.*, *Nature* **434**, 481 (2005).
8. T. Volz *et al.*, published online 8 May 2006 (http://arxiv.org/abs/cond-mat?papernum=0605184).
9. F. Gerbier, S. Fölling, A. Widera, O. Mandel, I. Bloch, *Phys. Rev. Lett.* **96**, 090401 (2006).
10. M. P. A. Fisher, P. B. Weichman, G. Grinstein, D. S. Fisher, *Phys. Rev. B* **40**, 546 (1989).
11. D. M. Harber, H. J. Lewandowski, J. M. McGuirk, E. A. Cornell, *Phys. Rev. A.* **66**, 053616 (2002).
12. K. Gibble, S. Chu, *Phys. Rev. Lett.* **70**, 1771 (1993).
13. C. Fertig, K. Gibble, *Phys. Rev. Lett.* **85**, 1622 (2000).
14. Y. Sortais *et al.*, *Phys. Scr.* **T95**, 50 (2001).
15. J. Stenger *et al.*, *Phys. Rev. Lett.* **82**, 4569 (1999).
16. E. G. M. van Kempen, S. J. J. M. F. Kokkelmans, D. J. Heinzen, B. J. Verhaar, *Phys. Rev. Lett.* **88**, 093201 (2002).
17. G. Baym, C. J. Pethick, *Phys. Rev. Lett.* **76**, 6 (1996).
18. M. W. Jack, M. Yamashita, *Phys. Rev. A* **67**, 033605 (2005).
19. M. Greiner, O. Mandel, T. W. Hänsch, I. Bloch, *Nature* **419**, 51 (2002).
20. O. Gygi, H. G. Katzgraber, M. Troyer, S. Wessel, G. G. Batrouni, *Phys. Rev. A.* **73**, 063606 (2006).
21. S. Fölling, A. Widera, T. Mueller, F. Gerbier, I. Bloch, published online 23 June 2006 (http://arxiv.org/abs/cond-mat?papernum=0606592).

22. The authors thank I. Bloch and S. Fölling for insightful discussions. This work was supported by NSF. L.G.M. also acknowledges support from Fundação de Apoio a Pesquisa do Estrado de São Paulo.

23 May 2006; accepted 7 July 2006
10.1126/science.1130365

Evidence for a Past High-Eccentricity Lunar Orbit

Ian Garrick-Bethell,* Jack Wisdom, Maria T. Zuber

The large differences between the Moon's three principal moments of inertia have been a mystery since Laplace considered them in 1799. Here we present calculations that show how past high-eccentricity orbits can account for the moment differences, represented by the low-order lunar gravity field and libration parameters. One of our solutions is that the Moon may have once been in a 3:2 resonance of orbit period to spin period, similar to Mercury's present state. The possibility of past high-eccentricity orbits suggests a rich dynamical history and may influence our understanding of the early thermal evolution of the Moon.

The Moon is generally thought to have accreted close to the Earth and migrated outwards in a synchronously locked low-eccentricity orbit. During the early part of this migration, the Moon was cooling and continually subjected to tidal and rotational stretching. The principal moments of inertia $A < B < C$ of any satellite are altered in a predictable way by deformation due to spin and tidal attraction. The moments are typically characterized by ratios that are easier to measure, namely, the libration parameters $\beta = (C - A)/B$ and $\gamma = (B - A)/C$, and the degree-2 spherical-harmonic gravity coefficients $C_{20} = (2C - B - A)/(2Mr^2)$ and $C_{22} = (B - A)/(4Mr^2)$, where M and r are the satellite mass and radius. Of these four values β, γ, and C_{20} can be taken as independent. Using the ratio $(C - A)/A$, Laplace was the first to observe that the lunar moments are not in equilibrium with the Moon's current orbital state (*1*). He did not, however, address the possibility of a "fossil bulge," or the frozen remnant of a state when the Moon was closer to the Earth. Sedgwick examined the lunar moments in 1898, as did Jeffreys in 1915 and 1937, and both authors effectively showed that β is too large for the current orbit, suggesting that the Moon may carry a fossil bulge (*2*–*5*). However, Jeffreys showed that the fossil hypothesis might be untenable because the ratio of $\gamma/\beta = 0.36$ does not match the predicted ratio of 0.75 for a circular synchronous orbit (equivalently, $C_{20}/C_{22} = 9.1$, instead of the predicted ratio of 3.33). Indeed, using data from (*6*), none of the three independent measures of moments represent a low-eccentricity synchronous-orbit hydrostatic form; $C_{20} = 2.034 \times 10^{-4}$ is 22 times too large for the current state, and $\beta = 6.315 \times 10^{-4}$ and $\gamma = 2.279 \times 10^{-4}$ are 17 and 8 times too large, respectively (*7*, *8*).

The inappropriate ratio of γ/β or C_{20}/C_{22} has led some to dismiss the fossil bulge hypothesis as noise due to random density anomalies (*9*, *10*). However, the power of the second-degree harmonic gravity field is anomalously high when compared to the power expected from back extrapolating the power of higher harmonics (*7*, *11*). This suggests that the bulge may be interpreted as a signal of some process. Degree-2 mantle convection has been proposed as a means of deforming the Moon (*12*, *13*), but the dissimilarity of all three principal moments violates the symmetry of any simple degree-2 convection model (*12*). The Moon's center-of-mass/center-of-figure offset influences the moment parameters slightly, but that problem is geophysically separate and mathematically insignificant to the degree-2 problem (*8*, *14*).

Because C_{20} is due primarily to rotational flattening, and C_{22} is due to tidal stretching, the high C_{20}/C_{22} ratio seems to imply that the Moon froze in its moments while rotating faster than synchronous. However, in such cases no constant face would be presented to the Earth for any C_{22} power to form in a unique lunar axis. This apparent dilemma can be avoided by considering that in any eccentric orbit with an orbit period to spin period ratio given by n:2, with $n = 2, 3, 4, \ldots$, the passage through pericenter results in higher C_{22} stresses throughout a single elongated axis (hereafter called the pericenter axis). When the stresses experienced over one orbit period are time-averaged, the highest stresses

Department of Earth, Atmospheric and Planetary Sciences, Massachusetts Institute of Technology, 77 Massachusetts Avenue, Cambridge, MA 02139, USA.

*To whom correspondence should be addressed. E-mail: iang@mit.edu

Appendix E

Parametric Amplification of Scattered Atom Pairs

This appendix contains a reprint of Ref. [19]: Gretchen K. Campbell, Jongchul Mun, Micah Boyd, Erik W. Streed, Wolfgang Ketterle, and David E. Pritchard *Parametric Amplification of Scattered Atom Pairs*, Physical Review Letters **96**, 020406 (2006).

Parametric Amplification of Scattered Atom Pairs

Gretchen K. Campbell, Jongchul Mun, Micah Boyd, Erik W. Streed, Wolfgang Ketterle, and David E. Pritchard*

MIT-Harvard Center for Ultracold Atoms, Research Laboratory of Electronics and Department of Physics, Massachusetts Institute of Technology, Cambridge, Massachusetts 02139, USA

(Received 12 September 2005; published 19 January 2006)

We have observed parametric generation and amplification of ultracold atom pairs. A ^{87}Rb Bose-Einstein condensate was loaded into a one-dimensional optical lattice with quasimomentum k_0 and spontaneously scattered into two final states with quasimomenta k_1 and k_2. Furthermore, when a seed of atoms was first created with quasimomentum k_1 we observed parametric amplification of scattered atoms pairs in states k_1 and k_2 when the phase-matching condition was fulfilled. This process is analogous to optical parametric generation and amplification of photons and could be used to efficiently create entangled pairs of atoms. Furthermore, these results explain the dynamic instability of condensates in moving lattices observed in recent experiments.

DOI: 10.1103/PhysRevLett.96.020406 PACS numbers: 03.75.Kk, 03.75.Lm, 05.45.−a

Nonlinear atom optics is a novel research area born with the advent of Bose-Einstein condensates of alkali atoms [1]. Unlike photons, ultracold atoms have a very strong nonlinearity directly provided by s-wave collisions, and therefore they do not need a nonlinear medium to provide effective interaction. A number of nonlinear processes first observed with photons have been demonstrated with matter waves such as four-wave mixing [2,3], solitons [4–7], second-harmonic generation [8–11], and sum-frequency generation [9]. Nonlinear atom optics, and, in particular, four-wave mixing, has previously been suggested as an ideal way to create entangled pairs of atoms [3,12,13]. However, in previous four-wave mixing experiments [2,3] using condensates in free space, the quadratic dispersion relation for free particles only allowed for the phase-matching condition to be fulfilled when the magnitudes of all four momenta were equal (in the center-of-mass frame). This is the only way in which two particles can scatter off each other and conserve energy and momentum. In particular, in free space, if a condensate is moving with momentum k_0, atoms within the condensate cannot elastically scatter into different momentum states, and therefore the analog to optical parametric generation of photons is not possible.

The situation is very different when an optical lattice is added. The lattice delivers energy in the form of the ac Stark effect and momentum in units of $2\hbar k_L$ to the atoms, where k_L is the wave vector of the optical lattice. The motion of atoms in this periodic potential is described by a band structure, which deviates from the quadratic free particle dispersion curve. In a lattice, as recently suggested [14], it becomes possible for two atoms in the condensate to collide and scatter into a higher and lower quasimomentum state and conserve energy. As we discuss below, this can lead to dynamic instabilities of the condensate, but also enables nondegenerate four-wave mixing and the atom-optics analog of optical parametric generation.

Phase matching is essential for high efficiency in nonlinear processes in quantum optics including optical parametric generation of photons [15], and a modification of the dispersion curve has been used to demonstrate optical parametric amplification in semiconductor microcavities [16]. In atom optics, dispersion management was used to modify the effective mass of atoms [17], and to create bright gap solitons [18]. Here we demonstrate that by modifying the dispersion curve using an optical lattice, scattering processes which cannot occur in free space become possible, and we realize the matter-wave analogue of an optical parametric generator (OPG) and an optical parametric amplifier (OPA).

To demonstrate the matter-wave analogue of an OPG, a ^{87}Rb Bose-Einstein condensate with quasimomentum k_0 was loaded into a one-dimensional optical lattice. To load the atoms at a given quasimomentum relative to the Brillouin zone, a moving optical lattice was adiabatically applied to a magnetically trapped condensate initially at rest in the lab frame. The lattice was created using two counter-propagating laser beams with frequency difference $\delta\nu$, giving the lattice a velocity of $v = \frac{\lambda}{2}\delta\nu$, where λ is the wavelength of the optical lattice. In the rest frame of the lattice, the condensate has quasimomentum $k_0 = \frac{m\lambda}{2\hbar}\delta\nu$, where m is the atomic mass. By changing the detuning between the lattice beams, $\delta\nu$, k_0 could be varied. As shown in Fig. 1(d), as the value of k_0 was varied we observed elastic scattering of atom pairs into final states k_1 and k_2. The range of possible final states varied with k_0 due to the phase-matching condition. For values of k_0 less than $\approx 0.55k_L$ the dispersion relation imposed by the Bloch structure of the optical lattice does not allow elastic scattering to occur. For our lattice depth of $V = 0.5E_{\mathrm{rec}}$, where $E_{\mathrm{rec}} = \hbar^2k_L^2/2m$, the values of k_2 which satisfied energy and momentum conservation were beyond the first Brillouin zone. Since the scattering process occurs within the first Bloch band, the atoms in state k_2 have a quasimomentum $k_2 = (2k_0 - k_1)\mathrm{Mod}\,(2k_L)$ [see Fig. 1(a)]. As the value for $\delta\nu$ (and the resulting value of k_0) is increased, the separation between k_0 and the allowed states k_1 and k_2 decreases as is clearly observed in Fig. 1(d). For values of

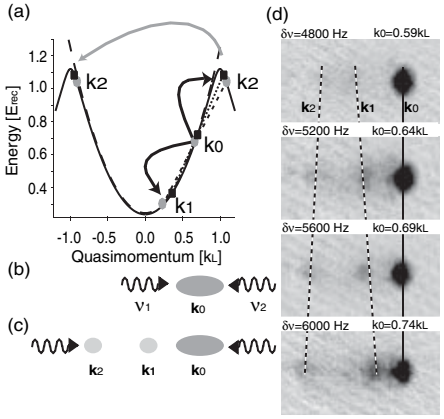

FIG. 1. Dispersion curve for the optical lattice and experimental setup. (a) Band structure for a lattice depth of $V = 0.5E_{\mathrm{rec}}$. The dashed line shows the free particle dispersion curve. The dispersion relation of the lattice allows two atoms with momentum k_0 to elastically scatter into the final momentum states k_1 and k_2. Energy and quasimomentum are conserved when k_0 is the average of k_1 and k_2 and the three points on the dispersion curve lie on a straight line. If k_0 is varied, the allowed values for k_1 and k_2 change. For values of k_0 below $\approx 0.55k_L$, where k_L is the wave vector of the optical lattice, atoms cannot scatter elastically into different momentum states. The circles (squares) show allowed states k_0, k_1, k_2 for $k_0 = 0.66k_L$ ($0.70k_L$). As k_0 is increased, the final momentum states move closer together. Since the scattering occurs within the lowest band of the lattice, the final momentum is $k_2 = (2k_0 - k_1)\mathrm{Mod}\,(2k_L)$. (b) A ^{87}Rb Bose-Einstein condensate is illuminated by two counter-propagating laser beams with detuning $\delta\nu$, which create a moving optical lattice. The condensate is initially held at rest. In the rest frame of the lattice, the condensate has quasimomentum $k_0 = \frac{m\lambda}{2\hbar}\delta\nu$. (c) As k_0 was varied, we observed elastic scattering into states k_1 and k_2. (d) Absorption images for different lattice detunings, $\delta\nu$, showing parametric generation. After ramping up the lattice, the atoms were held for 10 ms at a constant lattice depth. They were then released from the trap and imaged after 43 ms of ballistic expansion. The field of view is 0.5 mm $\times$ 0.3 mm.

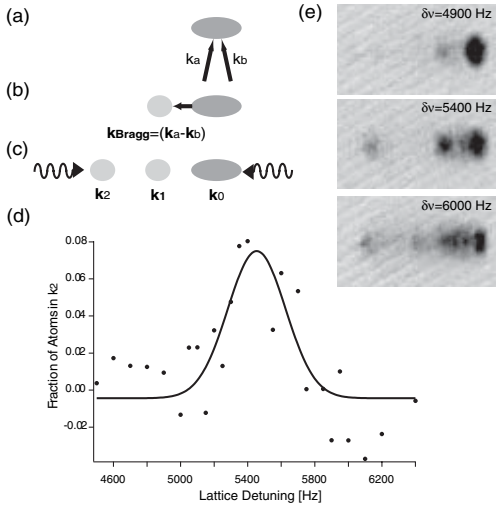

FIG. 2. Parametric amplification of scattered atom pairs in a 1D optical lattice. (a) First, a 2 ms Bragg pulse was applied to the condensate. (b) The Bragg pulse seeded atoms along the long axis of the condensate with momentum $k_{\mathrm{Bragg}} = (k_a - k_b)$ in the lab frame. (c) The optical lattice was then adiabatically ramped on and applied for 10 ms. When the phase-matching condition was fulfilled, parametric amplification of atoms in the seeded state k_1 and its conjugate momentum state k_2 was observed. (d) Resonance curve showing amplification of k_2, when k_1 was seeded. Amplification occurred only when the phase-matching condition was met. For a fixed k_{Bragg}, the resonance condition was found by varying the detuning $\delta\nu$ of the lattice. The data was taken for $k_{\mathrm{Bragg}} = 0.43k_L$. The fraction of amplified atoms was obtained by subtracting images with and without the seed pulse. (e) Absorption images showing amplification of k_1 and k_2 when the phase-matching condition is met. The center of the resonance was at $\delta\nu \approx 5450$ Hz, close to the calculated value of $\delta\nu \approx 5350$ Hz. The width of the resonance is determined by the Fourier width of the Bragg pulse. Most of the scattered atoms in the third image were independent of the seed pulse.

k_0 above $\approx 0.75k_L$, the final momentum states were no longer distinguishable, and the condensate became unstable.

To demonstrate the matter-wave analogue of an OPA, we first created a small seed of atoms with quasimomentum k_1 before ramping on the moving lattice (see Fig. 2). To create the seed we applied a Bragg pulse to the magnetically trapped condensate, outcoupling a small fraction of atoms into the momentum state k_{Bragg} [19]. Immediately after applying the pulse, the optical lattice was adiabatically ramped on. In the rest frame of the lattice, the seed has quasimomentum $k_1 = k_{\mathrm{Bragg}} + k_0$. The phase-matching condition for a given seed k_{Bragg} was found by varying the frequency difference $\delta\nu$ of the lattice, and therefore the quasimomenta k_0 and k_1 of the atoms. As shown in Fig. 2(d), when the phase-matching condition was fulfilled, we observed amplification of the seed k_1 as well as its conjugate momentum k_2. The growth of k_1 and k_2 as a function of time are shown in Fig. 3.

The experiments were performed using an elongated ^{87}Rb condensate created in a magnetic trap previously described in Ref. [20]. The magnetic trap had a radial (axial) trap frequency of 35(8) Hz. The condensate, containing between 0.5–3.0 $\times 10^5$ atoms, was produced in the $|5^2S_{1/2}, F = 1, m_F = -1\rangle$ state. The Bragg pulse was created with two laser beams derived from the same laser, which was red detuned from the $5^2S_{1/2}, F = 1 \rightarrow 5^2P_{3/2}, F = 1$ transition at $\lambda = 780$ nm by 400 MHz, and was π polarized. As shown in Fig. 2, the Bragg beams were aligned such that atoms were outcoupled along the long axis of the condensate. The intensity of the Bragg pulse was chosen such that less than 5% of the initial condensate was outcoupled into k_{Bragg}, and the length of the pulse was 2 ms. The angle between the Bragg beams could be varied to change the momentum of the outcoupled atoms. The optical lattice was created using two counter-

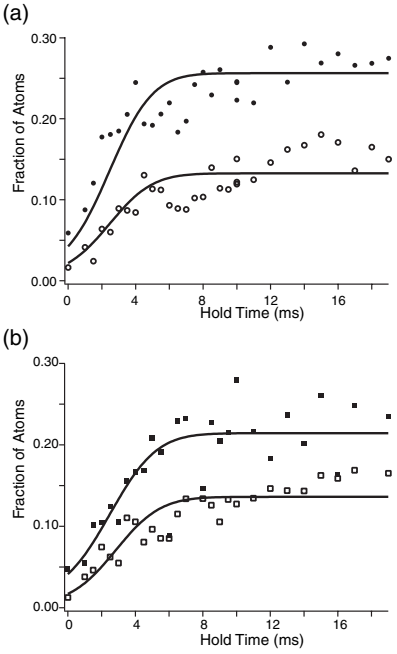

FIG. 3. Growth curve for atomic population in quasimomentum states k_1 and k_2 when the process was seeded. (a) Amplification of atoms with quasimomentum k_1 (solid points), and with the conjugate momentum k_2 (open points), when state k_1 was seeded. (b) Amplification of atoms in k_1 (solid points), and k_2 (open points), when k_2 was seeded. The values for k_0, k_1, k_2 were $0.66k_L$, $0.23k_L$, and $-0.92k_L$ respectively. The solid lines shows the expected gain using Eq. (1) with variable scale factors for each curve as the only free parameters.

propagating beams derived from the same laser with $\lambda = 1064$ nm, and the frequency of the two beams were controlled by two separate acousto-optic modulators (AOMs) driven with a frequency difference $\delta\nu$. The lattice was also aligned along the long axis of the condensate, and was ramped on in 1 ms using an exponential ramp. After the condensate was held in the lattice for a variable time τ it was then released from the trap and imaged after 43 ms of ballistic expansion.

For all of our experiments, the depth of the optical lattice was $V = 0.5E_{\mathrm{rec}}$ with a band structure shown in Fig. 1. When the process was not seeded, atoms were elastically scattered into a narrow band of states k_1 and k_2, where both energy and momentum were conserved. However, the population in neither state was large enough for amplification to be observed. When the process was seeded, amplification occurred when the quasimomentum was tuned such that energy and momentum were conserved for the states k_0, k_1, and the conjugate momentum k_2. In our experiment, the difference $\Delta k = k_0 - k_1$ between the quasimomenta of the condensate k_0 and seed k_1 was set by the angle of the initial Bragg pulse. For a given Bragg angle, there is only one set of quasimomenta k_0, k_1, and k_2 where the phase-matching condition is fulfilled. To find this point, we varied the velocity of the moving lattice for fixed hold times. Results for $k_{\mathrm{Bragg}} = 0.43k_L$ are shown in Fig. 2. The phase-matched value for k_2 is at $1.08k_L$, beyond the boundary of the first Briollouin zone. Therefore, the atoms are observed with a momentum $k_2 = -0.92k_L$. For $k_{\mathrm{Bragg}} = 0.43k_L$, $0.34k_L$, and $0.28k_L$, we observed resonances at $\delta\nu = 5450$ Hz, 5750 Hz, and 6100 Hz, respectively. For these Bragg angles and our lattice depth, the expected values were 5350 Hz, 5700 Hz, and 6050 Hz.

In Fig. 3, 5% of the initial condensate containing $N_0 = 1.3(3) \times 10^5$ atoms was outcoupled with $k_{\mathrm{Bragg}} = 0.43k_L$. The gain for the process is determined by the strength of the nonlinear interaction $U = \frac{4\pi\hbar^2 a}{m}$ between atoms in the condensate, where a is the s-wave scattering length. We can estimate the maximum amplification rate to be $\eta = 2n_0U/\hbar$ [3], with $\dot{N}_{1(2)} = \eta N_{2(1)}$, where $N_{1(2)}$ is the number of atoms in the momentum state $k_{1(2)}$, and n_0 is the condensate density. For $N_0 = 1.3(3) \times 10^5$, the maximum growth rate should be $\eta = 540$ Hz. The amplification rate will decrease as the state k_0 is depleted. However, for our small seeds, the amplification was limited by the loss of overlap between the condensate and the amplified pulses. The Thomas-Fermi radius (R_{TF}) of the condensate in the axial direction was 33 μm, and the recoil velocity (v_{rec}) for the final states k_1 and k_2 with respect to the initial condensate was $v_{\mathrm{rec}} = 1.8$ μm/ms and 6.8 μm/ms, respectively. The overlap integral between the amplified atoms and the initial condensate can be approximated as a Gaussian with time constant $\tau_c \approx 0.75R_{\mathrm{TF}}/v_{\mathrm{rec}}$, which for our parameters is 3.75 ms. We compare our results to the modified rate equation

$$\dot{N}_{2(1)} = \eta N_{1(2)} e^{-t^2/\tau_c^2}. \quad (1)$$

Since atoms are scattered into states k_1 and k_2 in pairs, one would expect that the final atom number in the two states (minus the initial seed) are equal. Instead, we observe a smaller number in state k_2 which we ascribe to the proximity of k_2 to the boundary of Brillouin zone. This leads to instabilities, where atoms in state k_2 are scattered into other momentum states or into higher bands. If we allow a variable scale factor in our model to correct for the loss of atoms in N_2, as shown in Fig. 3, the gain for $N_{1,2}$ is in agreement with the experimental data.

Amplification was also observed when atoms were seeded in state k_2. Because of the geometry of our experimental setup, we were unable to load atoms directly into $k_2 = -0.92k_L$. However when atoms with quasimomentum $k = 1.08k_L$ were loaded into the lattice, the ramp-up was no longer adiabatic due to their proximity to the boundary of the first Brillouin zone. Because of this, atoms from the seed were loaded into both the second Bloch band (with $k = 1.08k_L$) and the ground state (with $k = -0.92k_L = k_2$). As shown in Fig. 3(b), the gain for this process was almost identical to when atoms were seeded in state k_1.

The loss of overlap could be alleviated by using a more extreme trap geometry in which the condensate is more elongated, e.g., by confining atoms in a tight transverse optical lattice. In this configuration, it may be possible to observe the parametric scattering dynamics for longer time scales, which may allow for the observation of Rabi oscillations between k_0 and k_1, k_2 as predicted in Ref. [14]. For longer coherence times, parametric amplification could also be an efficient means of producing pairs of momentum entangled atoms for quantum information applications [12,13], but the issue of secondary collisions out of states k_1 and k_2 has to be carefully addressed.

For high atom numbers, and for large values of k_0, the condensate became unstable and scattered into a broad band of final momentum states [Fig. 2(e)]. For $k_{\mathrm{Bragg}} = 0.43k_L$, the energy of atoms outcoupled by the Bragg beams was ≈ 370 Hz, whereas the chemical potential of the condensate was ≈ 300 Hz. Because of this, if the atom number was increased significantly the momentum peaks were no longer distinguishable. When the chemical potential of the condensate was larger than the separation between the phase-matched momentum states, the process was self-seeded; i.e., the momentum spread of the initial condensate contained atoms with momentum k_0, k_1, and k_2, and considerable scattering occurred. Similarly, if the atom number was kept constant, and the value of k_0 was increased, the phase-matched momentum states moved closer together until they were no longer distinguishable. This occurred at values of k_0 above $\approx 0.75k_L$, and we observed a dynamic instability. For larger atom numbers, the critical value of k_0 decreases. For values of k_0 less than $0.55k_0$ elastic scattering cannot occur, and the system should be stable for all atom numbers. Instabilities of condensates in optical lattices has attracted much attention recently, both theoretically [21–28] and experimentally [29–33]. Most recently, dynamic instabilities of condensates in moving lattices were observed in Refs. [29,30]. In Ref. [30], the chemical potential was a factor of 3 higher than in our experiment, leading to a dynamic instability for all values of k_0 above $0.55k_L$. Although discrete momentum states could not be observed in those experiments, it is possible that the mechanism for the dynamic instability is self-seeded parametric amplification. Indeed, the phase-matching condition for parametric amplification is identical to the resonance condition for dynamic instability in the noninteracting limit [21]. After the submission of this Letter, recent work on period-doubling instabilities in a shaken optical lattice [34] was reinterpreted as parametric amplification [35].

In conclusion, we have demonstrated a matter-wave analogue of both optical parametric generation and optical parametric amplification using a condensate moving in a one-dimensional optical lattice. The optical lattice modified the dispersion curve and ensured phase matching. If the separation of the phase-matched momentum states becomes less than the speed of sound, a condensate will self-seed the process and become dynamically unstable.

The authors thank K. Mølmer for pointing out this physical process to us, M. Inguscio and M. Modugno for insightful discussions, M. Saba for helpful discussions and a critical reading of the manuscript, and P. Medley for experimental assistance. This work was supported by NSF and ARO.

*Electronic address: http://cua.mit.edu/ketterle_group/

[1] G. Lenz, P. Meystre, and E. M. Wright, Phys. Rev. Lett. **71**, 3271 (1993).
[2] L. Deng *et al.*, Nature (London) **398**, 218 (1999).
[3] J. M. Vogels, K. Xu, and W. Ketterle, Phys. Rev. Lett. **89**, 020401 (2002).
[4] J. Denschlag *et al.*, Science **287**, 97 (2000).
[5] S. Burger *et al.*, Phys. Rev. Lett. **83**, 5198 (1999).
[6] B. P. Anderson *et al.*, Phys. Rev. Lett. **86**, 2926 (2001).
[7] K. E. Strecker *et al.*, Nature (London) **417**, 150 (2002).
[8] R. Wynar *et al.*, Science **287**, 1016 (2000).
[9] J. R. Abo-Shaeer *et al.*, Phys. Rev. Lett. **94**, 040405 (2005).
[10] P. D. Lett *et al.*, Phys. Rev. Lett. **71**, 2200 (1993).
[11] J. D. Miller, R. A. Cline, and D. J. Heinzen, Phys. Rev. Lett. **71**, 2204 (1993).
[12] L.-M. Duan *et al.*, Phys. Rev. Lett. **85**, 3991 (2000).
[13] H. Pu and P. Meystre, Phys. Rev. Lett. **85**, 3987 (2000).
[14] K. M. Hilligsøe and K. Mølmer, Phys. Rev. A **71**, 041602(R) (2005).
[15] E. Rosencher, *Optoelectronics* (Cambridge University Press, Cambridge, England, 2002).
[16] P. G. Savvidis *et al.*, Phys. Rev. Lett. **84**, 1547 (2000).
[17] B. Eiermann *et al.*, Phys. Rev. Lett. **91**, 060402 (2003).
[18] B. Eiermann *et al.*, Phys. Rev. Lett. **92**, 230401 (2004).
[19] J. Stenger *et al.*, Phys. Rev. Lett. **82**, 4569 (1999).
[20] D. Schneble *et al.*, Science **300**, 475 (2003).
[21] B. Wu and Q. Niu, Phys. Rev. A **64**, 061603(R) (2001); New J. Phys. **5**, 104 (2003).
[22] A. Smerzi *et al.*, Phys. Rev. Lett. **89**, 170402 (2002); C. Menotti, A. Smerzi, and A. Trombettoni, New J. Phys. **5**, 112 (2003).
[23] M. Machholm *et al.*, Phys. Rev. A **69**, 043604 (2004).
[24] V. V. Konotop and M. Salerno, Phys. Rev. A **65**, 021602(R) (2002).
[25] R. G. Scott *et al.*, Phys. Rev. Lett. **90**, 110404 (2003).
[26] Y. Zheng, M. Kostrun, and J. Javanainen, Phys. Rev. Lett. **93**, 230401 (2004).
[27] M. Modugno, C. Tozzo, and F. Dalfovo, Phys. Rev. A **70**, 043625 (2004).
[28] C. Tozzo, M. Kramer, and F. Dalfovo, Phys. Rev. A **72**, 023613 (2005).
[29] L. Fallani *et al.*, Phys. Rev. Lett. **93**, 140406 (2004).
[30] L. De Sarlo *et al.*, Phys. Rev. A **72**, 013603 (2005).
[31] S. Burger *et al.*, Phys. Rev. Lett. **86**, 4447 (2001).
[32] F. S. Cataliotti *et al.*, New J. Phys. **5**, 71 (2003).
[33] M. Cristiani *et al.*, Opt. Express **12**, 4 (2004).
[34] N. Gemelke *et al.*, cond-mat/0504311.
[35] N. Gemelke *et al.*, Phys. Rev. Lett. **95**, 170404 (2005).

Appendix F

Continuous and Pulsed Quantum Zeno Effect

This appendix contains a reprint of Ref. [119]: Erik W. Streed, Jongchul Mun, Micah Boyd, Gretchen K. Campbell, Patrick Medley, Wolfgang Ketterle, and David E. Pritchard *Continuous and Pulsed Quantum Zeno Effect*, Physical Review Letters **97**, 260402 (2006).

Continuous and Pulsed Quantum Zeno Effect

Erik W. Streed,[1,2] Jongchul Mun,[1] Micah Boyd,[1] Gretchen K. Campbell,[1] Patrick Medley,[1] Wolfgang Ketterle,[1] and David E. Pritchard[1]

[1]*Department of Physics, MIT-Harvard Center for Ultracold Atoms, and Research Laboratory of Electronics, MIT, Cambridge, Massachusetts 02139, USA*

[2]*Centre for Quantum Dynamics, Griffith University, Nathan, QLD 4111, Australia*

(Received 14 June 2006; published 27 December 2006)

Continuous and pulsed quantum Zeno effects were observed using a ^{87}Rb Bose-Einstein condensate. Oscillations between two ground hyperfine states of a magnetically trapped condensate, externally driven at a transition rate ω_R, were suppressed by destructively measuring the population in one of the states with resonant light. The suppression of the transition rate in the two-level system was quantified for pulsed measurements with a time interval δt between pulses and continuous measurements with a scattering rate γ. We observe that the continuous measurements exhibit the same suppression in the transition rate as the pulsed measurements when $\gamma\delta t = 3.60(0.43)$, in agreement with the predicted value of 4. Increasing the measurement rate suppressed the transition rate down to $0.005\omega_R$.

DOI: 10.1103/PhysRevLett.97.260402 PACS numbers: 03.65.Xp, 03.75.Mn, 42.50.Xa

The quantum Zeno effect (QZE) is the suppression of transitions between quantum states by frequent measurements. It was first considered as a theoretical problem where the continuous observation of an unstable particle would prevent its decay [1]. Experimental demonstrations of the QZE [2–8] have been driven by interest in both fundamental physics and practical applications. Practical applications of the QZE include reducing decoherence in quantum computing [8–10], efficient preservation of spin polarized gases [3,4,6], and dosage reduction in neutron tomography [11].

The QZE is a paradigm and test bed for quantum measurement theory[12,13]. In one interpretation, it involves many sequential collapses of the wave functions of the system. Quantum Zeno experiments provide constraints for speculative extensions of quantum mechanics where the collapse of the wave function is created by extra terms in a modified Schrödinger equation [14]. It is still an open question how close one can approach the limit of an infinite number of interrogations due to the Heisenberg uncertainty involved in shorter measurement times. These conceptional questions provide the motivation to extend experimental tests of the quantum Zeno phenomenon. A major improvement to a quantum Zeno experiment with ultracold neutrons [15] is in preparation.

In this Letter we compare the suppression of the transition rate in an oscillating two-level system by continuous and pulsed measurements. Our QZE experiments were carried out with Bose-Einstein condensed atoms [16,17]. The long coherence time and the high degree of control of the position and momentum of the atoms created a very clean system and allowed us to observe much stronger quantum Zeno suppression than before [2,5,7]. In the experiment with pulsed measurements, up to 500 measurements could be carried out and survival probabilities exceeded 98%. Furthermore, we have performed the first quantitative comparison between the pulsed and continuous measurement QZE. This is important since any real pulsed measurement is only an approximation based on a series of weak continuous measurements [18,19].

Let us consider a two-level system which is externally driven at a Rabi frequency ω_R. Measurements of the state of the system project the system into one of the two states $|1\rangle$, $|2\rangle$. If the initial state of the system is in $|1\rangle$ and a measurement is made after short time δt ($\ll 1/\omega_R$), then the probability that the system is in $|1\rangle$ is $1 - (\omega_R\delta t/2)^2$. With N successive measurements the probability that the system remains in $|1\rangle$ is

$$P(N) = [1 - (\omega_R\delta t/2)^2]^N \approx \exp[-N(\omega_R\delta t/2)^2] = \exp[-(\omega_R^2\delta t/4)T] \quad (1)$$

with $T = N\delta t$ the total free evolution time. Instead of normal Rabi-type oscillation between two states, the initial state $|1\rangle$ decays with an effective decay rate $1/\tau_{EP}$ [20]. $1/\tau_{EP}$ is given by

$$1/\tau_{EP} = \omega_R^2\delta t/4. \quad (2)$$

The characteristic time τ_{EP} for the pulsed QZE is much longer than the characteristic time $1/\omega_R$ of normal Rabi-type oscillation . This shows the suppression of transition by the QZE.

For a continuous measurement, the atoms are continuously illuminated with laser light resonant with the transition energy between state $|2\rangle$ and another excited state. If atoms are in state $|2\rangle$, they spontaneously emit a photon at a rate γ. Because of the photon recoil, those atoms are removed from the coherently driven two-level system. The population of state $|1\rangle$ decays with the effective decay rate $1/\tau_{EC}$ which is given by the optical Bloch equations as

$$1/\tau_{EC} = \omega_R^2/\gamma. \quad (3)$$

In contrast, for measurements with randomly spaced pulses, the effective decay rate is $1/\tau_{EP} = \omega_R^2\langle\delta t^2\rangle/4\langle\delta t\rangle$. If the probability for measurement pulse during a time interval δt is $\gamma\delta t$, $\langle\delta t^2\rangle = 2/\gamma^2$ and $\langle\delta t\rangle = 1/\gamma$. The effective decay rate for this case is

$$1/\tau_{EP,\text{random}} = \omega_R^2/2\gamma. \quad (4)$$

Although the continuous beam leads to the same emission rate γ of state $|2\rangle$ as a random pulse measurement case, the wave function evolution from $|1\rangle$ to $|2\rangle$ is faster in the continuous measurement case than in random pulse measurement case. The decay rate for continuous measurements τ_{EC} [Eq. (3)] is twice the value of $\tau_{EP,\text{random}}$ [Eq. (4)].

In our study we have determined the lifetimes τ_{EP}, τ_{EC} with each type of measurement and used them to verify the prediction of Eq. (2) and (3) that pulsed measurements with time interval δt produce the same suppression of decay as continuous measurements with a scattering rate γ when $\gamma\delta t = 4$ [20]. In particular, by verifying Eq. (3), we show that the continuous measurement process cannot be simulated by a series of random pulses with a rate γ.

Our experimental system consisted of magnetically trapped ^{87}Rb Bose-Einstein condensate in the $5S_{1/2}|1,-1\rangle(|F,m_F\rangle)$ and $5S_{1/2}|2,+1\rangle$ states [21]. Pure condensates of $N_c = 5.0(0.5)\times 10^4$ atoms in the $|1,-1\rangle$ state were prepared in a $\{63, 63, 6.6\}$ Hz magnetic trap. Coherent oscillations between state $|1\rangle(|1,-1\rangle)$ and state $|2\rangle(|2,+1\rangle)$ were then driven at a rate ω_R by a two-photon transition (Fig. 1). The $|1,-1\rangle$ and $|2,+1\rangle$ states were selected because they have the same 1st order Zeeman shift at a magnetic field of 3.23 G [22].

Measurements of the population in state $|2\rangle(|2,+1\rangle)$ were performed by a laser beam of 780 nm π polarized

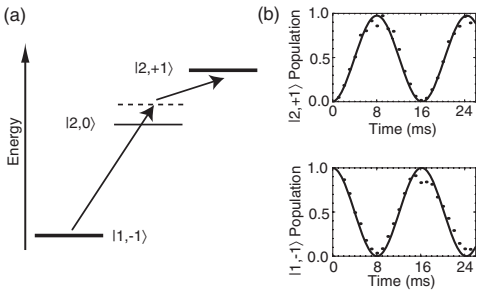

FIG. 1. Two-level Rabi oscillation. The two-level quantum system consisted of the $|1,-1\rangle$ and $|2,+1\rangle$ ground hyperfine states of ^{87}Rb. (a) Energy level diagram for relevant ^{87}Rb ground hyperfine states. Arrows depict the components of the two-photon transition between the $|1,-1\rangle$ and $|2,+1\rangle$ states. 6.8 GHz microwaves couple the $|1,-1\rangle$ to a virtual intermediate state detuned 420 kHz above resonance with $|2,0\rangle$. Radio frequency (rf) at 1.68 MHz resonantly completed the transition to the $|2,+1\rangle$ state. (b) Driven population of the $|1,-1\rangle$ and $|2,+1\rangle$ states as a function of time. Curves are fits to a two-photon transition rate of $\omega_R/2\pi = 61.5(0.5)$ Hz. No population was detected in $|2,0\rangle$.

light resonant with the $5S_{1/2}|2,+1\rangle \rightarrow 5P_{3/2}|3,+1\rangle$ transition. The 362 nK energy from a single photon recoil distinguished scattered atoms from the subrecoil $\mu = 15$ nK energy range of the condensate atoms. Successive scatterings would eject measured atoms from the trap. After each QZE experiment was completed the magnetic trap was turned off and the population of surviving atoms in each state was measured. To simultaneously measure the $|1\rangle$ and $|2\rangle$ populations we used an rf pulse and magnetic field sweep to transfer the atoms to other magnetic sublevels. Parameters were chosen in such a way that each initial state was partially transferred to a sublevel with a different magnetic moment. After Stern-Gerlach separation and 41 ms of ballistic expansion, the atoms were imaged and the populations in the two initial states could be read out simultaneously.

We quantified the QZE induced by repeated pulsed measurements. Optical measurement pulses of 172 μW ($s_0 = 0.15$, where $s_0 = I/I_{\text{sat}}$ is the transition saturation parameter) and $t_p = 10$ μs in duration were applied to the driven two-level system. Each pulse scattered $\sim$29 photons per atom and were separated by a free evolution time δt. The lifetime τ_{EP} for a particular measurement rate $1/\delta t$ [23] was determined by fitting the $|1\rangle$ atom lifetime to an exponential decay curve over a range of times $\gtrsim 2\tau_{EP}$. Figure 2(a) shows the dramatic increase in the observed lifetimes (solid symbols) as the measurement rate $1/\delta t$ was increased. The measured lifetimes for two different ω_R [boxes for $2\pi\times 54.6(0.5)$ Hz, triangles for $2\pi\times 24.7(0.1)$ Hz] are plotted along with their expected values (lower and upper lines, respectively). The measured lifetimes were not found to be strongly sensitive to variations in optical power, pulse width, or laser detuning. The lifetime enhanced by QZE can be compared to $1/\omega_R$, which would be the characteristic time without pulsed measurements. The longest lifetime was $198(16)\times 1/\omega_R$ at $1/\delta t = 25$ ms^{-1}.

Previous works [2,7,24] express the QZE in terms of the survival probability $P(N)$ for number of measurements N during a π pulse ($t = \pi/\omega_R$), a duration where without measurements 100% of the atoms would be transferred into the other state. Figure 2(b) displays our results in this way. In these terms the greatest Zeno effect is for $N = 506(2)$ measurements with a survival probability $P = 0.984(1)$.

The most frequent measurements [farthest right solid symbols in Fig. 2(a)] show significant deviation from expected lifetimes (lines). For a high measurement rate $1/\delta t$, the pulse duration t_p is not negligible compared to free evolution time δt between the pulses, and the process that occurs while the measurement pulse is on becomes more important. In our experiment the pulse duration $t_p = 10$ μs was 20% of the shortest time interval $\delta t = 40$ μs. In such cases the measured lifetime depends not only on the time interval δt but also on the pulse duration t_p. During the time interval, δt the population in state $|1\rangle$ transfers (“decays”) to state $|2\rangle$ with τ_{EP}. During the pulse

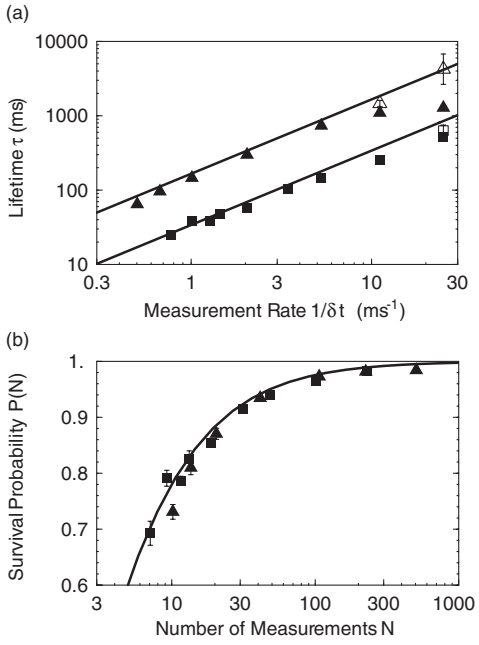

FIG. 2. Pulsed quantum Zeno effect. Increase in the lifetime (a) and the survival probability (b) of atoms in the initial $|1\rangle$ state as the measurement rate $1/\delta t$ is increased. Solid lines indicate the prediction for the pulsed QZE. Boxes (triangles) are data points for a transition rate $\omega_R/2\pi = 54.6(0.5)$ [24.7(0.1)] Hz. (a) Observed lifetimes (solid line) for $|1\rangle$ atoms measured with a time interval δt between measurement pulses. Lines indicate the expected QZE lifetime $\tau_{EP} = 4/(\omega_R^2 \delta t)$. Open symbols show lifetimes after correction for additional loss mechanism by Eq. (5). (b) The same data are displayed in terms of the survival probability for N measurements performed during a π pulse time $t = \pi/\omega_R$ (the time it would take to transfer 100% of the atoms from $|1\rangle$ to $|2\rangle$ without measurements). The solid line is the expected survival probability $P(N) = [\cos(\frac{\pi}{2N})]^{(2N)}$ for N ideal measurements.

duration t_p, state $|1\rangle$ can decay by different loss mechanisms. We made a separate measurement of this additional loss. The system was prepared in the same way except that the measurement pulse laser was kept on continuously. The lifetime $1/\Gamma_m$ of this system was measured and Γ_m was $3.41(0.14)\ \mathrm{s}^{-1}$ for $\omega_R/2\pi = 54.6$ Hz $[\Gamma_m = 2.96(0.22)\ \mathrm{s}^{-1}$ for $\omega_R/2\pi = 24.7$ Hz]. In order to find the origin of this additional loss, the measurements of lifetimes were made with removal of either the rf or the microwave component of the two-photon drive. The lifetime showed no change when the rf component was removed, but the lifetime increased by an order of magnitude without microwave component. This suggests that the loss occurring during pulse duration t_p is dominated by the virtual intermediate state $|2, 0\rangle$, which can be excited by the measurement laser to the excited state $5P_{3/2}|3, 0\rangle$.

To obtain the correct decay rate $1/\tau_{EP}$ for the pulsed QZE from our measurement this additional loss should be corrected. The observed decay rate $1/\tau$ is split into two components and can be written as

$$\frac{1}{\tau} = \frac{1}{\tau_{EP}} \frac{\delta t}{t_p + \delta t} + \Gamma_m \frac{t_p}{t_p + \delta t}, \tag{5}$$

where t_p is pulse duration. Data points in Fig. 2(a) where this correction had a significant impact on the lifetime are indicated by open symbols. The predicted lifetime is $\tau_{EP} = 4/(\omega_R^2 \delta t)$, slightly larger than the measured $\tau_{EP} = 0.836(0.014) \times 4/(\omega_R^2 \delta t)$. The discrepancy is possibly due to collisions between recoiling atoms and the remaining condensate leading to additional loss.

The same initial system was subjected to a weak continuous measurement instead of repeated strong measurements. Figure 3 shows the increase in lifetime with increasing measurement laser power. While showing this qualitative relationship is straightforward, several issues complicate a quantitative measurement of the continuous QZE. If the measurement laser is detuned from the optical resonance it will have a reduced scattering rate and also induce an ac Stark shift δ_{rf} in the resonance between $|1\rangle$ and $|2\rangle$, reducing the transfer rate from $|1\rangle$ to $|2\rangle$. In addition, imperfections in the beam can affect the intensity at the atoms. These issues are not important for the pulsed measurement as long as atoms scatter multiple photons. However, they are critical to properly characterizing the weak continuous measurement experiment.

We were able to address all of these issues simultaneously by measuring the ac Stark shift at several different laser detunings. For each laser detuning (δ_L) and optical power (s_0) we determined the ac Stark shift δ_{rf} by maximizing the reduction of atoms in state $|1\rangle$ as a function of rf frequency. Measurements of continuous QZE lifetime τ_{EC} [Eq. (3)] were then made varying saturation parameter s_0 and detuning δ_L of the measurement laser. Equation (3) can then be rewritten as

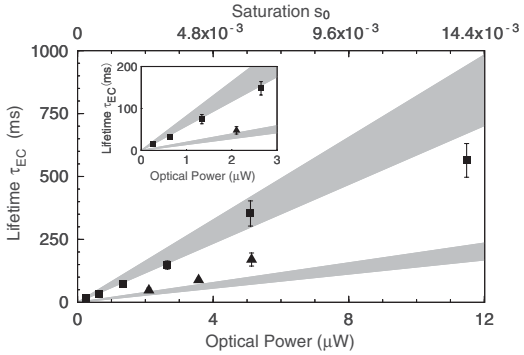

FIG. 3. Continuous quantum Zeno effect. Lifetime dependence on optical power with $\omega_R/2\pi = 48.5(0.9)$ Hz for laser detuning $\delta_L = 0$ MHz (■) and $\delta_L = -5.4$ MHz (▲). Gray bands indicates range of expected lifetimes which are calculated from measurements of ac Stark shift for $\delta_L = 0$ MHz (upper) and $\delta_L = -5.4$ MHz (lower). Inset highlights data from lower optical powers. The saturation parameter s_0 has an uncertainty of 17%.

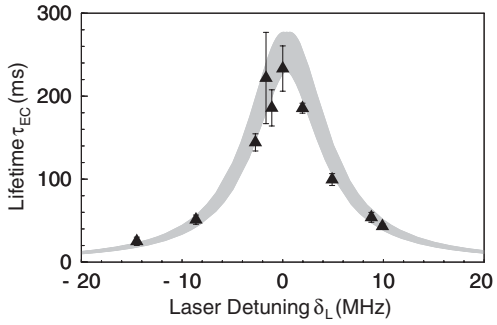

FIG. 4. Continuous quantum Zeno lifetime as a function of the measurement laser detuning δ_L. Gray band indicates range of expected lifetimes [Eq. (6)] from separately measured ac Stark shift parameters. The predicted linewidth is slightly Zeeman broadened by imperfections in the polarization. Data are for 3.5 μW laser power, $\omega_R = 45.5(1.0)$ Hz.

$$\tau_{EC} = \frac{\gamma}{\omega_R^2} = \frac{\Gamma s_0}{2\omega_R^2}\left(\frac{1}{1 + 4(\frac{\delta_L}{\Gamma})^2}\right) \tag{6}$$

which is a function of s_0 and δ_L with ^{87}Rb D_2 transition decay rate Γ. Figure 4 verifies Eq. (6) for various detunings δ_L. Figure 3 shows increasing lifetime with increasing measurement laser power, the signature of the continuous QZE. Similar to the longest lifetime point in the pulsed QZE data [upper right solid triangle, Fig. 2(a)], the data point with highest power in Fig. 3 shows significant deviation from the lifetime expected from Eq. (6). By matching the observed lifetimes for pulsed and continuous QZE measurements we find that each measurement type has the same QZE when $\gamma\delta t = 3.60(0.43)$, which is in agreement with the predicted ratio of 4 [20] but rules out randomly repeated pulse case in Eq. (4). Equation (4) gives the ratio of 2 instead of 4. The observed large quantum Zeno suppression dramatically illustrates the modification of a wave function by a null measurement, i.e., the observation that no light has been scattered [25]. The large fraction of atoms in the initial state $|1\rangle$ is caused by repeated measurements without scattering any photons.

We have extended previous work in pulsed QZE measurements [2,5,7] by exploiting advantages inherent to Bose-Einstein condensates. While in theory the Heisenberg uncertainty principal limits how frequently meaningful measurements can be performed, in practice imperfections in real measurements are the limiting factors [24,26]. In ion experiments optical pumping between states during the measurement pulses changed the observed population transfer [2], requiring significant corrections for the $N = 32$ and $N = 64$ pulse measurements (Table I in [2]) to observe a maximum survival probability $P(64) = 0.943(20)$ [2] [$\tau_{EP} = 54(30) \times 1/\omega_R$]. Previous demonstrations of the continuous QZE [3,4,6] observed qualitative but not quantitatively characterized QZE suppression effects up to 80% [4] with increasing laser intensity. Our observed quantum Zeno suppressions are substantially larger then both previous pulsed [2] and continuous [4] results, and is also greater then that expected from proposed experiments [11,15,24,26] in neutrons.

In conclusion, we have used a Bose-Einstein condensate to demonstrate the QZE for both continuous and pulsed measurements. Lifetimes for both cases were substantially enhanced by QZE to values close to $200 \times 1/\omega_R$. Pulsed and continuous QZE were quantified and compared. We observe that the continuous measurements exhibit the same suppression in the transition rate as the pulsed measurements when $\gamma\delta t = 3.60(0.43)$, which agrees with the predicted value of 4 [20] and rules out a simple model when a continuous measurement is replaced by a series of random pulses. A next generation experiment could demonstrate even stronger quantum Zeno suppression and study the transition from pulsed to continuous QZE by using pulse duration and intervals approaching the spontaneous emission time.

The authors thank Helmut Rauch for insightful discussion. This work was supported by NSF.

[1] B. Misra and E. C. G. Sudarshan, J. Math. Phys. Sci. **18**, 756 (1977).
[2] W. M. Itano, D. J. Heinzen, J. J. Bollinger, and D. J. Wineland, Phys. Rev. A **41**, 2295 (1990).
[3] B. Nagels, L. J. F. Hermans, and P. L. Chapovsky, Phys. Rev. Lett. **79**, 3097 (1997).
[4] K. Mølhave and M. Drewsen, Phys. Lett. A **268**, 45 (2000).
[5] M. C. Fischer, B. Gutiérrez-Medina, and M. G. Raizen, Phys. Rev. Lett. **87**, 040402 (2001).
[6] T. Nakanishi, K. Yamane, and M. Kitano, Phys. Rev. A **65**, 013404 (2001).
[7] C. Balzer *et al.*, Opt. Commun. **211**, 235 (2002).
[8] O. Hosten *et al.*, Nature (London) **439**, 949 (2006).
[9] J. D. Franson, B. C. Jacobs, and T. B. Pittman, Phys. Rev. A **70**, 062302 (2004).
[10] P. Facchi *et al.*, Phys. Rev. A **71**, 022302 (2005).
[11] P. Facchi *et al.*, Phys. Rev. A **66**, 012110 (2002).
[12] K. Koshino and A. Shimizu, Phys. Rep. **412**, 191 (2005).
[13] D. Home and M. A. B. Whitaker, Ann. Phys. (N.Y.) **258**, 237 (1997).
[14] S. L. Adler, Phys. Rev. D **67**, 025007 (2003).
[15] M. R. Jaekel, E. Jericha, and H. Rauch, Nucl. Instrum. Methods Phys. Res., Sect. A **539**, 335 (2005).
[16] M. H. Anderson *et al.*, Science **269**, 198 (1995).
[17] K. B. Davis *et al.*, Phys. Rev. Lett. **75**, 3969 (1995).
[18] T. A. Burn, Am. J. Phys. **70**, 719 (2002).
[19] C. M. Caves and G. J. Milburn, Phys. Rev. A **36**, 5543 (1987).
[20] L. Schulman, Phys. Rev. A **57**, 1509 (1998).
[21] E. W. Streed *et al.*, Rev. Sci. Instrum. **77**, 023106 (2006).
[22] D. M. Harber, H. J. Lewandowski, J. M. McGuirk, and E. A. Cornell, Phys. Rev. A **66**, 053616 (2002).
[23] Including short pulse duration t_p, the pulse repetition rate in the experiment was $1/(\delta t + t_p)$.
[24] P. Facchi *et al.*, Phys. Rev. A **68**, 012107 (2003).
[25] R. H. Dicke, Am. J. Phys. **49**, 925 (1981).
[26] H. Rauch, Physica (Amsterdam) **297B**, 299 (2001).

Appendix G

Photon Recoil Momentum in Dispersive Media

This appendix contains a reprint of Ref. [119]:Gretchen K. Campbell, Aaron E. Leanhardt, Jongchul Mun, Micah Boyd, Erik W. Streed,Wolfgang Ketterle, and David E. Pritchard, *Photon Recoil Momentum in Dispersive Media*, Physical Review Letters **94**, 170403 (2005).

Photon Recoil Momentum in Dispersive Media

Gretchen K. Campbell, Aaron E. Leanhardt,* Jongchul Mun, Micah Boyd, Erik W. Streed, Wolfgang Ketterle, and David E. Pritchard†

MIT-Harvard Center for Ultracold Atoms, Research Laboratory of Electronics and Department of Physics, Massachusetts Institute of Technology, Cambridge, Massachusetts 02139, USA

(Received 31 January 2005; published 4 May 2005)

A systematic shift of the photon recoil momentum due to the index of refraction of a dilute gas of atoms has been observed. The recoil frequency was determined with a two-pulse light grating interferometer using near-resonant laser light. The results show that the recoil momentum of atoms caused by the absorption of a photon is $n\hbar k$, where n is the index of refraction of the gas and k is the vacuum wave vector of the photon. This systematic effect must be accounted for in high-precision atom interferometry with light gratings.

DOI: 10.1103/PhysRevLett.94.170403 PACS numbers: 03.75.Dg, 39.20.+q, 42.50.Ct

The momentum of a photon in a dispersive medium is of conceptual and practical importance [1–6]. When light enters a medium with an index of refraction n, the electromagnetic momentum is modified [3–5]. Momentum conservation requires then that the medium also has a mechanical momentum. When a pulse of light enters the medium, the particles in the medium are accelerated by the leading edge of the pulse and decelerated by the trailing edge [5]. As a result, no motion is left in the medium after the pulse has passed. When light is absorbed or reflected in the medium, the momentum transfer occurs in units of $\hbar k$ or $n\hbar k$, where k is the vacuum wave vector. An absorbing surface is equivalent to photons leaving the medium without reflection and would therefore receive a momentum of $\hbar k$ per incident photon. In contrast, as shown in Ref. [5], a reflecting surface within the medium will recoil with a momentum of $2n\hbar k$ per photon. In this case, the standing wave formed by the incident and reflected light pulse transfers momentum to the medium which remains even after the light pulse has left. This modification of the recoil momentum has so far been observed only for light being reflected from a mirror immersed in a liquid [7,8].

Recently, there have been discussions about what happens when an atom within an atomic cloud absorbs a photon. If one assumes that after absorbing the photon, no motion is left in the medium, then the recoil momentum should be $\hbar k$ [9]. The same conclusion is reached when one assumes a very dilute, dispersive medium with the absorbing atom localized in the vacuum space between the particles of the medium [10]. However, Ref. [6] argues that the atom will recoil with a momentum of $n\hbar k$, which requires particles in the medium to receive a backward momentum (for $n > 1$) due to the interaction of the oscillating dipole moments of the particles in the dispersive medium and the absorbing atom. So both for reflection by a mirror and absorption by an atom, a photon in a dispersive medium behaves as if it has a momentum of $n\hbar k$.

In this Letter, we examine this issue experimentally, showing that the atom recoils with momentum $n\hbar k$. This has important consequences for atom interferometers using optical waves to manipulate atoms by the transfer of recoil momentum. High-precision measurements of the photon recoil are used to determine the fine-structure constant α [11–16]. Further improvements in the accuracy of photon recoil measurements, combined with the value of α derived from the $(g-2)$ measurements for the electron and positron [17–19], would provide a fundamental test of QED. At low atomic densities, where atom interferometers usually operate, the index of the refraction effect is relatively small. However, the accuracy of the best photon recoil measurements is limited by the uncertainty in the correction to the photon recoil due to the index of refraction. Here we operate an atom interferometer with Bose-Einstein

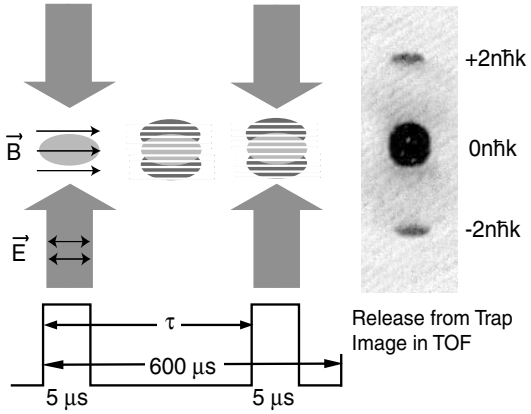

FIG. 1. Kapitza-Dirac interferometer. The first pulse outcoupled a small fraction of atoms into the $|\pm 2n\hbar k\rangle$ momentum states. The outcoupled atoms moved within the initial condensate. After a variable delay τ, a second pulse was applied, and atoms outcoupled by the second pulse interfered with those outcoupled by the first pulse. The laser beam was applied perpendicular to the long axis of the condensate; the polarization, $\vec{E}$, was parallel to it and to the applied magnetic field bias, $\vec{B}$. The atoms were imaged after 38 ms of ballistic expansion. The field of view is 0.5 mm × 1.5 mm.

condensates, which have a much higher density than laser cooled atomic clouds, and observe how the index of refraction modifies the atomic recoil frequency $\hbar\omega_{\rm rec} = \frac{\hbar^2 k^2}{2m}$, where m is the atomic mass.

The essential idea of our experiment is to measure the recoil frequency interferometrically using a two-pulse Ramsey interferometer. The two pulses are optical standing waves separated by a delay time τ (Fig. 1). The first pulse diffracts the atoms in a ^{87}Rb condensate into discrete momentum states. During the delay time τ the phase of each momentum state evolves at a different rate according to its recoil energy. The second pulse recombines the atoms with the initial condensate. The recombined components have differing phases leading to interference fringes that oscillate at the two-photon recoil frequency. By measuring the resulting frequency, ω as a function of the standing wave detuning from the atomic resonance, we found a distinctive dispersive shape for ω that fits the recoil momentum as $n\hbar k$.

The experiment was performed using an elongated ^{87}Rb Bose-Einstein condensate (BEC) created in a cloverleaf-type Ioffe-Pritchard magnetic trap previously described in Ref. [20]. The condensate, containing 1.5×10^6 atoms, was produced in the $|5\,^2S_{1/2}, F = 1, m_F = -1\rangle$ state, and had a Thomas-Fermi radius of 8 (90) μm in the radial (axial) direction, and the magnetic trap had a radial (axial) trap frequency of 81 (7) Hz.

The BEC was illuminated with an optical standing wave created by a retroreflected, π-polarized laser beam. Losses in the retroreflected beam were negligible. The polarization of the beam was optimized by suppressing Rayleigh superradiance [20]. The laser was detuned from the $5\,^2S_{1/2}, F = 1 \rightarrow 5\,^2P_{3/2}, F = 1$ transition at $\lambda =$ 780 nm, and had a linewidth γ much smaller than Γ, the natural linewidth of the transition. The intensity of the 5 μs long pulse was set to outcouple $\approx 5\%$ of the atoms into each of the $|\pm 2n\hbar k\rangle$ momentum states with no appreciable population in higher momentum states. This ensured that the density of the original condensate was nearly constant throughout the measurement. After a variable time τ, a second identical pulse was applied. The time between the first pulse and the shutoff of the magnetic trap was fixed at 600 μs, which was less than a quarter of the radial trap period. The momentum distribution of the condensate was imaged after 38 ms of ballistic expansion, long enough for the momentum states to be resolved. The images were obtained using resonant absorption imaging after first optically pumping the atoms to the $5\,^2S_{1/2}, F = 2$ state. To measure the effect of spontaneous light scattering from the standing wave, the density of the condensate (and associated mean-field shift) was determined after applying a single 5 μs pulse to the condensate, and then immediately releasing it from the magnetic trap. The number of atoms in the condensate was determined by integrating the optical density of the absorption image, which in turn was calibrated by fitting the Thomas-Fermi radius of unperturbed condensates in time of flight [21].

The recoil frequency was found by fitting the oscillations in the fraction of atoms in the $|0n\hbar k\rangle$ momentum state as a function of the delay τ (Fig. 2) with a cosine function and a Gaussian envelope:

$$A \exp\left(-\frac{\tau^2}{\tau_c^2}\right)\cos(\omega\tau + \phi) + C. \quad (1)$$

The observation of up to ten oscillations provided a precise value of the recoil frequency. The origin of the damping time τ_c and of the offset C will be discussed later.

Figure 3 shows our measured values for $\omega/2\pi$ as a function of the detuning, $\Delta/2\pi$. The measured values for the frequency clearly follow the dispersive shape of the index of refraction. The variation in $\omega/2\pi$ as a function of the detuning was 2 kHz across the resonance, much larger than the statistical error on the frequency fits of less than 100 Hz. This conclusively shows that the momentum transferred to the atom when a photon is absorbed is $n\hbar k$.

We now discuss in more detail how the atoms interact with optical standing waves. For the short duration of the applied pulses (5 μs) we can assume that the atoms do not move during the pulse and ignore the kinetic energy of the atoms (Raman-Nath approximation). The interaction can then be described by the application of the ac Stark potential due to the standing wave $V(z) = \frac{\hbar\omega_R^2}{\Delta}\sin^2(nkz)$, where

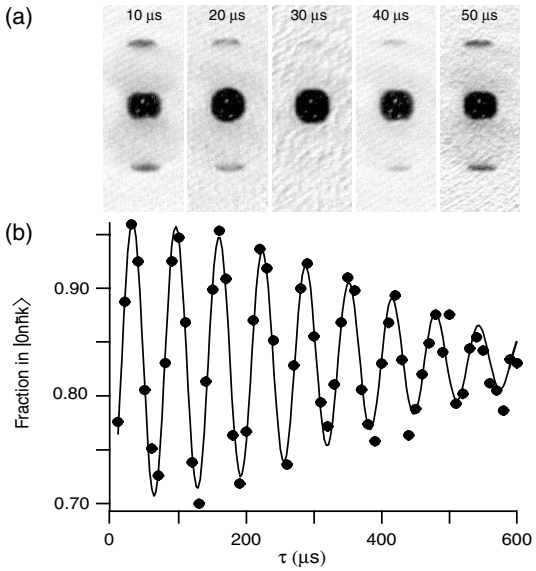

FIG. 2. Interference fringes oscillating at the recoil frequency. (a) Absorption images for $\tau = 10$–50 μs. The detuning was $\Delta/2\pi = +520$ MHz. The field of view is 0.5 mm $\times$ 1.5 mm. (b) Fraction of atoms in the $|0\hbar k\rangle$ momentum state as a function of τ. The fringes were fit using Eq. (1). The fitted frequency was $\omega = 2\pi \times 15\,627(39)$ Hz with decay constant $\tau_c =$ 461(25) μs. The signal was normalized using the total atom number in all momentum states. The systematic scatter of the data from the fit indicates the reproducibility of the single shot measurements.

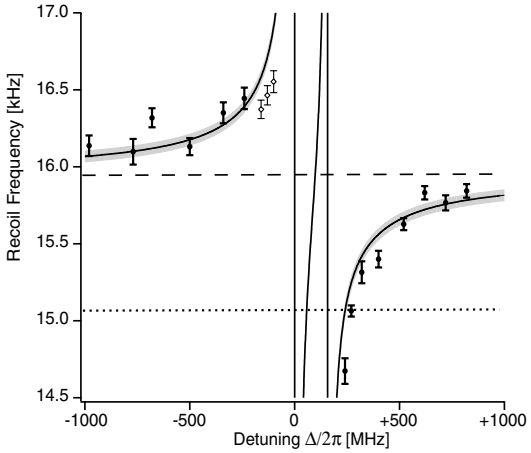

FIG. 3. Recoil frequency as a function of detuning, $\Delta/2\pi$, showing the dispersive effect of the index of refraction. The average density of the condensate for the solid points was $1.14(4) \times 10^{14}$ cm^{-3}, giving rise to a mean-field shift of 880 Hz. The shaded area gives the expected recoil frequency including the uncertainty in the density. The dashed line is at $\omega = 4\omega_{\rm rec} + \rho U/\hbar$, the expected value without index of refraction effects. The dotted line is at $4\omega_{\rm rec} = 15\,068$ Hz, the two-photon vacuum recoil frequency. The data shown as open diamonds had increased spontaneous light scattering due to $\sigma^{\pm}$ light contamination in the laser beam. The increased light scattering led to a lower initial density in the condensate, thus leading to a smaller mean-field shift. The $\sigma^{\pm}$ contamination allowed $\Delta m_F = \pm 1$ transitions, thus for small detunings the proximity to the $|1, -1\rangle \rightarrow |0', 0\rangle$ transition located at $\Delta/2\pi = -72$ MHz resulted in higher spontaneous scattering rates. The open points have been scaled upward to correct for this lower density.

Δ is the detuning between the optical frequency and the atomic transition, and $\omega_{\rm R}$ is the Rabi frequency. This equation is valid for large detuning, $\Delta^2 \gg \Gamma^2/4$. The short pulse limit, describing Kapitza-Dirac scattering, is valid for short interaction times $t_p \ll 1/\omega_{\rm rec} \approx 40\ \mu$s. The first pulse outcouples a fraction of atoms into the momentum states $|\pm 2\ell n\hbar k\rangle$, where the population in the ℓth momentum state is given by $P_\ell = J_\ell^2(\theta)$ [22,23], where for a square pulse, $\theta = \frac{\omega_{\rm R}^2 t_p}{2\Delta}$, and J_ℓ is the ℓth-order Bessel function of the first kind. For $\theta < 1$ a negligible fraction of atoms is diffracted into states with $\ell > 1$, and we can restrict our discussion to the $|\pm 2n\hbar k\rangle$ states. For our experimental parameters $\theta = 0.45$. During the delay time τ the phase of the $|\pm 2n\hbar k\rangle$ states evolves at a faster rate than the $|0n\hbar k\rangle$ state due to the recoil energy, $E_{\rm rec} = 4n^2\hbar\omega_{\rm rec}$; hence, the wave function evolves as

$$|\psi(\tau)\rangle = |\psi_o\rangle[J_1(\theta)|\pm 2n\hbar k\rangle e^{-i4n^2\omega_{\rm rec}\tau} + J_0(\theta)|0n\hbar k\rangle]. \quad (2)$$

At $t = \tau$ a second pulse is applied that partially recombines the momentum states. After applying the two pulses, the probability of finding the atoms in the $|0n\hbar k\rangle$ state, $\rho_0 = |\langle\psi(\tau + t_p)|0n\hbar k\rangle|^2$, is given by

$$\rho_0 = J_0^4(\theta) + 4[J_0^2(\theta)J_1^2(\theta) + J_1^4(\theta)]\cos(4n^2\omega_{\rm rec}\tau). \quad (3)$$

As a function of τ the density of the zero momentum peak oscillates at $4n^2\omega_{\rm rec}$.

So far, we have ignored the motion of the atoms during the delay time τ. The amplitudes of the recombined components interfere only where they spatially overlap. After the first pulse, the atoms in the $|\pm 2n\hbar k\rangle$ states move with the recoil velocity ($v_{\rm rec} \sim 12\ \mu$m/ms). As the overlap between the recoiling atoms and those at rest decreases, the interference fringes decay. The overlap integral for this decay is approximated as a Gaussian with time constant, $\tau_c \approx 0.75R_{\rm TF}/v_{\rm rec}$, where $R_{\rm TF}$ is the Thomas-Fermi radius of the condensate [24].

The index of refraction for the condensate is derived from its macroscopic polarization P. For a two level system, $P = \chi\epsilon_o E = i\rho\frac{\mu^2}{\hbar}\frac{E}{\Gamma - i\Delta}$, where χ is the atomic susceptibility, ϵ_o is the permittivity of free space, μ is the dipole matrix element, ρ is the atomic density of the condensate. In this experiment the light was π polarized and detuned by Δ from the $5\,^2S_{1/2}, F = 1 \rightarrow 5\,^2P_{3/2}, F' = 1$ transition. For this polarization the selection rule is $\Delta m_F = 0$, and there are two allowed transitions from $|F = 1, m_F = -1\rangle \rightarrow |1', -1\rangle$ and $|1, -1\rangle \rightarrow |2', -1\rangle$ that are separated by 157 MHz. Including both transitions in the derivation, the index of refraction, $n = \sqrt{1 + \chi}$, is given by

$$n = \sqrt{1 - 12\pi\rho\lambda\!\!\!^{-3}\left(\frac{5}{12}\frac{\Delta_1}{\Gamma}\frac{1}{1 + (2\frac{\Delta_1}{\Gamma})^2} + \frac{1}{4}\frac{\Delta_2}{\Gamma}\frac{1}{1 + (2\frac{\Delta_2}{\Gamma})^2}\right)}, \quad (4)$$

where Δ_1 and Δ_2 are the detunings relative to the $F = 1 \rightarrow F' = 1$ and $F' = 2$ transitions, respectively. This equation is valid in the limit $\rho\lambda\!\!\!^{-3} \ll 1$ [25], where $\lambda\!\!\!^{-} = \lambda/2\pi$. For our experimental parameters $\rho\lambda\!\!\!^{-3} \approx 0.2$. In addition to the index of refraction shift, the observed recoil frequency has a mean-field shift [26]; the atoms in the $|\pm 2n\hbar k\rangle$ state have twice the mean-field energy of those at rest due to the exchange term in the interatomic potential. Including both the mean-field shift and the index of refraction, the frequency of the observed interference fringes should be

$$\omega = 4n^2\omega_{\rm rec} + \frac{\rho U}{\hbar}, \quad (5)$$

where $\rho U = 4\pi\hbar^2 a\rho/m$, and a is the s-wave scattering length. The density $\rho = (4/7)\rho_o$, where ρ_o is the peak condensate density and the factor of $4/7$ is due to the inhomogeneous condensate density.

When the interference fringes were fit using Eq. (1), the average values for the amplitude A and offset C for all of the data points were 0.12(3) and 0.82(4), respectively. This is in reasonable agreement with the expected values of $A = 0.18$ and $C = 0.81$ for $\theta = 0.45$. For a Thomas-Fermi radius of 8 μm we would expect a decay time $\tau_c \approx 500\ \mu$s. There was an unexplained shift in the fitted value

for τ_c between the red and blue side of the resonances: on the red side the average value was 347(20) μs and on the blue, 455(40) μs.

The quadratic dependence in Eq. (5) on the index of refraction can be understood by considering the diffraction of atoms from the light grating created by the standing wave. When the first pulse is applied, the standing wave creates a grating with a periodicity $d = \lambda/2$. Within the condensate the index of refraction modifies the grating period by n, since $\lambda' = \lambda/n$. The momentum of atoms that diffract off the grating is changed by $\pm 2\hbar k'$, again within the condensate $k' = nk$, and the velocity of the atoms is modified. Assuming $n > 1$, when the second grating is applied the atoms have moved farther by a factor of n and the grating is shorter by n, changing the time scale for the interference fringes by a factor of n^2.

The increase in the momentum transferred to the atoms can also be explained by considering the momentum transferred to atoms by a classical field. A derivation using the Lorentz force applied to the atoms during the absorption of a photon can be found in [6]. In a dielectric medium with $n > 1$, the magnetic field and therefore the Lorentz force are not modified. However, the electric field is weaker, and therefore it takes longer for the atom to perform half a Rabi cycle and be transferred to the excited state. During that longer time, the Lorentz force imparts a momentum to the atom which is larger than $\hbar k$.

For Kapitza-Dirac scattering, atoms are diffracted symmetrically into the $|\pm 2\ell n\hbar k\rangle$ momentum states, so momentum is clearly conserved. However, for processes such as Bragg scattering, where the atoms are scattered in only one direction, the index of refraction has an additional effect. Assuming a $\pi/2$ pulse with counterpropagating beams, where half the atoms are diffracted, for $n > 1$ the recoil momentum is a factor of n higher than in vacuum. For momentum to be conserved, the remaining atoms must recoil backwards with momentum $p = 2(n-1)\ell\hbar k$. For small fractional outcoupling the effect is negligible, since the extra momentum is distributed among the remaining condensate. However, if a large fraction of the condensate is outcoupled and ℓ is large, this effect could potentially be resolved in ballistic expansion.

We have discussed here the dispersive effect on the photon momentum near a one-photon resonance. An analogous effect occurs near two-photon resonances. In this case, the atomic polarizability is determined in third-order perturbation theory, and the resulting index of refraction has a sharp, narrow dispersive feature near the two-photon resonance [27]. In recent experiments at Stanford [13], such two-photon effects have been the leading source of uncertainty in high-precision determinations of atomic recoil frequencies and the fine-structure constant α.

In conclusion, we have measured a systematic shift in the photon recoil frequency due to the index of refraction of the condensate. This is the first direct observation of the atomic recoil momentum in dispersive media. For high atomic densities, this shift can have a significant effect on atom interferometers, and is of particular importance for precision measurements of h/m and α with cold atoms [13,16].

The authors thank A. Schirotzek, S. Chu, S. Harris, and H. Haus for insightful discussions, and M. Kellogg for experimental assistance. This work was supported by NSF and ARO.

*Present address: JILA, Boulder, CO 80309, USA.
†Electronic address: http://cua.mit.edu/ketterle_group/

[1] H. Minkowski, Nachr. Ges. Wiss. Göttingen 53 (1908).
[2] H. Minkowski, Math. Ann. **68**, 472 (1910).
[3] M. Abraham, Rend. Circ. Mat. Palermo **28**, 1 (1909).
[4] M. Abraham, Rend. Circ. Mat. Palermo **30**, 33 (1910).
[5] J. P. Gordon, Phys. Rev. A **8**, 14 (1973).
[6] M. P. Haugan and F. V. Kowalski, Phys. Rev. A **25**, 2102 (1982).
[7] R. V. Jones and J. C. S. Richards, Proc. R. Soc. London A **221**, 480 (1954).
[8] R. V. Jones and B. Leslie, Proc. R. Soc. London A **360**, 347 (1978).
[9] J. M. Hensley, A. Wicht, B. C. Young, and S. Chu, in *Atomic Physics 17, Proceedings of the 17th International Conference on Atomic Physics*, edited by E. Arimondo, P. D. Natale, and M. Inguscio (AIP, Melville, NY, 2001).
[10] This argument has been made previously by one of the authors (W. K.).
[11] B. Taylor, Metrologia **31**, 181 (1994).
[12] D. S. Weiss, B. C. Young, and S. Chu, Phys. Rev. Lett. **70**, 2706 (1993).
[13] A. Wicht, J. M. Hensley, E. Sarajlic, and S. Chu, Phys. Scr. **T102**, 82 (2002).
[14] S. Gupta, K. Dieckmann, Z. Hadzibabic, and D. E. Pritchard, Phys. Rev. Lett. **89**, 140401 (2002).
[15] R. Battesti *et al.*, Phys. Rev. Lett. **92**, 253001 (2004).
[16] Y. L. Coq *et al.*, cond-mat/0501520.
[17] R. S. Van Dyck, P. B. Schwinberg, and H. G. Dehmelt, Phys. Rev. Lett. **59**, 26 (1987).
[18] T. Kinoshita, Phys. Rev. Lett. **75**, 4728 (1995).
[19] V. W. Hughes and T. Kinoshita, Rev. Mod. Phys. **71**, S133 (1999).
[20] D. Schneble *et al.*, Science **300**, 475 (2003).
[21] Y. Castin and R. Dum, Phys. Rev. Lett. **77**, 5315 (1996).
[22] P. Meystre, *Atom Optics* (Springer-Verlag, New York, 2001).
[23] S. Gupta, A. E. Leanhardt, A. D. Cronin, and D. E. Pritchard, C.R. Acad. Sci. IV Phys. **2**, 479 (2001).
[24] M. Trippenbach *et al.*, J. Phys. B **33**, 47 (2000).
[25] O. Morice, Y. Castin, and J. Dalibard, Phys. Rev. A **51**, 3896 (1995).
[26] J. Stenger *et al.*, Phys. Rev. Lett. **82**, 4569 (1999).
[27] A. Schirotzek, Diploma thesis, Universität Hamburg, 2004.

Bibliography

[1] J. R. Abo-Shaeer, C. Raman, J. M. Vogels, and W. Ketterle. Observation of vortex lattices in bose-einstein condensates. *Science*, 292:476, 2001.

[2] E. Altman, A. Polkovnikov, E. Demler, B. I. Halperin, and M. D. Lukin. Superfluid-insulator transition in a moving system of interacting bosons. *Physical Review Letters*, 95(2):020402, 2005.

[3] Ehud Altman, Walter Hofstetter, Eugene Demler, and Mikhail D Lukin. Phase diagram of two-component bosons on an optical lattice. *New Journal of Physics*, 5:113, 2003.

[4] M. H. Anderson, J. R. Ensher, M. R. Matthews, C. E. Wieman, and E. A. Cornell. Observation of Bose-Einstein Condensation in a Dilute Atomic Vapor. *Science*, 269(5221):198–201, 1995.

[5] Th. Anker, M. Albiez, R. Gati, S. Hunsmann, B. Eiermann, A. Trombettoni, and M. K. Oberthaler. Nonlinear self-trapping of matter waves in periodic potentials. *Physical Review Letters*, 94(2):020403, 2005.

[6] Neil W. Ashcroft and N. David Mermin. *Solid State Physics*. Brooks Cole, 1976.

[7] M Baranov, L Dobrek, K Góral, L Santos, and M Lewenstein. Ultracold dipolar gases – a challenge for experiments and theory. *Physica Scripta*, T102:74–81, 2002.

[8] Ghassan George Batrouni, Richard T. Scalettar, and Gergely T. Zimanyi. Quantum critical phenomena in one-dimensional bose systems. *Phys. Rev. Lett.*, 65(14):1765–1768, Oct 1990.

[9] Maxime Ben Dahan, Ekkehard Peik, Jakob Reichel, Yvan Castin, and Christophe Salomon. Bloch oscillations of atoms in an optical potential. *Phys. Rev. Lett.*, 76(24):4508–4511, Jun 1996.

[10] A. F. Bernhardt and B. W. Shore. Coherent atomic deflection by resonant standing waves. *Phys. Rev. A*, 23(3):1290–1301, Mar 1981.

[11] Immanuel Bloch. Ultracold quantum gases in optical lattices. *Nature Physics*, 1:23, 2005.

[12] Bose. Plancks gesetz und lichtquantenhypothese. *Zeitschrift fur Physik A Hadrons and Nuclei*, 26:178–181, 1924.

[13] M. S. Boyd. *Novel Trapping Techniques For Shaping Bose-Einstein Condensates*. PhD thesis, Massachusetts Institute of Technology, Cambridge, Massachusetts, October 2006.

[14] Ronald N. Bracewell. *The Fourier Transform & Its Applications*. McGraw-Hill Science/Engineering/Math, 3 edition, 1999.

[15] G. K. Campbell. *87 Rubidium Bose-Einstein Condensates in Optical Lattices*. PhD thesis, Massachusetts Institute of Technology, Cambridge, Massachusetts, 2006.

[16] Gretchen K. Campbell, Aaron E. Leanhardt, Jongchul Mun, Micah Boyd, Erik W. Streed, Wolfgang Ketterle, and David E. Pritchard. Photon recoil momentum in dispersive media. *Physical Review Letters*, 94(17):170403, 2005.

[17] Gretchen K. Campbell, Jongchul Mun, Micah Boyd, Patrick Medley, Aaron E. Leanhardt, Luis G. Marcassa, David E. Pritchard, and Wolfgang Ketterle. Imaging the Mott Insulator Shells by Using Atomic Clock Shifts. *Science*, 313(5787):649–652, 2006.

[18] Gretchen K. Campbell, Jongchul Mun, Micah Boyd, Patrick Medley, Aaron E. Leanhardt, Luis G. Marcassa, David E. Pritchard, and Wolfgang Ketterle. Imaging the Mott Insulator Shells by Using Atomic Clock Shifts. *Science*, 313(5787):649–652, 2006.

[19] Gretchen K. Campbell, Jongchul Mun, Micah Boyd, Erik W. Streed, Wolfgang Ketterle, and David E. Pritchard. Parametric amplification of scattered atom pairs. *Physical Review Letters*, 96(2):020406, 2006.

[20] B. Capogrosso-Sansone, N. V. Prokof'ev, and B. V. Svistunov. Phase diagram and thermodynamics of the three-dimensional bose-hubbard model. *Physical Review B (Condensed Matter and Materials Physics)*, 75(13):134302, 2007.

[21] F. S. Cataliotti, S. Burger, C. Fort, P. Maddaloni, F. Minardi, A. Trombettoni, A. Smerzi, and M. Inguscio. Josephson Junction Arrays with Bose-Einstein Condensates. *Science*, 293(5531):843–846, 2001.

[22] Steven Chu. Nobel lecture: The manipulation of neutral particles. *Rev. Mod. Phys.*, 70(3):685–706, Jul 1998.

[23] D. Clément, A. F. Varón, M. Hugbart, J. A. Retter, P. Bouyer, L. Sanchez-Palencia, D. M. Gangardt, G. V. Shlyapnikov, and A. Aspect. Suppression of transport of an interacting elongated bose-einstein condensate in a random potential. *Physical Review Letters*, 95(17):170409, 2005.

[24] Claude N. Cohen-Tannoudji. Nobel lecture: Manipulating atoms with photons. *Rev. Mod. Phys.*, 70(3):707–719, Jul 1998.

[25] E. A. Cornell and C. E. Wieman. Nobel lecture: Bose-einstein condensation in a dilute gas, the first 70 years and some recent experiments. *Rev. Mod. Phys.*, 74(3):875–893, Aug 2002.

[26] Franco Dalfovo, Stefano Giorgini, Lev P. Pitaevskii, and Sandro Stringari. Theory of bose-einstein condensation in trapped gases. *Rev. Mod. Phys.*, 71(3):463–512, Apr 1999.

[27] B. Damski, H.-U. Everts, A. Honecker, H. Fehrmann, L. Santos, and M. Lewenstein. Atomic fermi gas in the trimerized kagom[e-acute] lattice at 2/3 filling. *Physical Review Letters*, 95(6):060403, 2005.

[28] B. Damski, H. Fehrmann, H.-U. Everts, M. Baranov, L. Santos, and M. Lewenstein. Quantum gases in trimerized kagom[e-acute] lattices. *Physical Review A (Atomic, Molecular, and Optical Physics)*, 72(5):053612, 2005.

[29] K. B. Davis, M. O. Mewes, M. R. Andrews, N. J. van Druten, D. S. Durfee, D. M. Kurn, and W. Ketterle. Bose-einstein condensation in a gas of sodium atoms. *Phys. Rev. Lett.*, 75(22):3969–3973, Nov 1995.

[30] B. DeMarco, C. Lannert, S. Vishveshwara, and T.-C. Wei. Structure and stability of mott-insulator shells of bosons trapped in an optical lattice. *Physical Review A (Atomic, Molecular, and Optical Physics)*, 71(6):063601, 2005.

[31] Eugene Demler and Fei Zhou. Spinor bosonic atoms in optical lattices: Symmetry breaking and fractionalization. *Phys. Rev. Lett.*, 88(16):163001, Apr 2002.

[32] L.-M. Duan, E. Demler, and M. D. Lukin. Controlling spin exchange interactions of ultracold atoms in optical lattices. *Phys. Rev. Lett.*, 91(9):090402, Aug 2003.

[33] Karen Marie Hilligsøe and Klaus Mølmer. Phase-matched four wave mixing and quantum beam splitting of matter waves in a periodic potential. *Physical Review A (Atomic, Molecular, and Optical Physics)*, 71(4):041602, 2005.

[34] B. Eiermann, Th. Anker, M. Albiez, M. Taglieber, P. Treutlein, K.-P. Marzlin, and M. K. Oberthaler. Bright bose-einstein gap solitons of atoms with repulsive interaction. *Phys. Rev. Lett.*, 92(23):230401, Jun 2004.

[35] B. Eiermann, P. Treutlein, Th. Anker, M. Albiez, M. Taglieber, K.-P. Marzlin, and M. K. Oberthaler. Dispersion management for atomic matter waves. *Phys. Rev. Lett.*, 91(6):060402, Aug 2003.

[36] A. Einstein. *Sizber. Kgl. Preuss. Akad. Wiss.*, page 261, 1924.

[37] A. Einstein. *Sizber. Kgl. Preuss. Akad. Wiss.*, page 3, 1925.

[38] J. R. Ensher, D. S. Jin, M. R. Matthews, C. E. Wieman, and E. A. Cornell. Bose-einstein condensation in a dilute gas: Measurement of energy and ground-state occupation. *Phys. Rev. Lett.*, 77(25):4984–4987, Dec 1996.

[39] L. Fallani, L. De Sarlo, J. E. Lye, M. Modugno, R. Saers, C. Fort, and M. Inguscio. Observation of dynamical instability for a bose-einstein condensate in a moving 1d optical lattice. *Phys. Rev. Lett.*, 93(14):140406, Sep 2004.

[40] C. D. Fertig, K. M. O'Hara, J. H. Huckans, S. L. Rolston, W. D. Phillips, and J. V. Porto. Strongly inhibited transport of a degenerate 1d bose gas in a lattice. *Physical Review Letters*, 94(12):120403, 2005.

[41] Alexander L. Fetter and John Dirk Walecka. *Quantum Theory of Many-Particle Systems*. Dover Publications, 2003.

[42] Matthew P. A. Fisher, Peter B. Weichman, G. Grinstein, and Daniel S. Fisher. Boson localization and the superfluid-insulator transition. *Phys. Rev. B*, 40(1):546–570, Jul 1989.

[43] S. Fölling, F. Gerbier, A. Widera, O. Mandel, T. Gericke, and I. Bloch. Spatial quantum noise interferometry in expanding ultracold atom clouds. *Nature*, 434:481, 2005.

[44] Simon Fölling, Artur Widera, Torben Müller, Fabrice Gerbier, and Immanuel Bloch. Formation of spatial shell structure in the superfluid to mott insulator transition. *Physical Review Letters*, 97(6):060403, 2006.

[45] C. Fort, L. Fallani, V. Guarrera, J. E. Lye, M. Modugno, D. S. Wiersma, and M. Inguscio. Effect of optical disorder and single defects on the expansion of a bose-einstein condensate in a one-dimensional waveguide. *Physical Review Letters*, 95(17):170410, 2005.

[46] J. K. Freericks and H. Monien. Strong-coupling expansions for the pure and disordered bose-hubbard model. *Phys. Rev. B*, 53(5):2691–2700, Feb 1996.

[47] J. J. García-Ripoll, M. A. Martin-Delgado, and J. I. Cirac. Implementation of spin hamiltonians in optical lattices. *Phys. Rev. Lett.*, 93(25):250405, Dec 2004.

[48] Fabrice Gerbier. Boson mott insulators at finite temperatures. *Physical Review Letters*, 99(12):120405, 2007.

[49] Fabrice Gerbier, Artur Widera, Simon Fölling, Olaf Mandel, Tatjana Gericke, and Immanuel Bloch. Phase coherence of an atomic mott insulator. *Physical Review Letters*, 95(5):050404, 2005.

[50] S. Giorgini, L. P. Pitaevskii, and S. Stringari. Thermodynamics of a trapped bose-condensed gas. *Journal of Low Temperature Physics*, 109:309–355, 1997.

[51] Phillip L. Gould, George A. Ruff, and David E. Pritchard. Diffraction of atoms by light: The near-resonant kapitza-dirac effect. *Phys. Rev. Lett.*, 56(8):827–830, Feb 1986.

[52] M. Greiner, O. Mandel, T. Esslinger, T. W. Hänsch, and I. Bloch. Quantum phase transition from a superfluid to a mott insulator in a gas of ultracold atoms. *Nature*, 415:39, 2002.

[53] Markus Greiner, Immanuel Bloch, Olaf Mandel, Theodor W. Hänsch, and Tilman Esslinger. Exploring phase coherence in a 2d lattice of bose-einstein condensates. *Phys. Rev. Lett.*, 87(16):160405, Oct 2001.

[54] Axel Griesmaier, Jörg Werner, Sven Hensler, Jürgen Stuhler, and Tilman Pfau. Bose-einstein condensation of chromium. *Physical Review Letters*, 94(16):160401, 2005.

[55] A. Griffin, D.W. Snoke, and S. Stringari, editors. *Bose-Einstein Codensation*. Cambridge University Press, 1996.

[56] Kevin Gross, Chris P. Search, Han Pu, Weiping Zhang, and Pierre Meystre. Magnetism in a lattice of spinor bose-einstein condensates. *Phys. Rev. A*, 66(3):033603, Sep 2002.

[57] Subhadeep Gupta, Aaron E. Leanhardt, Alexander D. Cronin, and David E. Pritchard. Coherent manipulation of atoms with standing light waves. *C.R.Acad.Sci. Paris, Serie Iv*, page 479, 2001.

[58] Zoran Hadzibabic, Peter Krüger, Marc Cheneau, Baptiste Battelier, and Jean Dalibard. Berezinskii–kosterlitz–thouless crossover in a trapped atomic gas. *Nature*, 441:1118–1121, 2006.

[59] E. W. Hagley, L. Deng, M. Kozuma, M. Trippenbach, Y. B. Band, M. Edwards, M Doery, P. S. Julienne, K. Helmerson, S. L. Rolston, and W. D. Phillips. Measurement of the coherence of a bose-einstein condensate. *Phys. Rev. Lett.*, 83(16):3112–3115, Oct 1999.

[60] D. M. Harber, H. J. Lewandowski, J. M. McGuirk, and E. A. Cornell. Effect of cold collisions on spin coherence and resonance shifts in a magnetically trapped ultracold gas. *Phys. Rev. A*, 66(5):053616, Nov 2002.

[61] Tin-Lun Ho and Qi Zhou. Intrinsic heating and cooling in adiabatic processes for bosons in optical lattices. *Physical Review Letters*, 99(12):120404, 2007.

[62] Kiyohito Iigaya, Satoru Konabe, Ippei Danshita, and Tetsuro Nikuni. Landau damping: Instability mechanism of superfluid bose gases moving in optical lattices. *Physical Review A (Atomic, Molecular, and Optical Physics)*, 74(5):053611, 2006.

[63] S. Inouye, T. Pfau, S. Gupta, A. P. Chikkatur, A. Görlitz, D. E. Pritchard, and W. Ketterle. Phase-coherent amplification of atomic matter waves. *Nature*, 402:641, 1999.

[64] D. Jaksch, H.-J. Briegel, J. I. Cirac, C. W. Gardiner, and P. Zoller. Entanglement of atoms via cold controlled collisions. *Phys. Rev. Lett.*, 82(9):1975–1978, Mar 1999.

[65] D. Jaksch, C. Bruder, J. I. Cirac, C. W. Gardiner, and P. Zoller. Cold bosonic atoms in optical lattices. *Phys. Rev. Lett.*, 81(15):3108–3111, Oct 1998.

[66] P.S. Julienne, A.M. Smith, and K. Burnett. Theory of collisions between laser cooled atoms. *Advances In Atomic, Molecular, And Optical Physics*, 30:141, 1992.

[67] V. A. Kashurnikov, N. V. Prokof'ev, and B. V. Svistunov. Revealing the superfluid˘mott-insulator transition in an optical lattice. *Phys. Rev. A*, 66(3):031601, Sep 2002.

[68] V. A. Kashurnikov, N. V. Prokof'ev, and B. V. Svistunov. Revealing the superfluid˘mott-insulator transition in an optical lattice. *Phys. Rev. A*, 66(3):031601, Sep 2002.

[69] W. Ketterle, D. S. Durfee, and DM Stamper-Kurn. Making, probing and understanding Bose-Einstein condensates. *Varenna Summer school*, 1999.

[70] Wolfgang Ketterle. Nobel lecture: When atoms behave as waves: Bose-einstein condensation and the atom laser. *Rev. Mod. Phys.*, 74(4):1131–1151, Nov 2002.

[71] Toshiya Kinoshita, Trevor Wenger, and David S. Weiss. Observation of a One-Dimensional Tonks-Girardeau Gas. *Science*, 305(5687):1125–1128, 2004.

[72] M. Krämer, C. Menotti, L. Pitaevskii, and S. Stringari. Bose-einstein condensates in 1d optical lattices. *The European Physical Journal D*, 27:247–261, 2003.

[73] M. Krämer, L. Pitaevskii, and S. Stringari. Macroscopic dynamics of a trapped bose-einstein condensate in the presence of 1d and 2d optical lattices. *Phys. Rev. Lett.*, 88(18):180404, Apr 2002.

[74] W. Krauth and N. Trivedi. Mott and superfluid transitions in a strongly interacting lattice boson system. *Europhys. Lett.*, 14(7):627–632, 1991.

[75] Werner Krauth, Michel Caffarel, and Jean-Philippe Bouchaud. Gutzwiller wave function for a model of strongly interacting bosons. *Phys. Rev. B*, 45(6):3137–3140, Feb 1992.

[76] A. E. Leanhardt. *Microtraps and Waveguides for Bose-Einstein Condensates*. PhD thesis, Massachusetts Institute of Technology, Cambridge, Massachusetts, 2006.

[77] Anthony J. Leggett. Bose-einstein condensation in the alkali gases: Some fundamental concepts. *Rev. Mod. Phys.*, 73(2):307–356, Apr 2001.

[78] Maciej Lewenstein, Anna Sanpera, Veronica Ahufinger, Bogdan Damski, Aditi Sen(de), and Ujjwal Sen. Ultracold atomic gases in optical lattices: mimicking condensed matter physics and beyond. *Advances in Physics*, 56(2):243–379, 2007.

[79] J. E. Lye, L. Fallani, M. Modugno, D. S. Wiersma, C. Fort, and M. Inguscio. Bose-einstein condensate in a random potential. *Physical Review Letters*, 95(7):070401, 2005.

[80] M. Machholm, C. J. Pethick, and H. Smith. Band structure, elementary excitations, and stability of a bose-einstein condensate in a periodic potential. *Phys. Rev. A*, 67(5):053613, May 2003.

[81] M. R. Matthews, B. P. Anderson, P. C. Haljan, D. S. Hall, C. E. Wieman, and E. A. Cornell. Vortices in a bose-einstein condensate. *Phys. Rev. Lett.*, 83(13):2498–2501, Sep 1999.

[82] J. McClelland, R. Scholten, E. Palm, and R. Celotta. Laser-focused atomic deposition. *Science*, 262:877–880, 1993.

[83] Roger W. McGowan, David M. Giltner, and Siu Au Lee. Light force cooling, focusing, and nanometer-scale deposition of aluminum atoms. *Opt. Lett.*, 20(24):2535, 1995.

[84] C. Menotti, M. Krämer, L. Pitaevskii, and S. Stringari. Dynamic structure factor of a bose-einstein condensate in a one-dimensional optical lattice. *Phys. Rev. A*, 67(5):053609, May 2003.

[85] M. Modugno, C. Tozzo, and F. Dalfovo. Role of transverse excitations in the instability of bose-einstein condensates moving in optical lattices. *Phys. Rev. A*, 70(4):043625, Oct 2004.

[86] Henning Moritz, Thilo Stöferle, Michael Köhl, and Tilman Esslinger. Exciting collective oscillations in a trapped 1d gas. *Phys. Rev. Lett.*, 91(25):250402, Dec 2003.

[87] Oliver Morsch and Markus Oberthaler. Dynamics of bose-einstein condensates in optical lattices. *Reviews of Modern Physics*, 78(1):179, 2006.

[88] Jongchul Mun, Patrick Medley, Gretchen K. Campbell, Luis G. Marcassa, David E. Pritchard, and Wolfgang Ketterle. Phase diagram for a bose-einstein condensate moving in an optical lattice. *Physical Review Letters*, 99(15):150604, 2007.

[89] Qian Niu, Xian-Geng Zhao, G. A. Georgakis, and M. G. Raizen. Atomic landau-zener tunneling and wannier-stark ladders in optical potentials. *Phys. Rev. Lett.*, 76(24):4504–4507, Jun 1996.

[90] C. Orzel, A. K. Tuchman, M. L. Fenselau, M. Yasuda, and M. A. Kasevich. Squeezed States in a Bose-Einstein Condensate. *Science*, 291(5512):2386–2389, 2001.

[91] Tobias J. Osborne and Michael A. Nielsen. Entanglement in a simple quantum phase transition. *Phys. Rev. A*, 66(3):032110, Sep 2002.

[92] A. Osterloh, Luigi Amico, G. Falci, and Rosario Fazio. Scaling of entanglement close to a quantum phase transition. *Nature*, 416:608–610, 2002.

[93] Yu. B. Ovchinnikov, J. H. Müller, M. R. Doery, E. J. D. Vredenbregt, K. Helmerson, S. L. Rolston, and W. D. Phillips. Diffraction of a released bose-einstein condensate by a pulsed standing light wave. *Phys. Rev. Lett.*, 83(2):284–287, Jul 1999.

[94] B. Paredes, A. Widera, V. Murg, O. Mandel, S. Fölling, I. Cirac, G.V. Shlyapnikov, T. W. Hänsch, and I. Bloch. Tonks–girardeau gas of ultracold atoms in an optical lattice. *Nature*, 429:277–281, 2004.

[95] P. Pedri, L. Pitaevskii, S. Stringari, C. Fort, S. Burger, F. S. Cataliotti, P. Maddaloni, F. Minardi, and M. Inguscio. Expansion of a coherent array of bose-einstein condensates. *Phys. Rev. Lett.*, 87(22):220401, Nov 2001.

[96] C.J. Pethick and H. Smith. *Bose-Einstein Codensation in Dilute Gases*. Cambridge University Press, New York, 2002.

[97] William D. Phillips. Nobel lecture: Laser cooling and trapping of neutral atoms. *Rev. Mod. Phys.*, 70(3):721–741, Jul 1998.

[98] A. Polkovnikov, E. Altman, E. Demler, B. Halperin, and M. D. Lukin. Decay of superfluid currents in a moving system of strongly interacting bosons. *Physical Review A (Atomic, Molecular, and Optical Physics)*, 71(6):063613, 2005.

[99] Han Pu, Weiping Zhang, and Pierre Meystre. Ferromagnetism in a lattice of bose-einstein condensates. *Phys. Rev. Lett.*, 87(14):140405, Sep 2001.

[100] A. M. Rey, V. Gritsev, I. Bloch, E. Demler, and M. D. Lukin. Preparation and detection of magnetic quantum phases in optical superlattices. *Physical Review Letters*, 99(14):140601, 2007.

[101] R. Roth and K. Burnett. Superfluidity and interference pattern of ultracold bosons in optical lattices. *Phys. Rev. A*, 67(3):031602, Mar 2003.

[102] J. Ruostekoski and L. Isella. Dissipative quantum dynamics of bosonic atoms in a shallow 1d optical lattice. *Physical Review Letters*, 95(11):110403, 2005.

[103] M. Saba, T.A. Pasquini, C. Sanner, Y. Shin, W. Ketterle, and D.E. Pritchard. Optical measurement of the phase of bose-einstein condensates. *Science*, 307:1945–1948, 2005.

[104] Subir Sachdev. *Quantum phase transition*. Cambridge University Press, 2001.

[105] L. Santos, M. A. Baranov, J. I. Cirac, H.-U. Everts, H. Fehrmann, and M. Lewenstein. Atomic quantum gases in kagomé lattices. *Phys. Rev. Lett.*, 93(3):030601, Jul 2004.

[106] L. De Sarlo, L. Fallani, J. E. Lye, M. Modugno, R. Saers, C. Fort, and M. Inguscio. Unstable regimes for a bose-einstein condensate in an optical lattice. *Phys. Rev. A*, 72(1):013603, 2005.

[107] Craig M. Savage, editor. *Bose-Einstein Condensation: From Atomic Physics to Quantum Fluids*. World Scientific Publishing Company, 2001.

[108] L. S. Schulman. Continuous and pulsed observations in the quantum zeno effect. *Phys. Rev. A*, 57(3):1509–1515, Mar 1998.

[109] T. Schulte, S. Drenkelforth, J. Kruse, W. Ertmer, J. Arlt, K. Sacha, J. Zakrzewski, and M. Lewenstein. Routes towards anderson-like localization of bose-einstein condensates in disordered optical lattices. *Physical Review Letters*, 95(17):170411, 2005.

[110] Y. Shin. *Experiments with Bose-Einstein condensates in a double-well potential*. PhD thesis, Massachusetts Institute of Technology, Cambridge, Massachusetts, 2006.

[111] Y. Shin, M. W. Zwierlein, C. H. Schunck, A. Schirotzek, and W. Ketterle. Observation of phase separation in a strongly interacting imbalanced fermi gas. *Physical Review Letters*, 97(3):030401, 2006.

[112] Anders Sørensen and Klaus Mølmer. Spin-spin interaction and spin squeezing in an optical lattice. *Phys. Rev. Lett.*, 83(11):2274–2277, Sep 1999.

[113] D. M. Stamper-Kurn, A. P. Chikkatur, A. Görlitz, S. Inouye, S. Gupta, D. E. Pritchard, and W. Ketterle. Excitation of phonons in a bose-einstein condensate by light scattering. *Phys. Rev. Lett.*, 83(15):2876–2879, Oct 1999.

[114] D.M. Stamper-Kurn. *Peeking and poking at a new quantum fluid: Studies of gaseous Bose-Einstein condensates in magnetic and optical traps*. PhD thesis, Massachusetts Institute of Technology, Cambridge, Massachusetts, 2000.

[115] J. Stenger, S. Inouye, A. P. Chikkatur, D. M. Stamper-Kurn, D. E. Pritchard, and W. Ketterle. Bragg spectroscopy of a bose-einstein condensate. *Phys. Rev. Lett.*, 82(23):4569–4573, Jun 1999.

[116] Thilo Stöferle, Henning Moritz, Christian Schori, Michael Kohl, and Tilman Esslinger. Transition from a strongly interacting 1d superfluid to a mott insulator. *Phys. Rev. Lett.*, 92(13):130403, 2004.

[117] E. W. Streed. *87 Rubidium Bose-Einstein Condensates: Machine Construction and Quantum Zeno Experiments*. PhD thesis, Massachusetts Institute of Technology, Cambridge, Massachusetts, 2006.

[118] E. W. Streed, A. P. Chikkatur, T. L. Gustavson, M. Boyd, Y. Torii, D. Schneble, G. K. Campbell, D. E. Pritchard, and W. Ketterle. Large atom number bose-einstein condensate machines. *Review of Scientific Instruments*, 77:023106, 2006.

[119] Erik W. Streed, Jongchul Mun, Micah Boyd, Gretchen K. Campbell, Patrick Medley, Wolfgang Ketterle, and David E. Pritchard. Continuous and pulsed quantum zeno effect. *Physical Review Letters*, 97(26):260402, 2006.

[120] K.A. Suominen. Theories for cold atomic-collisions in light fields. *Journal of Physics B*, 29:5981–6007, 1996.

[121] Masao Takamoto, Feng-Lei Hong, Ryoichi Higashi, and Hidetoshi Katori. An optical lattice clock. *Nature*, 435:321–324, 2005.

[122] G. Timp, R. E. Behringer, D. M. Tennant, J. E. Cunningham, M. Prentiss, and K. K. Berggren. Using light as a lens for submicron, neutral-atom lithography. *Phys. Rev. Lett.*, 69(11):1636–1639, Sep 1992.

[123] Shunji Tsuchiya and Allan Griffin. Damping of bogoliubov excitations in optical lattices. *Phys. Rev. A*, 70(2):023611, Aug 2004.

[124] D. van Oosten, P. van der Straten, and H. T. C. Stoof. Quantum phases in an optical lattice. *Phys. Rev. A*, 63(5):053601, Apr 2001.

[125] J. M. Vogels, K. Xu, and W. Ketterle. Generation of macroscopic pair-correlated atomic beams by four-wave mixing in bose-einstein condensates. *Phys. Rev. Lett.*, 89(2):020401, Jun 2002.

[126] J. M. Vogels, K. Xu, C. Raman, J. R. Abo-Shaeer, and W. Ketterle. Experimental observation of the bogoliubov transformation for a bose-einstein condensed gas. *Phys. Rev. Lett.*, 88(6):060402, Jan 2002.

[127] T. Walker and P. Feng. Measurements of collisions between laser-cooled atoms. *Advances In Atomic, Molecular, And Optical Physics*, 34:125, 1993.

[128] John Weiner, Vanderlei S. Bagnato, Sergio Zilio, and Paul S. Julienne. Experiments and theory in cold and ultracold collisions. *Rev. Mod. Phys.*, 71(1):1–85, Jan 1999.

[129] Stefan Wessel, Fabien Alet, Matthias Troyer, and G. George Batrouni. Quantum monte carlo simulations of confined bosonic atoms in optical lattices. *Phys. Rev. A*, 70(5):053615, Nov 2004.

[130] Biao Wu and Qian Niu. Landau and dynamical instabilities of the superflow of bose-einstein condensates in optical lattices. *Phys. Rev. A*, 64(6):061603, Nov 2001.

[131] Biao Wu and Junren Shi. Critical velocities for a superfluid in a periodic potential. *cond-matt/0607098*, 2006.

[132] K. Xu, Y. Liu, D. E. Miller, J. K. Chin, W. Setiawan, and W. Ketterle. Observation of strong quantum depletion in a gaseous bose-einstein condensate. *Physical Review Letters*, 96(18):180405, 2006.